Author:
Tretiak, Iryna

Title:
Effect of voids on the interlaminar failure of carbon/epoxy composites

EFFECT OF VOIDS ON THE INTERLAMINAR FAILURE OF CARBON/EPOXY COMPOSITES

Iryna Tretiak

A dissertation submitted to the University of Bristol in accordance with the requirements for award of the degree of Doctor of Philosophy in the Faculty of Engineering

December 2018

Word Count: 49148

ABSTRACT

Porosity is a common manufacturing defect in composite materials. It can be caused by inadequate debulk, curing cycles or trapped air, and has significant effects on the matrix-dominated properties of a composite. It is almost impossible to eliminate voids during manufacturing, and they can lead to the development of other defects such as delamination.

Many researchers have investigated the influence of void content on the mechanical performance of composites. However the size, shape and location of voids are important parameters often not characterised. With knowledge of the size, shape and location of voids it is possible to not only qualitatively understand the failure of composites under load, but also to quantitatively compare their effects using numerical modelling techniques.

The main objective of this thesis is to understand the effect of void features on the strength of composite materials, and to identify the void characteristics most influential in affecting the failure of composites. To achieve this goal, it was necessary develop a technique to manufacture samples with a controlled void content. A novel pressure and temperature-controlled method was used, and by varying manufacturing parameters, such as compaction temperature and pressure, it has been shown that samples with a range of void contents can be produced. Furthermore, two different material systems and lay-ups have been investigated.

To characterise the voids, each sample has been analysed by X-ray Computed Tomography, which is a non-destructive technique that is allows the size, morphology and location of every void in a sample to be extracted and post-processed. However, accurate characterisation of the voids requires accurate identification of the void boundary and separation of the void from the surrounding composite material. A new, simple, rigorous, reproducible and accurate CT-segmentation thresholding method is proposed to characterise voids in a wider range of composite systems and with reduced errors than previously known threshold methods.

To characterise the effect of voids on strength, the short beam shear (SBS) test was used, and then results were correlated to the void morphology, size and location. This provided valuable information that helps to better understand the failure behaviour of composites containing void defects, and specifically how the voids influence the failure. Furthermore, a simplified finite element model was developed and compared to the experimental results.

This investigation has been undertaken on two different material systems, revealing useful information on the criticality of particular void features in composites that may be used in more detailed finite element models, such as micro-mechanical models, and may also inform manufacturing tolerances for acceptable engineering design.

-In loving memory of my grandparents

PUBLICATIONS

The following publications were produced during the course of this Research Project. In particular, the author would like to acknowledge that Section 2.2 and Chapter 3, reuses work published in [1a]. Section 4.1, Section 4.2 and Section 4.5, Section 5.1, Section 5.2 and Section 5.3.1 contain some results from [2a] and [3a],

Journal Publications

[1a] Tretiak, I, & Smith, R. (2018). A parametric study of segmentation thresholds for X-ray CT porosity characterisation in composite materials. Composites Part A. Accepted subject to corrections.

Conference Papers

[2a] Gagauz, I, Kawashita L.F., Hallett, S.R. (2016). Effect of voids on interlaminar behaviour of carbon/epoxy composites. 17th European Conference on Composite Materials.

[3a] Gagauz, I, Kawashita L.F., Hallett, S.R (2017). Understanding the effect of void morphology and characteristics on laminate mechanical properties. 21st International Conference on Composite Materials (ICCM-21)

ACKNOWLEDGEMENTS

I would like to express my sincere gratitude to my supervisors, in particular to Prof. Stephen Hallett, who gave me an opportunity to work in a world-leading composite institute and provided me with guidance throughout my PhD, and to Prof. Robert Smith, who welcomed me in his research group, gave me knowledge in X-Ray CT and analysis of defects, and was always available to discuss results.

I am also grateful to Prof. Michael Wisnom, who monitored my progress during my thesis. His expertise, comments and suggestions, as well as our discussions were very helpful.

The numerical aspects of my work are in part due to the assistance I received from Dr. Luiz Kawashita and Dr. Bassam El Said.

I would like also to thank my colleagues Ms Katie Smith, Dr. Ollie Nixon-Pearson, Dr. Yusuf Mahadik and Dr. Christina Fraij for their support in X-Ray CT.

Also, I appreciated the help of people who assisted me in manufacturing and preparing my samples – Mr Ian Chorley, Mr. Simon Ball and Mr Pete Whereat. Furthermore, I am grateful to Dr. Steven Rae, whose help in the lab was priceless.

I would also like to acknowledge Rolls-Royce plc who funded this research project.

I wouldn't be able to go through this PhD without the support of my close family, in particular my mom and my sister who supported me spiritually throughout these years. However, I can't be grateful enough to my amazing husband David, who have been with me throughout the whole journey of my PhD, believing in me, supporting me and giving me strength to continue.

DECLARATION

I declare that the work in this dissertation was carried out in accordance with the requirements of the University's *Regulations and Code of Practice for Research Degree Programmes* and that it has not been submitted for any other academic award. Except where indicated by specific reference in the text, the work is the candidate's own work. Work done in collaboration with, or with the assistance of, others, is indicated as such. Any views expressed in the dissertation are those of the author.

SIGNED: ..... DATE:.....

CONTENTS

LIST OF TABLES

LIST OF FIGURES

LIST OF ABBREVIATIONS AND ACRONYMS

AFP	Automatic Fibre Placement
CPT	Cured Ply Thickness
CT	Computed Tomography
DSC	Differential Scanning Calorimetry
DSLR	Digital Single-lens Reflex Camera
FE	Finite Element
FEA	Finite Element Analysis
FVF	Fibre Volume Fraction
ILSS	Interlaminar Shear Strength
LAC	Linear Attenuation Coefficient
MSE	Mean Squared Error
RTM	Resin Transfer Moulding
SBS	Short Beam Shear
SBSS	Short Beam Shear Strength
SD	Standard Deviation
SEM	Scanning Electron Microscopy
2D	Two-Dimensional
3D	Three-Dimensional
μCT	Micro-Computed Tomography

LIST OF APPENDICES

1 INTRODUCTION

1.1 Motivation

Fibre reinforced composites have become increasingly attractive for structural applications, particularly in the aerospace industry, due to their increased specific strength, durability, corrosion resistance, resistance to fatigue, and damage tolerance characteristics. Composite materials can also be tailored to meet precise design requirements and offer significant weight reductions in comparison with conventional materials, such as metals.

The size and shape of a particular part often dictates the manufacturing processes that can be used to make it, from the basic hand lay-up approaches, to more advanced automated fibre placement (AFP) processes, and moulding processes, such as resin transfer moulding (RTM). All of these manufacturing processes have the potential to introduce defects into the composites, and it is almost impossible to achieve a defect-free part, with each manufacturing process introducing defects in different ways.

Defects in composites can be divided into three categories – matrix, fibre and interface defects [1]. Partially cured composites, resin-rich areas, and voids are all matrix defects, fibre misalignments, waviness, and irregularities of the fibre distribution in the matrix are all examples of fibre defects, whereas delamination can be formed at the interface (see Figure 1-1).

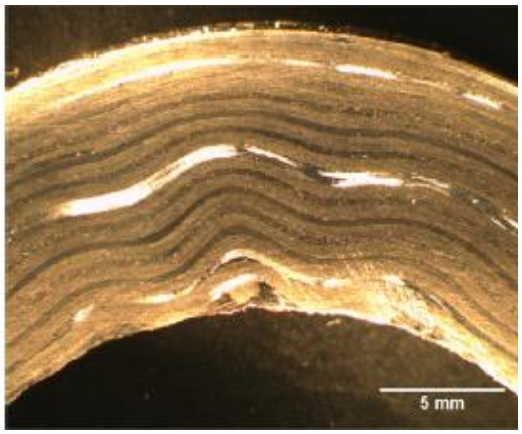

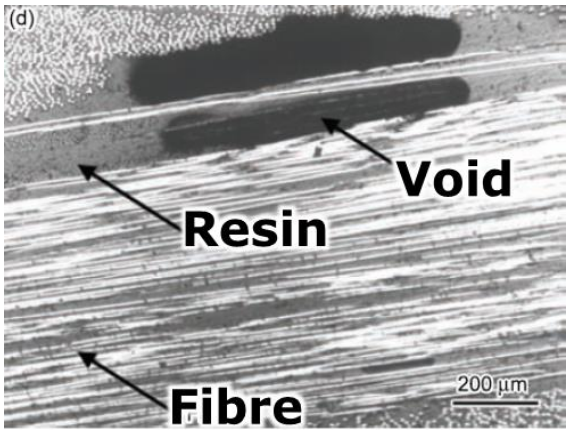

Fibre waviness [2] **Voids [3]**

Figure 1-1. Common defects in composites

Arguably, voids tend to be one of the most critical manufacturing defects, as it is difficult to eliminate them during manufacture, they can cause other defects, such as delamination, and have been shown to have a detrimental effect upon the mechanical performance of composite materials. Currently, industry typically applies a criterion that the void content within a part should not exceed 2% average void content, and any parts having a larger void content should be discarded. However, this method assumes a homogeneous distribution of the void content in a part and is therefore not conclusive in determining the usability of a part. For example, some sections of a part may contain higher percentages of voidage in critical locations that will inevitably lead to premature failure. Alternatively, a part may have an average void content higher than 2%, but the voids are concentrated in low stress areas. In this case, the part may be discarded even though it would be suitable for service.

The inconsistency of the overall void content criteria is also apparent when considering the effect of individual voids and their interactions with other voids. For instance, a part may have an apparently small void content, but contain one large void that can act as stress concentrator and can cause premature failure. The part may also include many voids located in close proximity to each other, such that during operation of the part cracks migrate and merge the voids together, thereby leading to premature failure of the structure.

It may therefore be important to also take into account specific void features, such as size, shape, position, and distribution, which may be critical to the failure of the structure.

1.2 Technical Challenges

The identified key technical challenges and unanswered questions are highlighted below:

Previously, the majority of work has been focused on the correlation of the average void content to the mechanical properties of composites. However, the size, shape, distribution and location of voids will all affect the composite strength, and these void characteristics are also likely to interact, such that a combination of these void features is required to predict the failure behaviour. To obtain this void information, it is essential to use a modern non-destructive testing (NDT) tool, such as X-ray CT. However, despite the usage of X-ray CT to characterise porosity in recent studies, there is no accurate and simple post-processing tool that can reliably be used to separate composite from void, and thereby detect the boundary of the voids. Thresholding methods are the easiest post-processing tool, however there is no established agreement regarding which threshold provides the minimum error in a wide range of composite materials.

The formation of voids in composite materials is a complex process that is difficult to predict and control. The distribution, morphology, and sizes of the voids can differ greatly for different process parameters, different materials, and different stacking sequences. Even under the same conditions, two manufactured panels can form quite different voids. It is very challenging to manufacture samples with a desirable void content in a controllable manner. A manufacturing process that can be used to develop specimens with controlled void content would be beneficial in further investigating the influence of voids.

Although many research groups have investigated the influence of voids on composite properties, there remains a lack of experimental data on the void features that are most critical to the mechanical performance of composites, and a lack of understanding of their effect on the mechanical performance of composites. This data can be used to identify simple analytical expressions that help to estimate the failure strength of composites containing voids. It may also eventually be used to develop micromechanical models that provide a more in-depth understanding of void effects and help the development of improved industry standards and knock-down factors.

Modelling the behaviour of laminates containing voids can be also challenging. Detailed finite element (FE) analysis, such as micromechanical modelling, is complex, computationally expensive, and typically only feasible for analysing particular portions of a larger specimen. Even then, the implementation of these models requires many

assumptions and simplifications to be made with respect to the experimental testing. A simple and accurate model is generally preferred by industry that can be used to pass or fail composite components based on homogenised information of porosity at a component, or ply level.

1.3 Objectives

Based on the technical challenges, the objectives of this thesis can be summarised as follows:

1) Development of a thresholding method for the accurate characterisation of voids, specifically for accurate identification of the void boundary, *i.e.* separation of the void from the surrounding composite material.
2) Development of a manufacturing technique to produce samples with controlled void content.
3) Generation of a void features dataset, which can be used in a detailed analysis of the effect of critical void features on the failure of composite materials.
4) Development of a simple analytical and finite element (FE) tools to predict the short beam shear strength of composites, based on void information.

1.4 Novelty of the work

In overcoming these technical challenges, the following points of novelty are found:

1) A simple model was developed to simulate the CT-response to porosity. This provides the 'true' value of the void volume fraction and therefore the size of the voids.
2) With knowledge of the 'true' value of the void volume fraction, it was shown that that a commonly used segmentation method '50% thresholding method' is most accurate amongst other investigated thresholds in all but a few situations.
3) A new adaptive threshold was introduced. This method is the first known thresholding method to provide an optimal solution for the full range of commonly encountered grey level histograms.
4) A temperature and pressure-controlled method was successfully introduced to manufacture samples with the range of void contents.
5) An extensive experimental data set has been obtained, containing 3-D information of all voids within each sample using X-ray CT.

6) The critical void features were identified using statistical analysis of the X-ray CT dataset and experimental results. A ‘critical void size’ was found, below which the voids don’t contribute to the failure and can be neglected.
7) A novel comparative analysis of pairs of samples, with the same void content but different strength level, was introduced. This analysis provided important information of critical void features that affect the failure of composites.
8) A simple analytical tool to predict the Short Beam Shear strength of carbon/epoxy composites, based on the void information obtained from X-ray CT, was introduced. This method allows for a quick check of the effect of voids on the strength of the composite structures without testing.
9) A simplified FE model was developed to simulate the effect of voids in composites for different lay-ups. By knowing only the average void content of the composite it is possible to predict the failure strength by reducing certain parameters.

1.5 Structure of thesis

Based on the research objectives set in this thesis, the outline is described below:

Chapter 2 ‘Literature review’ presents a review of the literature relating to void formation, void characterisation, and the effect of voids on the mechanical properties of composite materials, particularly the interlaminar shear strength (ILSS)

Chapter 3 ‘**A parametric study of segmentation thresholds for X-ray CT porosity characterisation in composite materials’** proposes a simple and accurate X-ray Computed Tomography (CT) segmentation thresholding method to characterise voids in composites. Sources of uncertainties in the results are investigated using a developed simulation, and recommendations are made to minimise those uncertainties. This Chapter is based on Objective 1 (section 1.3) and discusses Novelties 1-3 (section 1.4) in detail.

Chapter 4 ‘Effect of the manufacturing process on voids in composite laminates’ introduces a novel manufacturing process that allows the production of samples with a range of void contents for two material systems – IM7/8552 and IMA/M21. The effect of the manufacturing parameters on the void content and void morphology are also discussed in this chapter. This Chapter is based on Objective 2 (section 1.3) and discusses Novelty 4 (section 1.4) in detail.

Chapter 5 'Statistical analysis of the effect of void features on composite strength' provides statistical analysis of the void features on short beam shear (SBS) strength, in which critical void features are identified. This analysis is based on the extensive void dataset obtained from X-ray CT. This Chapter is based on Objective 3 (section 1.3) and discusses Novelties 5-7 (section 1.4) in detail.

Chapter 6 'Prediction of SBS strength of carbon/epoxy composites' contains a comparison of different methods of predicting the SBS strength in carbon/epoxy composites for different material systems and different lay-ups, using information about voids obtained from X-ray CT. This Chapter is based on Objective 4 (section 1.3) and discusses Novelty 8 (section 1.4) in detail.

Chapter 7 'Modelling the failure behaviour of the laminated composites containing voids' presents a simplified FE model to simulate a short beam shear (SBS) test for two laminate lay-ups: cross-ply and angle ply. A parametric investigation is shown in order to identify the most critical material damage model properties and their correlation to the average void content. This Chapter is based on Objective 4 (section 1.3 and discusses Novelty 9 (section 1.4) in detail.

Chapter 8 'Conclusions' summarises the main conclusions of the work and provides recommendations for future work.

2 LITERATURE REVIEW

2.1 Void formation in composite materials

The mechanisms that determine the formation of voids are complex, and depend on many material properties, processing parameters, and geometrical constraints [4]. This makes it challenging to predict the level of porosity in a particular region of a composite part, and even more challenging to predict the distribution, size, shape, and morphology of the voids within that region.

Even so, it is known that voids primarily form in two ways:

(1) Volatiles (such as moisture and solvents) dissolved within the resin during the processing and storage of the resin, which are then released during the cure process; and
(2) Air trapped during the manufacturing processes when producing the composite.

In the case of volatiles, if the resin pressure drops such that it is below the vapour pressure of the dissolved volatiles within the resin, then the volatiles will be released from the resin and form voids within the composite [5]. The void will then continue to grow until its internal pressure is at equilibrium with the hydrostatic pressure of the resin. It is therefore logical that the quantity of volatiles dissolved within the resin will have an effect upon the level of porosity. In fact, Boey and Lye [6] showed that uncured resins stored and exposed to humid conditions for extended periods absorbed moisture from the air, and as a result produced composites with a higher void content.

2.1.1 The effect of processing parameters on void formation

Boey and Lye [6] also showed that the void content of the final part could be reduced by the application of a large pressure during the cure process, although it was not possible to produce a completely void-free sample. Grunenfelder and Nutt [7] also showed that a high resin pressure helped to suppress the dissolved moisture from forming into voids for both autoclave and vacuum bag manufacturing processes.

This effect is seen in pure resin systems and pre-impregnated fibres (prepregs) [8], demonstrating the importance of maintaining a controlled atmosphere during the manufacture of composites.

Although it has been shown that not only is it important to apply a high pressure in order to counteract the effect of dissolved moisture, it is also important to apply the pressure early in the cure cycle due to the lower viscosity of the resin in the early stages of the cure cycle [9].

The applied pressure is also important in the reduction of voids caused by entrapped air, as shown by Olivier *et al.* [10] for two different carbon/epoxy prepreg material systems. This study also showed that the void shape is affected by the applied pressure, particularly when the maximum pressure is applied when the viscosity is at its lowest. The result is that the voids become more elongated, presumably as they try to evacuate from the material system.

Liu *et al.* [11] also showed that the timing of the maximum applied pressure is important and that it should be matched to the minimum viscosity of the resin, although this can be countered by increasing the dwell time of the applied pressure if necessary, albeit at the cost of increasing the processing time.

The synergy between the applied pressure and the viscosity of the resin clearly indicates that the temperature of the composite during the cure process is also an important parameter. Hernandez *et al.* [12] showed that delaying the gelation of the resin (*i.e.* having a longer processing period) resulted in a lower void content, and that this processing period allowed the voids to evacuate from the system. The low viscosity and long processing period also allowed the remaining voids to elongate along the fibre direction, presumably as a result of trying to escape.

This change in the void shape during the cure process is clearly not instantaneous, as Agius *et al.* [13] showed by quenching IM7/8552 carbon/epoxy composite samples at different stages of the cure cycle. This showed that during the second temperature ramp of this material system, the voids increased in size although the average void content stayed the same. It seems that the increased resin flow during this portion of the cure cycle caused the smaller voids to merge.

In a later study, Hernandez [14] was able to produce samples of very low porosity (<0.2%) by optimising the temperature cycle to maximum the processing period. In addition, it was found that voids tended to cluster in resin rich areas, due to these resin

rich areas being supported by the fibre rich regions that surrounded them. As a result, the pressures on these resin rich areas were reduced and the voids were corresponding larger.

It's therefore abundantly clear that the cure cycle is very important to the resultant void content. And in fact, in some cases the manufacturers recommended cure cycle is less than ideal when trying to reduce the formation of voids [15].

2.1.2 The effect of material properties on void formation

Whilst the processing parameters are important in controlling the void content of composites, the role of the materials used to make the composite should not be overlooked. For instance, Thorfinnson *et al.* [16] found that reducing the impregnation of prepreg fibres reduced the porosity, because the dry areas within the prepreg allowed the volatiles and trapped air to escape more easily. Although, if the resin viscosity profile is not carefully tailored then poor impregnation can lead to significant porosity, as the resin is not able to take advantage of the pathways created by material system [17].

Clearly a balance needs to be struck between an initially viscous resin that allows dry areas to persist and the successful evacuation of air, and a low viscosity resin that allows full impregnation and the avoidance of dry areas in the final part but is more prone to excessive bleeding and void formation.

Void formation can also be caused by improper mixing of the resin, or poor preparation, as large amounts of air bubbles can be introduced into the resin that act as nucleation sites for further voids to form [5]. Therefore, it is common practice to degas resins before use to reduce the void content of the final part [18].

When there is air trapped within a laminate, the air will try to escape along the path of least resistance, which is generally the fibre direction. However, the distribution of these paths to the edge of the composite are not uniform due to the varying compaction levels through the thickness of the sample. Grunfelder [19] showed that the void content in the middle of the sample is increased as a result of the increased compaction, as the compaction causes an decrease in the permeability in these middle plies.

The importance of providing air evacuation channels is important in unidirectional laminates, however the challenges are even greater when using woven fabrics as the fabrics contain much more space for air to be entrapped [20]. Although the relative contributions to the void content resulting from the stacking sequence itself and the defects that arise from the stacking sequence are hard to differentiate [21].

2.1.3 The effect of geometry on void formation

The geometry of a composite part can also have a significant effect upon the formation of voids, and these problems increase with the complexity of the geometry. For instance, Ma *et al.* [22] investigated the voids that arise in corners. In particular, it was shown that the void content increased linearly with an increase in the thickness of the corner, although the increase varied depending on whether the corner was convex or concave (relative to the tooling). For convex corners the increase in void content with thickness was similar to the increase in void content observed in flat panels, however for concave corners the increase was much greater due to the reduced compaction and resin accumulation.

The challenges in minimising void content only increase as the size of the manufactured part increases, due to the difficulty in maintaining an even compaction pressure, the decreased number of air evacuation channels, the increased travel distance for voids trying to escape, and a proportional decrease in the breathing along the edges of the part [23].

2.1.4 Introducing voids into composites

Applying this knowledge of void formation (discussed in sections 2.1.1-2.1.3) to create composite samples with specified void contents allows the effect of voids on the mechanical properties of composites to be investigated. To effectively investigate the effects, it is important to have as much control over the void content as possible, as well as the distribution, size, and shape of the individual voids. This presents many challenges, and so alternative methods have been devised for introducing controlled porosity into composites.

For instance, it is possible to introduce PTFE (Teflon) monofilaments, tubes and strips to produce artificial voids [24], and it has been demonstrated that the effect of these artificial PTFE-voids has no significant effect on the mechanical properties beyond what an equivalent void would have.

2.2 Void Characterisation

Non-destructive testing (NDT) techniques are used to inspect composite structures after manufacture to remove the possibility of unacceptable defects. The most common non-destructive method to check for porosity in composites is ultrasound through-thickness attenuation measurements [25]–[27]. Defects in laminates such as delamination,

inclusions, voids, interlaminar cracks and foreign objects all cause attenuation of the ultrasound, which can be detected by comparison of ultrasonic pulse-echo (back-wall echo) or through-transmission amplitude measurements with a threshold. The measured attenuation can be correlated with through-thickness average void volume fraction but the correlation is poor due to the dependencies of attenuation on the other porosity parameters such as pore size and distribution. Whilst ultrasonic attenuation is sensitive to void volume fraction, size distribution and depth distribution, standard through-thickness attenuation measurements cannot differentiate between these. The result is that the uncertainties in the quantification of bulk porosity are large, making it very difficult to reliably achieve the desired low levels of porosity in production. For example, if 2% void volume fraction, V_{v} is the maximum allowable and the 95% single-sided confidence limit in the measurement is 1.2%, then the measured V_{v} must be less than 0.8% to give the required 5% probability that the actual porosity V_{v} is less than 2%.

Frequency dependence of ultrasonic attenuation provides an estimation of size distribution but has not been used successfully for porosity measurements in an inhomogeneous anisotropic solid [28]. Recent attempts to decompose the frequency-dependent pulse-echo response into separate contributions from porosity and thickening of resin layers by [29], [30] and [31] have had some success in producing a 3D map of local porosity. Whilst these methods have shown potential, they still need further work to improve the decomposition process.

Other NDT methods such as thermography and use of microwaves could be applicable in porosity determination but with some difficulties in practical use [32]–[34].

Acid digestion is an alternative technique that is able to give an estimate of the void content in a specimen [35],[36], although the technique is destructive, does not provide details of void morphology and has uncertainties that are generally larger than required for validation of NDT methods. Reliable information regarding void morphology and distribution can be determined by optical microscopy [11], [37], [36], [38]; however, this technique is restricted to 2D and requires samples to be cut in multiple sections, which leads to a loss of some information, and of the sample itself. Furthermore, microscopy is very inaccurate due to the possibility of inclusions appearing as a result of the polishing process. These inclusions might be indicated as voids on the micrographs.

Micro X-ray computed tomography (CT) is a promising non-destructive technique, which can give information about pore location, size and shape in three dimensions [38]–

[43],[44]–[46]. However, the technique is only able to accommodate small sample sizes, if a high-resolution image of the individual pores is to be obtained. Usually, validation of the CT images is performed by comparison with optical microscopy of slices of the sample, which give high-fidelity measurements of the individual voids captured during CT-imaging.

After CT-scan reconstruction, the object is represented as a set of voxels. Each voxel has a grey level, which is directly related to the effective linear attenuation coefficient (LAC) for X-rays of the incident photon-energy distribution in the corresponding voxel of the specimen. If the voxel contains more than one material, such as the edge of a pore and some composite, the effective LAC is comprised of a simple volume-weighted combination of the LACs of the constituent materials [47] – the 'simple volumetric mixture rule' – which is particularly important for the work in this thesis. The value stored at each CT voxel is called the grey level and is related to the effective LAC via contrast (gain) and brightness (offset) controls [47] and a transfer function that is primarily linear but, unfortunately, can vary slightly within the scan due to complications such as beam hardening. For the purposes of this thesis, a constant, linear transfer function will be assumed. The grey-level histogram of the sample generally has two peaks, which represent air and composite material; sometimes, if there are thick resin layers or other resin-rich regions, it is possible to detect three peaks, which correspond to air, resin-only and composite. However, in most of the cases, the resin-only and composite peaks are merged due to similarities in their attenuation coefficients and the width of their scattering-noise distributions. To identify and characterise the morphology of voids in the specimen, an image 'segmentation' must be applied, which is simply a rule-based decision about whether a given voxel is inside a pore or not. Thus, image segmentation assigns voxels to one of the groups: 'air' or 'material'. The simplest tool is to use a global threshold to separate these voxels: below the threshold is 'air', above the threshold is 'material'.

A segmentation threshold can be manually selected [48], however its selection relies heavily on user interpretation. This introduces uncertainty to the results, as the results can be highly sensitive to changes of the threshold, particularly when the pore size is small so that there is a high ratio of pore-edge voxels, including part of the edge of a pore, to internal pore voxels. Researchers have suggested improvements to manual threshold selection in which a reference sample is CT-scanned at high resolution, so that a threshold is manually determined based on high resolution scans and then subsequently used for

the remaining lower resolution specimens [49], [50]. Optical microscopy has similarly been utilised for calibration of the chosen threshold [45], however these techniques are flawed for morphology characterisation because they will affect each pore size and shape differently.

Other works have used the 'Otsu threshold' of minimization of variance between the material and air voxel populations [51], which is basically a first-moment method to segment the histogram, analogous to a centre-of-mass calculation. Some researchers based their threshold on a local variance method from Niblack [52], adapting the threshold according to the mean and standard deviation of the higher-attenuation peak, belonging to the composite material in this case [12]. Others used algorithms embedded in image processing software, such as Avizo [53], Fiji™[46] and ScanIP [44]. Kastner *et al.* [39] did a comparison of the effect of different thresholds on the porosity measurement by comparison with acid digestion. They selected one of the investigated thresholds for comparison with acid digestion, and showed a correlation coefficient of 0.993 between the methods. However, the void content determined from acid digestion is known to vary depending on factors such as the amount of acid used, the digestion time, and the temperature during digestion. Experimental errors are also introduced by the accuracy of the weight measurement scales, and accuracy of the physical densities of the fibre and resin used in the calculations [54].

Plank *et al.* [55] used reference samples with artificial porosity created by drilling holes, with diameters of 0.2 and 0.3 mm, in order to assess and compare different thresholding methods. The void content of the reference samples was determined by taking an average of the measured diameters of the holes, calculated manually from high-resolution microscopy images assuming an ideal cylindrically shaped hole. However, an average value is required in order to tackle the inherent inaccuracies of the method. For instance, the drill is unlikely to be perfectly perpendicular to the composite surface during drilling, and the drilling itself is liable to introduce delamination, fibre splitting, and breakout of the back surface of the laminate, which are difficult to observe and impossible to account for with this method. More recent work by Plank *et al.* [56] used high-resolution Micro-CT scans to determine the true porosity and then showed that the required threshold to give the true average V_v increased with increasing voxel size.

Nikishkov *et al.* [41] also used samples with porosity created by drilling holes with a diameter of 0.1 mm. The manufactured samples were used to compare different thresholding techniques and, in particular, to validate a proposed density-based

contouring method, which is based on the assumption that CT grey values are proportional to material density. The method uses sub-pixel contour generation for the average of the air and material grey values obtained in CT scans. The results showed that a threshold at 0.5 (on a normalised grey scale where the air peak is at zero and the composite peak is at 1) is the most accurate thresholding method of those investigated (other thresholding techniques including minimum threshold, Fuzzy C-means threshold, sub pixel edge detection). Although the authors showed that the threshold at 0.5 for pore detection works well, they did not compare the measured void content with the true value or conduct a parametric study of bias in the measurements, as this could not be achieved experimentally.

In fact, the predilection of comparisons to experimentally produced reference samples has meant that no works have investigated the effects of different X-ray, sample or porosity parameters on porosity characterisation.

2.3 The effect of voids on mechanical properties

Voids have been of interest in the field of composite materials since the 1960's, due to the detrimental affect they have on the mechanical properties. It is therefore important to understand how voids affect the mechanical properties and to quantify this effect, particularly as the effect is more pronounced for matrix-dominated properties, such as interlaminar shear, compressive and flexural strength.

2.3.1 Tensile properties

The effect of voids on the longitudinal tensile properties has been shown by a number of studies to be minimal due to it being a fibre-dominated property, although the effects are not entirely insignificant. For instance, Olivier *et al.* [10] showed that whilst the longitudinal tensile modulus and Poisson's ratio are not affected by void content, there was a moderate longitudinal tensile strength decrease of up to ~12% in specimens with large void contents (< 10%), which could be attributed to the voids causing local fibre deformations. Subsequent studies have also shown the insensitivity of the modulus to void content [11] and a similar small decrease in the tensile strength [11], [57]–[59], although in some studies the effect of voids is so small as to be negligible [60].

Zhu *et al.* [3] investigated the effect of voids on different quasi-isotropic lay-ups, finding that the lay-up did have some marginal effect on the shape of the voids, wherein samples with larger voids had a lower tensile strength. Gurdal *et al.* [61] similarly showed the

effect of voids in quasi-isotropic lay-ups, showing that when plies with the same fibre orientation were adjacent, larger voids were likely to form that had a greater effect on the strength.

However, the effect on the tensile strength was small, and negligible for the tensile modulus. Naganuma *et al.* [62] also showed that the type of voids could have an effect on the tensile strength, by showing that voids open to a free surface of the specimen (*e.g.* along the thickness outer surface) had a greater affect than voids enclosed within their woven composite samples.

In contrast to the effect of voids on longitudinal tensile properties, the relative effect on the transverse tensile properties for unidirectional laminates is greater. For instance, Olivier *et al* [10] found that at an average void content of ~10% the transverse tensile strength decreased by ~30%, whilst the transverse modulus decreased by ~9%. This is in comparison to the longitudinal modulus, which showed a negligible decrease, and the longitudinal strength, which decreased by a moderate ~12%. Similar reductions in the transverse stiffness and strength have been found in other composite prepreg composites [63] and resin transfer moulded laminates [64].

2.3.2 Compressive failure

The effect of voids on the compressive failure is not so clear, with some studies showing as much as a 27% compressive strength reduction at a void content of ~11% [65], whilst others show only a moderate decrease of the compressive strength with increasing void content [14], [58], or no clear effect at all [66]. This variability in the effect of voids on the compressive properties could be due to the interrelation the voids have with the performance of the fibres, with the decrease in compressive strength having been attributed to a combined effect of multiple composite defects including voids, fibre waviness, and fibre misalignment [67].

The effect of the void is to reduce the matrix-fibre interfacial bonds, thereby decreasing the lateral support of the matrix on the fibres [68]. Liebig *et al.* [69] showed that this loss of fibre stability could lead to fibre kinking/buckling, and as a result cause premature failure of a sample. The matrix-fibre load transfer capacity therefore depends significantly on the morphology of the voids, with a decreased fibre stability for fibres adjacent to voids elongated in the fibre direction [70]. Similarly, Hernandez *et al.* [14] showed that the distribution of voids was important, with clustered voids having a greater effect on the compressive strength.

2.3.3 Flexural properties

Decreases in the flexural strength and stiffness have been recorded due to the presence of voids [11], [63], [71], [72]. Stamopoulos *et al.* [63] suggested that the voids interacted with the damage mechanisms and thereby accelerated failure, and this was why flexural strength is affected by the presence of voids more than the flexural stiffness. Hayashi *et al.* [73] showed that the reduction in flexural properties in unidirectional properties was reduced for chopped fibre tapes compared to prepreg cross-ply laminates. It was suggested this was due to the increased spread in fibre orientations for the chopped fibre laminates, although a detailed analysis of the different void morphologies was not conducted.

The interaction of voids with the damage mechanisms led to Chambers *et al.* [74] to show that the effect on the flexural fatigue performance can be even greater, and that a 'critical defect' volume existed, whereby voids smaller than a certain size (*i.e.* 0.03mm^3) did not meaningfully contribute to the failure. Furthermore, above the 'critical void' volume, the void characteristics, such as void shape and size, became more critical to the flexural failure than the average void content of a specimen.

The effect of voids can also increase the thickness of a composite. Hagstrand *et al.* [75] showed that even though the flexural stiffness and strength decrease due to the presence of voids, the increase in thickness of the samples (due to voids) caused a slight increase in the overall rigidity and load capacity due to the increase in structural moment of inertia.

2.3.4 Interlaminar toughness

There are surprisingly few papers reporting the effect of voids on the interlaminar toughness of composites. Asp and Brandt [76] studied the effects of voids on the mode I, mode II and mixed mode properties. This study showed that there was a small decrease in the strain energy release rate at crack growth initiation for both pure mode II and mixed mode testing, but no effect on mode I. However, the voids caused changes in the failure mechanisms of the propagating cracks, such that the cracks jumped between plies and caused interlaminar toughening. The strain energy release rate of crack propagation in mode I testing was therefore moderately increased. This effect was observed in the mixed mode tests, although the effect was diminished as the mixed mode became proportionally more mode II dominated.

Mouritz [77] subsequently looked at the effect of voids on the mode I interlaminar toughness, and showed that the voids caused a decrease of the strain energy release rate

at crack initiations and propagation. This was said to be due to the crack branching not being extensive enough to travel between plies.

2.3.5 Void effect on interlaminar shear strength

The ability of a composite material to resist delamination damage relies heavily on the interlaminar shear strength (ILSS) of the material. ILSS is a property dominated by the matrix and the matrix/fibre interface, and so it is very sensitive to the presence of voids.

Some of the earliest work in this research field goes back to 1968, when Bascom and Romans [78] and Kohn *et al.* [79] investigated glass-filament wound composites that contained voids. Many other studies have since investigated the reduction of the ILSS due to voids [43], [58], [80]. The work of Kohn *et al.* [79] was one of the first to identify the linear regression of ILSS with an increase of the average void content, showing a good linear correlation coefficient of 0.95 in the range of 0.08% to 7.4% void volume fraction.

This linear relationship between the ILSS of a specimen and its average void content is also found in many other studies up to void contents of 30% [77], for different material systems, such as glass-fibre reinforced composites [57], [77], carbon-fibre reinforced composites [11], [25], [81], and natural fibre systems [82], different resin systems [83], and different manufacturing processes, such as for composites manufactured by out-of-autoclave techniques [84], resin transfer moulding (RTM) and from pre-impregnated plies [85].

The linear relationship has also been found in samples containing artificially created voids, such as from hollow polymer microspheres [77] and hollow tubes [86], and is not restricted to unidirectional composite laminates, as it has also been shown when testing different quasi-isotropic laminates [3].

It has also been shown that, whilst the relationship remains linear, many of these parameters affect the rate at which the ILSS decreases with average void content. For example, Thomason [87] showed that the slope depends significantly on the fibre surface coating, whilst Costa *et al.* [88] found that a hygrothermal environment could amplify the effect of voids on the ILSS.

However, the results of some studies suggest that the relationship may actually be non-linear. For instance, Koushyar *et al.* [89] showed very little effect on the ILSS at low average void content (<1%) and then a rapid decrease at higher average void contents.

Tang *et al.* [90] showed a similar non-linear relationship, although the low number of experimental points limits confidence in the degree of non-linearity.

2.3.5.1 Attenuation coefficient correlation to the void content and ILSS.

One of the major tools for the inspection of composites with defects has been ultrasound inspection, using through-thickness attenuation measurements. In the case of voids, this is due to the correlation that has been identified between the attenuation coefficient and the average void content, and therefore also the ILSS.

Stone and Clark [25] showed that there is a bi-linear relationship between the attenuation coefficient and the average void content. It is said that this bi-linearity is due to the difference in the void shapes at different void contents, for instance the samples with average void contents below 1.5% tended to have more spherical voids, whilst samples with average void contents above 1.5% tended to have voids that were more flattened and elongated. This may also help to explain the non-linear relationship between ILSS and average void content, which is generally linear at average void contents below 2% but decreases asymptotically with further increases.

In a later study, de Almeida and Neto [71] proposed a criterion to correlate ultrasound attenuation (or void content) and ILSS (Eq. 2-1), which was based on the equation proposed by Mar and Lin [91] for tensile failure of fibre reinforced composites with holes. This criterion showed good agreement with the experimental results from Stone and Clark [25], and is given by:

$$\boldsymbol{\sigma_f} = \begin{cases} \boldsymbol{\sigma_{f_0}} & \textbf{if} \quad \boldsymbol{\alpha \leq \alpha_{cr}} \\ \boldsymbol{H(\alpha)^{-m}} & \textbf{if} \quad \boldsymbol{\alpha > \alpha_{cr}} \end{cases} \qquad \textbf{(2-1)}$$

wherein $\sigma_{f0}$is the fracture stress of a laminate with low void content (as zero void content predicts infinite strength), α_{cr} is the critical value of the absorption coefficient, empirical factor H is the composite toughness, the exponent m (typically between 0.28 and 0.35) is the order of the singularity of a crack with its tip at the interface of two materials.

The critical value of the absorption coefficient can be obtained using the following equation:

$$\log a_{cr} = -\frac{1}{m}\log\left(\frac{\sigma_{f0}}{H}\right) \qquad \textbf{(2-2)}$$

This approach has been successfully implemented by a number of other researchers [36], [92], [93]. However, Mouritz [77] showed in a study on glass woven polyester

composites that the Mar-Lin theory was not applicable for highly porous composites (above 12% average void content).

2.3.5.2 Effect of void morphology on ILSS

As will be discussed in Section 4.5, different material systems, process parameters, and stacking sequences can affect the void distribution and void morphology. In turn, these void features influence the ILSS.

For instance, Olivier *et al.* [10] investigated two different carbon/epoxy laminates, which each showed a different decrease of ILSS with average void content increase. Whilst this may be partly due to the different material systems themselves, it was also found that the material system with the larger voids showed the larger decrease in ILSS. This suggests that the sizes of voids within a composite are important in determining the ILSS, and should be used in combination with the average void content to provide a better indication of the expected ILSS.

The importance of void size has also been shown in a number of other studies [85], [86], [94], with Goodwin *et al.* [85] and Zhu *et al.* [94] also suggesting the importance of other void characteristics, such as length and shape.

This can be explained by the effect of void morphology on the failure of composites, as the voids can act as stress concentrators that initiate failure [24]. The shape of the voids can also influence the crack direction by redirecting the cracks, bifurcating the crack, and providing a crack path through multiple voids [89], [94], [95]. This behaviour was shown in a post-mortem analysis of samples with voids by Zhu *et al.* [94] (See Figure 2-1).

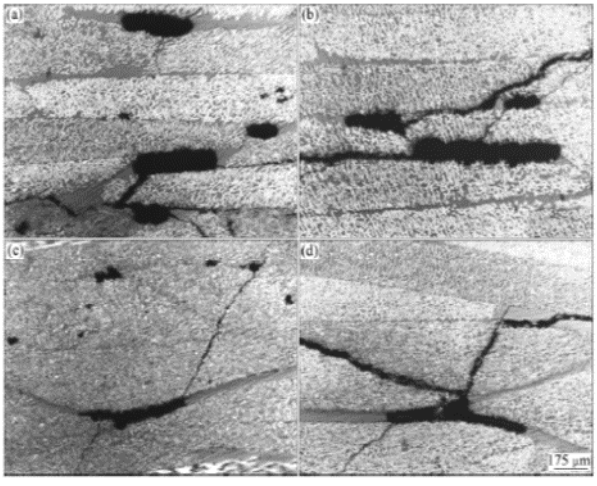

Figure 2-1 Micrographs of tested specimens with different average void contents showing cracks emanating from the voids: Average Void Content (%) - (a) 3.9%, (b) 6.5%; (c) 1.7%; (d) 4.7% [94].

2.3.5.3 Prediction of the ILSS

There have been many attempts to predict the effect of voids in composites, in addition to the Mar-Lin failure criteria [71], for example, Bowles and Frimpong [96] used micromechanical equations developed by Murthy and Chamis [97] to correlate the ILSS with void content, producing the following expressions for the ratio between ILSS of a laminate contacting voids ($ILSS_v$) and that of pristine, void-free laminate $ILSS_0$.

Spherical voids:

$$\frac{\mathbf{ILSS_v}}{\mathbf{ILSS_0}} = \mathbf{1} - \mathbf{0.785}\left[\frac{\mathbf{6}\,\boldsymbol{V_v}}{\boldsymbol{\pi}\,(\mathbf{1}-\boldsymbol{V_{fv}})}\right]^{\mathbf{2/3}}, \qquad \textbf{(2-3)}$$

Cylindrical voids:

$$\frac{\mathbf{ILSS_v}}{\mathbf{ILSS_0}} = \mathbf{1} - \left[\frac{\mathbf{4}\,\boldsymbol{V_v}}{\boldsymbol{\pi}\,(\mathbf{1}-\boldsymbol{V_{fv}})}\right]^{\mathbf{1/2}}, \qquad \textbf{(2-4)}$$

where V_v is the void content, V_{fv} is the fibre volume fraction.

In applying these equations, Bowles and Frimpong [96] found that although the voids in the composites were mostly cylindrical, a much better fit was found assuming a spherical void shape. The reason for this result is not understood, although it is suggested by the authors that that this is could be due to the distribution of the voids, or that the voids behave as small delaminations or cracks, and the equation that relates the ILSS to this delamination/crack behaviour coincidentally happens to have a similar form as eq. 2-2.

Koushyar *et al.* [89] also applied the micromechanical equations developed by Murthy and Chamis [97] and found good agreement with the experimental data for specimens with low average void content (< 1%). However, when the average void content increases the equation increasingly deviates from the experimental data. In contrast to Bowles and Frimpong [96], Koushyar *et al.* [89] found a marginally better fit when assuming cylindrical voids (*i.e.* eq. 2-3). This is consistent with the voids observed in the samples, which appeared to be elongated in the fibre direction.

Another simple model can be introduced that assumes the voids are cylindrical and packed in a periodic array, such that the reduction in ILSS can be correlated to the reduction of the composites cross-section, (*i.e.* net section analysis),

$$\boldsymbol{\tau_{ILSS}(V_f) = \tau_{ILSS}(0\%)\left[1 - \left(\frac{4V_f}{\pi}\right)^{1/2}\right]} \quad \textbf{(2-5)}$$

where $\tau_{ILSS}(0\%)$ is the ILSS for a void-free laminate.

This was originally investigated by Wisnom *et al.* [24], who showed that the theory predicts the ILSS well when compared with experimental results, although the experimental data was very limited. In addition, the voids were created artificially using PTFE (poly-tetrafluoroethylene) tape and so had idealised shapes.

Hernandez *et al.* [12] also compared the net section analysis to a limited set of experimental results and showed that the general trend of the ILSS reduction was well captured by the net section analysis at larger average void contents (> 1%). However, the ILSS was overestimated for the composites with void content below 1%. It is suggested that this discrepancy is related to the differing shapes of the voids at average void contents above and below 1%, although this is not confirmed.

2.4 Modelling of Voids in Composites

Surprisingly, the effects of voids on the mechanical properties of composite materials haven't been widely investigated using numerical finite element (FE) models. Most of the modelling work that has been done has looked at the microstructural scale.

For example, Vajari *et al.* [98], [99] investigated the effect of multiple voids in unidirectional composites under transverse normal and longitudinal shear loading using a 3D representative volume element (RVE) FE model in Abaqus. The models included two different types of randomly distributed voids – inter-fibre voids (voids extending between adjacent fibres) and circular matrix voids (voids entirely enveloped by matrix). The fibres were modelled as isotropic and elastic, however, in order to capture the brittle behaviour of an epoxy matrix, the matrix is modelled using a modified form of the Drucker-Pragel model developed by Lubliner [100].

In contrast , Huang and Talreja [101] looked more closely at the behaviour of a single void by modelling one-eighth of an RVE containing a single cigar-shaped void (with an elliptical cross-section) in a homogeneous composite. The results showed good agreement with an analytical model, and were also found to agree well with experimental data available in the literature. More recently, Carraro *et al.* [102] replicated the real geometry of a void obtained using optical microscopy, modelling the plies as homogeneous and orthotropic. The 2D model displacement boundary conditions and

assumed plane strain, and was able to show agreement with the crack initiation and propagation found from the experimental results.

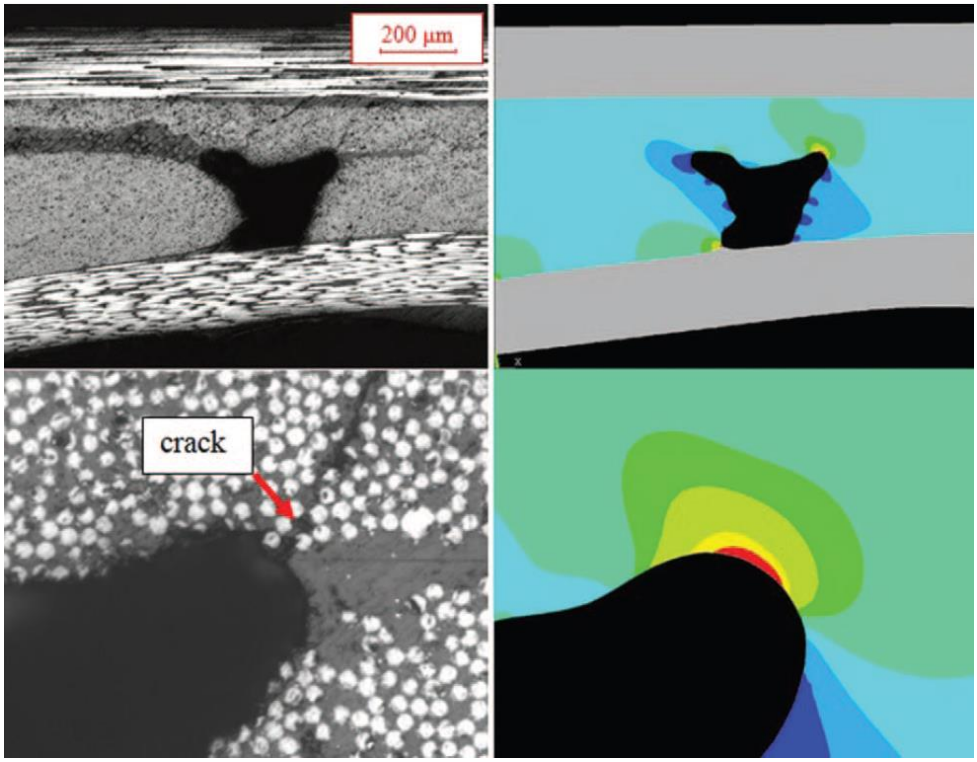

Figure 2-2. Example of the principal strain plot in FE analysis carried out on geometry extracted from micrographic image [102].

These models do not however give a good overall picture of the effect on structural performance due to voids as they are too small scale and not related to overall void content of a sample. The microstructural level is therefore a level below what is the focus of the work in this thesis, which is instead aimed at the engineering structural capability.

Nikishkov *et al.* [103] developed a mesoscale short beam shear test FE model. Voids were introduced into the model based their detection from CT-images of real composite specimens, with the properties of the voids simulated by reducing the stiffness of the elements in void locations and voids smaller than the element size neglected from the analysis. This showed that a single large void in the critical area can cause a greater reduction in the mechanical properties than a number of voids spread throughout the composite.

For small scale structural capability, ply-by-ply models with individual damage modes included are becoming increasingly common and have been shown to be an accurate and useful tool. These models include for example, continuum damage models for matrix cracking [104]–[106], cohesive interface elements for delamination [107]–[110] and fibre failure criteria [105], [106], [111], [112]. They have been used effectively to

investigate geometric features such as open-hole failure [113]–[117] and to predict failure due ply terminations in tapered laminates [118]–[121]. More recently, ply-by-ply models have been used to investigate manufacturing defects, such as wrinkles [2], [122].

However, to the knowledge of the author, no work has been done so far to investigate how to model the effects of voids at a ply-by-ply scale.

2.5 Concluding Remarks

As has been shown in the literature, voids are difficult to eliminate and have a significant effect upon the mechanical properties of composite materials. This has resulted in many studies on voids in composites, although gaps remain in the literature that will be addressed in this thesis. New methods to characterise voids are now available, such as micro-CT scanning, which allow the voids to be fully characterised in 3-dimensions, in more detail and more accurately than before. This is expected to provide better understanding of the effect of voids in composites than previous studies.

However, there is no established segmentation method that can be quickly and accurately post-process CT-images in order to identify and characterise voids. Using information obtained from CT, and after applying the correct segmentation method, it will be possible to investigate the effect of void size, morphology and position on the mechanical properties. Furthermore, this information can be used to develop simple analytical and FE models as easy and quick tools to predict the strength of the structure with voids. However, a large data set needs to be provided from which statistical determinations can be made.

3 A PARAMETRIC STUDY OF SEGMENTATION THRESHOLDS FOR X-RAY CT POROSITY CHARACTERISATION IN COMPOSITE MATERIALS

Non-destructive testing (NDT) techniques are used to inspect composite structures after manufacture in order to identify the extent of any defects and to help assess their potential impact on mechanical performance. Micro X-ray computed tomography is a promising NDT technique which can give information about pore location, size, and morphology, in three dimensions. To identify and characterise voids in a specimen, an image 'segmentation' must be applied to the full CT dataset, which is simply a rule-based decision about whether a given voxel is inside a pore or not.

The work in this chapter uses a simple model to analyse and compare the effectiveness of previously accepted threshold methods for segmentation across a range of values of several different material and porosity parameters. A new CT-segmentation thresholding method is proposed and evaluated for characterising voids in a wider range of composites exhibiting reduced errors than the accepted segmentation methods, in certain scenarios. The sources of uncertainties in the results are investigated by modelling the porosity and analysing the effects of the simulated voids, and recommendations are made to minimise these uncertainties. In this chapter, a 'normalised grey level' scale will be used where the grey level of air is set to zero and the grey level corresponding to the 'nominal' fibre-volume fraction (V_f) of composite is set to unity. Grey level varies with V_f, which is not uniform in the composite, but this is treated as one of the parameters in the parametric study later.

The objectives of this Chapter are to propose a simple, rigorous, reproducible and accurate CT-segmentation thresholding method to characterise voids in composites, to study the sources of uncertainties in the results using modelling and simulation, and to recommend methods to minimise those uncertainties.

In Section 3.1, the segmentation method is described and justified based on the physics and known properties of X-ray CT imaging methods. In Section 3.2, the model used for simulation of the multi-dimensional parametric study is described. In Section 3.3, the model is validated by comparing it with experimental data. In Section 3.4, a parametric study of the segmentation thresholds is shown. In Section 3.5, improvements to the threshold are described for particular cases.

3.1 Proposed segmentation method.

The segmentation method has to determine whether a given voxel is to be counted as inside a pore or not, based purely on its grey level. Grey level is assumed to be linearly related to the effective linear attenuation coefficient (LAC) in the voxel, which is a combination of the LACs of the voxel's component materials for the relevant photon-energy distribution [123]. These materials contribute to the effective LAC using a simple volume-weighted mixture rule, which means that the threshold on grey level is effectively a threshold on the relative volumes of air and composite in the voxel, neglecting any variations in the transfer function due to changes in the photon-energy distribution across the scan volume. Obviously, the critical voxels for measuring pores are the ones that straddle the edge of a pore, containing some air and some composite, and the segmentation threshold has to apportion these in a way to minimise any bias in the resulting pore measurements, including the full-volume void volume fraction, V_v.

The basic assumption in the proposed thresholding method is that a voxel should count as a pore-voxel if more than half of its volume is air, otherwise it is not counted as in a pore. The statistical reasoning behind this assumption is that the errors in apportioning pore-edge voxels as air should be fully compensated by the errors in apportioning pore-edge voxels as composite. This is shown in Figure 3-1, in which the histogram displays a roughly constant count of pore-edge voxels (between 0.1 and 0.9). The threshold is set at 0.5 (50%) in this example.

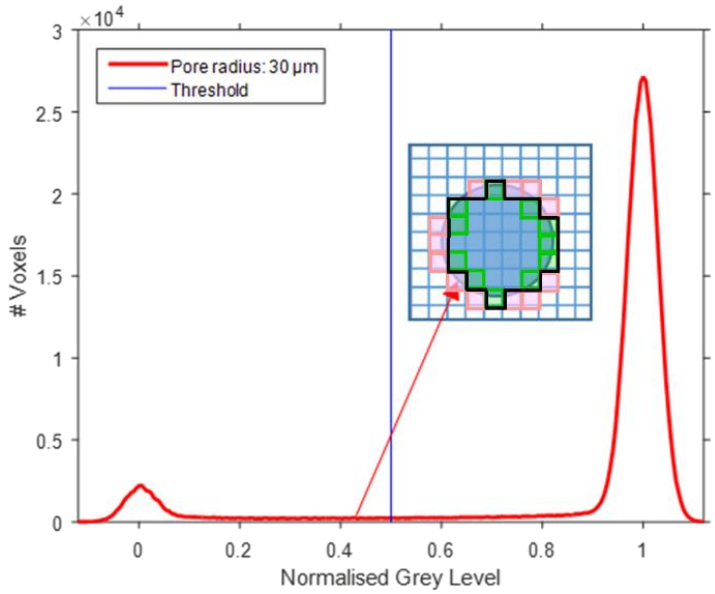

Figure 3-1. Simulated grey-level histogram of the composite with V_v = 15%, scattering noise standard deviation: 0.03 (normalised grey level), showing where the edge voxels appear in the histogram and (inset) how they are classified as above (red) or below (green) a segmentation threshold of 0.5. The resulting apparent pore morphology is shown as a black-edged shape.

Whilst this would appear to be logical for total void-volume fraction (V_v) measurements, for pore characterisation of linear sizing (length, width, etc) and morphology, the segmentation method needs to accurately track the pore edges and there are known errors in edge-location when using this 50% threshold for curved edges – see inset diagram in Figure 3-1. The assumption of the 50% segmentation threshold is that the location of the edge of the pore is at the centre of a voxel with a normalised grey level of 0.5. Errors can occur due to the shape of the pore edge – if it is flat then the error is zero, but any curvature will cause an error in the use of the voxel centre as the pore edge [124].

There are also some cases in which the total V_v is overestimated, due to *e.g.* scattering noise. This is shown in Figure 3-2, in which the simulated histogram has wide composite and air peaks due to scattering noise. In this case, the 50% threshold will overestimate the pore sizes, on average, and the total V_v, and so the threshold needs to be set at a lower percentage to compensate for this effect. Section 6 will explore methods for automating the setting of this threshold level, based on the histogram.

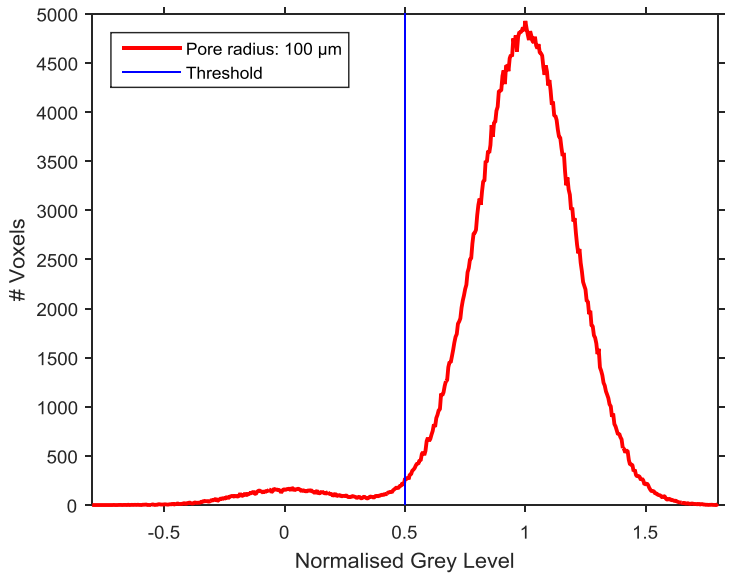

Figure 3-2. Simulated grey-level histogram of the composite with V_v = 15%, scattering noise standard deviation:0.2 (normalised grey level)

3.2 Model description

For this model, the ratio of the measured-to-actual total void volume fraction was chosen as a metric to investigate sources of bias and uncertainty in the characterisation of pore sizes. In each model with spherical pores of a single size, the actual void volume fraction depends on the single pore radius, *R* and the number of pores per unit volume. Different shapes of pores could be created but, for most of the modelling in this chapter, the pores are spheres, so the volume of the pore, *V* can be obtained using the simple equation for the volume of a sphere

One pore is created within a virtual cube in the data and the ratio of the pore volume to that cube volume is equal to the V_v. The location of the pore within its virtual cube is varied randomly so that, with numerous pores in the model, the relationship between pore-edge locations and voxel centres is randomised and all values of V_v within a voxel are possible, giving a relatively flat but non-zero histogram between the air and composite peaks – see Figure 3-1. The use of this random pore location avoids a source of systematic errors in the measurements of V_v where certain spikes in the histogram would appear due to specific repeated locations of pore edges within voxels.

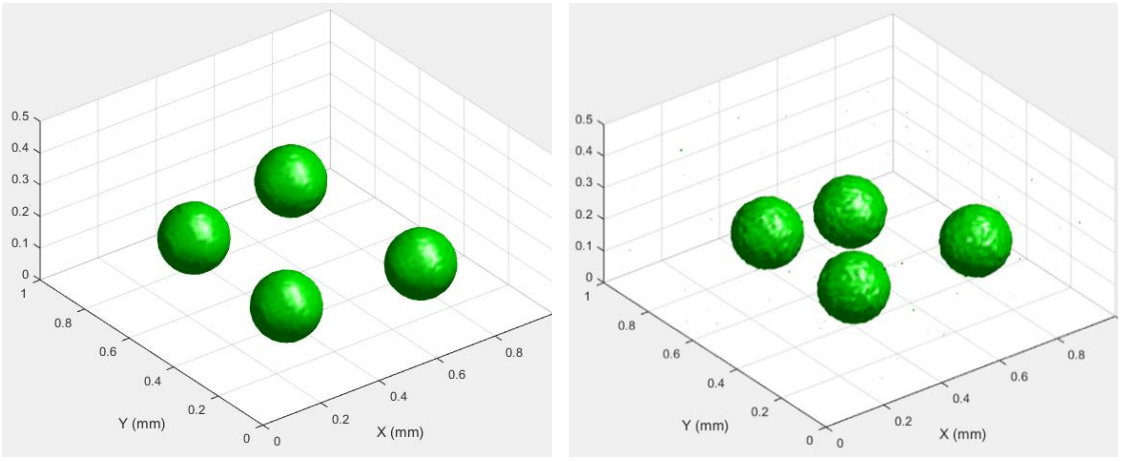

(a) **(b)**

Figure 3-3. Pore segmentation from the simulator using 50% threshold, scattering noise standard deviation: (a) 0.05 (b) 0.15

The simulated CT data set is generated as a 3D set of voxels, each containing a single scalar value of normalised grey level, based on the following methodology and assumptions:

(a) Grey level is linearly related to effective linear attenuation coefficient [47]:

$$\boldsymbol{G = a\mu + b} \tag{3-1}$$

where G is the CT grey level, μ is the effective linear attenuation coefficient in the voxel, a is a contrast, and b is brightness.

For this model, a 'normalised grey level' is used, in which 0 corresponds to air and 1 corresponds to composite of the 'nominal' fibre volume fraction.

$$\boldsymbol{G_{norm} = \frac{\mu - \mu_{air}}{\mu_{composite} - \mu_{air}}} \tag{3-2}$$

The simple volumetric mixture rule has been established as being appropriate for converting the linear attenuation of composite, $\mu_{\text{composite}}$ and air, μ_{air} within a voxel into an effective linear attenuation μ:

$$\boldsymbol{\mu = V_v\,\mu_{air} + (1 - V_v)\,\mu_{composite}} \tag{3-3}$$

where $\mu_{\text{composite}}$ is the linear attenuation of the composite, μ_{air} is the linear attenuation coefficient of the air and V_v is the void volume fraction.

(b) Voxels at pore edges are divided into sub-voxels for determining grey level.

In the model, voxels that are completely within or entirely outside pores have normalised grey levels of 0 or 1, respectively. A voxel at the edge of a pore takes a normalised grey

level equal to the proportion of its volume that is outside the pore. This is calculated by dividing the voxel into 1000 sub-voxels (*i.e.* 10 × 10 × 10). Each sub-voxel is checked to see whether its centre is inside the pore or not, thus determining whether its normalised grey level should correspond to 'air' or 'composite' (0 or 1). The normalised grey level of the voxel is taken as the mean of the 1000 sub-voxel normalised grey levels

(c) In addition, there will be an influence from the X-ray scattering noise during CT-scanning.

This is caused by spurious photons arriving at the detector from scattering interactions in voxels other than on the direct X-ray path. To investigate this, randomly-generated normally-distributed incoherent noise (with a mean of zero and a specified standard deviation as a normalised grey-level) is added to the modelled voxel grey levels in the CT data set.

(d) There will be some structural (coherent) noise caused by FVF variations in the composite.

This will affect the effective LAC of the voxels in the composite but not in pores, so this normally-distributed noise (with a mean of zero and a specified standard deviation as a normalised grey-level) was only added to the composite voxels where it is effectively combined with the scattering noise in quadrature to give a single normal distribution with a standard deviation equal to the square-root of the sum of the squares of the two (coherent and incoherent) standard deviations.

(e) Resin-only layers between plies and other resin-rich regions exist in composites.

Voxels in these resin regions will take the grey level corresponding to the LAC for resin only, plus the added scattering-noise distribution. By default, the resin-only normalised grey level used in the simulator for this chapter was set to 0.8, except for the section where the influence of this parameter is explored. If these resin-only regions become an appreciable proportion of the total volume, then a third peak in the histogram can appear. This is simulated as actual resin-only layers in the model and a similar volumetric mixture rule issued to determine the grey value for resin-edge voxels.

(f) Finally, a histogram is generated for the whole model as this can easily be analysed to determine the volume above and below a given threshold in order to calculate the 'measured' void volume fraction.

3.3 Modelling Results and Validation

There are different parameters that can be varied in the model in order to explore their influence on the proposed segmentation methods: (a) sample dimensions; (b) voxel size; (c) resin layer parameters (position and proportion of total volume); (d) void volume fraction, V_v; (e) porosity radius; (f) coherent noise standard deviation due to structural fibre volume fraction (V_f) variations; and (g) incoherent noise standard deviation due to X-ray scattering. However, it is possible to eliminate several parameters that have minimal impact on void measurement. Furthermore, pore radius, void volume fraction (V_v) and number of pores in a sample are inter-related, although they may not all have a significant effect on void measurement.

Figure 3-4 shows a surface plot of the actual V_v, as a function of pore radius and number of pores in a fixed sample volume of: 0.5 mm^3 with the chosen assessment metric for the parametric study – measured/actual V_v – plotted as a colour on the surface. The model was run on a sample size of 1 mm × 1 mm × 0.5 mm, voxel size of 10 μm, scattering-noise standard deviation (in normalised grey level) of 0.05, using a segmentation threshold of 0.5 (50%). The radius, number and locations of pores were varied between models but all pores within a single model were the same size.

Inspection of Figure 3-4, where each cross symbol indicate the result of a simulation for a given number of pores of a particular size, shows pore radius to have the dominant influence on the measurement bias, *i.e.* Measured/Actual V_v. This bias is thought to be due to either the lower number of voxels describing the edges of a smaller pore, or the higher curvature of the edges of smaller pores and this is investigated later (in Section 3.3.3).

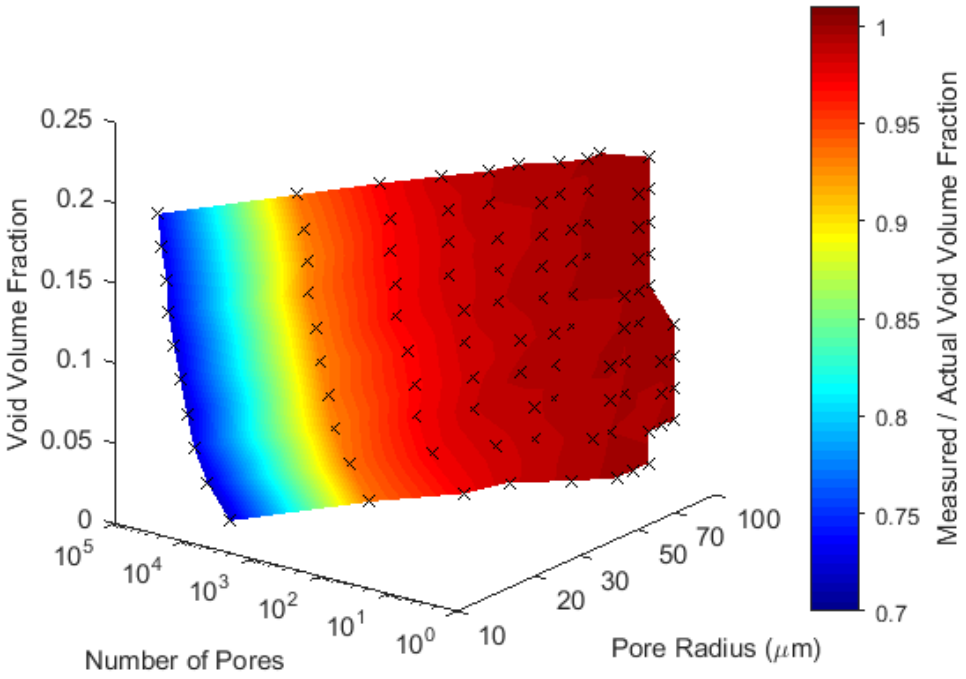

(a)

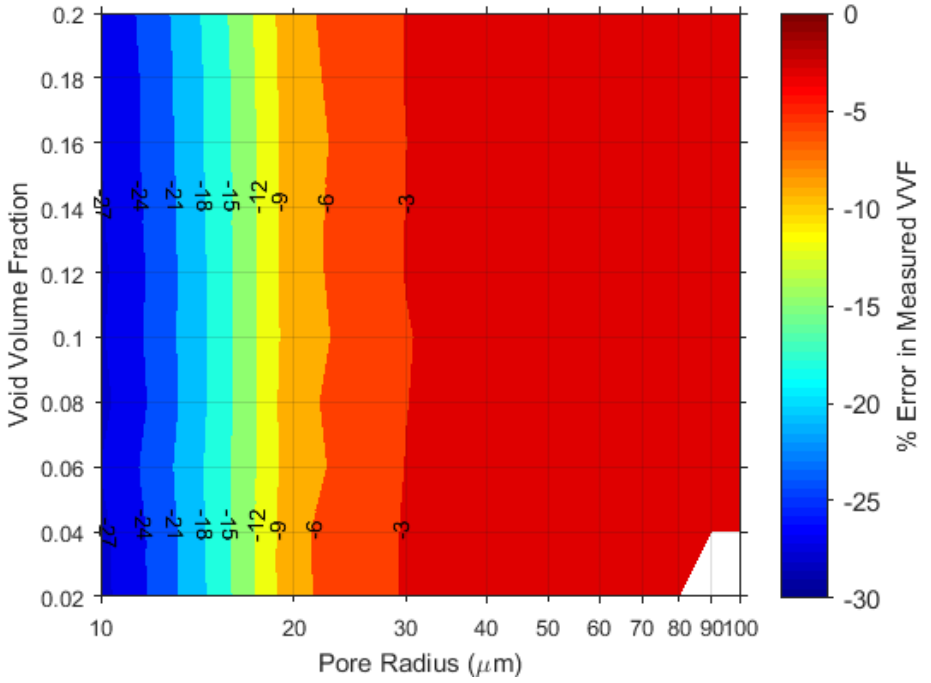

(b)

Figure 3-4. (a) 3D surface plot of actual void volume fraction (V_V) as a function of pore radius and number of pores in a fixed volume of 0.5 mm^3 with an overlaid colour plot of measured to actual void volume fraction (V_V) and (b) 2D surface plot of actual void volume fraction (V_V) as a function of pore radius with overlaid contour plot of error in measured V_V using a 50% segmentation threshold.

3.3.1 Effect of pore-radius to voxel-size ratio.

One of the important parameters governing CT image quality is voxel size, which should be smaller than the structural features that need to be imaged. The minimum achievable voxel size is dictated by two factors: 1) the focal spot size in the source which dictates the geometric unsharpness such that it is pointless reducing the voxel size further; and 2) the ratio of the maximum size of the specimen, or region within a specimen that is to be imaged, perpendicular to the CT rotation axis, to the number of detector pixels across the detector in that direction. For this reason, it can be almost impossible to achieve a voxel size smaller than all the pore sizes in realistic sized test coupons. Therefore, it is important to understand the dependence of V_v measurement on the ratio of pore size to voxel size.

A simple example of this effect is to consider a cube of 2 × 2 × 2 voxels, containing a pore centred at the cube centre, where the pore volume in each voxel is just less than 50% of the voxel volume. In this case, each voxel will register 1 (not in a pore), the measured pore volume will be zero, but the actual pore volume will be just less than 4 voxels. If the pore is spherical, this corresponds to a pore radius of 0.985 of the voxel size. Thus, the 50% threshold will gradually underestimate pore volume as pore radius reduces to 0.985 voxels, at which point the measured pore volume could reduce to zero if the pore is centred on a node between voxels, or anything up to 4 (voxels) if the pore is not at a node. For numerous pores at random locations, an average V_v of zero is reached when the pores all have a volume less than 50% of the voxel volume – *i.e.* when the pore radius is less than 0.49 of the voxel size. This effect is demonstrated for random pore locations using the simulator in Figure 3-5.

Figure 3-6 shows the dependence of bias on pore-radius / voxel-size ratio for segmentation thresholds of 40%, 45%, 50%, 55% and the Otsu threshold [51], which is recalculated for each model and will vary depending on void volume fraction. Statistical variations in the curves were reduced by using a larger total volume of the model but larger models take longer to run so this was a compromise. It can be seen that the 50% threshold and Otsu threshold provide the most accurate segmentation for larger pore sizes (radius greater than 3 voxels). However, none of the thresholds work well with a pore radius less than 4 voxels, at which point the bias is an underestimate of 2% for the 50% threshold and an overestimate of approximately 1% for the Otsu threshold. As in Figure 3-5, the 50% threshold curve is tending to zero at a pore radius of approximately 0.5 voxels, as predicted by the above analysis for a pore at the centre of 8 voxels.

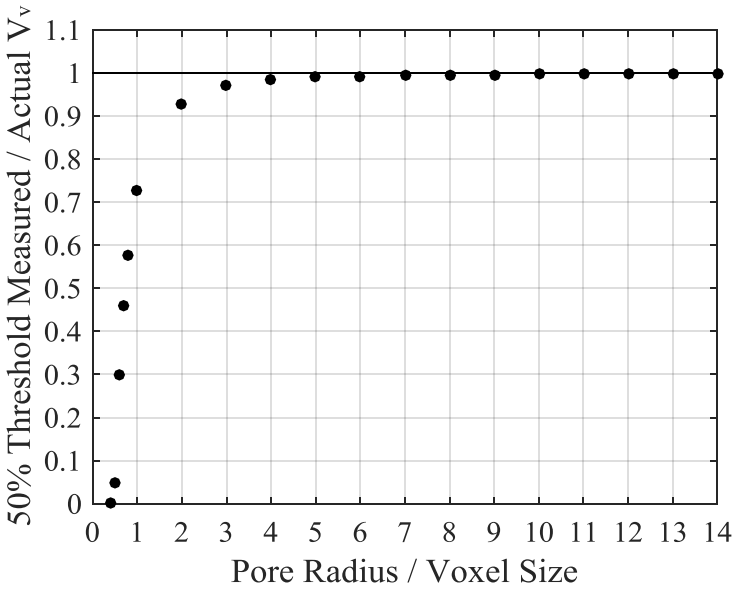

Figure 3-5. Effect on the 50% threshold measured / actual V_v ratio of the pore-radius / voxel-size ratio.

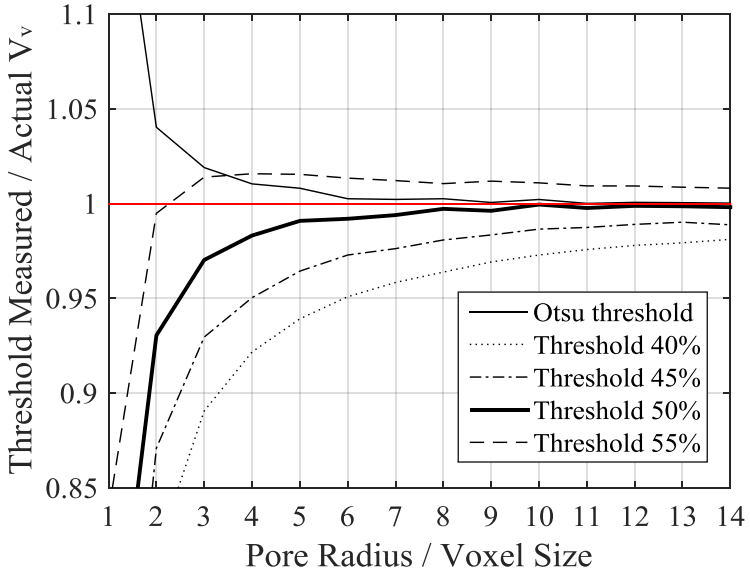

Figure 3-6. Error as a function of the pore size for the different thresholds, V_V=10%, scattering-noise standard deviation of 0.05 (as normalised grey level).

The 55% threshold gives an exact measurement (zero bias) for one particular pore size. This is where the underestimate due to size or curvature of the pore is exactly cancelled by the general slight overestimate in pore measurements due to the higher threshold. Due to this effect, it has been suggested by Plank *et al.* [125] that the threshold should be increased for larger voxel sizes (lower pore-radius / voxel-size ratio) but real composites contain a distribution of pore sizes, requiring a different threshold for each pore size. A single threshold above 50% may give a more accurate total V_v but the segmentation of

void morphology would underestimate the sizes of small pores and overestimate the sizes of large pores.

Figure 3-7 shows the same data plotted to show the bias in V_v as a function of the segmentation threshold value for selected values of pore radius (in voxels). The slope of each curve is used in the following section for validation of the model against experiment, where total V_v has been measured for a known pore-size distribution.

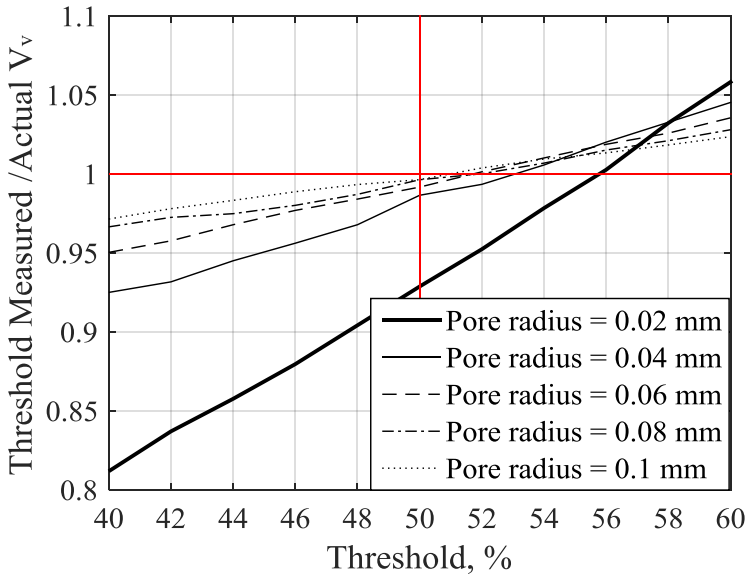

Figure 3-7. Bias in V_v as a function of threshold for different pore radii/voxel size, where the actual V_v in the model was 10%.

The conclusion of this study of the accuracy of porosity measurement as a function of pore size is that all small pores will be underestimated in size more than large pores, for any single segmentation threshold. If a threshold above 50% is used, then larger pores could be overestimated in size.

3.3.2 Model validation

Small samples (230 mm × 10 mm × 2.6 mm) with porosity introduced by deliberately adjusting the cure-cycle parameters were manufactured according to the procedure that will be outlined in chapter 4. The samples were subsequently scanned using X-ray CT at 55 kV source voltage, 2000 projections, 4 frames per projection, source current 140 mA using a Nikon XTH320 system. The data was post-processed within a large volume just inside the edges of the specimen (*i.e.* excluding air from outside the specimen) using the 50% segmentation threshold. This allowed characterisation of each pore within the samples, in order to determine their morphology, size and location. Quantitative comparisons were made between high-magnification optical microscopy images and the

μCT-scans using a 50% segmentation threshold at the same locations within a chosen specimen (as shown in Figure 3-8). The results showed excellent correlation in terms of the void shape, dimensions, and distribution [126].

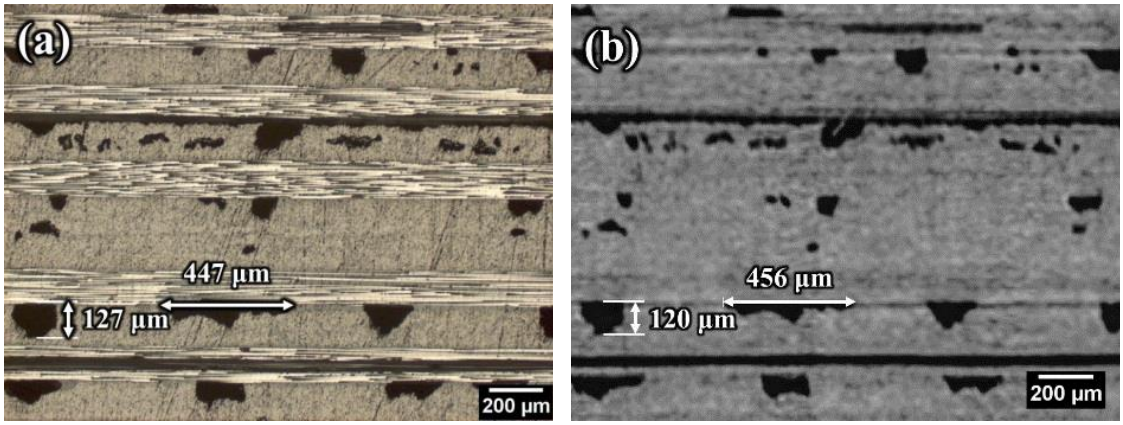

Figure 3-8. Comparison of void size, shape and distribution using: (a) microscopy; (b) CT-scanning [126].

To validate the model described above, the CT results of the samples with introduced porosity were analysed to determine the relative dependence of total V_v on segmentation threshold to check the slope of this dependence for a known pore-size distribution against a weighted average of the slopes for each size in Figure 3-7. Firstly, the average void content was calculated from the experimental CT data using different thresholds in the range of 40-60% (Figure 3-9) within the VG Studio Max software. The voxel size of the CT-scanned sample is 13.1 μm. The 50% threshold determined an average void content of 3.69% with a bias that depends on the threshold (Figure 3-9), with the non-dimensional slope of the least-squares fitted line equal to 0.0626.

In order to validate the modelling methodology, the experimentally determined slope can be compared with a predicted slope based on a weighted average using the pore-size distribution to determine the weightings. The above analysis and discussion justifies an assumption that the smallest dimension and highest curvature of a given pore will govern the bias in its volume measurement by segmentation. For the investigated material system (IM7/8552), voids tend to be needle-like in shape and elongated in the fibre direction [126]. As a result, the void size in the thickness direction is used for this analysis, as the void size in this dimension will be smallest and therefore will be the dominant contribution to the bias in the V_v measurement and its slope relative to the threshold. Figure 3-10 shows the experimental thickness-direction void-size distribution of the sample.

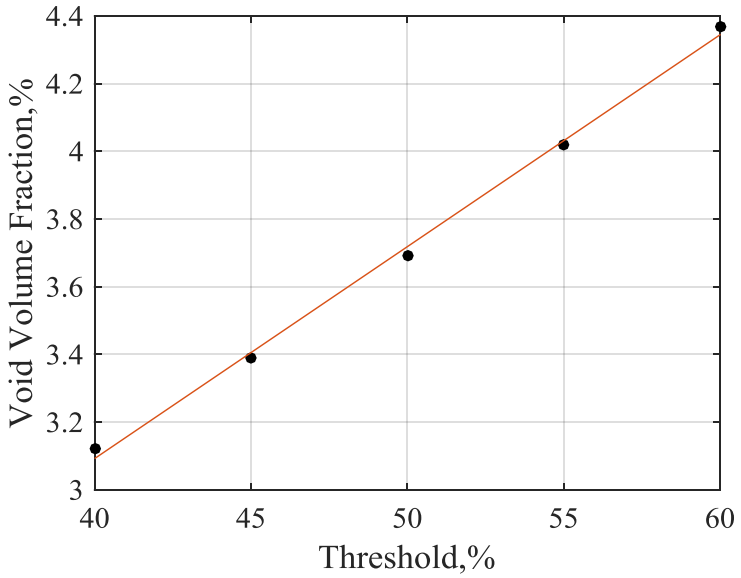

Figure 3-9. Effect of threshold on void volume fraction for experimental results, (Voxel size = 13.1 µm, the red line shows the best fit of the experimental data).

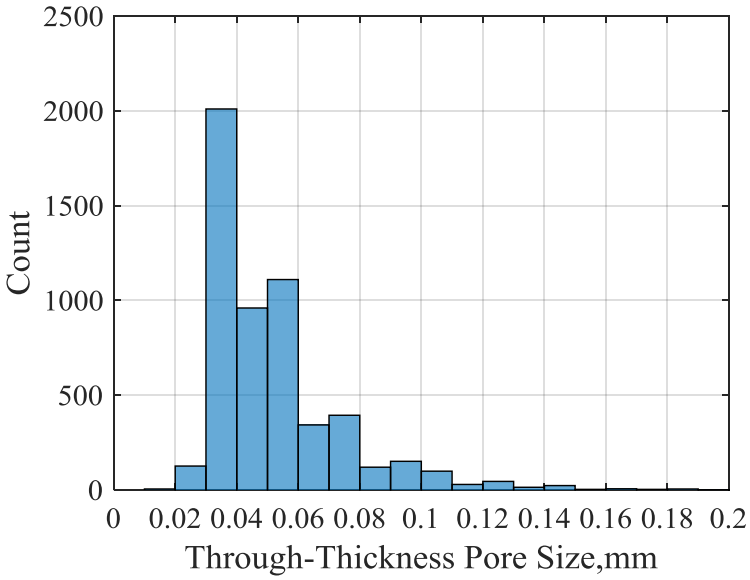

Figure 3-10. Distribution of through-thickness pore sizes. V_v=3.69% (50% threshold), voxel size = 0.013 mm.

The simulator was used to predict the slope of V_v against threshold for the range of pore radii in the pore-size histogram in Figure 3-10, using a simulated voxel size of 13.1 µm to match the experimental voxel size. Each model uses random void locations but is simplified by creating all voids spherical and of equal size. The results of the analysis are shown in Figure 3-11, which also shows that the slopes of the graphs differ from the experimental results, probably due to the distribution of void sizes in the actual samples where the mean pore size is approximately 50 µm, so the equivalent mean pore radius is 25 µm.

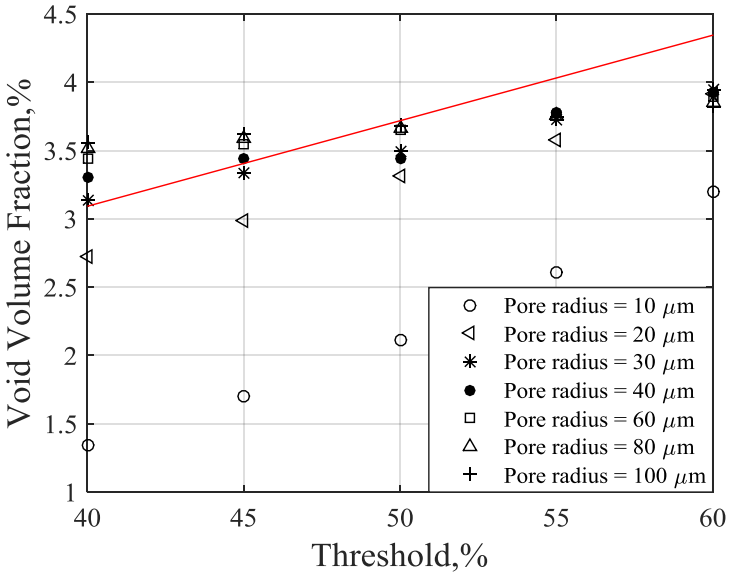

Figure 3-11. Void volume fraction vs threshold for different pore radii (modelling results), actual *V*v=3.7%, voxel size = 0.0131 mm. The red line shows the best fit from the experimental data in Figure 3-9.

To enable comparison of the modelling and experimental results, a weighted-average slope, ξ, was calculated using the distribution in Figure 3-10 as the weighting for each bar of the graph using a pore size at the middle of the bar:

$$\xi = \frac{\sum_{i=1}^{n} w_i \, \xi_i}{\sum_{i=1}^{n} w_i} \qquad \textbf{(3-4)}$$

where N is number of analysed bars in the graph in Figure 3-10, w_i is the number of pores in the range of sizes represented by bar i in Figure 3-10, ξ_i is the gradient of void volume fraction *vs.* threshold for a pore radius corresponding to the middle of bar i.

The model-predicted weighted-average slope is 0.0552, which is 12% less than the experimental value of 0.0626. This provides an acceptable agreement between model and experiments considering the experimental pore shapes are not spherical and it is difficult to know which dimension of pore size to use for the comparison.

3.3.3 Effect of the pore-edge curvature

It is not obvious whether the underestimation of pore size for small pores is due to the size itself or more to do with the increased curvature of the edges. In order to investigate the effect of edge curvature on pore segmentation, spherical and cubic pores were compared see Figure 3-12). Although cubes have a large amount of surface with no curvature, they do of course have a very high curvature at edges and corners, so this is not a perfect test.

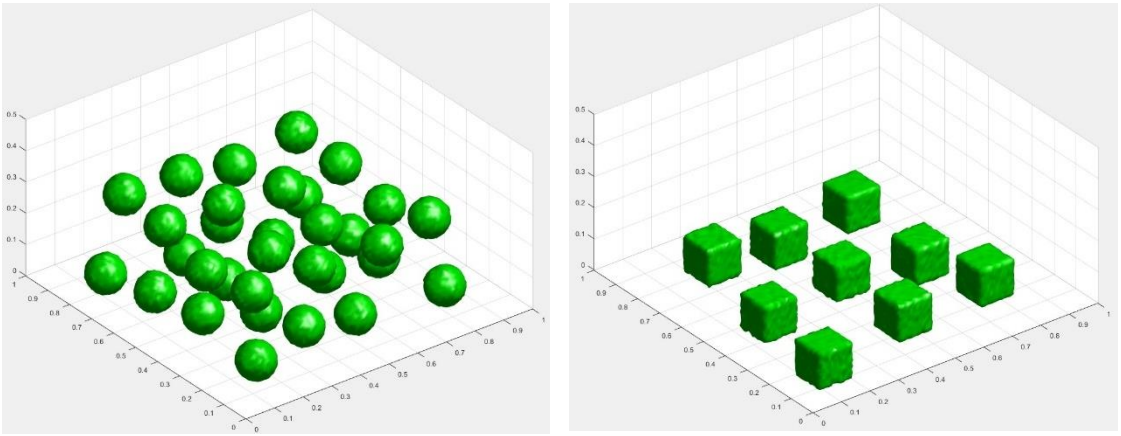

(a) **(b)**

Figure 3-12. (a) Spherical and (b) cubic pores with the R = 60 µm, V_v = 10%, voxel size = 10 µm, scattering noise 0.1

The effect is illustrated in Figure 3-13, in which it is shown that at smaller pore radius/voxel sizes the error using spherical pores is larger than for the cubic pores. The conclusion is that there is a curvature effect working in combination with the pore-size *vs.* voxel-size effect discussed above.

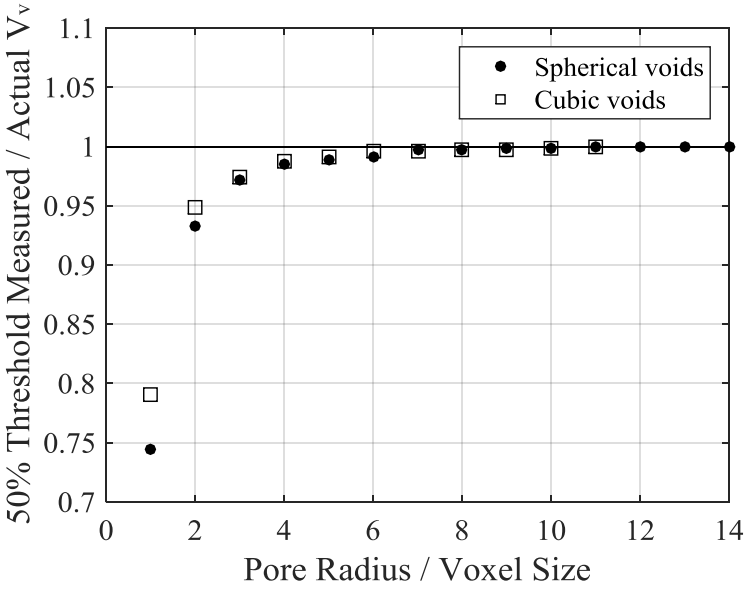

Figure 3-13. Effect of pore shape on measured V_v using 50% thresholds. Scattering noise: 0.1, V_v = 10%.

3.4 Parametric study of segmentation thresholds

3.4.1 Effect of the (incoherent) scattering noise

Scattering noise is one of the most common CT artefacts, and can affect the segmentation boundary of the pores on the CT-images. It is possible to reduce it by increasing the number of images (shots) per projection and averaging them, or by applying the noise

filter in the reconstruction software, if provided. Scattering noise will affect the measured grey value of each voxel. It is assumed that, in the histogram of grey levels, the scattering noise manifests itself as a normal distribution around the mean grey value for the relevant material. In the simulator, the scattering noise is added by specifying a standard deviation for that normal distribution but the mean value of the distribution for that material is not affected.

From experience, for optimised CT-scanning, an acceptable normalised grey-level scattering noise is between 0.1 and 0.15. Figure 3-14 shows the grey-level histogram of the experimental CT-scan of the porosity sample. Scattering noise standard deviation calculated from the experimental histogram is 0.11 (Figure 3-14).

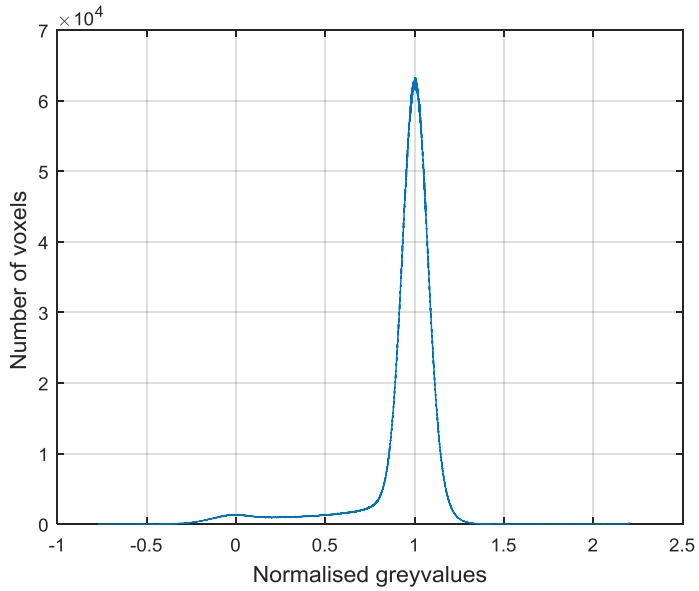

Figure 3-14. Experimental normalised grey-level histogram of the porosity sample.

Both the 50% and Otsu thresholds show increasing over-estimation of void volume fraction with increasing scattering noise (Figure 3-15). In addition, the behaviour is erratic, and bias is high for the Otsu threshold with a scattering-noise standard deviation above 0.15. For the 50% threshold, a maximum bias of 18% occurred at a pore radius of 10 voxels and scattering noise of 0.2, but the behaviour of the 50% threshold is more stable than the Otsu threshold for all levels of scattering noise

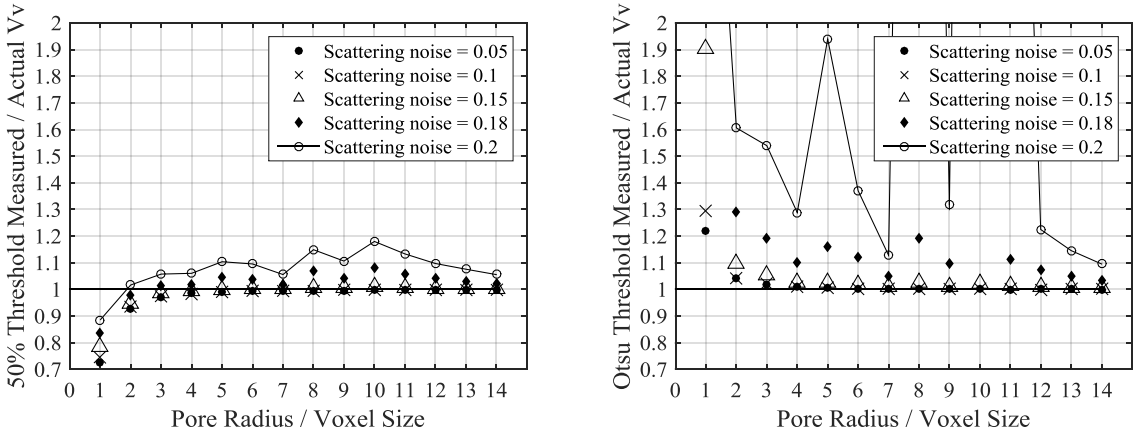

(a) **(b)**

Figure 3-15. Effect of the scattering noise level (given in the legend as a normalised grey-level standard deviation) on the pore detection for (a) 50% threshold and (b) Otsu threshold, V_v =10%.

3.4.2 Effect of (coherent) structural noise

Additional noise can contribute to the 'composite' peak distribution due to fibre volume fraction, V_f, changes because fibres and resin have different LAC values. The normalised grey level takes a value of unity for the LAC of a 'nominal' V_f and the default resin-only normalised grey level used in this paper is 0.8, although this is varied later in a study of this parameter. Note that a nominal V_f of 60% was used in the simulator for the composite regions. Thus, a standard deviation in V_f of 10%, which would be a large manufacturing deviation, corresponds to a large deviation in the normalised grey level of 0.033.

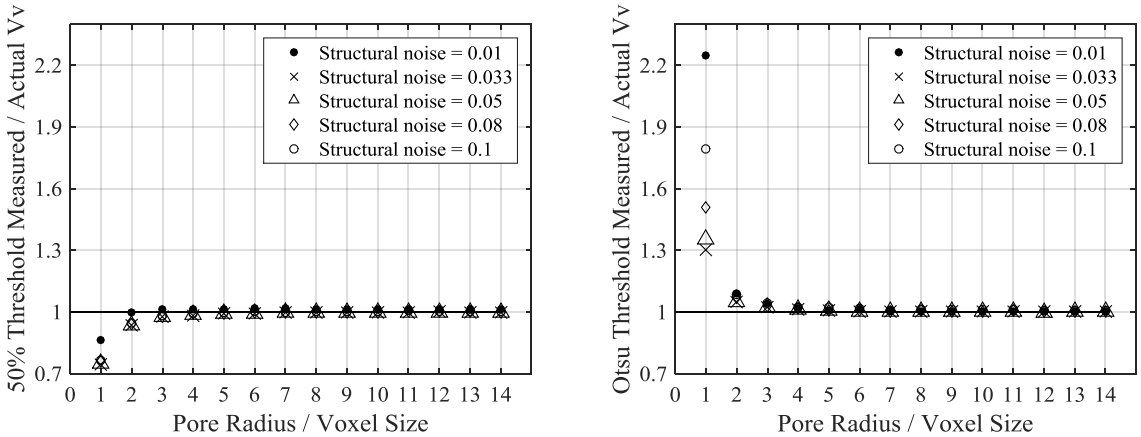

(a) **(b)**

Figure 3-16. Effect of the structural noise V_f standard deviation for (a) 50% threshold and (b) Otsu threshold, V_v = 10% and scattering-noise standard deviation of 0.1.

From Figure 3-16, it can be seen that both of the compared thresholds (*i.e.* 50% and Otsu) perform well, with bias of less than 5%, even with a large standard deviation (10%) in the V_f, above a pore radius of twice the voxel size.

3.4.3 Effect of the resin-layer parameters.

3.4.3.1 Grey level of resin *vs.* composite

The grey-level histogram of a composite-material CT-scan usually comprises three peaks that correspond to 'air, 'resin' and 'composite', in order of increasing effective LAC. The LAC of a material is based on the chemical formula, which defines its effective atomic number [127] and its electron density. Therefore, by changing a composite's material constituents (*e.g.* resin or fibre materials), or by changing the nominal fibre volume fraction, the normalised grey level of the resin peak may vary significantly. For the purposes of this parametric study, it has been allowed to vary from 0.6 to 0.9 in the normalised grey-value histogram (Figure 3-17).

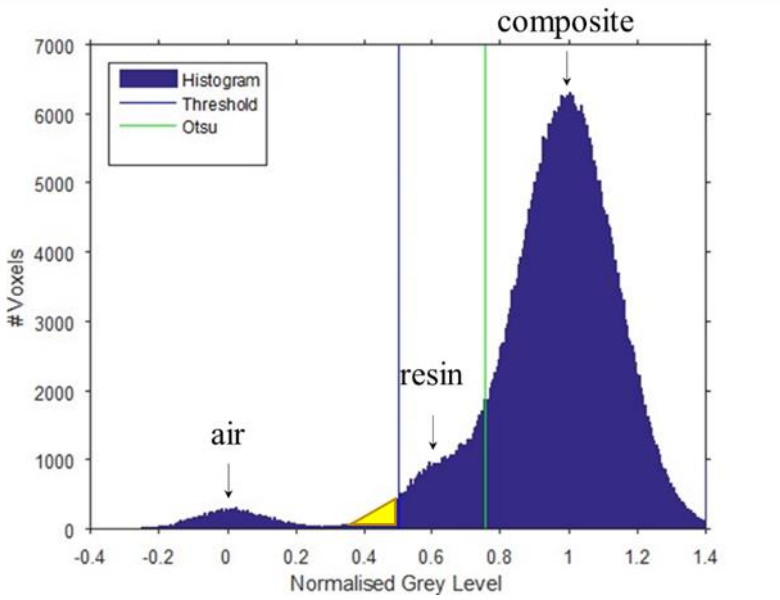

Figure 3-17. A composite material's grey-level histogram showing the 'air', 'resin', and 'composite' peaks with the 50% threshold (blue) and the Otsu threshold (green). The region marked in yellow shows where resin-only voxels have been erroneously counted as porosity by the 50% method; it does not go down to the baseline because there are some voxels that should be counted, which are only at those grey levels because they are at the edge of the pore.

In some composites, such as most carbon/epoxy composites, the 'resin' and composite' peaks will be merged due to similarities in their LAC. However, when the resin's normalised grey level is low and/or the scattering noise is high, there is a chance that the

lower tail of the resin peak will cross the 50% threshold, causing resin voxels to be counted as air and resulting in an overestimate in porosity V_v as shown in Figure 3-17.

Figure 3-18 and Figure 3-19 show the effect of varying the resin-only normalised grey level, as a function of scattering noise, on porosity segmentation. A fibre volume fraction (V_f) standard deviation of 10%, equivalent to a normalised grey level of 0.033, is used as discussed previously, and the proportion of resin layer to total volume is chosen as 0.1 as this corresponds to an average of widely used composite material systems.

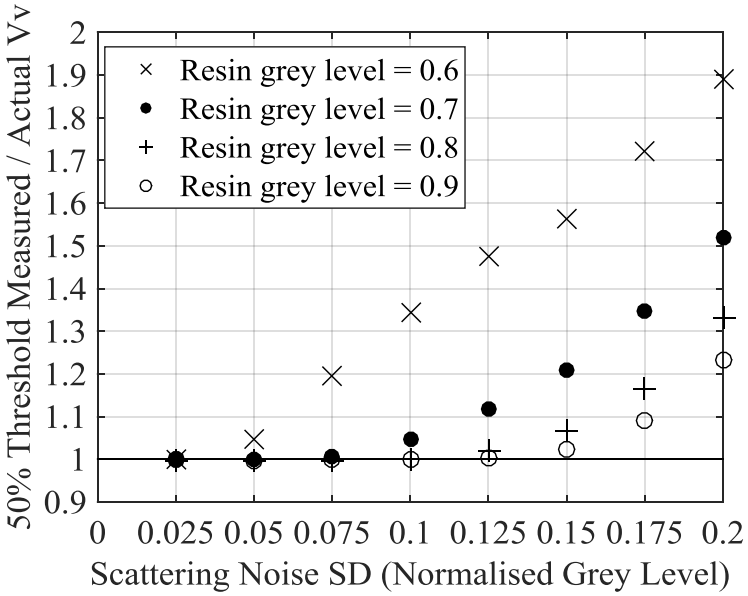

Figure 3-18. Effect of resin normalised grey level on void volume fraction (V_v) using the 50% threshold, V_v = 10%, V_f SD = 0.033, pore radius = 100 µm, voxel size = 10 µm.

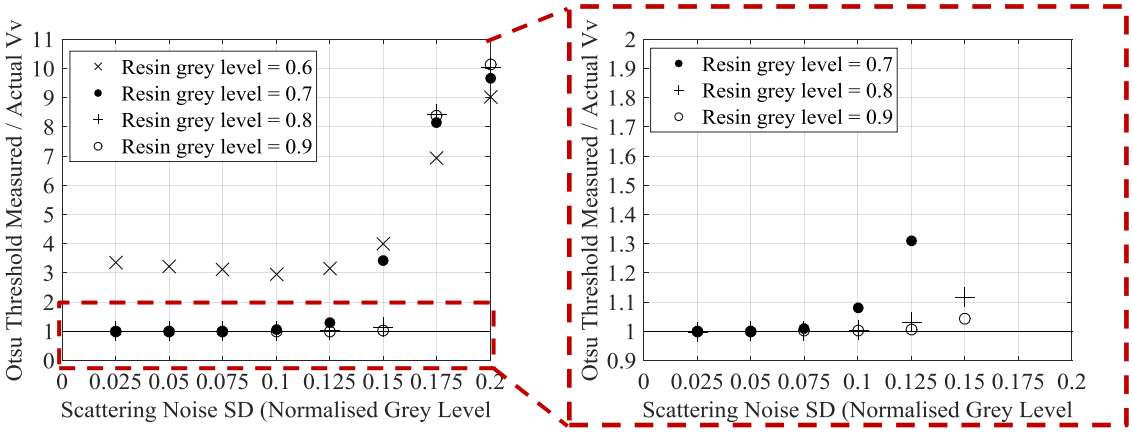

Figure 3-19. Effect of the resin layer on void volume fraction using the Otsu threshold, V_v = 10%, V_f SD = 0.033, pore radius = 100 µm, voxel size = 10 µm.

Both of the thresholds (as shown in Figure 3-18 and Figure 3-19) show significant sensitivity to both the resin-only grey level and the scattering noise, both of which can act to increase the voxels that masquerade as pores, to the left of the threshold. In fact,

the Otsu threshold failed to perform at a resin-only normalised grey value of 0.6 for any noise level (see Figure 3-19), whilst the 50% threshold functioned well at a resin normalised grey value of 0.6 for scattering noise levels below 0.05. Both thresholds performed well (bias less than 5%) for scattering-noise standard deviations below 0.15 (around the largest normally seen) at a resin-only normalised grey level of 0.8 (relative to composite at 1 and air at 0), as used in the rest of this paper as a default.

3.4.3.2 Thickness of the resin layers

Another potentially significant parameter is the thickness of the inter-ply resin layer as a proportion of the ply spacing, as this will change the height of the resin peak in the histogram relative to the composite peak and a higher resin peak will have more voxels masquerading as pore voxels to the left of the threshold. The resin-layer thickness may vary for different types of fibre-resin systems, particularly with particle-toughened resin layers, which tend to be thicker – up to 25% of the ply spacing. This variation in the relative height of the resin peak may affect porosity measurement during CT-image segmentation if the resin peak overlaps the 50% threshold.

The results in Figure 3-20a show a high sensitivity of both thresholds to resin-layer thickness at a resin grey value of 0.6. More acceptable behaviour can be seen for the resin grey value of 0.8, providing a maximum error of less than 1% and 2.5 % for Otsu and 50% threshold respectively.

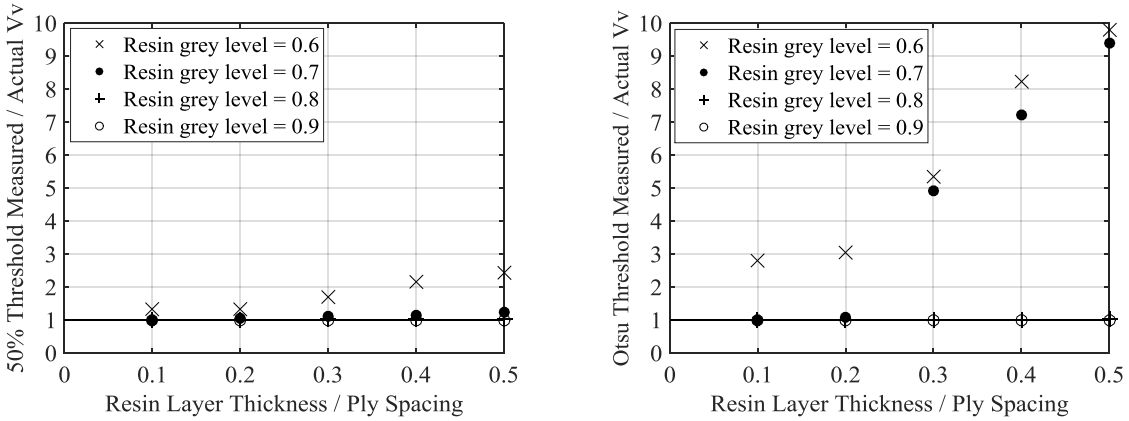

(a) **(b)**

Figure 3-20. Effect of resin-layer thickness (as a proportion of ply spacing) on measured/actual void volume fraction (V_v), for different resin grey levels, for (a) 50% threshold and (b) Otsu threshold, V_v = 10%, V_f SD = 0.033, pore radius = 100 µm, voxel size = 10 µm, scattering noise = 0.1.

3.5 An adaptive threshold

The 50% threshold shows very good results for void measurement in most cases but does not perform well in situations where the resin peak encroaches upon the 50% threshold because either the histogram has three distinctive peaks or the noise level (scattering and/or structural) is high. In these cases, the threshold needs to be reduced below 50%, otherwise it will overestimate the void fraction and the segmentation of each void will incorrectly determine void size. The problem is how to determine what threshold will minimise the error. As explained above, the crucial factors are how much the lower part of the resin peak overlaps the 50% threshold and how much of the histogram in that overlap is genuinely air. This overlap is characterised by two parameters – the relative height of the overlap and its positive slope.

The adaptive algorithm that is proposed to determine the appropriate threshold, or the 50% threshold if this is appropriate, involves the following steps (Figure 3-21):

- The grey-level histogram should be smoothed to remove local minima due to noise, using a moving average, the width of which depends on the noise structure of the histogram (as opposed to the scattering noise in the CT scan which just spreads the peaks).
- The air peak, (g_{air}, f_{air}), is determined from the smoothed histogram where g is the grey level and f is the frequency of voxels in the histogram at that grey level.
- The first minimum, (g_{min}, f_{min}) above the air peak is identified.
- The greater of $f_{air}/2$ and f_{min} is used as the frequency threshold, $f_{threshold}$.
- The algorithm then searches upwards from g_{min} for the next positive-going crossing of $f_{threshold}$. This grey-level value is the proposed threshold, $g_{threshold}$.
- Use as the threshold the least of $g_{threshold}$ and 0.5.

Figure 3-22 shows the effect of the resin-peak overlap, varied by changing the scattering-noise standard deviation, on void segmentation using both the 50% and proposed adaptive thresholds. The new adaptive threshold is equivalent to the 50% threshold up to a scattering noise level of 0.125. An increase of the scattering noise beyond this level causes the error of the 50% threshold to increase and deviate from the proposed threshold. As a result, once the resin histogram overlaps the grey value of 0.5 (indicated in this case by a scattering noise level greater than 0.1 for resin grey values of 0.6 and 0.7 and a scattering noise level of 0.125 for resin grey values of 0.8 and 0.9), estimation of the void volume fraction is improved by adopting the new adaptive threshold. The maximum error

in V_v with the proposed adaptive threshold is less than 10%, whilst the 50% threshold shows significantly higher errors

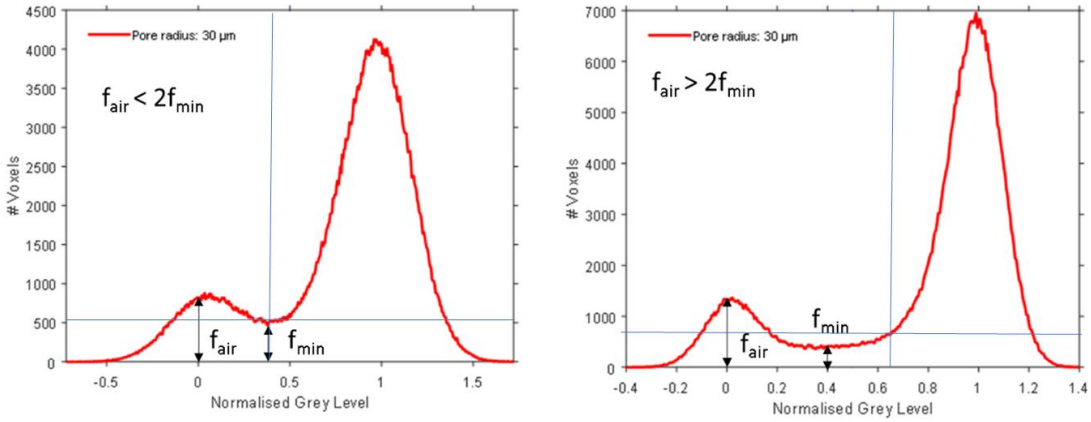

Figure 3-21. Graphical explanation of the adaptive threshold selection based on the algorithm defined in the text. The horizontal blue line is at $f_{threshold}$ and the vertical blue line is at $g_{threshold}$.

Figure 3-23 shows the effect of adjusting the amount of overlap of the 50% threshold by changing the resin-layer thickness, and thus the proportion of resin by volume. In comparison with the 50% threshold, the adaptive threshold works very well with thick resin layers. Its application reduces the maximum error to 3.5%. There is no observed detrimental effect from using the adaptive threshold for any of the tested ranges of noise level, resin grey level or resin-layer thickness.

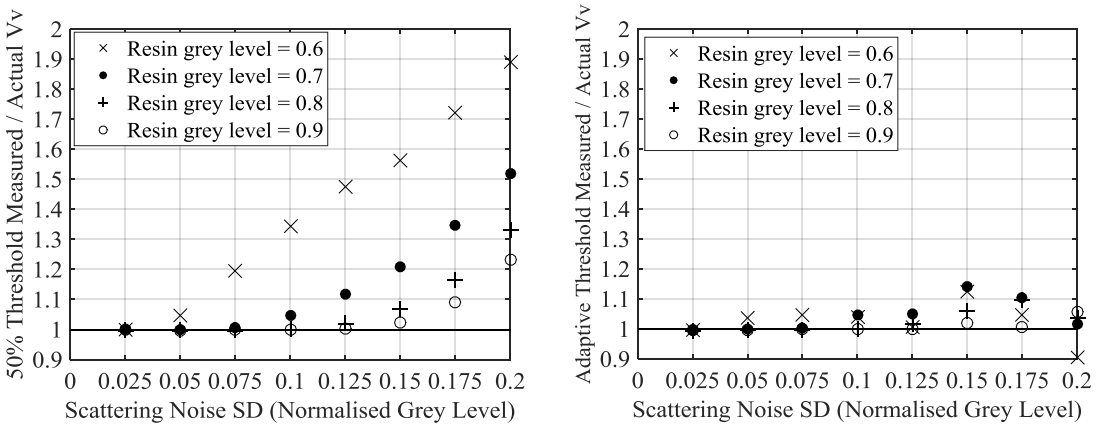

(a) **(b)**

Figure 3-22. Effect of scattering noise, for different resin grey levels, on void volume fraction using (a) 50% threshold; (b) new adaptive threshold. V_v = 10%, V_f SD = 0.033, pore radius = 100 µm, voxel size = 10 µm.

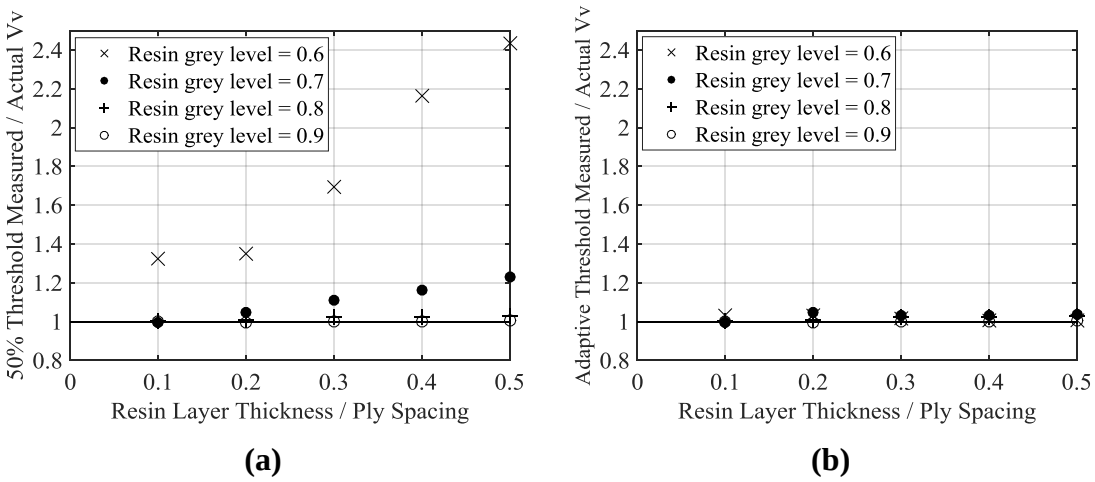

(a) **(b)**

Figure 3-23. Effect of resin-layer thickness (as a proportion of ply spacing), for different resin grey levels, on measurement of void volume fraction for (a) 50% threshold; (b) new adaptive threshold V_v = 10% , V_f SD = 0.033, pore radius = 100 µm, voxel size = 10 µm.

3.6 Concluding Remarks

Using X-ray computed tomography alongside simple and accurate image segmentation methods allows the detection and measurement of critical void defects (*i.e.* the void location, shape, and size). This information is essential for the understanding and assessment of the effect of defects on the composite structural performance. However, until now there has been a lack of understanding of the systematic effects of the choice of segmentation threshold level when characterising porosity. This chapter has used a simple model to simulate the CT response to porosity in order to be certain of the 'true' value of void volume fraction, allowing a full parametric study to be performed.

A common CT-segmentation thresholding method (50% threshold), based on the assumption that a voxel should count as a pore-voxel if more than half of its volume is air, otherwise it is not counted as a pore, has been shown to be more accurate than other methods in all but a few situations. The accuracy of this 50% threshold method has been demonstrated for a range of properties: material (resin-layer grey level and thickness), porosity (pore radius and void volume fraction) and CT (scattering noise and voxel size). Smaller pores relative to the voxel size are underestimated in size by this method (as by most thresholds) due to the curvature of the pore edge. Noise, either scattering (incoherent) or structural (coherent), causes overestimation of pore sizes, particularly when the resin attenuation is low compared with the composite, such as with glass fibre reinforced polymers.

The application of the 50% threshold on unidirectional carbon/epoxy samples, containing porosity, demonstrated excellent correlation to the microscopic measurements, both qualitatively and quantitatively. Comparison of the 50% threshold to the other thresholds showed the 50% threshold performed better in most cases, such as with composites that have thin resin layers, carbon/epoxy composites with a resin peak grey level of approximately 0.8, and for images with low-to-medium scattering noise.

In some situations, for instance in the presence of a high level of scattering noise and/or a low grey value of the resin peak, the threshold needs to be set to a lower value to reduce the overestimation of porosity due to resin voxels masquerading as pores because they are below the 50% threshold. To address this issue, a new adaptive algorithm has been proposed to find an appropriate threshold. This algorithm has been demonstrated using simulations to have significantly improved porosity measurement capabilities and reduced bias in the measurements.

All of the carbon/epoxy composites investigated in this work showed ‘two-peak histograms’, and so the 50% threshold was used as the primary tool to identify void sizes and shapes from the CT-images. However, in case of other material systems (*e.g.* glass fibre and epoxy resins), it is advisable to use the adaptive threshold as the materials give a ‘three-peak histogram’ due to their different linear attenuation coefficients.

4 EFFECT OF THE MANUFACTURING PROCESS ON VOIDS IN COMPOSITE LAMINATES

To investigate and evaluate the effect of void features on the mechanical performance in composite materials, it is important to be able to manufacture samples with a range of controlled void content. A typical criterion of less than 2% of porosity is acceptable for industry. However, it is important to investigate the range of the void contents, as voids are typically unevenly distributed in composite parts, and so there is likely to the be a local void higher than 2% in some sections of the structures. In this Chapter, a novel manufacturing process will be introduced that allows panels with a range of void contents to be manufactured in a controlled manner, whilst achieving a uniform porosity distribution

This involved investigating the manufacturing parameters, such as time, pressure and temperature, that are most likely to affect the manner in which the voids are formed in a particular specimen, and as a result control the void content and morphology of the voids in that specimen.

It will also be shown that the specific material system and lay-up of the sample also alters the void morphology, and therefore influences the required manufacturing process. A review of the literature has shown that voids mostly influence the matrix- dominated properties. Since the majority of voids are located between the plies, in the interface, a dominant effect on the interlaminar shear strength (ILSS) can be expected. Poor ILSS leads to through-thickness failure, which is the major concern for composite structures. Hence, in this work this material property is selected for further investigation. Furthermore, the test method that allows the ILSS to be calculated is the Short Beam Shear (SBS) Test. This test requires small samples, the length and width of each are based

on the selected laminate thickness. These small samples are ideal for achieving good scan resolutions when characterising the voids by X-Ray CT.

4.1 Materials and specimen preparation

Two carbon/epoxy toughened prepreg systems, developed by Hexcel, were investigated:

- HexPly® IM7/8552, with a nominal cured ply thickness (CPT) of 0.125 mm; and
- HexPly® IMA/M21 with a CPT of 0.184 mm.

In the IM7/8552 carbon fibre/epoxy system a thermoplastic toughening phase is dispersed within the plies throughout the bulk of the resin, whilst in the IMA/M21 carbon fibre/epoxy system an extra layer of thermoplastic particles are dispersed as a distinct 'interlayer' between the plies.

There are two types of voids that can be observed in laminates:

- intra-ply voids, which are located within plies; and
- inter-ply voids, which appear between plies.

Both types of voids can be inadvertently introduced into composites due to inadequacies in the manufacturing process; furthermore, the particular lay-up is also expected to affect the development of inter-ply voids due to the different interface between the plies.

The challenge in this work was to manufacture samples with bespoke void contents so that their effects can be better understood. In real world structures multi-directional layups are used, and so it would not be appropriate to only investigate unidirectional materials. Initially the simplest form of a multi-directional lay-up was chosen, a cross ply lay-up, as it is expected this will encourage the development of inter-ply voids due to the maximum difference in orientation of adjacent plies. The manufacturing process for IM7/8552 panels is described in Section 4.2 and the manufacturing process for IMA/M21panels is described in Section 4.3.

Each panel of IM7/8552 consisted of 19 plies in a symmetric cross-plied layup; whilst for IMA/M21 the total number of plies was 11. The number of plies was selected to ensure a similar thickness for both material systems. Some investigations prior to this work were undertaken in order to obtain the optimal lay-up. It showed that having two 90° plies in the midplane (i.e. total 20 plies for IM7/8552 and 12 plies for IMA/M21) leads to a shear crack initiating first in these 90° plies. Thus, by reducing number of 90° plies in the midplane, this type of failure can be eliminated and make the lay-up more

suitable for investigating the effect of voids on failure behaviour. The plies were cut to a size of 120 mm by 120 mm. The lay-up was undertaken in a clean room following standard lay-up procedures, except that the debulking step (undertaken for 10 minutes at room temperature) was undertaken at the end of the lay-up. This deviates slightly from the standard procedure of debulking every four plies, although due to the panel being thin and flat the effects were shown to be negligible.

After manufacturing the panels, samples were prepared for short beam shear (SBS) testing according to the ASTM standard D2344 [128]. 10 mm wide strips were cut from the panels using a water lubricated diamond cutting-wheel. The ASTM standard for short beam shear tests dictates that a span-to-thickness value of between 4 and 5 should be used, and so a span-to-thickness ratio of ~4.5 was chosen. As the thickness of the strips was shown to vary between 2.3 and 2.6 mm, the distance between the two bottom rollers (see Figure 5-1) was varied accordingly. To ensure that the samples were longer than the distance between the rollers, so that interference effects were reduced, the length of the SBS samples was chosen as 20-22 mm.

It should also be noted that the chosen manufacturing process for this study (as described in Section 4.2) is a compaction method that uses heater plates. These heater plates have a thermocouple close to the contact surfaces, which leaves a small defect on the composite laminates. The samples therefore had to be cut from the material around this thermocouple imprint, so as to avoid this surface defect on the samples, and thus the number of samples cut from each panel varied between 8 and 16.

The samples were μCT-scanned prior to testing, which was able to provide a high-resolution assessment of each sample's voidage due to their small size. Each scan consisted of analysing four stacked specimens simultaneously as the quality of the scans depends partly on the aspect ratio of the scanned cross section; individual specimens were then be 'separated' digitally during post-processing.

The scanning was undertaken using a Nikon™ XTH320 CT-scanner at a source voltage of 55 kV and source current of 140 μA, using four images per projection averaged to reduce the scattering noise; this achieved a scan resolution (voxel size) of 12.6-13 μm. The void content and morphology were visualized and analysed further using post-processing software VG Studio™ MAX version 2.2 with the porosity analysis plug-in. For post-processing, the 50% threshold was used, as discussed in Chapter 3.

4.2 Manufacturing process for IM7/8552

The manufacturing process is based on that developed by Nixon-Pearson *et al.* [129], in which the authors investigated the compaction behaviour of laminates and showed that voids were introduced into the laminates prior to compaction, and that no changes in the void content were observed for specimens consolidated at room temperature, but that the void content decreased with increasing compaction temperature.

Manufacturing panels with porosity involved a two-step manufacturing process:

1. Compaction of the samples at a given temperature and pressure
2. Additional curing in a hot air oven to ensure the laminates were fully cured.

Compaction of the panels at the chosen temperature and pressure levels was achieved via custom made heater plates, that were mounted in an Instron™ testing machine.

The heater plates were run through a Carrol&Meynell transformer with a maximum power of 1.5kVA and controlled by a single-channel Watlow EZ-ZONE PID controller.

The heater plates were heated up to a given temperature, and then the samples were placed between these plates. Afterwards the pressure was applied at a speed of 5N/s up to the given value (as shown in Table 4-1). When the pressure reached the selected value, samples were held under that pressure for a given time (Table 4-1) and then immediately removed from the heater plates and placed in a preheated to 180°C oven for 5 hours to complete the cure. The set-up of the experiment is shown in Figure 4-1.

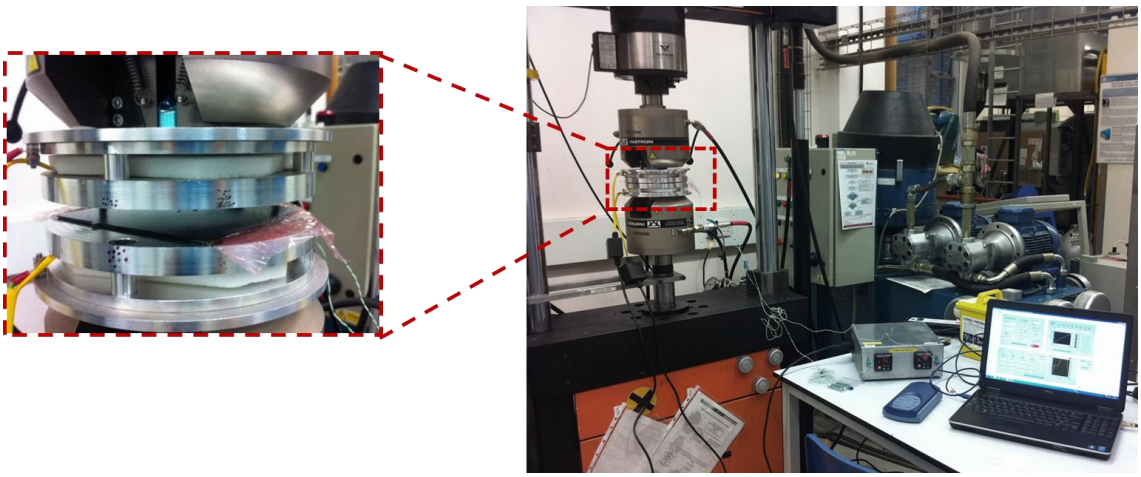

Figure 4-1. Experimental set-up for manufacturing panels with controlled void content.

Several process parameters were varied to investigate their influence on the void content: (i) temperature of the heater plate; (ii) consolidation pressure; and (iii) time of pressure

hold. Combinations of these variables were tested in order to provide samples having a range of void contents, as shown in Table 4-1.

Table 4-1. Manufacturing process of the IM7/8552 laminates.

	Consolidation				Curing in the oven	
	Temperature, °C	Pressure, MPa	Pressure ramp time, min	Time of hold, min	Temperature, °C	Time, h
Batch 1	30	0.3	15	1	180	5
Batch 2	90	0.3	15	1	180	5
Batch 3	120	0.3	15	1	180	5
Batch 4	90	0.3	15	10	180	5
Batch 5	90	0.3	15	30	180	5
Batch 6	90	0.6	30	10	180	5
Batch 7	120	0.3	15	10	180	5
Batch 8	120	0.6	30	10	180	5
Batch 9	Reference – Autoclave curing (see Figure 4-2)					

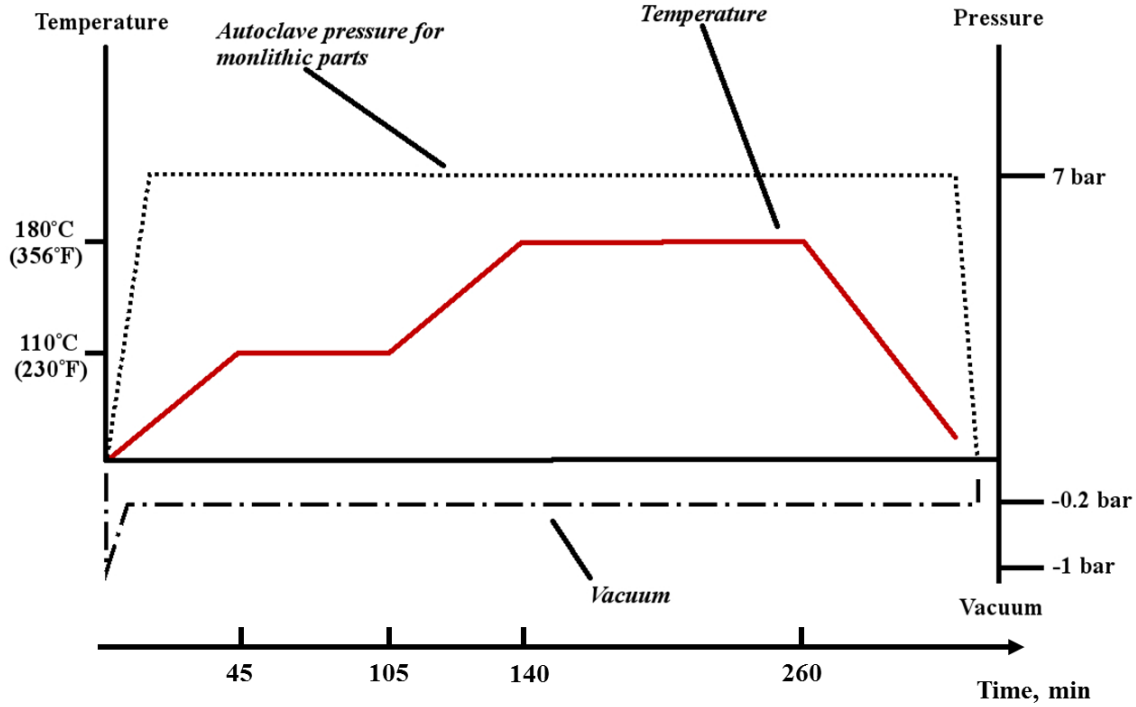

Figure 4-2. Autoclave cure cycle for IM7/8552 panels, as recommended by the manufacturer [130].

By changing the process parameters, it was possible to vary the average void content, as shown in Figure 4-3. Note, that the average void content for the reference batch (Batch 9)

is 0%. Detailed information about the data used to plot Figure 4-3 is provided in Appendix 1, Table 1. The influence of these process variables on porosity is described in the following sub-sections.

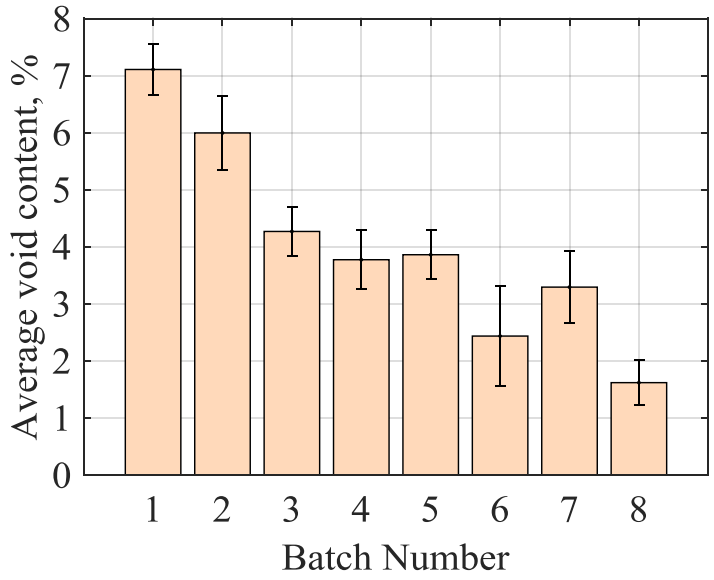

Figure 4-3. Average void content in different batches IM7/8552.

4.2.1 Effect of the heater plate temperature

It can be expected that the temperature of compaction will affect the average void content of samples due to the decreasing viscosity of the resin at higher temperatures, and therefore increasing resin flow. The effect can be most easily investigated by looking at batches 1, 2 and 3 in which all other variables are constant (see Table 4-1). These panels were exposed to the chosen temperature for approximately 16 minutes, consisting of increasing the pressure to the desired pressure of 3 MPa (15 minutes) and holding the pressure (1 minute).

Figure 4-4 shows that the ‘cold’ consolidation at 30°C leads to extensive voidage in the panels (around 7%). Increasing of the temperature of the heater plates to 120°C decreases the average void content down to around 4%.

As previously mentioned, this is due to the viscosity of the 8552 resin decreasing at higher temperatures, thereby causing it to flow more easily (see the viscosity plot of Figure 4-5, taken from the Hexcel datasheet [130]). It can be suggested that this flow helps any trapped air to escape, hence the voidage in samples to reduce.

However, there is still a high level of porosity in all samples, even those samples that have been consolidated at 120°C. This can be explained by the low compaction pressure and time of consolidation at the chosen temperature.

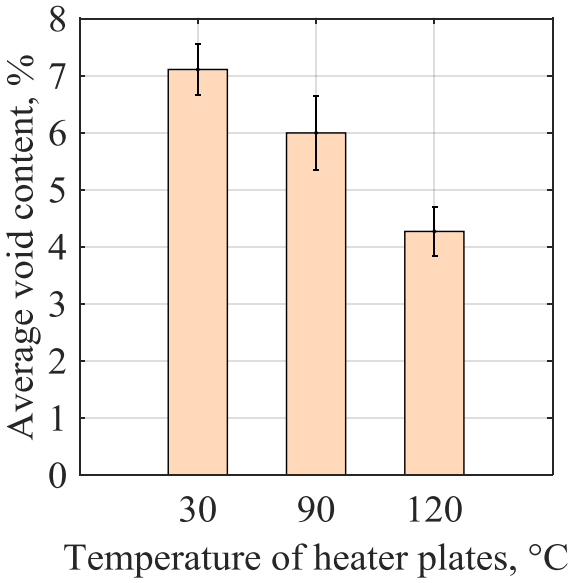

Figure 4-4. Effect of the compaction temperature on average void content.

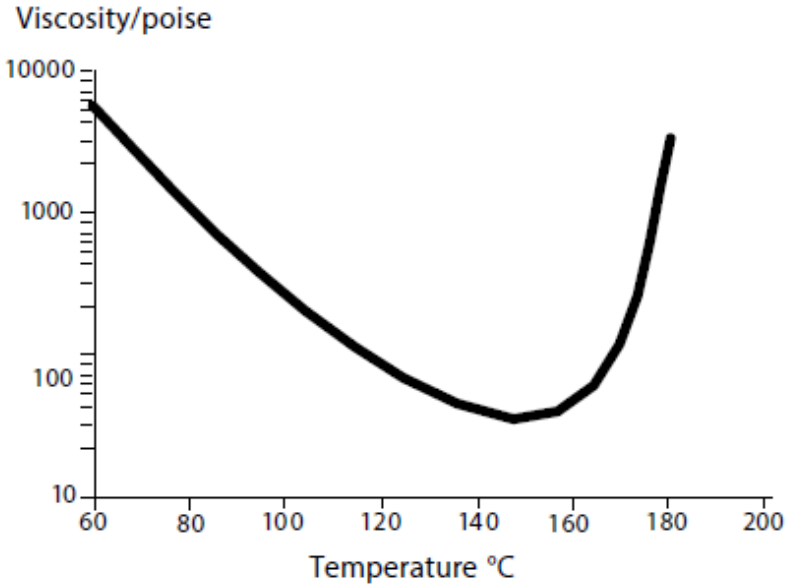

Figure 4-5. Rheology of 8552 resin [130].

4.2.2 Effect of the consolidation time on average void content

The second parameter of the compaction process that has been investigated is the hold time. As seen in Section 4.2.1, the temperature of the heater plates has a significant effect on the average void content. However, the hold time for those batches was only one minute, which is thought to be insufficient to allow air to escape. By increasing the

pressure hold time, it was thought that the average void content in the panels would be decreased.

Three panels (batch 2, 4, and 5 – with reference to Table 4-1) were manufactured using the same compaction temperature (90°C) and pressure (0.3 MPa); however, they have been compacted at this pressure for different periods – 1 minute, 10 minutes and 30 minutes (Figure 4-6a). It is observed that increasing the time of compaction up to ten minutes reduced the average void content by about 40%. However, further consolidation for 30 minutes did not further affect porosity in the panels, which stayed constant at 3.8%. It can be surmised that for these process parameters (*i.e.* T = 90°C and P = 0.3 MPa) resin flow occurs, which allows trapped air to be squeezed out of the composite panels. At this point a steady-state is reached at which the void content is at equilibrium for the given temperature and pressure profile on the panel. The same behaviour was observed for the panel compacted at 120°C (Figure 4-6b), which achieved a void content reduction of 40% by increasing the time of compaction from 1 minute to 10 minutes.

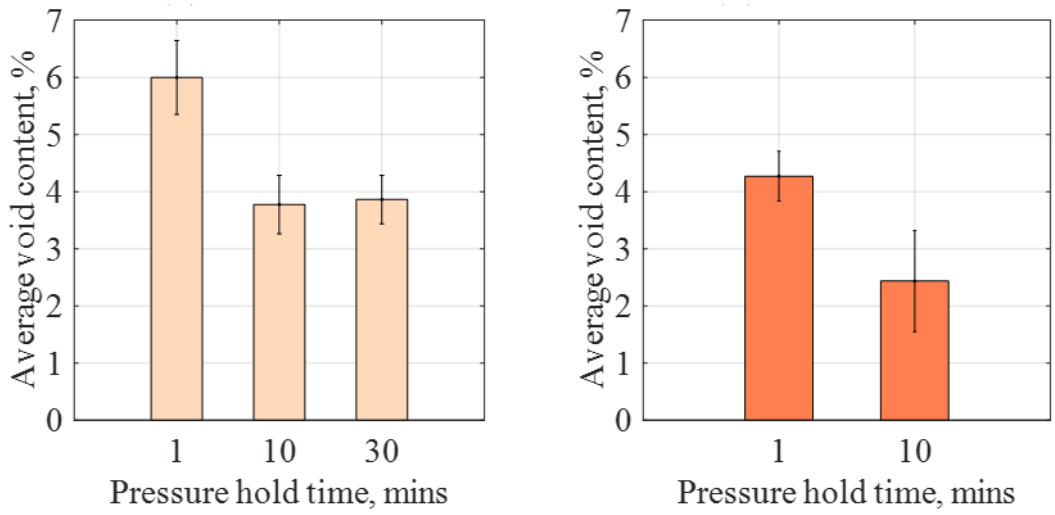

(a) T = 90°C **(b) T = 120°C**

Figure 4-6. Effect of 0.3 MPa pressure hold time on average void content at: (a) 90°C and (b) 120°C.

4.2.3 Effect of the compaction pressure on average void content

The pressure of the compaction process is another significant process parameter that is likely to affect the porosity in composite panels. In this work, in order to introduce voids into the laminates and 'lock' them within the panels, a lower pressure than the 0.7 MPa recommended by the manufacturer for autoclave curing was applied, and only on the first step of compaction (not for instance during subsequent curing).

To compare the effect of pressure levels on the average void content, two pressure values – 0.3 MPa and 0.6 MPa – were investigated.

As expected, with an increase of pressure the average void content decreases, so that for panels that had been compacted at 90°C (Figure 4-7a) a reduction of 12% in the void content is achieved. This decrease in void content is more pronounced at higher temperature, for example Figure 4-7b shows that at a temperature of 120°C porosity reduces by 30% (when comparing samples compacted at 0.3MPa and 0.6MPa). This is due to the higher resin flow caused by the lower viscosity at elevated temperatures (see Figure 4-5).

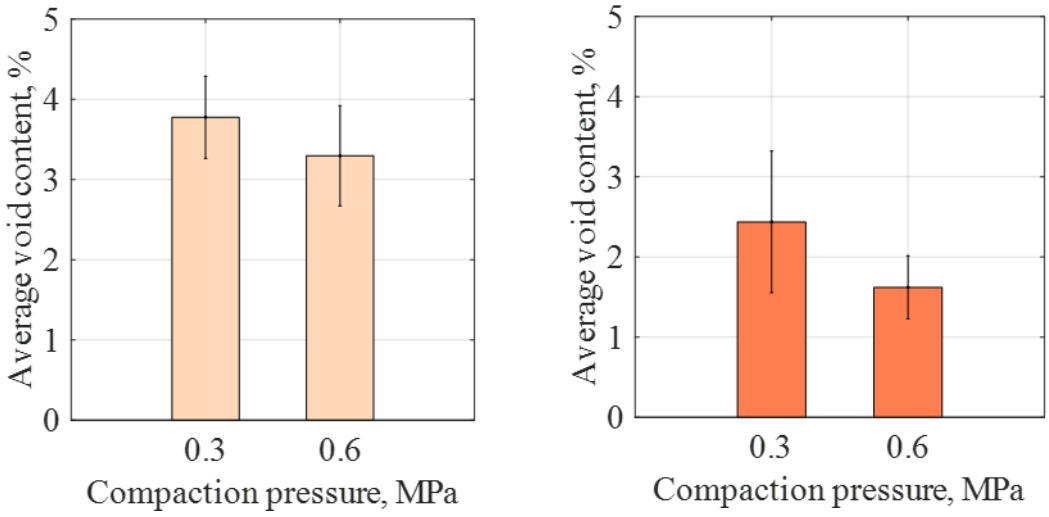

(a) T = 90°C **(b) T = 120°C**

Figure 4-7. Effect of the pressure on the average void content during compaction at: (a) 90°C and (b) 120°C. (Time of pressure hold is 10 minutes).

4.2.4 Curing in the oven

Following compaction, an important stage of the manufacturing process is oven curing the panels in order to produce samples that are fully cured. In [129], the authors reported that the internal architecture of consolidated panels could be 'frozen' by oven curing at 100°C for 12 hours with no applied pressure; this allowed further investigation of the void morphology to be undertaken. However, 100°C is insufficient to complete the cross-linking reactions in the resin and so the panel remains partially cured.

It can therefore be expected that the temperature of the oven will need to be increased, and so an investigation of the effects of curing temperature on the voids in the composite panels has been undertaken. The investigation involved taking two sets of compacted panels, and exposing one set of panels to 100°C for 17 hours and another set to 180°C for 5 hours.

The results can be seen in Table 4-2, which showed that the panels that were cured at 180°C had almost double the volume of voids as the panels cured at 100°C. In Campbell *et al.*[5], it is explained that voids grow if the internal pressure of the void exceeds the pressure of the liquid resin. As the viscosity of the resin at 180°C is lower and the void gas expansion greater than at 100°C, the voids are able to grow more easily and therefore requires a correspondingly larger resin pressure to suppress their growth. Once gelation occurs the voids are 'locked' in the sample.

Table 4-2.Effect of the curing temperature and time on average void content.

	Average void content, %	
	Curing in the oven at 100°C for 17 hours	Curing in the oven at 180°C for 5 hours
Compaction at 30°C	4.87 (±0.68)	7.1 (±0.45)
Compaction at 90°C	1.82 (±0.36)	5.99 (±0.64)

For the sake of clarity, samples cured at 100°C exhibited very low degree of cure (46-51%), as confirmed by differential scanning calorimetry (DSC). They were thus were not used in any further testing. Samples that were cured in the oven at 180°C for 5 hours showed 84-89% of cure degree. This time and temperature are recommended in the manufacturer's datasheet in order to achieve the correct cure degree.

4.3 Manufacturing of IMA/M21 panels

The manufacturing process used to introduce voids in the IM7/8552 panels was also used to introduce voids in the IMA/M21 panels, however the resultant panels possessed an extremely high void content (30-35%). As a result of the toughening particles, the surface of the IMA/M21 prepreg is rougher and less tacky than the IM7/8552, and therefore appears to have increased the amount of air entrapped during the layup process. Furthermore, during the oven cure, the void pressure increases as the temperature rises, which leads to further void formation and expansion. This effect is not counteracted as there is no pressure applied during oven curing to reduce the void content by collapsing the voids. To mitigate this problem, a vacuum pressure was applied during the oven cure, which reduces the average void content within the samples to a level comparable to the upper end of the IM7/8552 panels' void content (*i.e.* 8-11%).

Different batches were manufactured, as shown in Table 4-3, with each batch varying the temperature of the heater plates, the consolidation pressure, and the hold time. All the

panels were subsequently cured in the oven at 180°C for 3 hours to ensure the laminates were fully cured.

The average void content for each batch of the IMA/M21 laminates is shown in Figure 4-9.Note, that the average void content for the reference batch is 0%. Detailed information about the data used to plot Figure 4-9 is provided in Appendix 1, Table 2. Even when applying a vacuum pressure to the IMA/M21 panels, the panels still have a very high void volume. Furthermore, the variability in void content within the panels is also greater for IMA/M21. This can be explained by the presence of the interlayer of toughened particles in IMA/M21 that means that a high pressure is required to suppress the trapped air that would have otherwise grown into a void once the temperature increased. This is a good example of the influence of material morphology on porosity quantity and distribution.

Table 4-3. Manufacturing process of the IMA/M21 laminates

	Consolidation				Curing in the oven*[2]	
	Temperature, °C	Pressure, MPa	Pressure ramp time, min	Time of hold, min	Temperature, °C	Time, h
Batch 1	30	0.3	15	1	180	3
Batch 2	90	0.3	15	1	180	3
Batch 3	120	0.3	15	1	180	3
Batch 4	150	0.3	15	1	180	3
Batch 5	90	0.3	15	10	180	3
Batch 6	90	0.3	15	30	180	3
Batch 7	90	0.6	30	10	180	3
Batch 8*[1]	90	0.3	15	20	180	3
Batch 9	180	0.3	15	180	No oven was used	
Batch 10	Reference – Autoclave curing (see Figure 4-8)					

*[1] Vacuum was applied during consolidation. *[2] Vacuum pressure was applied during curing in the oven

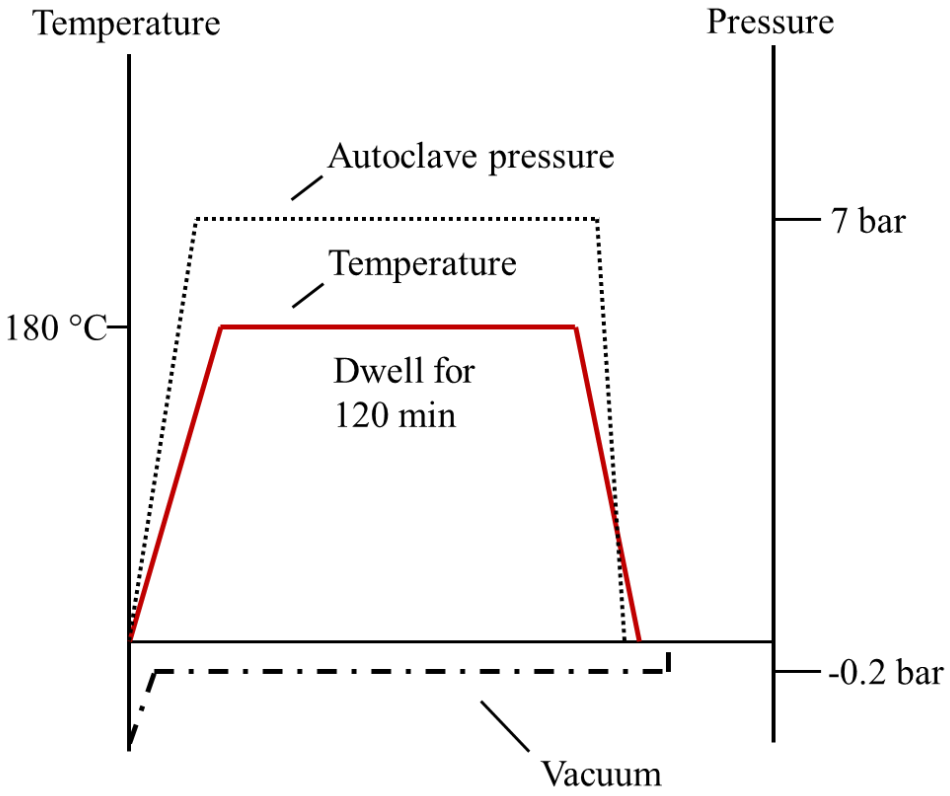

Figure 4-8. Autoclave cure cycle for M21 resin recommended by manufacturer [131].

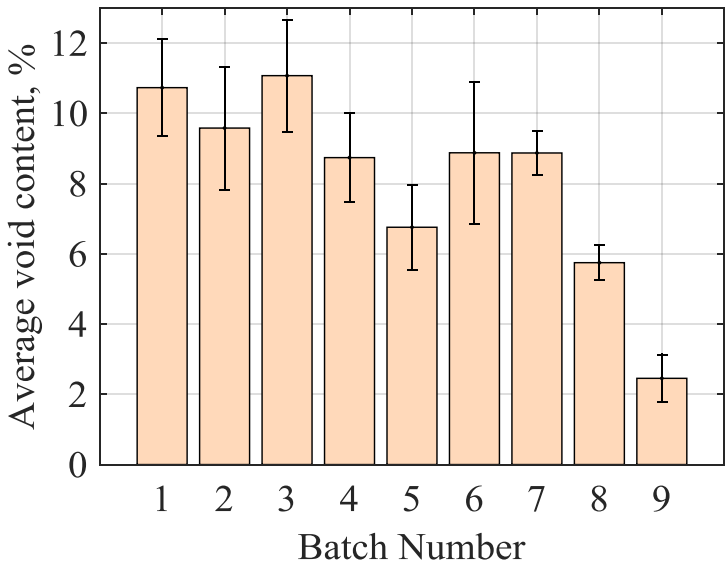

Figure 4-9. Average void content in IMA/M21 laminates manufactured using different process parameters (see Table 4-3).

4.3.1 Temperature effect on the average void content in IMA/M21 laminates

The 8552 and M21 resins have different viscosity profiles (see Figure 4-5 and Figure 4-10). A rapid decrease of the viscosity with increasing temperature can be observed for

the 8552 resin, however the viscosity of IMA/M21 'plateaus' for temperatures between 100°C and 160°C. To take this into account, a further testing temperature of 150°C is investigated.

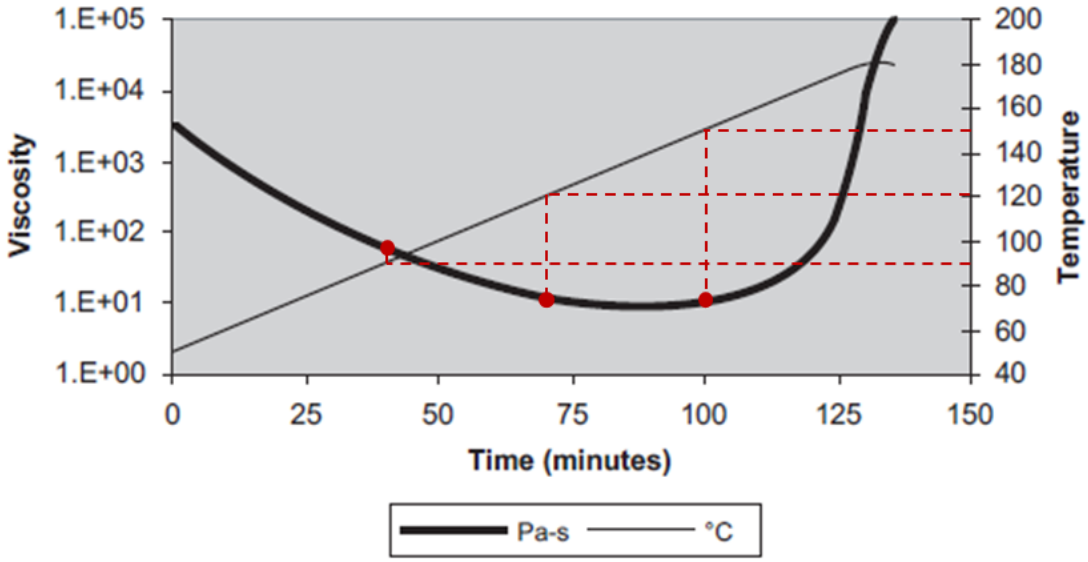

Figure 4-10. Viscosity profile for the M21 resin [131].

Figure 4-11 shows the distribution of the void content as the consolidation temperature is increased. At the coldest compaction temperature (*i.e.* 30°C) a large number of voids are introduced into the panels, whereas by increasing the temperature to 90°C the average void content is decreased by 18%. Further elevation of the temperature does not significantly affect the porosity. This analysis shows that this material system (*i.e.* IMA/M21) is not as sensitive to the temperature of compaction as IM7/8552.

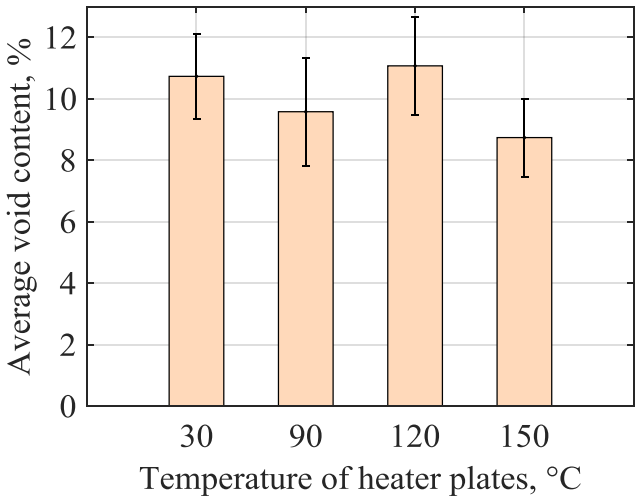

Figure 4-11. The effect of consolidation temperature on the average void content for IMA/M21 laminates.

4.3.2 Effect of consolidation time on the average void content for IMA/M21 laminates

As shown in section 4.3.1, the temperature of the heater plates doesn't lead to a significant reduction in the average void content. However, it is expected that the time of pressure hold will have a greater effect on void formation.

To investigate this, three different panels were manufactured using the heater plates, each heated up to 90°C and consolidated at a pressure of 0.3 MPa. Once the consolidation pressure was reached, the pressure on each panel was held for either 1, 10 or 30 minutes. Increasing the time that the pressure was held from 1 minute to 10 minutes was found to reduce the void content by 30% (Figure 4-12), however, perhaps surprisingly, further increase of the consolidation time to 30 minutes resulted in an increase in the void content compared to a consolidation time of 10 minutes. This is potentially explained by the resin being given sufficient time to reach the hold temperature (*i.e.* 90°C) and therefore having a lower viscosity (see Figure 4-10). Thus, this is likely to promote void growth unless sufficient pressure is applied.

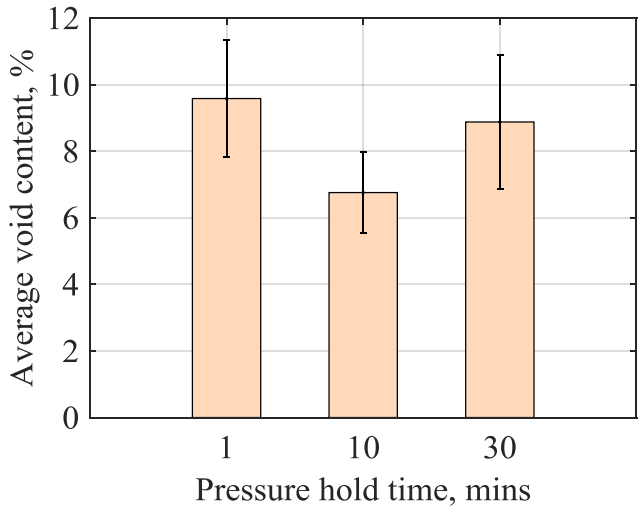

Figure 4-12. Effect of consolidation time on average void content for IMA/M21.

4.3.3 Pressure effect on the average void content for IMA/M21 laminates

The compaction pressure has previously been shown to have a significant effect on the average void content of IM7/8552 laminates (section 4.2.3). A similarly significant effect could be expected for this material system (*i.e.* IMA/M21), although due to the toughening particles an investigation of its effects is required. Two compaction pressures – 0.3 MPa and 0.6 MPa – were compared at a heater plate temperature of 90°C and hold time of 10 minutes.

The average void content for the respective batches, manufactured using the selected compaction pressures, is shown in Figure 4-13.

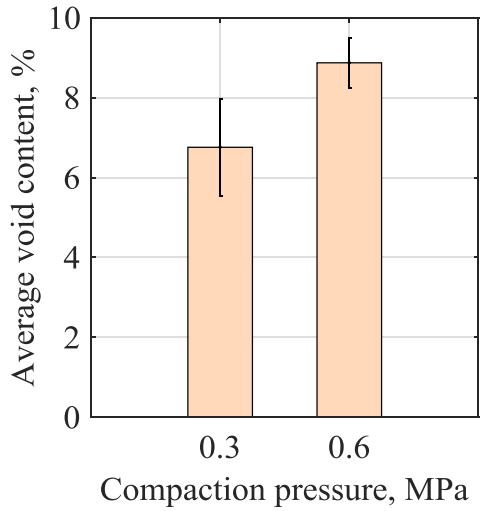

Figure 4-13. Effect of compaction pressure on the average void content for IMA/M21 laminates (average of 12 samples).

The effect of the pressure on this material system is shown to be different to the IM7/8552, in that an increase of the compaction pressure led to an increase in porosity within the panels. This is likely due to the increased time required to reach the higher compaction pressure of 0.6 MPa (approximately 30 minutes) in comparison to the compaction pressure of 0.3 MPa (approximately 15 minutes), and therefore the increased time provided to the panel to reach the hold temperature (*i.e.* 90^{o}C). As also discussed in Section 4.3.2, the viscosity of the resin will be lower if the resin is allowed to homogeneously reach the prescribed hold temperature, and as a consequence of this lower viscosity the void is able to grow larger if sufficient pressure is not applied to collapse it [5]. Furthermore, the higher pressure might also close off gas escape channels and trap the voids within the laminates.

4.3.4 Developing the manufacturing method to reduce the void content in IMA/M21 panels

It is clear that there are significant challenges to manufacturing IMA/M21 panels with controlled quantities of voids, and that no specific technique has been shown that can provide samples with the desired void content. Furthermore, the variation of the void content in each sample cut from the cured panels is dependent on its location in the panel, in particular showing a slightly lower porosity near the edges of the panels.

Some of the factors that result in this variability and unpredictability are discussed by Lukaszewicz and Potter [132] who showed that the surface of the IMA/M21 prepreg is rough, and that the interply zone doesnot form a continuous layer but is instead highly localised into discrete patches. These factors can therefore be expected to contribute to inhomogeneities in the void distribution and can furthermore be expected to exacerbate if the manufacturing process is sub-optimal.

In order to manufacture samples with an average void content of below 2% (*i.e.* acceptable by the aerospace industry) an improved compaction method has been implemented.

The improved compaction method comprises maintaining a vacuum pressure on the panel from manufacture of the completed uncured lay-up, until the panel is fully cured in the oven. This ensures gas initially present in the laminates is drawn out before the air escape channels are closed up when the resin viscosity drops.

The manufacturing process includes firstly, applying a vacuum pressure to the panels after lay-up. Keeping the vacuum on, the panel (in the vacuum bag) is placed on the heater plates at a compaction pressure of 0.3 MPa (see Figure 4-14) and held for 20 minutes. The panel then undergoes a final oven cure at 180°C for 3 hours, after which the vacuum pressure is released.

This method decreased the average void content to 5.75% (±0.5%), which is a 14% reduction from the lowest value achieved in the manufacturing methods of Sections 4.3.1, 4.3.2, 4.3.3, but is still far higher than required.

To further decrease the void content, the pressure applied during manufacture needs to be increased above that of vacuum pressure (*i.e.* 0.1 MPa). This is achieved by curing the panels in the heater plates whilst applying a constant pressure of 0.3 MPa.

The manufacturing process comprised the steps of heating the heater plates up to 90°C, applying a pressure of 0.3 MPa (at a ramp rate of 1 N/min), and then subsequently increasing the temperature of the heater plates up to 180°C for 3 hours.

This method allowed fully cured samples with an average void content of 2.46% (±0.67%) to be achieved.

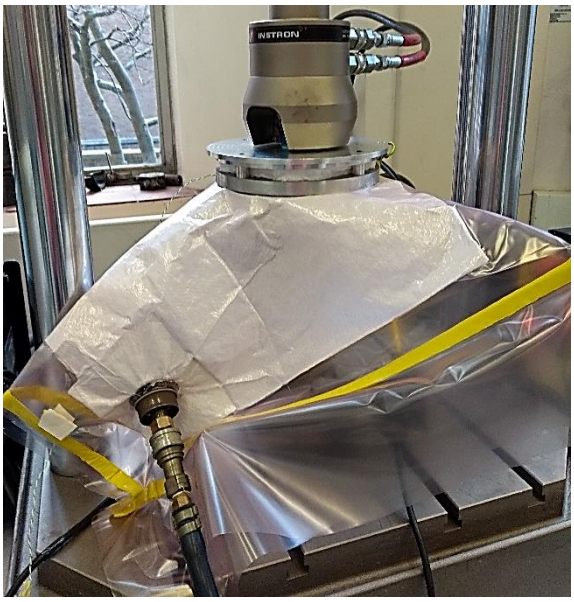

Figure 4-14. Compaction of IMA/M21 laminates using heater plates with applied vacuum pressure.

4.4 Effect of laminate lay-up on the average void content for IM7/8552

In Section 4.2, the effect of various manufacturing parameters on the void formation of IM7/8852 cross-ply laminates was investigated. However, it is well-known that many laminates include lay-ups in which the respective plies are oriented at oblique angles (*i.e.* not 90°), yet it is not currently known how void formation will be affected in such a laminate and whether this is different to a cross-ply lay-up.

To investigate these features a new lay-up was selected with the same number of plies as the IM7/8552 cross-ply laminates previously investigated (*i.e.* 19 plies) but having angled plies. The following lay-up was chosen:

$[(0, +30,-30)_3, 0, (-30, +30, 0)_3]$

(**Note:** this angle lay-up was selected in order to achieve a different failure behaviour during SBS tests – as shown in Chapter 5).

The manufacturing process parameters, shown in Table 4-4, were chosen based on the results on cross-ply laminates to attempt to achieve void contents between 2% and 5%.

After manufacturing, panels were cut to the required SBS test specimen size according to ASTM D2344 and μCT-scanned, as described in Section 4.1.

Table 4-4. Manufacturing process of the IM7/8552 laminates with angled lay-up.

	Consolidation				Curing in the oven	
	Temperature, °C	Pressure, MPa	Pressure ramp time, min	Time of hold, min	Temperature, °C	Time, h
Batch 1	90	0.6	30	10	180	5
Batch 2	120	0.3	15	1	180	5
Batch 3	120	0.3	15	10	180	5
Batch 4	120	0.6	30	10	180	5
Batch 5	Reference – Autoclave curing (see Figure 4-2)					

Figure 4-15 shows the effect of the manufacturing parameters on the average void content for the angled ply lay-up, and a comparison with the void content for the cross-ply samples produced using the equivalent manufacturing process.

These results indicate that there is no significant effect of the temperature of the heater plates on the void content for the angle ply lay-up, *i.e.* when comparing batch 1 and batch 4, however this contrasts with the behaviour observed for cross-ply laminates in which an increase in temperature led to a reduction of the void content. Furthermore, the hold time did not show any significant effect on the porosity content, *i.e.* when comparing batch 2 and batch 3.

In contrast, the compaction pressure level is shown to have a significant effect on the void content for the angle ply lay-up composites (*i.e.* batch 3 and batch 4), showing a 37% reduction in the average void content when increasing pressure from 0.3 MPa to 0.6 MPa.

Whilst differences between the average void contents of the cross-ply and angle ply laminates were observed, the relatively limited parametric study revealed no obvious pattern between the manufacturing processes of the two lay-ups.

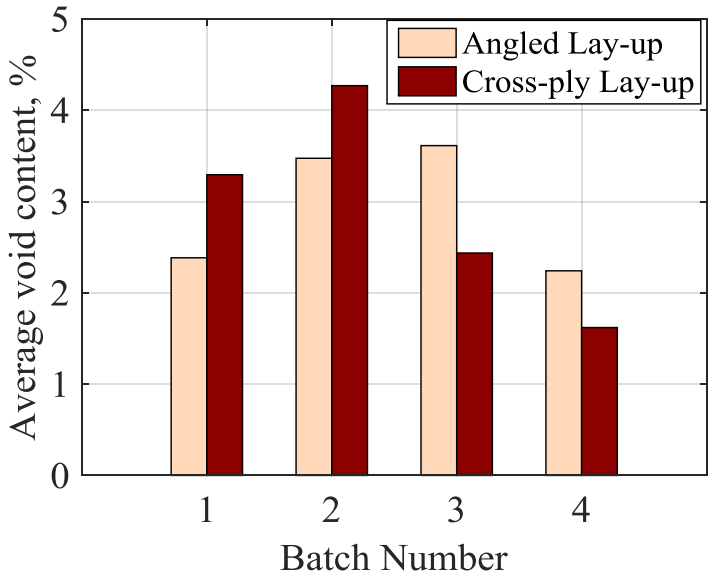

Figure 4-15. Comparison of the average void contents between two lay-ups: angle ply ([(0, +30,-30)$_3$, 0, (-30, +30, 0)$_3$]) and cross ply ([(0,90)$_4$,0,90,0,(90,0)$_4$]), with reference to batch numbers presented in Table 4-4 for both lay-ups.

4.5 Effect of material system and lay-up on the void morphology

Different types of materials, different stacking sequences, and different processing parameters are likely to affect the distribution, location, shape and size of voids developed during manufacturing. Furthermore, two types of voids can be found in composites: intra-ply voids, that are located within the plies of the laminates, and inter-ply voids, that are located at the interface in between the plies.

For both material systems – IM7/8552 and IMA/M21 – and for both lay-ups (cross-ply and angle ply), *intra-ply* voids are needle-like in shape and elongated in the direction of the fibres they are located within (*i.e.* in the 0°, 90°, +30° or −30° directions), and have a non-uniform distribution through the thickness of the laminate.

However, *inter-ply* voids show different characteristics for each material system and lay-up. For IM7/8552 cross-ply they have the same shape as intra-ply voids, *i.e.* elongated in the direction of the fibres of one of its adjacent plies, whereas the *interply* voids of the IM7/8552 angle ply samples are elongated but have a curved shape that combines the path of both angled plies at the interface, *e.g.* the void follows lay-up changes from 0° to +30° or 0° to −30°. Inter-ply voids in IMA/M21 are completely different to those seen in the IM7/8552 laminates, as they tended to be more circular, disc-like shaped, and are likely influenced by the pattern of the thermoplastic particles that are located at the interface.

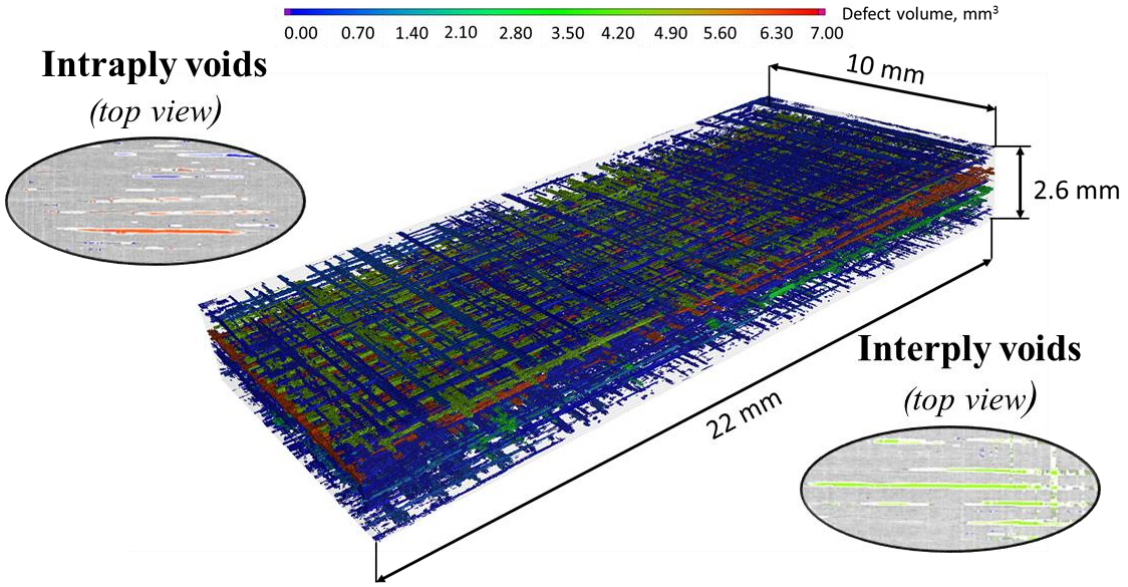

Figure 4-16. CT-image of the cross-ply IM7/8552 sample showing elongated intraply and interply needle-like shaped voids.

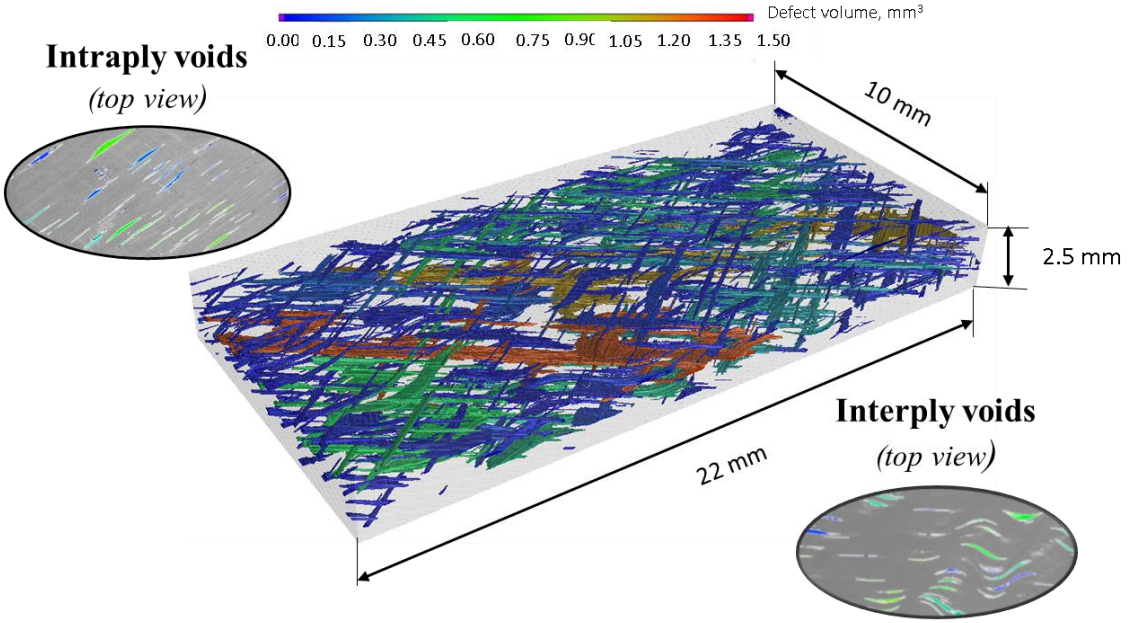

Figure 4-17. CT-image of the angle-ply IM7/8552 sample showing straight intraply and curved interply voids, elongated in the fibre direction.

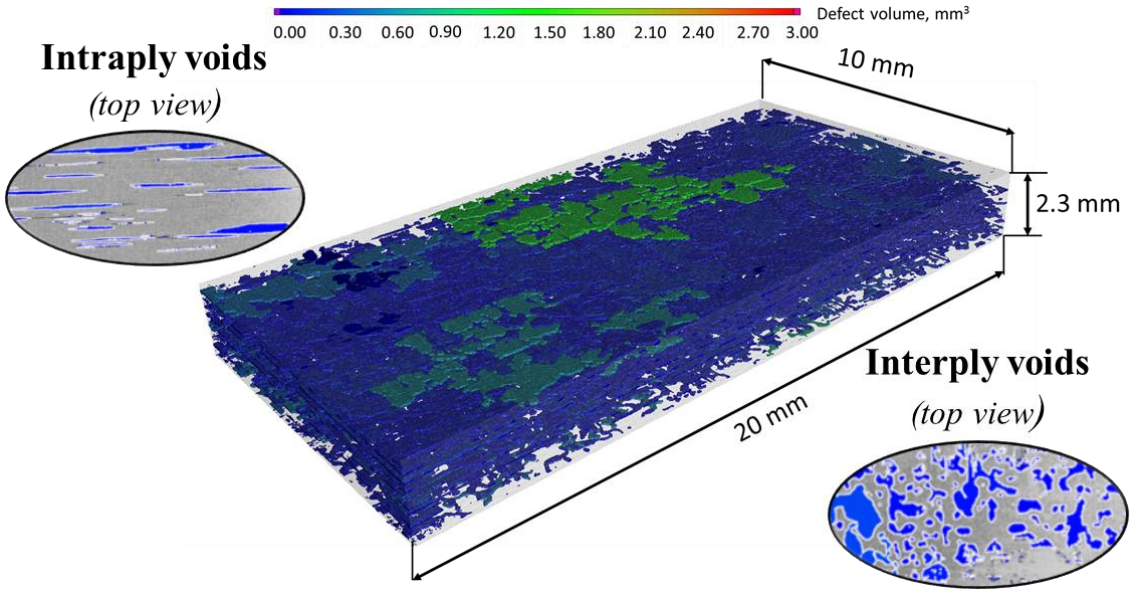

Figure 4-18. CT-image of the cross-ply IMA/M21 sample showing intraply and interply voids with different shapes.

4.6 Concluding Remarks

In this Chapter, it was shown that it is possible to produce samples that can be used to investigate the effect of voids on mechanical properties. In doing so, it has been shown that the void content and void morphology are significantly affected by a number of factors, such as the material system, laminate lay-up, and manufacturing conditions.

A new manufacturing technique has been introduced that is able to manufacture composite samples containing voids. Although it is not possible to produce samples with uniform void distribution using this method, it is possible to obtain samples with different void contents and different void sizes by varying different manufacturing parameters. Three different manufacturing parameters were varied in this research: temperature of the heater plates, the applied pressure, and the hold time of pressure.

All of three parameters have been shown to have a significant effect on the average void content for IM7/8552 cross-ply samples. For instance, it has been shown that with an increase of the temperature of the heater plates from 30°C to 120°C, the average void content decreased from ~7% to ~4%. This is presumably due to the increased resin flow of the samples, which could potentially help entrapped air to flow through the resin and escape. Although the increase of temperature decreased the void content in the samples, it did not eliminate voids completely from the laminates. This may be due to insufficient 'hold time' of the applied pressure or insufficient pressure applied to the specimen. It has

been shown that by increasing the compaction hold time a further decrease in the average void content is achieved. However, it was shown that for hold times above 10 minutes, there were no appreciable benefits. This is potentially due to the temperature of the specimen having reached an equilibrium temperature by 10 minutes, such that no further processes occur, and the voids are 'frozen' in position. Increasing the compaction pressure also decreased the average void content. However, a combination of all three parameters reduced the average void content most significantly.

The presence of toughened particles in IMA/M21 prepreg samples has been shown to greatly affect both the development of voids and the morphology of voids within the samples, such that the void content is greater and variability of void content within each panel is increased in comparison with IM7/8552 laminates. It was necessary to apply a vacuum pressure during oven curing in order to counter the increased porosity; otherwise the average void content was far too high (30-35%), although the void content was still found to be quite high (~7-12%). The effect of varying the manufacturing parameters was minimal in comparison to that observed in IM7/8552 processing, although some reduction in the void content was observed when increasing the hold time from 1 minute to 10 minutes. However negative effects (*i.e.* increasing void contents) were observed at longer hold times and higher compaction pressures, and this is thought to be due to viscosity effects in the samples. For instance, the longer hold time of 30 mins provides more time for the temperature to reach the compaction temperature, and thus decrease the viscosity and cause the voids to grow (in the absence of sufficient pressure to counteract their growth). Even when increasing the compaction pressure (from 0.3 MPa to 0.6 MPa) the void content was shown to increase, and this is again suspected to be due to changes in the viscosity, specifically it is thought to be due to the slow application of the load (5N/s) and the increased time for the sample with the compaction pressure of 0.6 MPa to reach the temperature equilibrium point compared to the sample at 0.3 MPa. To decrease the void content to ~2%, a compaction pressure of 0.3 MPa was applied throughout the consolidation and cure process, such that the laminate was cured in the heater plates at 0.3 MPa rather than in an oven at vacuum pressure (*i.e.* 0.1 MPa).

In the case of angled plies of IM7/8552, it has been shown that the dependence of the average void content on manufacturing parameters is different to the cross-ply laminates investigated in Section 4.2. In particular, the compaction pressure was found to be the most critical parameter for the angle-ply composites, whilst the temperature of the heater plates and the hold time did not significantly affect the porosity in these composite panels.

In terms of the morphology, μCT-scanning of the samples has shown that, whilst intra-ply voids (voids that are located within the plies) are elongated in the direction of the fibres and are mostly unaffected by the particular material system and laminate lay-up, the inter-ply voids (voids that are located in the interface between plies) dependent strongly on the particular material system and laminate lay-up. IMA/M21 cross ply interply voids appear to be circular (coin-like shaped), whilst IM7/8552 cross-ply voids are needle-like shaped and follow the fibre direction of the one of the adjacent plies. *Interply* voids of the IM7/8552 angle ply samples are elongated but have a curved shape that combines the path of both angled plies at the interface.

5 STATISTICAL ANALYSIS OF THE EFFECT OF VOID FEATURES ON COMPOSITE STRENGTH.

In this Chapter, an investigation of the effect of voids on composite mechanical performance has been undertaken using the samples manufactured in Chapter 4. As discussed previously in Chapter 4 and the literature review (Chapter 2), voids mostly influence of the matrix- dominated properties and, being located between the plies, at the interface, a dominant effect on the ILSS or Short Beam Shear (SBS) strength can be expected. Thus, the work in this Chapter is focused on this material property. It is expected that the size, morphology, and location of each of the voids within each sample will contribute to reducing the SBS strength, whilst the distribution of the voids within each sample is also expected to influence the failure behaviour.

A detailed investigation of the void features that affect SBS strength will be shown, indicating the void characteristics most critical to the failure behaviour.

5.1 Test method description

The Short Beam Shear (SBS) test consists of a three-point bending test on a specimen of small span to thickness ratio, and is arranged according to ASTM D2344 [128].

The SBS testing rig consisted of a cylindrical loading roller of 6 mm diameter suspended above a composite specimen having a span-to-thickness ratio of ~4.5, and two cylindrical support rollers of 3 mm diameter beneath the specimen (as shown in Figure 5-1). The width of the samples was chosen as 10 mm. The length of the samples was chosen between 20 mm and 22 mm so that a span-to-thickness ratio of ~4.5 could be achieved with additional material either side of the rollers.

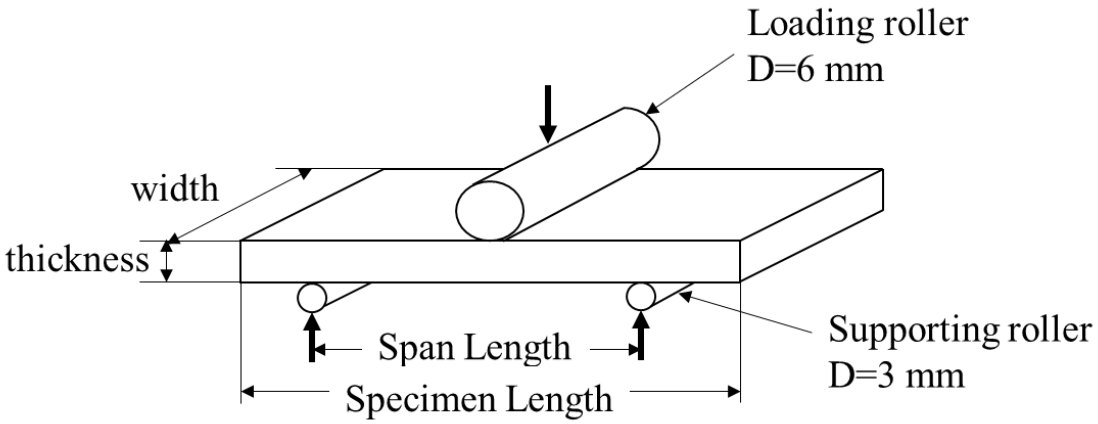

Figure 5-1. Schematic diagram of loading in a SBS test according to ASTM D2344.

The SBS rig was installed on a Shimadzu testing machine equipped with a 10 kN load cell configured to load the specimen at a crosshead speed of 0.5 mm·min^{-1} until a load drop-off of 30% was observed. The short beam shear strength of the composite was then obtained from the ASTM standard's assumption of a parabolic through-thickness shear distribution, *i.e.*:

$$\tau_{SBS} = \frac{3P_{max}}{4wt} \quad \textbf{(5-1)}$$

where P_{max} is the maximum load obtained during the test, and w and t are the specimen width and thickness, respectively.

5.2 Description of failure modes

5.2.1 Failure modes for cross-ply laminates of IM7/8552 and IMA/M21

Batches were manufactured using different process parameters, such as compaction temperature, pressure and hold time, in order to achieve panels with different void contents (see Table 4-1 and Table 4-3 in Chapter 4). Eight to sixteen samples of each batch were tested using the SBS configuration after undergoing X-ray CT-scanning.

All of the samples, for both material systems, failed via multiple matrix cracks followed by delamination Figure 5-2, as confirmed by the small load drop in the recorded load-displacement curves Figure 5-3 and Figure 5-4and the audible cracking noise during each test. The matrix cracking occurs due to thermal residual stresses and low mechanical properties in the transverse direction. However, it was observed that the IMA/M21 samples with higher void content displayed plastic-like behaviour (Figure 5-4) as

opposed to the sudden failure displayed by all of the IM7/8552 samples (Figure 5-3) and by the reference samples of IMA/M21.

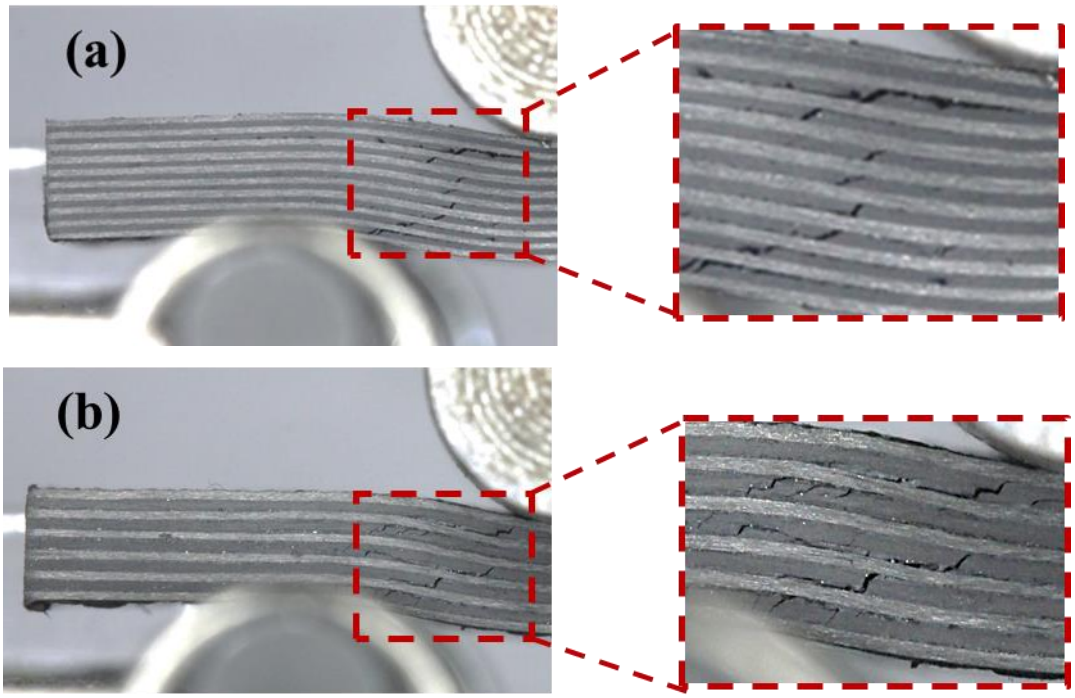

Figure 5-2. SBS test of the (a) IM7/8552 and (b) IMA/M21 samples, showing failure through multiple cracks. Note: the bottom rollers are attached to the testing jig by means of the springs which is obscuring the view of the lower roller.

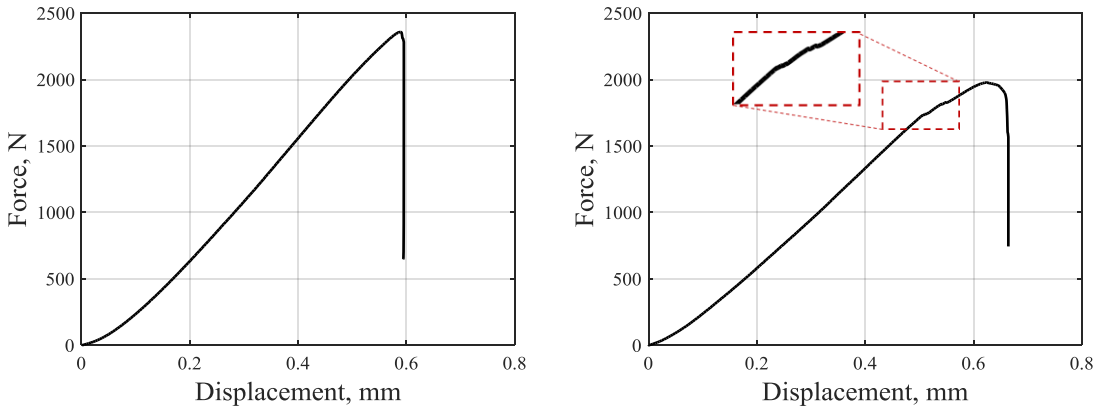

(a) **(b)**

Figure 5-3. Load-displacement graphs for the SBS tests for the IM7/8552 samples (a) reference sample; (b) Batch 2, sample No. 5, average void volume (*Vv*) = 5.38%.

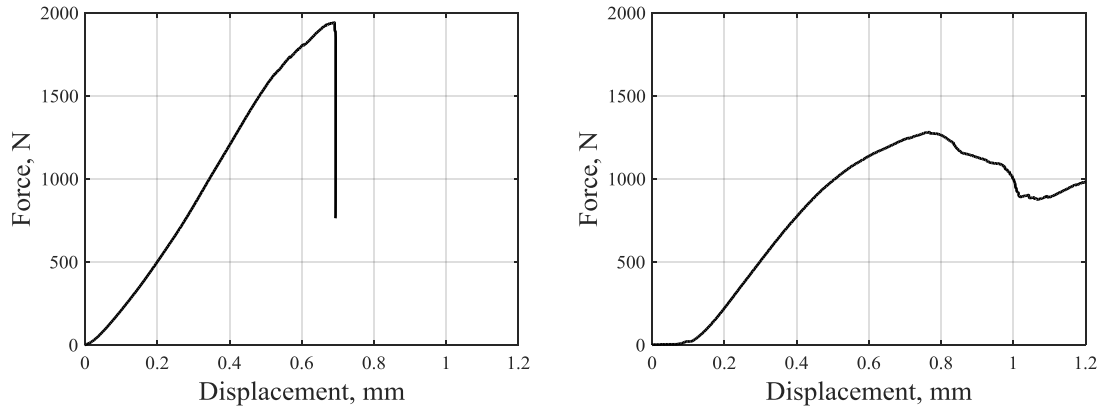

(a) **(b)**

Figure 5-4. Load-displacement graphs for the SBS tests for the IMA/M21 samples. (a) reference sample; (b) Batch 3, sample No. 1, average void volume (*V*v) = 8.05%.

The failure mode observed in cross ply laminates is different to the more commonly presented SBS tests on unidirectional laminates, which fail via delamination. As a result, the value of strength obtained in the reference samples is lower than the reported interlaminar shear strength (ILSS) for the same materials, and therefore cannot be referred as ILSS, and so is instead referred to as short beam shear strength (SBSS) through this work.

The failure mode is not only affected by the laminate stacking sequence, but also the presence of voids, which influence both the failure initiation and crack propagation. Tested samples were characterised by SEM, as shown in Figure 5-5. These images show how voids promote the development of many individual cracks within the material, and that the propagation of these cracks can involve redirection due to the voids. Furthermore, there is some evidence that the shape of the voids may influence the initiation and propagation of cracks. For example, voids of triangular cross-section appear to show cracks at the vertices, due to the radius of curvature being smaller and the resultant stress concentration being higher.

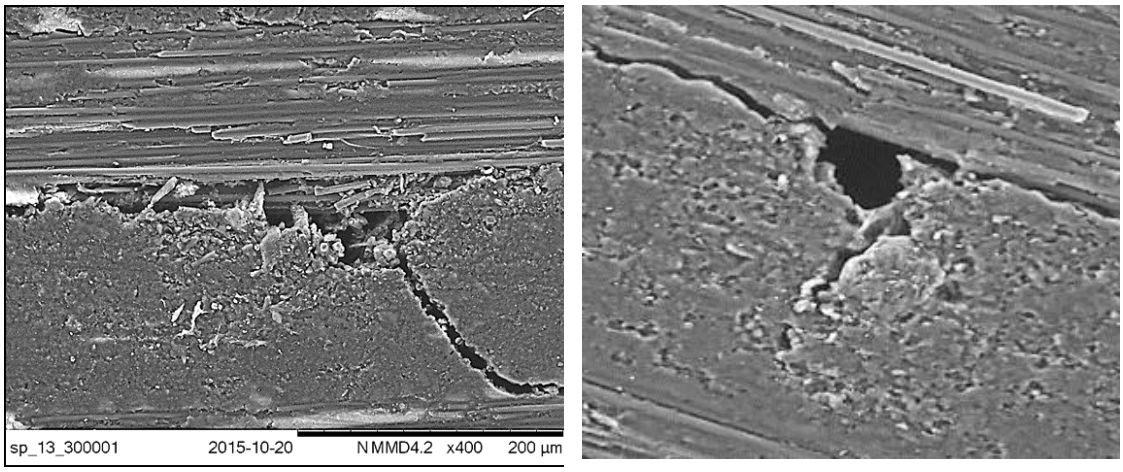

Figure 5-5. Scanning electron micrograph (SEM) of tested IM7/8552 samples with 4.35% void level, showing cracks emanating from (or propagating through) voids.

5.2.2 Failure modes for angle-ply laminates of IM7/8552

A different failure mode was observed for IM7/8552 angle-ply samples in comparison with cross-ply laminates. Specifically, the angle-ply samples failed via delamination first, at the +30/-30 interface, followed by matrix cracking (see Figure 5-6). This failure behaviour is contrary to that observed in the cross-ply laminates, which initially failed via multiple matrix cracking followed by delamination (see the discussion in Section 5.2).

5.3 Assessment of the critical void features

5.3.1 Effect of the average void content on SBS strength

As expected, the SBS strength decreases with an increasing average void content for both material systems, as shown in Figure 5-7 and Figure 5-8. The results show a linear correlation between the average void content and SBS strength, with coefficients of correlation of 0.9384 and 0.9274 for IM7/8552 and IMA/M21, respectively. However, significant scatter is observed in the fitting of the linear correlation. In fact, some of the samples with different void contents were found to have the same SBS strength, and conversely samples with the same void content failed at different SBS strength levels. To assess the reasons behind these observations, an analysis of the void features that affect SBS strength has been undertaken.

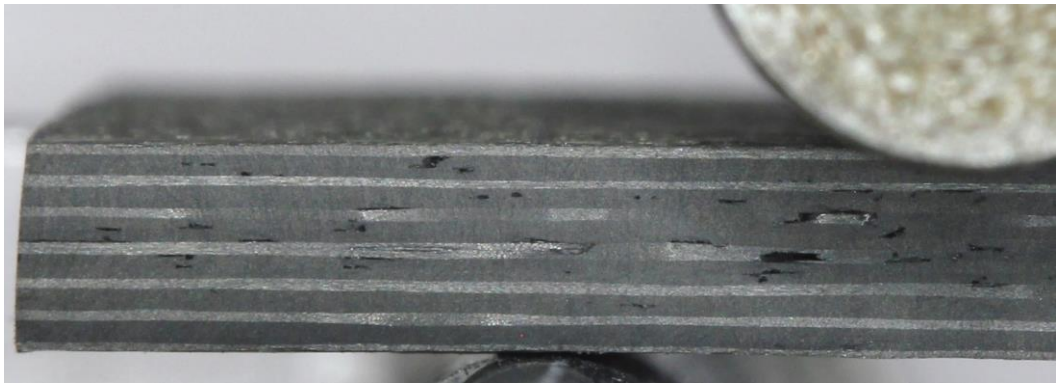

(a) Prior to the test

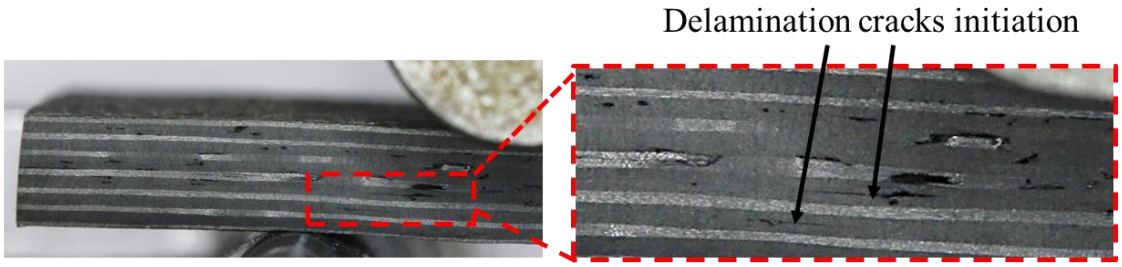

(b) During the test

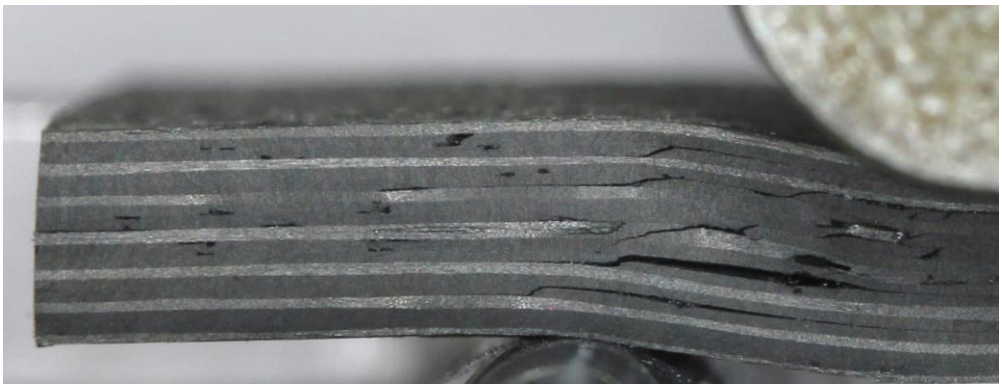

(c) After the test

Figure 5-6. Short beam shear (SBS) test of an angle-ply IM7/8552 sample showing initiation of delamination (recorded in the middle of the test) with further propagation of matrix cracks.

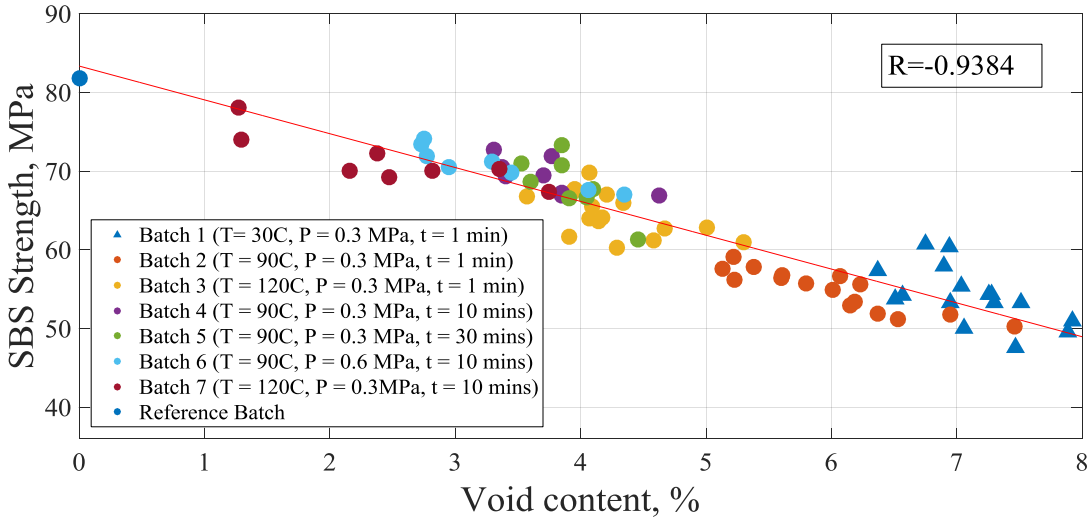

Figure 5-7. Reduction of SBSS with increasing of void content for IM7/8552 samples. Note, the reference value was taken as the average of 16 samples, SBS = 81.78 MPa (SD=4.92) .

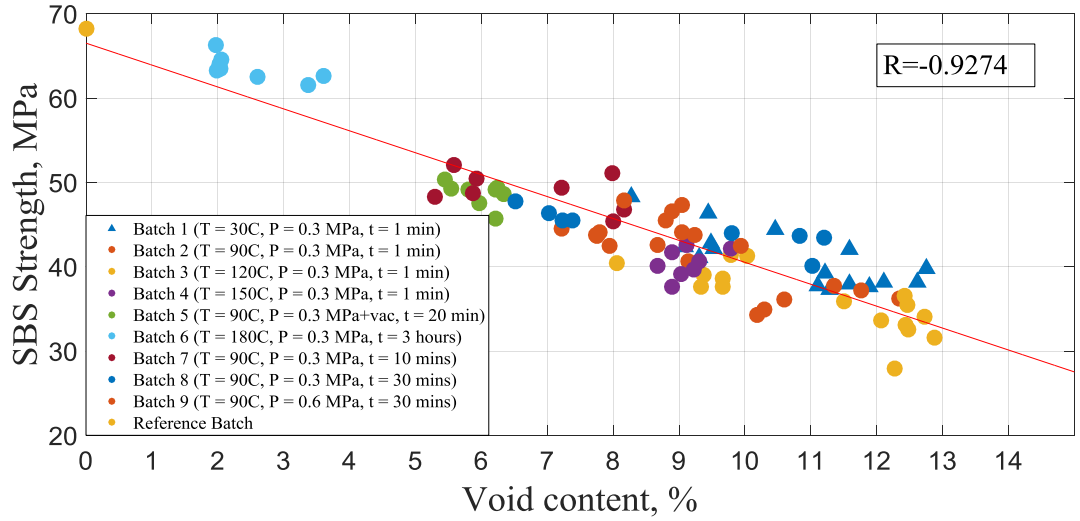

Figure 5-8. Reduction of SBSS with increasing of void volume fraction for IMA/M21 samples. Note, the reference value was taken as the average of 16 samples, SBS = 68.20 MPa (SD=2.52).

The relationship between average void content and SBS strength for the angle-ply lay-up displays the typical linear trend, such that a higher void content generally results in a lower SBS strength (Figure 5-9). However, there is significantly more scatter than that observed in the equivalent IM7/8552 cross-ply samples, shown in Figure 5-7.

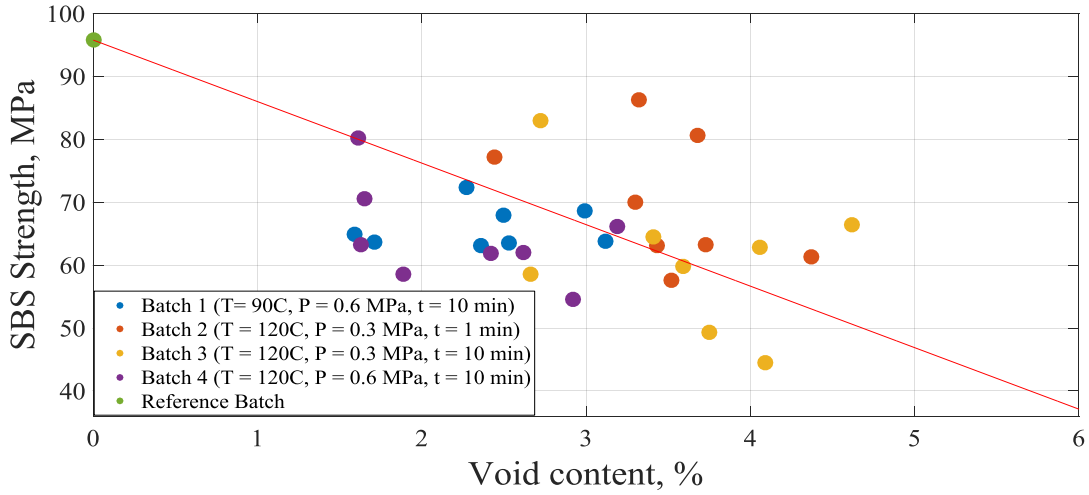

Figure 5-9. Reduction of SBS strength with increasing of average void content for angle-ply IM7/8552. Note, the reference value was taken as the average of 16 samples, SBS = 95.77 MPa (SD=7.7).

The cause of this scatter is likely due, at least in part, to the complex shape of the voids in the angle-ply laminates. In both the IM7/8552 cross-ply samples and angle-ply laminates the voids tend to be elongated in the fibre direction of the adjacent plies, and therefore the angle-ply are elongated in one of three directions (*i.e.* 0°, +30° or −30°). However, the interply voids of the angle-ply samples are further complicated in that they have a curved shape that combines the path of both adjacent plies at the interface (Figure 5-10).

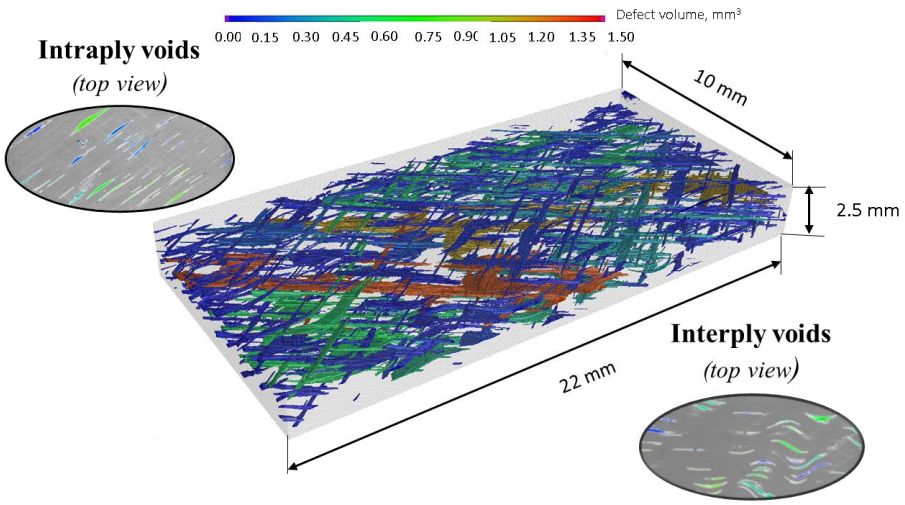

Figure 5-10. CT image of the angle ply IM7/8552 sample showing the shape of the voids.

The result of this is likely to have contributed to the observed scatter in the results, and in fact is likely to be a contributing factor in the failure behaviour that differs from that observed for the IM7/8552 cross-ply laminates.

Several angle ply laminates were tested in order to provide some initial insight into the effect of different lay-ups on the SBS strength and to provide an assessment of the different void shapes, how these differ from the voids produced in the cross-ply laminates, and to evaluate how these voids affected the failure.

The remaining sections of this chapter will show statistical analysis of key features of the voids in the samples in order to find ways of improving the correlation to the SBSS. However, due to the significant scatter in the angle-ply laminate results, only the void features of the cross-ply laminates will be investigated.

5.3.2 Analysis of void shape

The reduction of the mechanical properties of a laminate with voids depends on the detailed features of each individual void, and the mutual interaction of those voids with the laminate. These features can be divided into three categories, (i) void size, (ii) void shape, and (iii) void location. Void size can be characterised by volume, diameter or length in a particular direction. Void shape can be represented by aspect ratio, compactness or sphericity. The critical locations for voids were assumed to be the regions of maximum stress within the samples, where failure is most likely to occur.

5.3.2.1 Void shape for IM7/8552 samples

In IM7/8552 samples with low void content (*e.g.* less than 5%) the voids are generally constrained to a single plane, and even the largest voids do not significantly cross between ply layers (Figure 5-11a). However, Figure 5-11b shows that within the cross-section of this plane the voids form a network of interconnected needle-shaped voids. Note that VG Studio will consider voids as interconnected even if one voxel bridges between the voids, although it is unclear if these voids will behave as one larger interconnected void.

However, when the average void content increases in the IM7/8552 samples (*e.g.* above ~5%), the void networks expand and bridge between adjacent plies, as shown in Figure 5-12a. As a result, for IM7/8552 samples, the largest void, as identified by the VG Studio post-processing software, is actually a network of multiple voids connecting to each other, as evidenced by the CT-images in Figure 5-12a and Figure 5-12b.

This demonstrates the complex shape of the voids on IM7/8552 samples, especially with increase of the average void content.

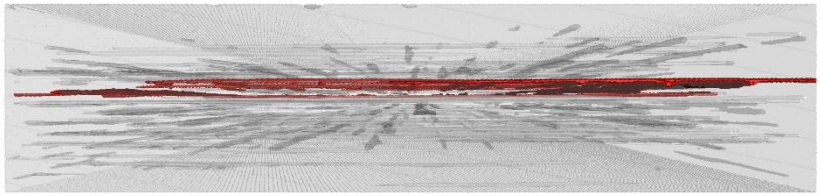

(a) 3D front view

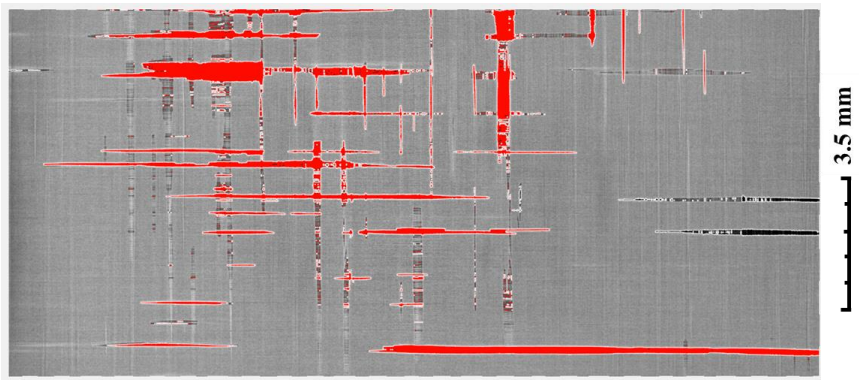

(b) Top view through large void (red colour)

Figure 5-11. A CT-image of the sample of IM7/8552 (V_v = 2.38%), (a) showing the front view with position of the largest voids; (b) cross-section (length-width plane), showing the joining of individual needle-like voids to form a single large void between 0° and 90° plies.

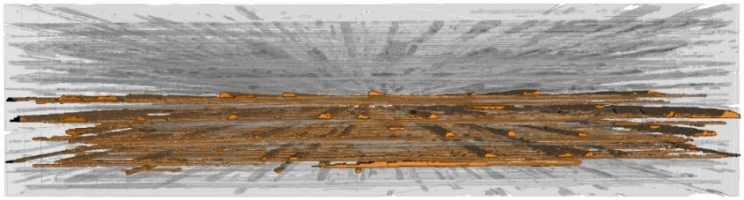

(a) 3D front view

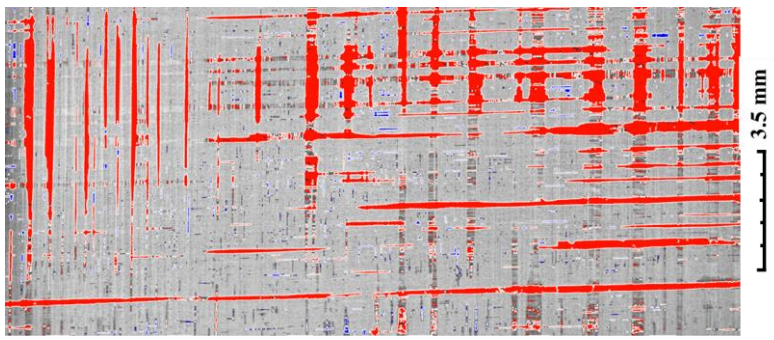

(b) Top view through largest void (red colour)

Figure 5-12. A CT-image of the sample of IM7/8552 (V_v = 7.89%), (a) showing the merging of voids through the thickness into one large void (total volume 17.12 mm^3); (b) Cross-section (length-width plane), showing the joining of individual needle-like voids to form a single large void between 0° and 90° plies.

5.3.2.2 Void shape for IMA/M21 samples

IMA/M21 samples have been shown to have different void shapes (see Chapter 4), and in particular it has been shown that the majority of the voids are located within the interface. As was observed for IM7/8552 at high void contents, some of the IMA/M21 samples with higher void content (*e.g.* more than ~5.5%) also showed merging of the voids through the thickness (Figure 5-13a), however most of them do not merge significantly in-plane (Figure 5-13b), and as a result the maximum void size reported by VG Studio MAX is significantly lower than found in IM7/8552 samples.

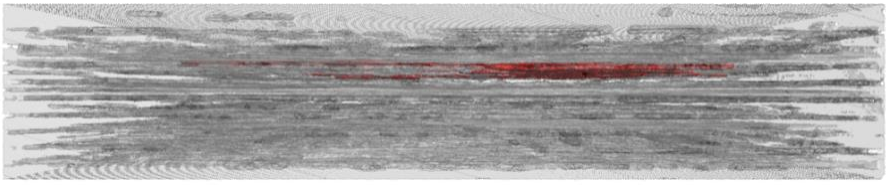

(a) 3D front view

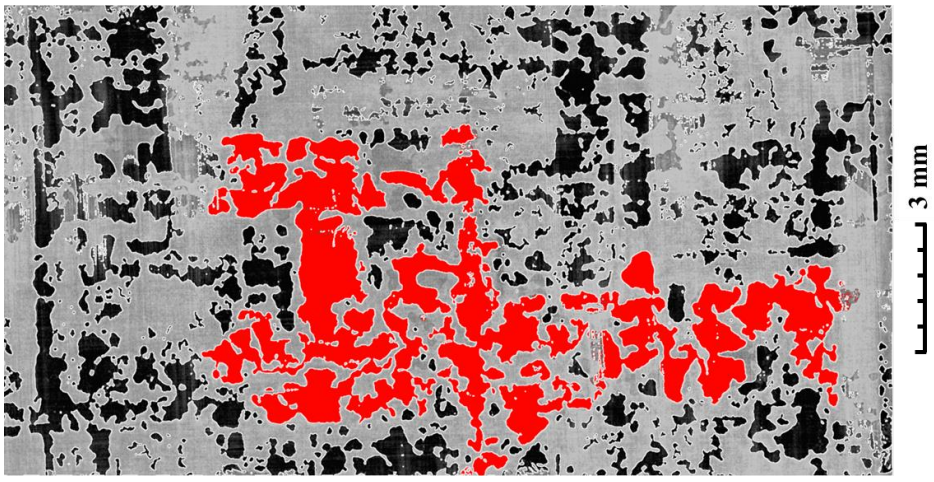

(b) Top view through the largest void (red colour)

Figure 5-13. A CT-image of IMA/M21 sample with *V*v = 10.6%, showing the position of the largest void (a) front view; (b) top view of the cross-section through void

Perhaps unsurprisingly, samples with smaller average void content do not exhibit a network of connected voids through the thickness or in-plane (see Figure 5-14), and instead show a more spherical void shape.

The difference of the void shapes between the material systems is likely to have many consequences for the failure behaviour of the samples, and the ability for the SBS strength to be predicted, as will be demonstrated below.

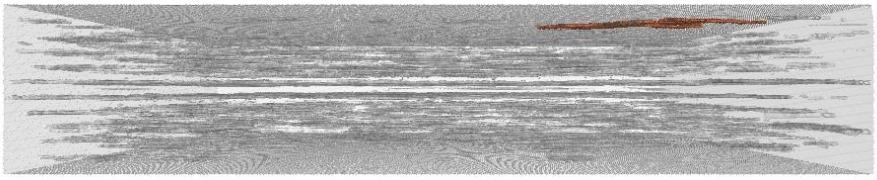

(a) Front view

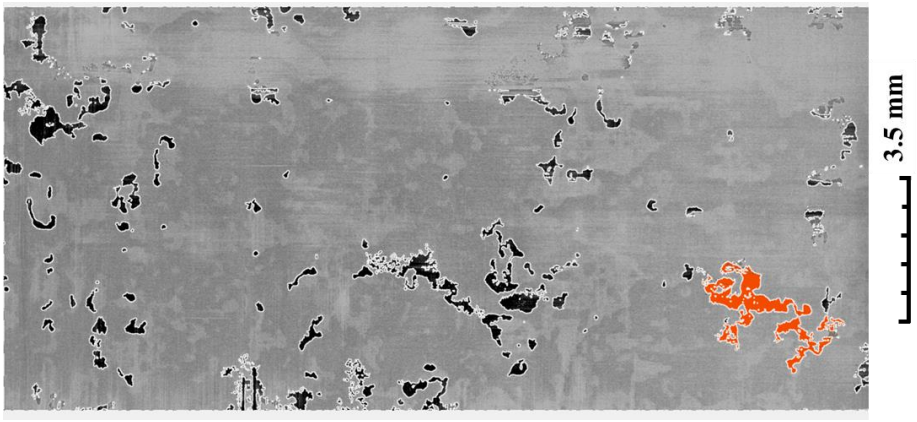

(b) Top view through the largest void (red colour)

Figure 5-14. A CT-image of IMA/M21 sample with *V*v = 2.6%, showing the position of the largest void (a) front view; (b) top view of the cross-section through void.

5.3.3 Number of voids within a sample

Each sample contains a large number of voids of varying sizes (up to 50,000 in some cases), although many of them are very small (*e.g.* less than 0.005 mm^3). For IM7/8552 samples, there are more smaller voids in the samples, and in fact there is a general increase in the number of voids as the voids become smaller, as shown in Figure 5-15a. For IMA/M21, a slightly different distribution is found (see Figure 5-15b), in that there is a peak in the quantity of voids for voids of approximately 3×10^{-4} mm^3 in volume. There are increasingly fewer voids of bother larger and smaller sizes.

The exact reason for this difference in behaviour is unclear, although it can be surmised that the toughened resin layer plays a key role.

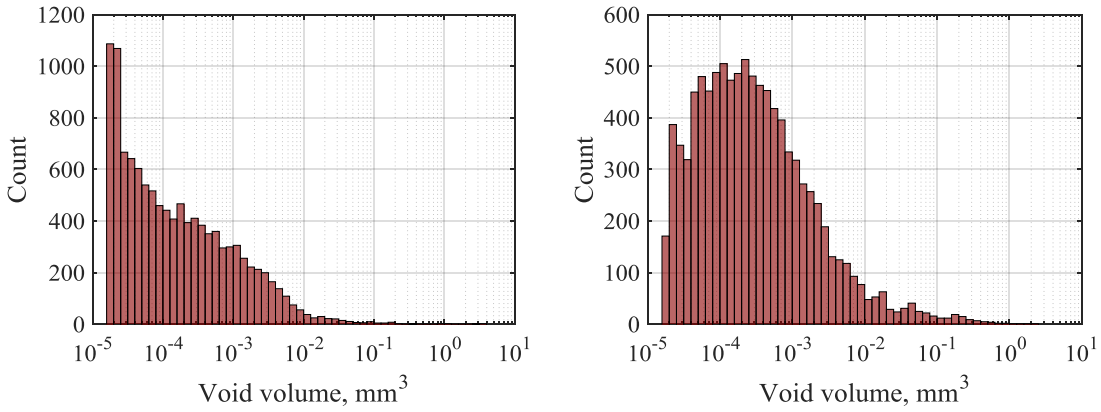

(a) IM7/8552 **(b) IMA/M21**

Figure 5-15. Void volume distribution in a sample of (a) IM7/8552, V_v = 6.01%, and (b) IMA/M21, V_v = 10.18%.

Figure 5-16 shows the distribution of the number of voids in each sample with the corresponding void content of that panel.

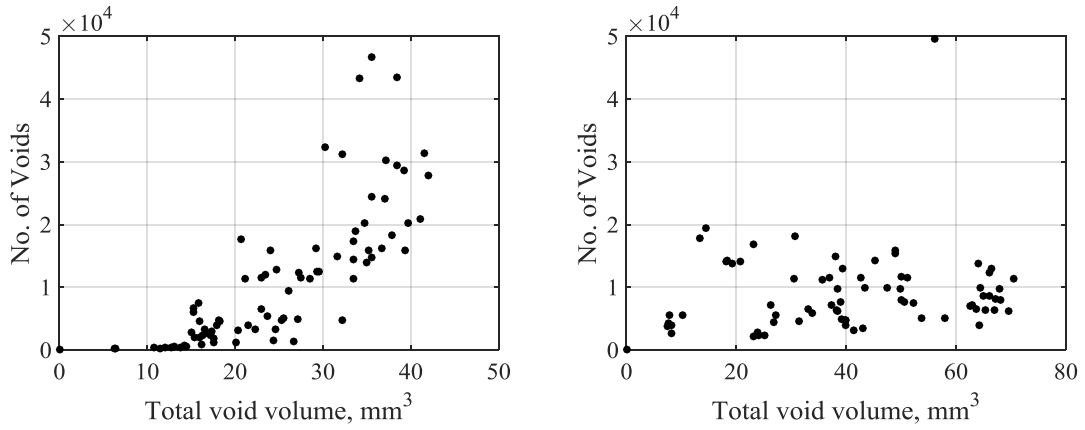

(a) IM7/8552 **(b) IMA/M21**

Figure 5-16. Total void volume plotted against number of number of voids in all samples of (a) IM7/8552, (b) IMA/M21.

From the graphs it is clear that void content does not correlate well to the number of voids in each sample. This is due to the distribution of void sizes in each sample, which varies; presumably at least in part due to the different manufacturing processes used. It is notable however, that the correlation for IM7/8552 is much clearer than for IMA/M21.

In comparing the IMA/M21 and IM7/8552 samples, it can be seen that the IMA/M21 samples generally comprise a larger number of voids in samples with lower void contents (with a minimum number of voids equal to 2,258 in comparison with 212 for IM7/8552). However, at larger void contents the IM7/8552 have a much larger number of voids. Overall, the number of voids in the IMA/M21 samples is much more consistent at all void contents, and this is likely due to the toughened interlayer in the IMA/M21 prepreg

which helps to form discrete boundaries between the voids to prevent them merging into one larger void.

Figure 5-17 shows the dependence of SBSS on the number of voids within each sample, which indicates there is little correlation between these two parameters, although there is a better correlation for IM7/8552. However, overall therefore the number of voids is not a good parameter (in isolation) to assess the void effect on the mechanical properties in these material systems.

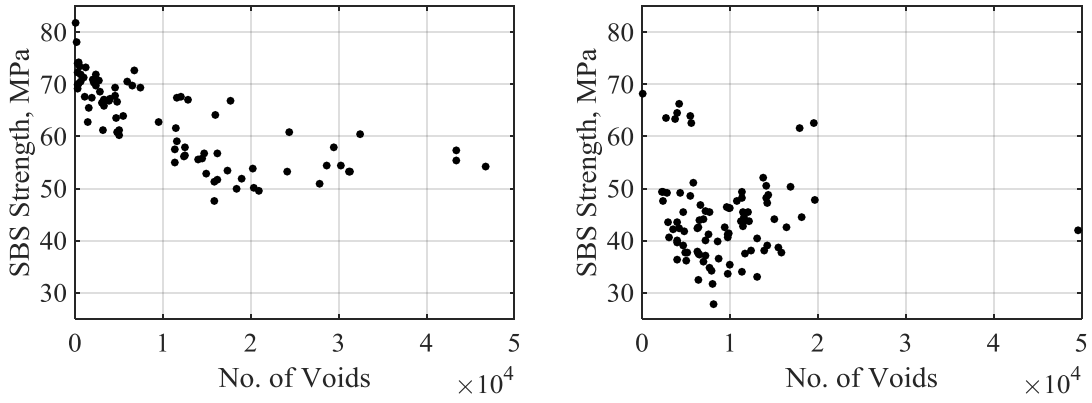

(a) IM7/8552 **(b) IMA/M21**

Figure 5-17. SBS strength plotted against number of voids for the both material systems. Note: reference sample with no voids is included in this graph.

5.3.4 Void Volume Distribution

It was shown in Section 5.3.2 that there are a large number of voids within each sample. However, after analysing the samples of IM7/8552 it was noticed that for samples with an average void content larger than around 5% there is typically one significantly large (by volume) void, or at least a small number of very large voids, whilst the remaining voids are smaller in comparison and gradually decrease in size (Figure 5-18a). For samples, having less than around 5% void content, the maximum void size (by volume) is only slightly bigger than the second largest void (*i.e.* there is no void that is significantly larger than all the others), as shown in Figure 5-18b. Furthermore, there is also a more gradual decrease in the void volume from the largest to the smallest voids. This can be explained by the complex shape of the voids, especially in samples with high void content, as these large voids are the result of a coalescence of several smaller neighbouring voids to form one large void 'network', as explained in Section 5.3.2.

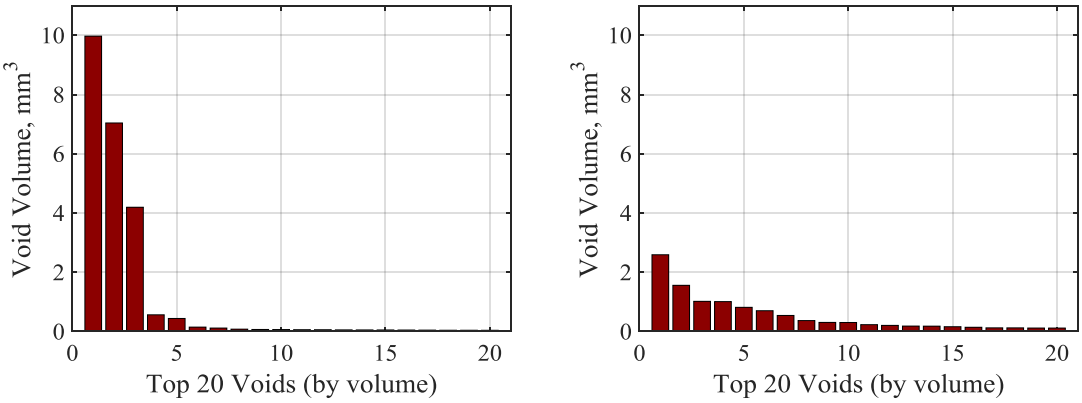

(a) V_v = 7.3% **(b) V_v = 2.59%**

Figure 5-18. Void volume distribution of the 20 largest voids in IM7/8552 samples with different void content.

For IMA/M21 samples, the size of the voids (by volume) is similar to IM7/8552, in that at large void contents (above ~5.5%) the samples typically have one particularly large void (Figure 5-19a), whereas below ~5.5% of the average void content the maximum volume void is only slightly bigger than the subsequent biggest voids (Figure 5-19b).

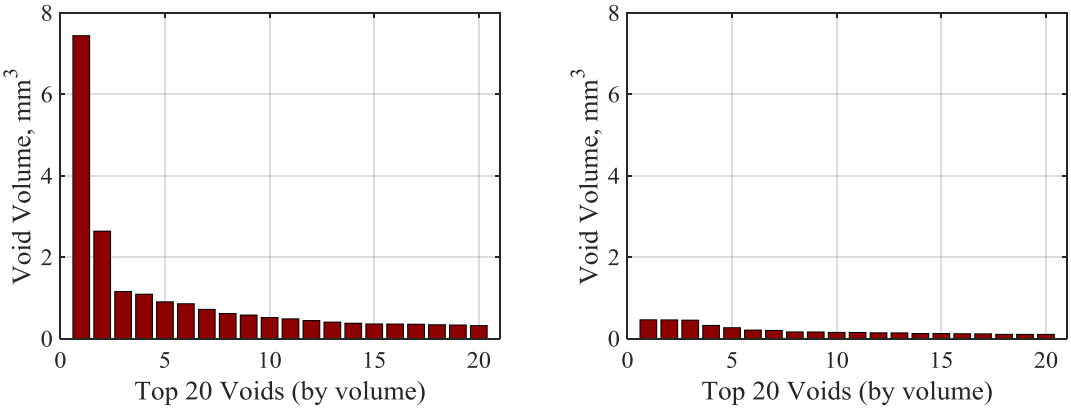

(a) V_v = 11.1% **(b) V_v = 5.3%**

Figure 5-19. Void volume distribution of the 20 largest voids in IMA/M21 samples with different void content.

In addition, the IMA/M21 laminates, in contrast to the IM7/8552 laminates, have a much more gradual decrease in void size. For instance Figure 5-20a shows that for a typical IM7/8552 laminate, the void size of the 150th largest void is 0.015 mm^3, whereas, for a typical IMA/M21 laminate, the void size of the 150th largest void remains above 0.022 mm^3.

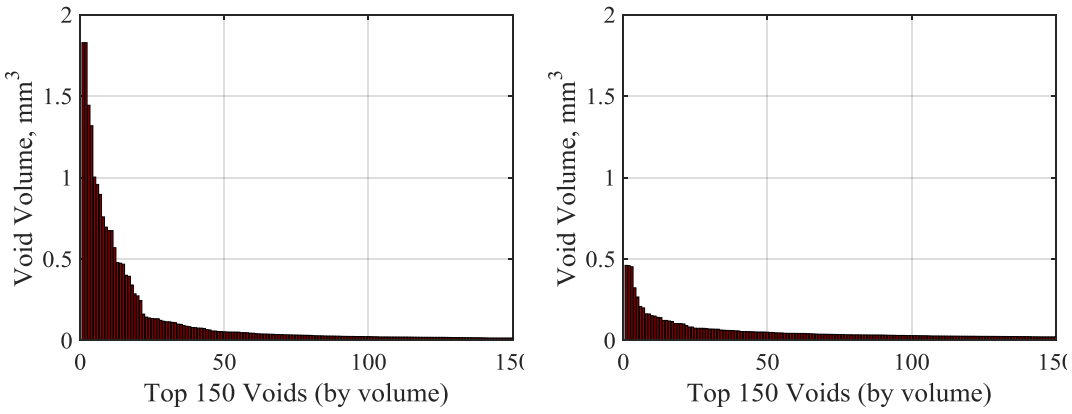

(a) IM7/8552, V_v= 5.38% **(b) IMA/M21 V_v = 5.3%**

Figure 5-20. Comparison of the volume of voids in samples of (a) IM7/8552 and (b) IMA/M21 that have similar overall void content.

5.3.4.1 Void maximum dimension

Whilst the size distribution of voids in a particular sample is likely to have a significant effect upon the failure strength, the complex and subtle differences between the specimens means it is difficult to directly correlate the void distribution to the strength of the specimen. However, it can be surmised that the largest void in a sample would have a dominant effect upon the failure strength, and therefore make it possible to extract this parameter in isolation to predict the SBS strength. The effect of the largest void in a sample can in investigated in a number of ways, for instance by means of the maximum dimension of the void, or the void volume.

Figure 5-21 shows the relationship between maximum void dimension (as calculated by VG Studio Max) and SBSS for both material systems, showing that for IM7/8552 samples (Figure 5-21a) the maximum void dimension is clustered between 20 mm and 22 mm, with very few samples having a smaller maximum dimension. This can be due to the 'network' of long needle-like voids in this material system that create one large void with a 'largest dimension' that isnot strictly representative of the void morphology but is really related to the specimen maximum dimension. As a result, of the consistency in the maximum void dimension for the IM7/8552 samples, the SBS strength shows no dependence on the maximum void dimension.

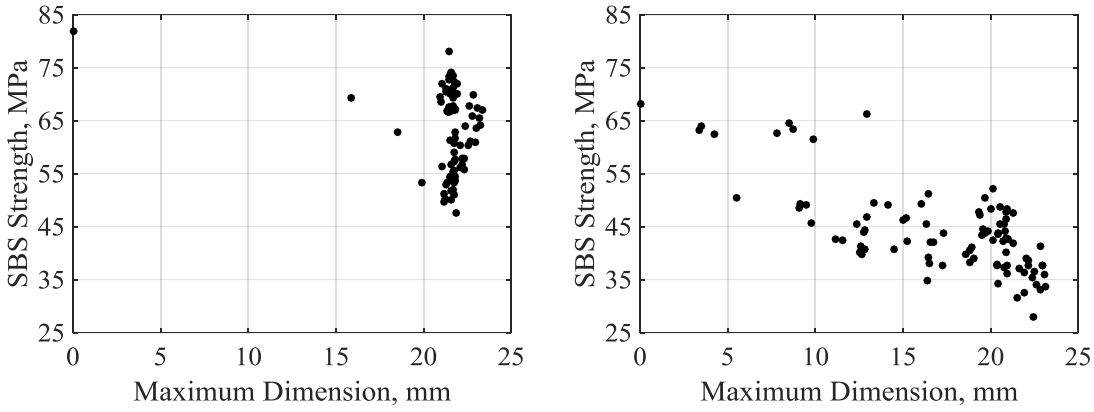

(a) IM7/8552 **(b) IMA/M21**

Figure 5-21. SBS strength plotted against the maximum void dimension for: (a) IM7/8552, (b) IMA/M21.

In contrast, IMA/M21 samples show a variety of maximum void dimensions between 3 mm and 22 mm, which provides a better correlation to the SBS strength. This is due to the voids being of a more planar and circular in shape, presumably due to the presence of toughening particles. However, the correlation is still relatively poor, particularly in comparison of SBS strength with the average void content of the samples (see Figure 5-7 and Figure 5-8).

5.3.4.2 Maximum void volume

The maximum void volume might have a significant effect on the failure properties. Certainly, it can be assumed that larger voids will have a greater effect upon the SBSS. However, as shown in Figure 5-22, the linear correlation between the single largest void in each sample and the SBSS is very poor (R=0.6115 for IM7/8552, and R=0.5943 for IMA/M21). In fact, the relationship shows a cubic relationship.

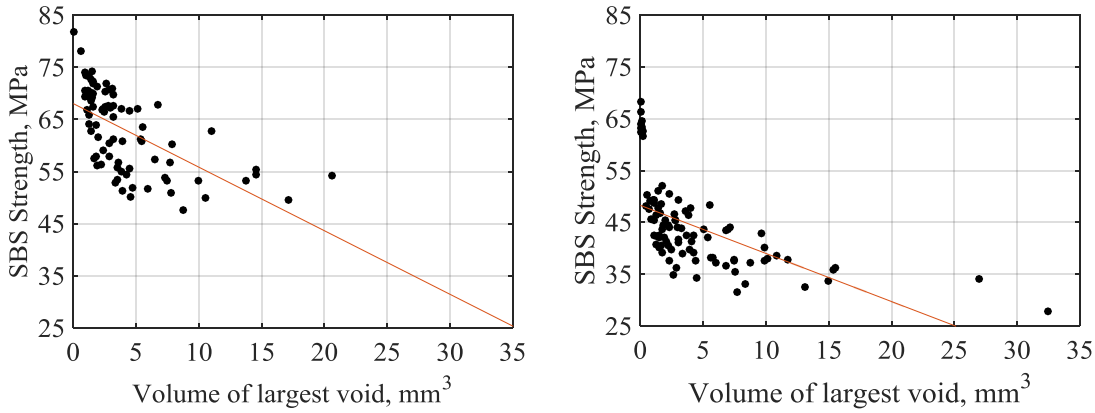

(a) IM7/8552, R = 0.6115 **(b) IMA/M21, R = 0.5943**

Figure 5-22. SBS strength plotted against the void effective radius for: (a) IM7/8552, (b) IMA/M21.

However, a linear measure of the void volume can be obtained by calculating the radius of an equivalent sphere. This is referred to as an 'effective radius', *i.e.* the radius of a sphere with the same volume, and is given by:

$$r_{eff} = \sqrt[3]{3V/4\pi} \tag{5-2}$$

where V is the volume of the void.

Figure 5-23 shows the SBSS plotted against the maximum effective radii found in each specimen.

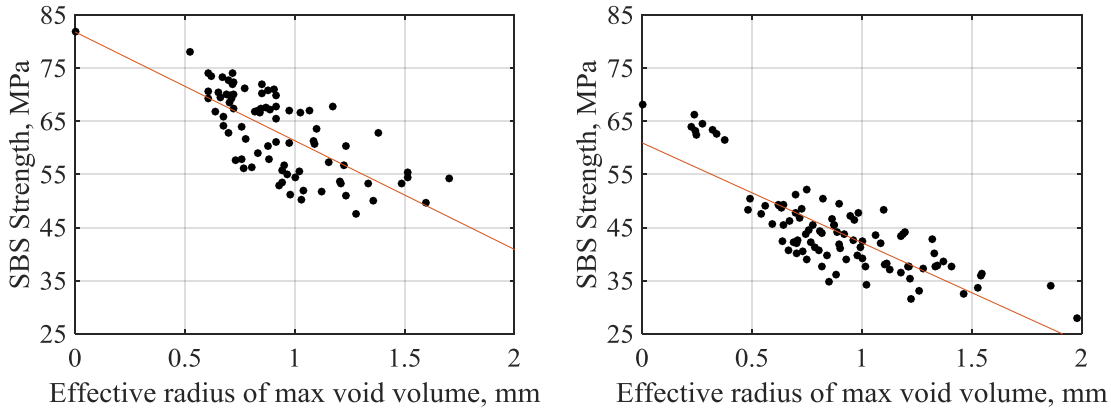

(a) IM7/8552, R = 0.7186 **(b) IMA/M21, R=0.8180**

Figure 5-23. SBS strength plotted against the void effective radius for: (a) IM7/8552, (b) IMA/M21.

For both material systems, the correlation of the SBS strength with the effective radius is better than the correlation with the maximum void dimension or volume of the largest void, however the correlation coefficients for effective radius against SBS strength (R = 0.7186 for IM7/8522 and R = 0.8180 for IMA/M21) are still significantly less than that obtained using the average void content for each sample (R = 0.9384 for IM7/8552 and R = 0.9274 for IMA/M21), as shown previously in Figure 5-7 and Figure 5-8. Although, the correlation coefficient is higher for IMA/M21, potentially due to the reduction in the extent of interconnected void networks than compared to the voids in the IM7/8522 specimens. However, it does not provide an excellent correlation to the strength, indicating the unreliability in using the properties of just one void to determine the mechanical properties of an entire specimen.

5.3.5 Minimum defect size that needs to be taken into analysis

It is shown in Section 5.3.3 that there are a large number of voids within each sample with various void volumes. However, many of these voids are quite small and are unlikely

to greatly affect the failure strength, and in fact it can be surmised that a critical defect size exists below which the void will not 'participate' in the failure of the sample. If such a critical defect size exists, this could potentially be used to limit the number of voids needed to provide an accurate assessment of the SBSS, thereby potentially simplifying numerical modelling of the samples.

To assess the influence of void dimension, the voids (*i.e.* defects) above a given size (in either the length, width or thickness direction) were selected for each sample. The volumes of these voids were then summed to provide 'effective void volume', V_{eff}, that neglected all voids below the assessed defect size L_{thr}, *i.e.:*

$$\boldsymbol{V_{\text{eff}} = \sum V_i\,,\ \text{for all voids } i \text{ where } L_i > L_{\text{thr}}} \qquad \textbf{(5-3)}$$

The 'effective void volume' V_{eff} was then used to calculate a coefficient of correlation in relation to the SBS strength. The results are shown in Figure 5-24, indicating a generally downward trend in the correlation coefficient as the minimum considered defect size is increased, although a plateau exists for both material systems at lower values of the minimum defect size.

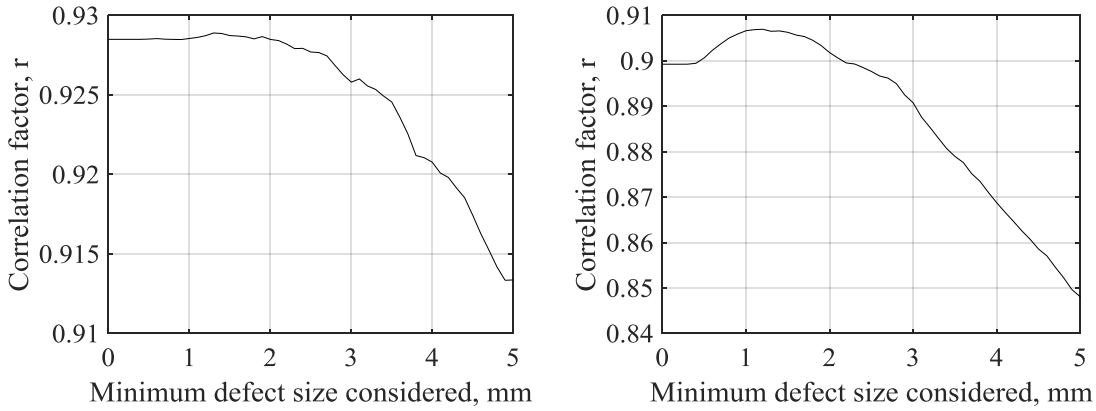

(a) IM7/8552 **(b) IMA/M21**

Figure 5-24. Effect of the minimum dimension of the void considered in analysis on the correlation coefficient.

The plateau shows that voids with a dimension below a certain threshold, approximately 2 mm for IM7/8552 and 1.5 mm for IMA/M21, provide a negligible change in the correlation coefficient. This would seem to be defining a critical defect size, below which the voids are not able to initiate a crack.

Failure mechanics provides a simplified analysis of this phenomenon that can be used to indicate a minimum dimension of the voids. Critical defect size can be estimated using Griffith equation, by assuming the defect is a 2D crack in an infinite plane:

$$G = \frac{\sigma^2 \pi a}{E} \quad \textbf{(5-4)}$$

where G is fracture toughness of the material; σ is failure stress; E is Young's modulus; a is the radius along the crack.

For the SBS test, where shear stresses are propagating cracks in mode II, the crack length is given by:

$$a = \frac{G_{IIC} E_2}{\tau^2 \pi} \quad \textbf{(5-5)}$$

where G_{IIC} is the mode II critical fracture toughness (0.8 N/mm for IM7/8552 [133] and 0.950 N/mm for IMA/M21 [134]), τ is the SBSS for the reference samples (81.8 MPa for IM7/8552 and 68.21 MPa for IMA/M21), and E_2 is the transverse Young's modulus (11.38 GPa for IM7/8552 and 8.62 GPa for IMA/M21).

The calculated critical crack length obtained for IM7/8552 is 0.87 mm, and 1.1 mm for IMA/M21.

The predicted crack length values from the fracture mechanics show a good indication of the size at which voids become important to the SBSS, although the fact that these equations (equations 5-4 and 5-5) are formulated for an isotropic homogeneous material that fails in pure mode II shear (whereas we have observed 90° plies failing in tension) means that the exact value provided by this theory should not be relied upon.

5.3.6 Correlation of the voids in the critical position to SBSS

It has been shown in the previous sections that individual void features (such as maximum void size and dimension) are not able to improve the linear correlation that between the average void content and SBSS (see Figure 5-7 and Figure 5-8). However, it may be possible to isolate critical regions in which it is known that high stresses exist. In fact, it is known that the shear stress distribution is approximately parabolic through the thickness, such that the maximum stress occurs near the mid-plane.

To investigate the effect of this 'critical area' on the correlation to SBSS, the total void volume of all voids in the middle one fifth of the volume through the thickness of the laminates is plotted against SBSS for both material systems (see Figure 5-25). It can be observed that there is a poor correlation for IM7/8552 – with a correlation coefficient

R = 0.5603, whilst for IMA/M21 the correlation is slightly improved (R = 0.7879), yet not satisfactory.

However, when correlating the total void content in the middle three sections out of five through the thickness, there is a significant improvement in the correlation for both IM7/8552 and IMA/M21 (as shown in Figure 5-26). Increasing of the critical area can be justified due to the highly non-linear shear stress/strain response, which gives a much flatter distribution of the shear stresses through the thickness of the laminate than the normally assumed parabolic distribution [135], *i.e.* the mid-three sections of the laminate are subjected to approximately the same shear stress. This however still does not give as good a correlation as the average void content that is shown in Figure 5-7 and Figure 5-8.

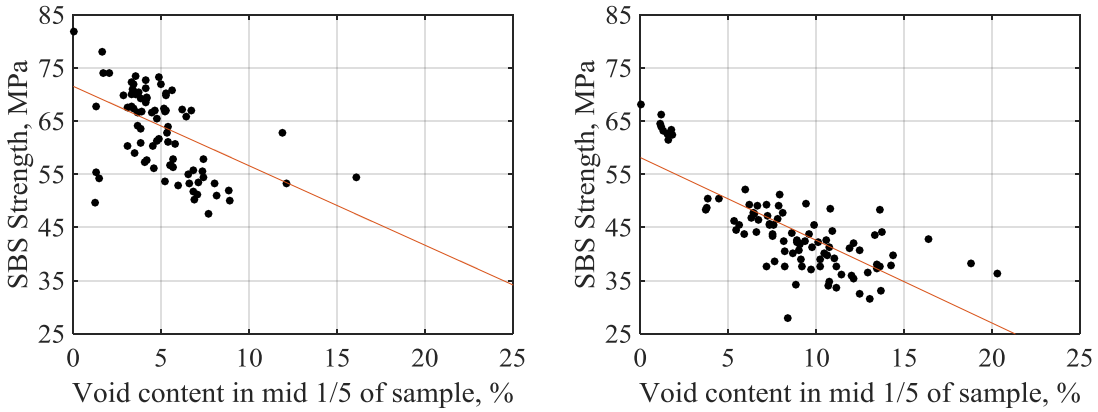

(a) IM7/8552, R = 0.5366 **(b) IMA/M21, R = 0.7682**

Figure 5-25. Correlation of the total void volume in the middle section through the thickness of the sample to SBSS.

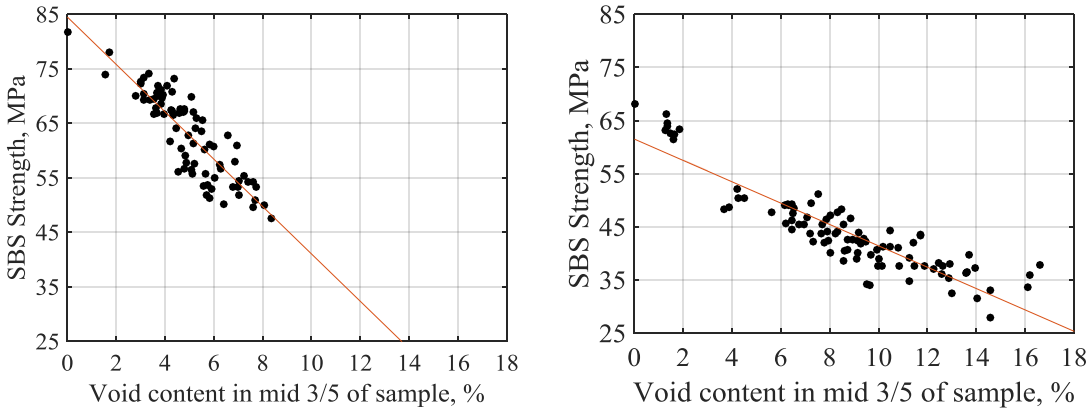

(a) IM7/8552, R = 0.8717 **(b) IMA/M21, R = 0.9004**

Figure 5-26. Correlation of the total void volume in the three middle sections through the thickness of the samples to SBSS.

As shown in Figure 5-27 and Figure 5-28, this correlation is largely unaffected by taking into account the effective void volume in these mid-regions (*i.e.* when neglecting voids below the critical length).

This shows that whilst the critical crack length is a good parameter to reduce the number of voids that are considered in an analysis (and potentially in a computational model), neglecting smaller voids appears to provide little advantage in terms of estimating the SBSS from the available void information.

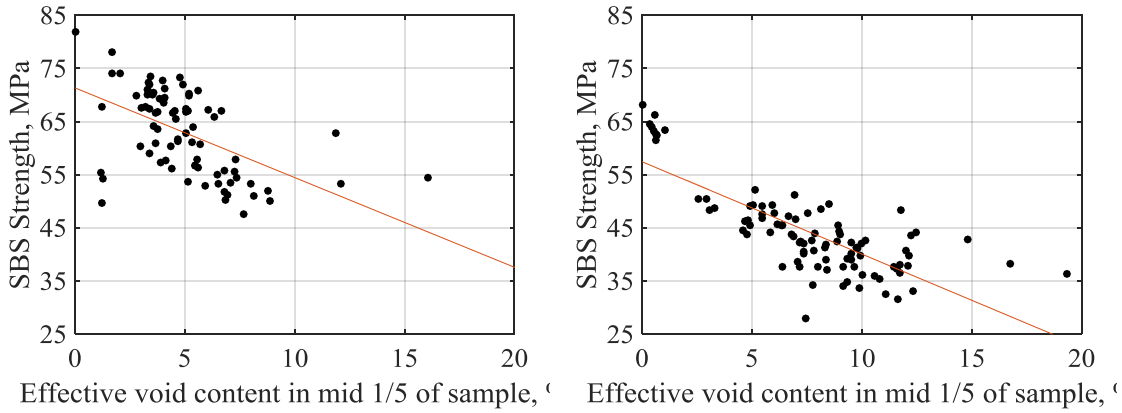

(a) IM7/8552, *R* = 0.5339 **(b) IMA/M21, *R* = 0.77742**

Figure 5-27. Correlation of the effective void volume in the middle section through the thickness of the sample to SBSS.

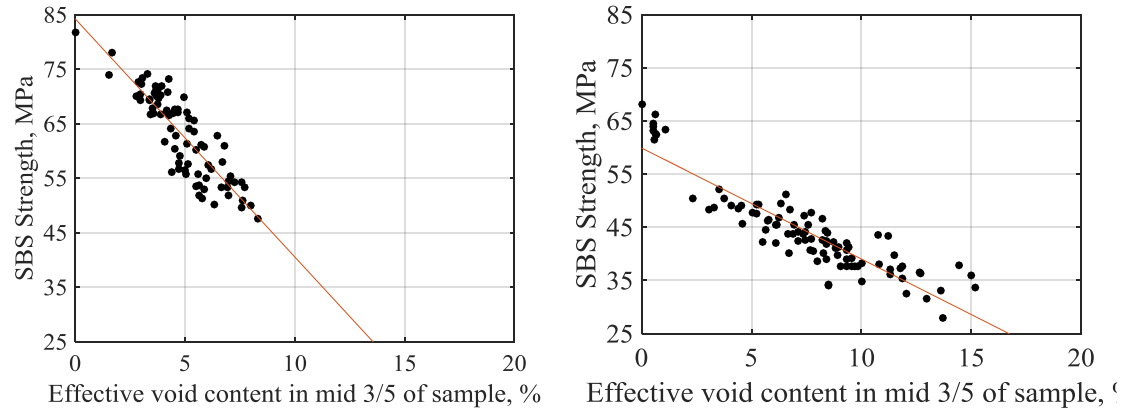

(a) IM7/8552, *R* = 0.8731 **(b) IMA/M21, *R* = 0.9015**

Figure 5-28. Correlation of the effective void volume in the three middle sections through the thickness of the samples to SBSS.

5.3.7 Individual ply analysis

After analysing CT-images of the samples, it was observed that each sample has a specific ply through the thickness of the laminate where the majority of the voids (by volume) are located. This ply will be referred to herein as the ‘critical ply’. As the voids through the laminate can be considered as stress concentrators, it is reasonable to assume

that this 'critical ply' will have a dominant effect on the specimen strength, and thereby the void content of the 'critical ply' will correlate to the failure strength.

Figure 5-29 shows the correlation of the 'critical ply' void volume against SBS strength for IM7/8552 and IMA/M21 samples, showing that the relationship between these parameters is non-linear. Furthermore, there is a specific void content for both material systems where the dependence breaks down and a significant increase in the scatter of results is observed (*i.e.* ~4-5 mm^3 for IM7/8552 and ~5.5 mm^3 for IMA/M21). This is likely due to the significant increase in the through-thickness dimension of the voids observed above these void levels, *i.e.* ~4% for IM7/8552 and ~5% for IMA/M21, as shown in Figure 5-30. In fact, many of these larger voids span a significant number of plies (in some cases more than half).

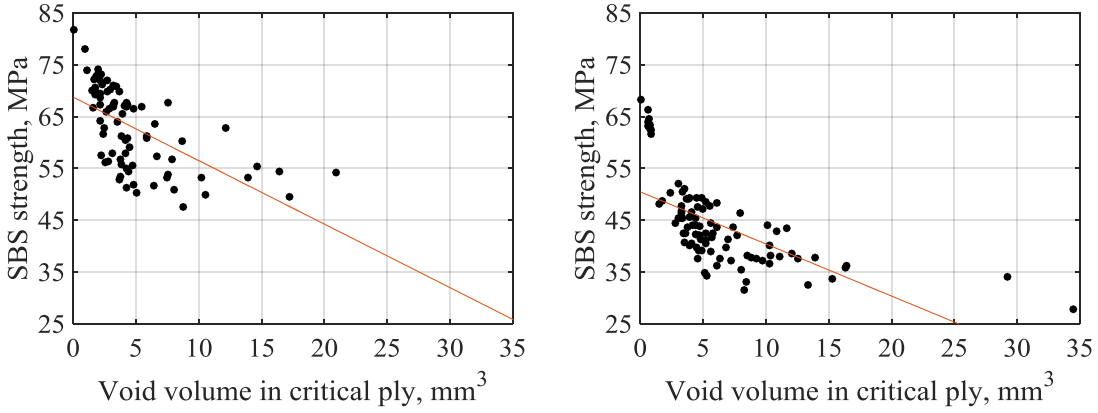

(a) IM7/8552, *R* = 0.6052 **(b) IMA/M21, *R* = 0.6426**

Figure 5-29. Correlation of the maximum void volume in a ply and SBS strength for (a) IM7/8552 and (b) IMA/M21.

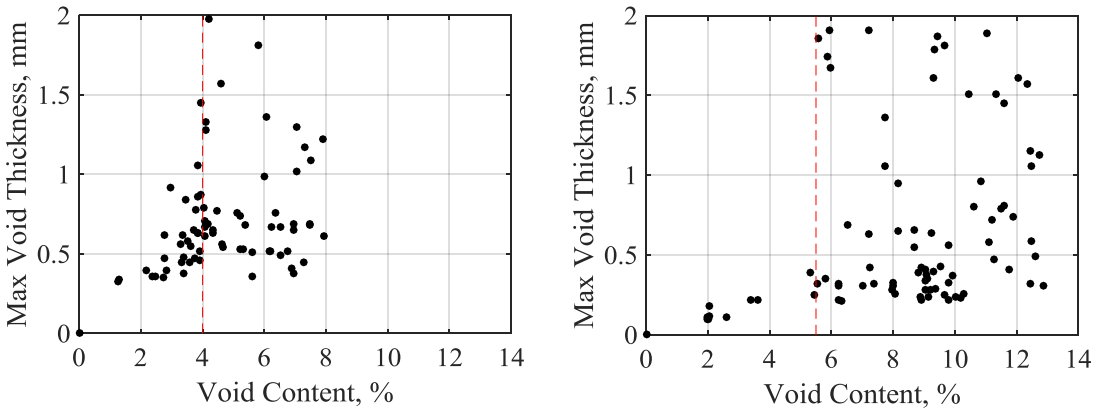

(a) IM7/8552 **(b) IMA/M21**

Figure 5-30. Changing of the thickness of maximum void with increase of average void content.

5.3.8 Void feature analysis based on pairs of samples

For both material systems, it is observed from Figure 5-7 and Figure 5-8 that there are pairs of samples that have a similar void content but fail at different SBS strengths. As a result, multiple pairs of samples with this type of behaviour have been analysed to investigate the features of their voids. The samples for analysis were chosen by finding pairs of samples with closely matching total void content (*i.e.* within ±0.08%) and a discrepancy in failure strength (SBS strength) of at least 5MPa. For IM7/8552 23 pairs were identified, whilst IMA/M21 had 11 such pairs.

5.3.8.1 Results of analysis for IM7/8552

To investigate the causes of the difference in SBS strength between the samples of each pair, the 'effective void volume' was calculated (*i.e.* the summation of all voids in a sample above the critical defect size – determined as 2 mm for IM7/8552 from Figure 5-24). Figure 5-31 shows the comparison of the 'effective void volume' for the chosen pairs of IM7/8552, indicating that most of the samples that failed at the lower SBS strength in a pair with similar total void content have a larger 'effective void volume' than the samples with higher SBS strength. This provides further evidence that the size of the voids is a critical feature when assessing the effect of a void on the SBS strength, showing that voids smaller than a critical dimension can be neglected.

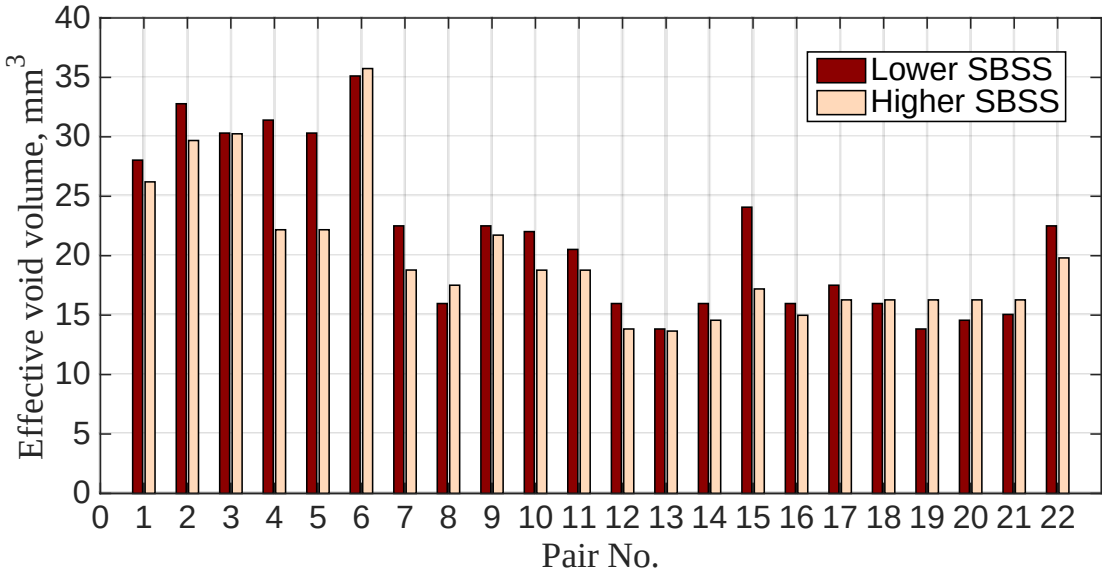

Figure 5-31. Comparison of the 'effective void volume' V_{eff} , (*i.e.* the total void volume of all voids larger than the critical dimension) for IM7/8552 sample pairs having the same void content but different SBS strength.

However, there are several pairs of samples that do not show this behaviour – *i.e.* samples with higher SBSS have the larger 'effective void volume' (See pair numbers 3, 6, 8, 13 and 19-21), indicating that there are other void features that must be taken into account, for instance the position of the voids, due to the through-thickness shear stress distribution.

To investigate the effect of void position in these samples, the thickness of the samples was divided into five equal sections. The shear stress distribution through the thickness of the specimens is nominally assumed to be parabolic, although in practice the shear stress/ strain response of the material is highly non-linear and has a much flatter shear stress distribution near the midplane [135], such that at least the middle fifth of the specimen (in the through-thickness direction) has approximately the same shear stress. It is therefore reasonable to assume that voids in this middle section will have a greater effect on the SBSS than voids further from the mid-plane.

In fact, it has been observed that in 4 of the 7 pairs (pairs 3, 13, and 20-21) the largest void (by volume) is located in the mid-section of these five sections – *i.e.* the section across the midplane - as shown in Figure 5-32a and Figure 5-33a for pair numbers 3 and 21, respectively. In each of these cases the largest void of the lower SBSS specimen in the mid-section is at least 210% larger than the largest void of the higher SBSS specimen located in the mid-section. It therefore appears clear that the position of the largest voids in a sample is a critical void feature.

It is notable that the effective void volume in each of the five sections (*i.e.* the void volume discounting voids smaller than the critical length) is not as clear, as shown in Figure 5-32b and Figure 5-33b for pair numbers 3 and 21, respectively.

This provides evidence that, when the largest total effective void volume of a pair of samples does not indicate the sample with the lower SBSS (as is the case for pairs 3, 13 and 20-21), the size of the maximum void in the specimen may be able to provide a clearer indication (see Figure 5-32a and Figure 5-33a) than looking at the effective void volume distribution through the thickness (See Figure 5-32b and Figure 5-33b).

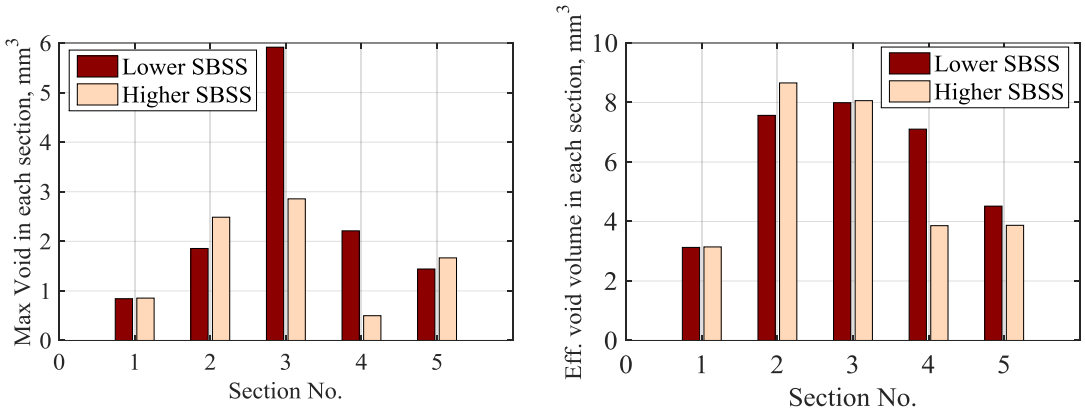

(a) **(b)**

Figure 5-32. Pair analysis for IM7/8552 Pair No.3: (a) maximum void (by volume) in each of five equal sections through the thickness; (b) effective void volume in five equal sections through the thickness of the samples.

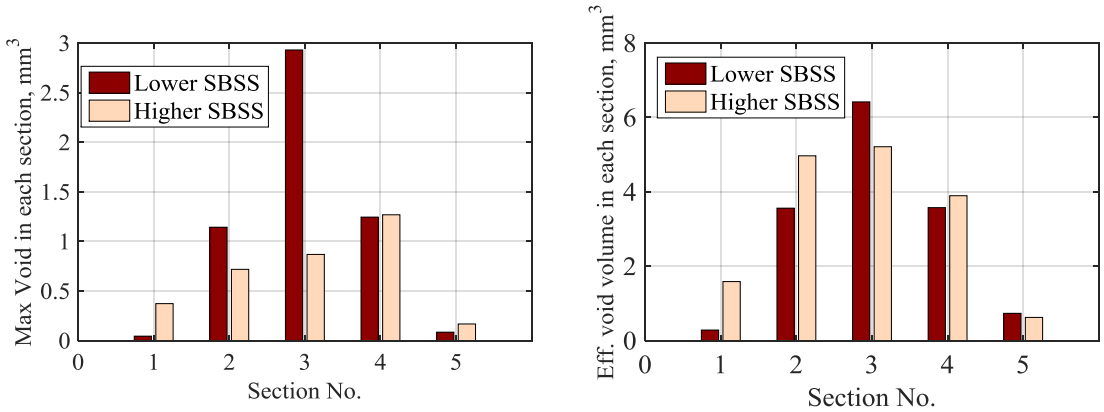

(a) **(b)**

Figure 5-33. Pair analysis for IM7/8552 Pair No.21: (a) maximum void (by volume) in each of five equal sections through the thickness; (b) Effective void volume in five equal sections through the thickness of the samples.

However, there are still pairs of samples that have discrepancies in their SBSS that is not explained when taking into account the critical defect size or the position of the largest void (*i.e.* pairs 6, 8 and 19).

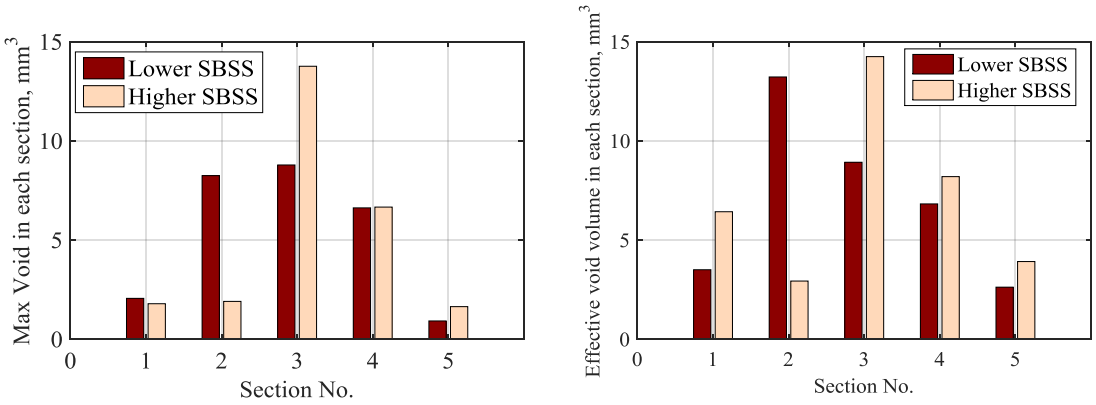

(a) **(b)**

Figure 5-34. Pair analysis for IM7/8552 Pair No.6: (a) maximum void (by volume) in each of five equal sections through the thickness; (b) effective void volume in five equal sections through the thickness of the samples.

One of these pairs (pair no. 6) is shown in Figure 5-34, showing that the sample with higher SBSS has the largest void at its mid-section. However, it is notable that the sample with the lower SBSS has multiple large voids in and around the midplane (in sections 2, 3, 4) which have a combined void content greater than the two large voids shown for the sample with higher SBSS in this region.

In fact, CT-analysis of these samples shows that the two largest voids of the sample with lower strength, positioned in sections 2 and 3 (8.79 mm^3 - red colour and 8.25 mm^3 - orange colour in Figure 5-35a, respectively), are located close to each other. Whereas, the largest voids of the samples that failed at higher strength – 13.77 mm^3 (red colour) and 6.67 mm^3 (green colour) (Figure 5-35b) – are positioned with a small distance between them. Therefore, whilst the sample with the largest void at the mid-section has the higher SBSS, the two largest voids of the lower SBSS sample may effectively behave as one void due to their closer proximity, thereby suggesting that not only is it important to consider the individual void features, but also to consider the interactions between the voids in a sample.

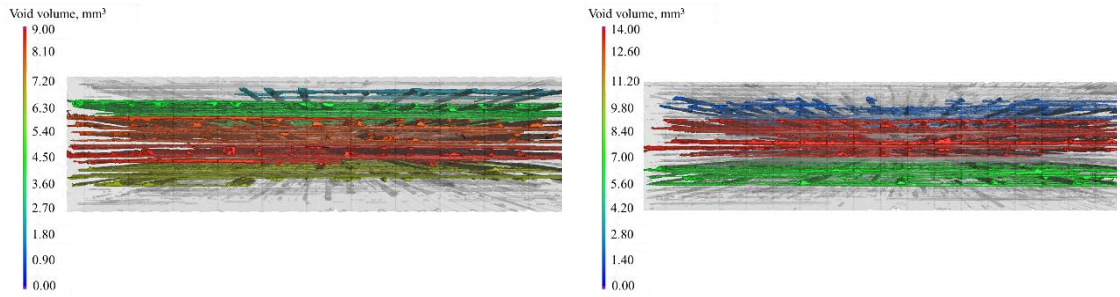

Sample with lower SBS strength **Sample with higher SBS strength**

Figure 5-35. CT-images showing the position of the largest voids for the samples of pair No. 6 (IM7/8552).

5.3.8.2 Results of analysis for IMA/M21

As done for IM7/8552, the differences in SBS strength between the samples of pairs with similar total void volume fraction were investigated, and the 'effective void volume' V_{eff} was calculated (*i.e.* the summation of all voids in a sample above the critical defect size – 1.5 mm for IMA/M21 from Figure 5-24). The results are provided in Figure 5-36, showing that all but one of the pairs of IMA/M21 that failed at lower SBSS have a larger 'effective void volume' than the equivalent samples that have higher SBS strength.

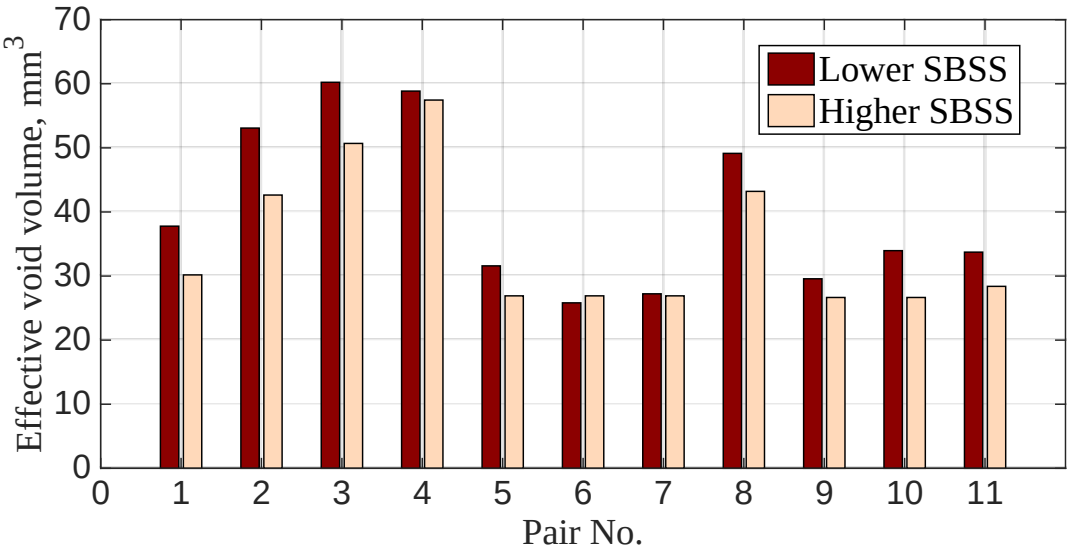

Figure 5-36. Comparison of the 'effective void volume' (*i.e.* the total void volume of all voids larger than the critical dimension), V_{eff}, for IMA/M21 sample pairs having the same void content but different SBS strength.

The fact that only one out of 11 pairs of IMA/M21 showed results contrary to that expected when considering the critical defect size, in contrast to the seven out of 22 pairs for IM7/8552, is likely due to the more consistently sized void volumes in IMA/M21, meaning that there were very few samples having 'one' particularly large void in

comparison to the others, and instead the specimens tend to have many 'medium' sized voids. As a result, it would be unhelpful to try and correlate the largest void in the mid-section to the sample with the lower SBSS (as described in Section 3.4.6.1), particularly in view of the importance of proximity shown previously.

Therefore, for this material system the total of the 10 largest voids is compared in each of the 5 sections of the laminate, as shown in Figure 5-37a, as well as the effective void volume in each of the five sections, as shown in Figure 5-37b.

Both of these figures (*i.e.* Figure 5-37a and Figure 5-37b) indicate that the larger voids are located in the mid-section close to the midplane for the lower SBSS sample, thereby causing the reduction of the SBSS in comparison to the higher SBSS sample. It should be noted that a similar result is found when comparing a lower number of largest voids in each sample, although the results are most pronounced for 10 voids (as evidenced by the lower void content in section No.3 in Figure 5-37b when including all voids above the critical crack length – 77 voids for the lower SBS sample and 88 voids for the high SBSS sample).

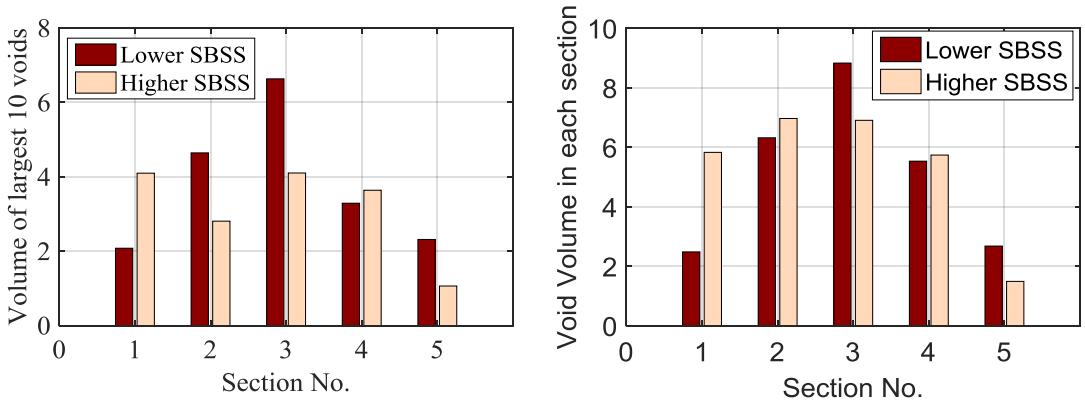

(a) **(b)**

Figure 5-37. Pair analysis for IMA/M21 Pair No.6: (a) total volume of the 10 largest voids in five equal sections through the thickness of the samples; (b) effective void volume in five equal sections through the thickness of the samples.

5.4 Conclusions

As expected, there is a linear dependence between average void volume fraction and SBS strength, although some scatter can be observed due to the varying size, shape, and location of the voids. To investigate the effects of these void features, several parameters were analysed to find the critical void features that affect the failure strength.

It is shown that the number of voids is not a good parameter for void analysis due to the different sizes of voids in each sample, whilst it is equally difficult to predict the SBS strength when considering the single largest void (in dimension or volume), or the 'critical ply' where most of the voids in a sample are located. This is particularly the case when the voids are not confined to a single ply and instead bridge between the plies, as is the case for samples having high void content and particularly for IM7/8552 samples having high void content.

Despite this, it has been shown that by analysing a few of the largest voids in a sample it is possible to explain discrepancies between pairs of samples with equivalent void contents but different SBS strengths. In the IM7/8552 samples, which have one very large void, it is possible to explain the discrepancies by comparing each materials single largest void or the proximity of a few of the largest voids. For the IMA/M21 samples, which have many large voids of similar size, it is necessary to consider the cumulative effect of more voids, *e.g.* the 10 largest voids.

In addition, it has been shown that many of the smallest voids can be neglected. This has been shown by the limited effect of neglecting the smallest voids on the correlation coefficient between SBSS and 'effective void volume' (*i.e.* the void content when neglecting voids below a certain size), and when directly comparing pairs of samples. It is suggested that this is due to a critical defect size (*i.e.* void dimension), as predicted by fracture mechanics, below which the voids do not contribute to failure. As a result, a significant number of the smaller voids can be neglected from the analysis.

Overall, no parameter has been identified that correlates to the SBSS better than the average void content of the samples. However, it is worth noting that the void distribution in the length-width plane for these samples is generally uniform (although there are inevitably variations in the void distribution at smaller scales – See Figure 5-13). This would most likely not be the case for more complex geometries (*e.g.* corners and ply-drops), and therefore the average void content may not be a good measure of the ILSS.

6 PREDICTION OF SBS STRENGTH OF CARBON/EPOXY COMPOSITES

The presence of voids in composite materials has the effect of reducing the materials strength, particularly matrix-dominated properties such as short beam shear (SBS) strength. Up until now there has been no satisfactory way to reliably predict the effect of voids on the SBS strength, and instead there has been a reliance on using the average void content to assess the linear reduction of strength with increasing void content. However, in order to develop a ‘knock-down’ factor using the linear relationship, an extensive testing program is required for each material system in order to reliably determine the linear dependence.

It would be beneficial to provide a scheme that predicts the strength of materials, using only knowledge of the voids in a sample, and without resorting to complicated FE modelling.

There are a lot of factors that could affect the overall reduction in strength of a composite material, such as: void size, void shape, void location, and the proximity between voids. It has been shown in Chapter 5 that none of these individual void characteristics can be used in isolation to predict the strength reduction, however it is expected that their combined effect upon the cross-sectional area (across the length-width plane) through the thickness will provide useful information for predicting the SBSS (short beam shear strength). This is due to the shear stresses in the length-width plane, and the assumption that there will be a 'critical plane' across which the stress will be largest and provide the best correlation to the material’s strength. The location of this plane will depend on the void size, void shape, and void location in relation to the through-thickness stress distribution.

6.1 Theory Background

The estimation of the strength of composites using a reduced cross-sectional area was investigated in the early 1990's by Gurdal *et al.* [61] and Wisnom *et al.* [24].

Gurdal *et al.* investigated the out-of-plane tensile strength of two laminates with different stacking sequences: $(\pm 45/0_2/\mp 45/90_2)_S$ and $(\pm 45/90_2/\mp 45/0_2)_S$. The reduction of cross-sectional area was calculated as a function of void length, void volume, void projected surface, and overall porosity, by extrapolating estimates of these values taken from microscopy images. For the first stacking sequence, the predicted strength matches the experimental data very well. However, for the second lay-up the strength was over-estimated, particularly at higher levels of porosity. This was taken to be due to the non-uniformity of void distribution at higher levels of porosity, particularly as it was noted that there was a higher concentration of voids in the central 0° plies, whereas the theoretical model assumes a uniform void distribution.

Wisnom *et al.* similarly postulated the importance of a reduced cross-sectional area, along with the importance of larger voids that were likely to initiate failure. A very good prediction was found to determine the interlaminar shear strength (ILSS) when using the reduced cross-sectional area as a knock-down factor (with respect to the ILSS of a reference sample). The uniform distribution of the voids and the limited scope of their experimental program limited confidence in the applicability of this approach. Furthermore, the prediction was only compared to voids introduced into a unidirectional laminate.

In this work, a similar approach will be adopted to predict the SBS strength of the laminates, *i.e.* using the reduced cross-sectional area, $A_{reduced}$:

$$\boldsymbol{\tau_{predicted} = \tau_{pristine} \frac{A_{reduced}}{A_{total}} = \tau_{pristine} \frac{A_{total} - A_{porosity}}{A_{total}}} \quad \textbf{(6-1)}$$

where $A_{porosity}$ – is the cross-sectional area of the voids in a particular plane of a sample and A_{total} – is the cross-sectional area of the sample

Unlike with earlier work, a detailed characterisation of the internal void location and morphology can now be obtained through X-ray CT scanning of each sample, prior testing. This CT-dataset can then be used to find the 'critical plane' in each sample, *i.e.* the length-width plane with the maximum cross-sectional area of voids, $A_{porosity}$.

This ‘critical plane’ could be positioned at any through-thickness location, however it is well known that the shear stress distribution is not uniform through the thickness (see *e.g.* [24], [135]). As a result, the ‘critical plane’ calculated by equation (6.1) is merely the plane with the greatest proportion of voids, irrespective of the stress level.

To additionally account for this non-uniformity in the shear stress distribution, a stress concentration factor (SCF) is introduced to the equation:

$$\boldsymbol{\tau_{predicted} = \tau_{pristine} \frac{(A_{total} - A_{porosity} * SCF)}{A_{total}}} \quad \textbf{(6-2)}$$

According to ASTM D2344 [136], the SBS strength in the experimental tests is calculated based on the maximum shear stress at the mid-plane taken from a parabolic shear stress distribution given by linear elasticity. However, this assumption is not strictly true as the shear stress distribution actually has a more uniform stress near the mid-plane, akin to a flattened parabolic distribution, as shown in Figure 6-1. This is due to the shear strength being a matrix dominated property, and the fact that polymer resins are highly non-linear materials in comparison to composite fibres. The actual response has been investigated by He and Makeev [135], who showed that the shear stress distribution is closer to a ‘flattened parabolic’.

As a result, the SCF is similarly taken to be a ‘flattened parabolic’ distribution, with the value of the stress concentration factor, SCF, extracted from [135], shown on Figure 6-1 and given by:

$$\boldsymbol{SCF = -18.85y^4 + 0.74y^2 + 1} \quad \textbf{(6-3)}$$

where y ranges between -0.5 and 0.5.

In this case, the maximum shear stress occurs in and around the mid-plane of the laminate to provide a SCF equal to 1. Moving the selected plane away from this region reduces the SCF, which tends towards zero at the top and bottom of the specimen.

Note that the study conducted by He and Makeev [135] is based on unidirectional laminates, however this is assumed to be adequate for comparative purposes since through-thickness shear is matrix dominated for all layups.

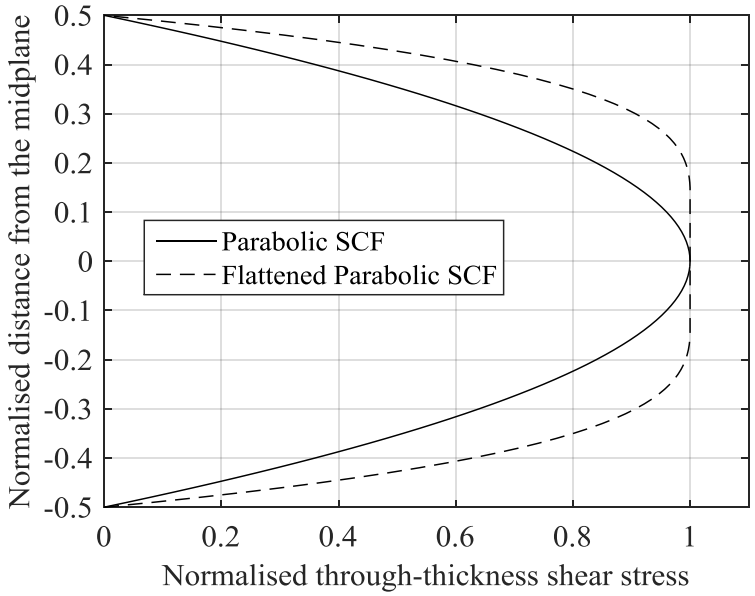

Figure 6-1. Through-thickness shear distribution, showing the parabolic shear stress distribution assumed by the ASTM standard (ASTM D2344) and the flattened parabolic distribution from [135].

The predictions using equation 6-2 will be compared to the experimental results presented in Chapter 5 for SBS strength. See, for instance, Figure 5-6 (for IM7/8552) and Figure 5-7 (for IMA/M21), which show the average void content *vs*. SBS strength of the samples.

6.2 Prediction of the short beam shear (SBS) strength

Accurately determining the cross-sectional area of the voids through the thickness of each sample provides many challenges. Whilst the Defect Detection VG-Studio plug-in automatically provides information regarding many of the characteristics of each void (*e.g.* void volume, surface area, position, projected area, and length), it doesnot automatically provide the planar void content through the thickness of the samples (*i.e.* A_{porosity}), and so alternative schemes are presented for estimating the cross-sectional void content.

6.2.1 Prediction using the actual cross-sectional area from the CT-image

Calculation of the actual cross-sectional area of the voids across any given plane of a sample is possible directly by using the CT-images. To achieve this, every slice through the thickness of the laminate needs to be analysed to find the slices (in the length-width plane) with the maximum cross-sectional area of voids (see the example in Figure 6-2), although the position of this cross-section must also be taken into account by the means

of the SCF, such that the 'critical plane' is identified which has the maximum combined effect upon the SBS strength (see Equation 6.2). This process is very time-consuming, especially when analysing large numbers of samples (as is the case here).

As a trial of the method, several samples with different void contents from both material systems have been selected in order to review their usefulness in predicting the SBS strength.

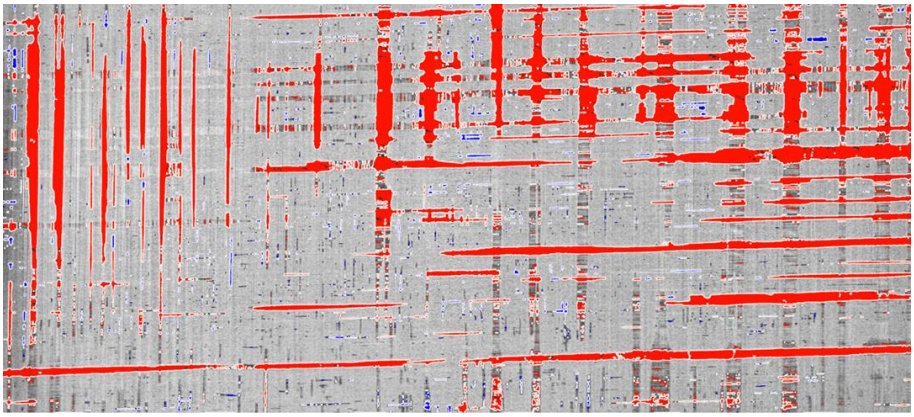

(a) IM7/8552, V_v = 7.26%

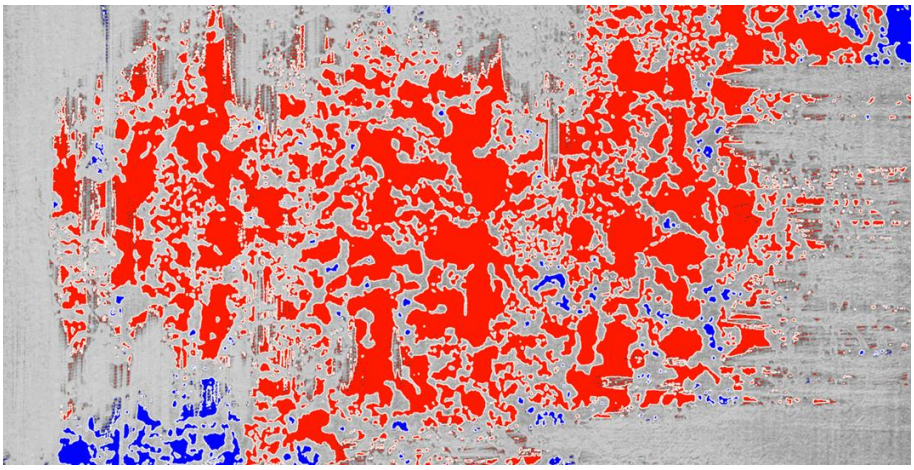

(b) IMA/M21, V_v = 12.88%

Figure 6-2. Example of the voids on the 'critical plane' in samples of: (a) IM7/8552; (b) IMA/M21. The maximum void in each sample is highlighted in red, and smaller voids are highlighted in blue.

Figure 6-3 shows the comparison of the actual SBS strength and the SBS strength predicted using the SCF and the cross-sectional area of the voids on a critical plane measured directly from the CT-images, A_{porosity}, plotted against the specimens' average void content.

For IM7/8552, the prediction overestimates the experimentally determined SBS strength, and this overestimation increases (*i.e.* the error between the predicted and actual SBS strength increases) as the void content of the samples increases. This is likely due to the

void shape, which is actually more of a network of interconnected voids (see *e.g.* Section 5.3.2) that extend across multiple plies through the thickness. The through-thickness extent of these void-networks isnot taken into account in this analysis, and that is thought to be a key factor in the observed error in the predictions.

For IMA/M21 the prediction is typically better than for IM7/8552, however the error is still significant and generally increases with increasing void content. The improved prediction, particularly at low void content (<6% void content), is likely due to the fact the voids in IMA/M21 are mostly positioned in the resin layer region between the plies (see *e.g.* Section 5.3.2) and do not show such extensive void-networks bridging between the plies as seen in IM7/8552.

Given that this technique is very time-consuming and does not provide particularly accurate results, there is clearly a need for an alternative and more efficient method to evaluate the cross-sectional area of the voids in any given plane, *i.e.* A_{porosity}, that provides an equivalent or superior prediction of the SBS strength. In the following sections, suggestions are put forward for improving this evaluation and thereby improving the predictions.

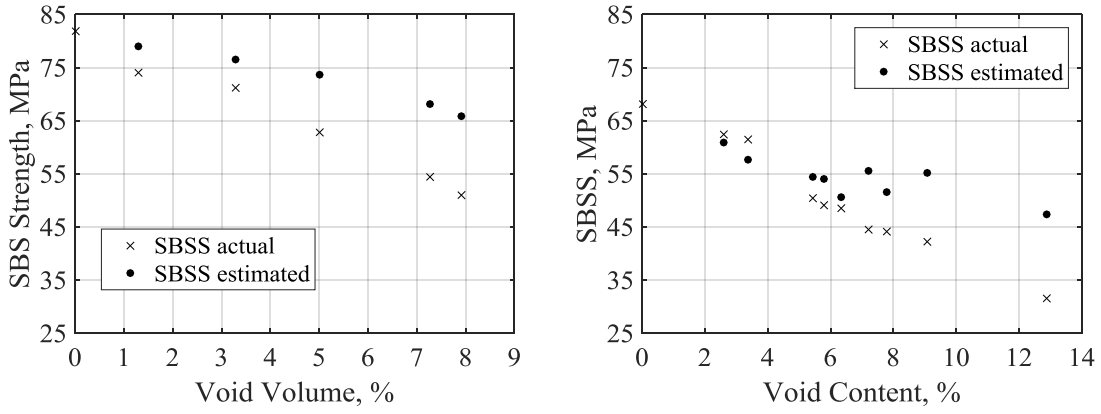

(a) IM7/8552 **(b) IMA/M21**

Figure 6-3. Prediction of the short beam shear (SBS) strength from the reduced cross-sectional area, calculated using the SCF and the actual cross-sectional area determined from CT-slices in the length-width plane.

6.2.2 Prediction assuming a constant cross-sectional area of the voids

In order to calculate the total cross-sectional area of all the voids in a particular plane for each sample in a less time-consuming manner, the cross-sectional area of each void is calculated using the following equation:

$$A_{\mathbf{void}} = \frac{V_{\mathbf{void}}}{t_{\mathbf{void}}} \quad \textbf{(6-4)}$$

where V_{void} is the void volume and t_{void} is the maximum void thickness

Note that V_{void} and t_{void} are parameters automatically supplied by the Defect Defection plug-in of VG Studio, and so the cross-sectional area of each void, A_{void}, is easy to obtain. This equation makes the assumption that each void has a constant cross-section in the thickness direction. The total cross-sectional area, A_{porosity}, in each plane is then calculated by adding together the cross-sectional area, A_{void}, of each void that extends through the particular plane in question.

The comparison between the predicted and actual SBS strength for both material systems is shown in Figure 6-4.

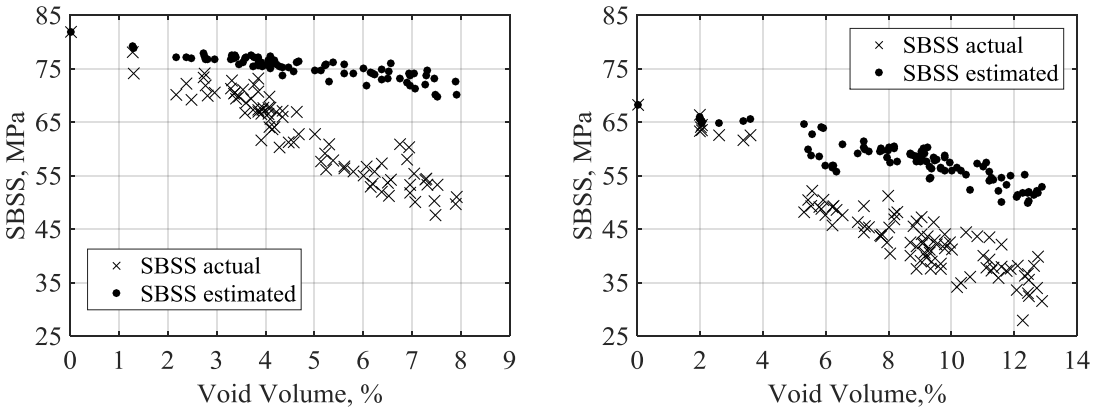

(a) IM7/8552 **(b) IMA/M21**

Figure 6-4. Prediction of the short beam shear strength from the reduced cross-sectional area, calculated assuming a constant cross-sectional area of the voids in the thickness direction.

It can be observed from Figure 6-4 that for both material systems the prediction overestimates the SBS strength, although better results are obtained for samples with smaller average void content (<4% void content). Even so, the overall behaviour of the estimated curve is unsatisfactory with a large error in comparison to the experimentally determined SBS strength, and a greater error than that observed when calculating the actual reduced cross-sectional area from CT-slices.

This is likely in part due to the error associated with assuming a constant cross-sectional area of the voids, whereas the voids actually have a complex shape which form a void-network of interconnected voids. As a result, the voids extend between multiple plies and

therefore the stress is not constrained to a single plane (as discussed in Chapter 5, Section 5.3.2).

This is particularly seen for IM7/8552 at the higher average void contents (above approximately 4% void content), where samples include large void-networks extending through the thickness of the laminates. For IMA/M21, the prediction is slightly better due to the more constant shape of the voids and the reduced penetration of the voids between plies.

6.2.3 Prediction using the projected area of the single largest void-network

To try and take into account that the voids extend in the through-thickness direction, the projected area of the voids (when viewed in the length-width plane) has been used to calculate the reduced cross-sectional area. Each length-width plane of each sample is analysed to find any voids whose centre lies on the plane in question. As the centre of two voids is unlikely to exactly match, it therefore means that the calculation effectively calculates the projected area of the single largest void-network.

The projected area is the (two-dimensional) measurement of the projected shape of the (three-dimensional) void onto an arbitrary plane (see Figure 6-5). The ‘critical plane’ is then found by also taking into account the stress concentration factor (SCF).

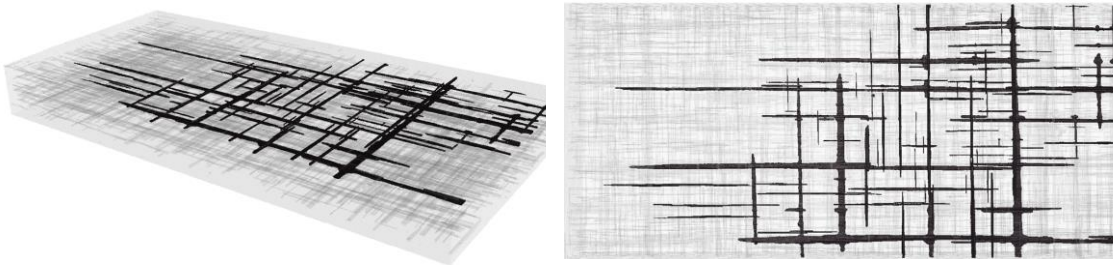

(a) 3D image of the sample with selected largest void-network

(b) Projected area on the length-width plane of the selected void-network

Figure 6-5. The selection of the projected area of the voids: (a) a 3D view of a void-network, (b) The projected area of that void onto the length-width plane.

The section with the largest projected surface area (after taking into account the SCF) is then selected as the ‘critical plane’.

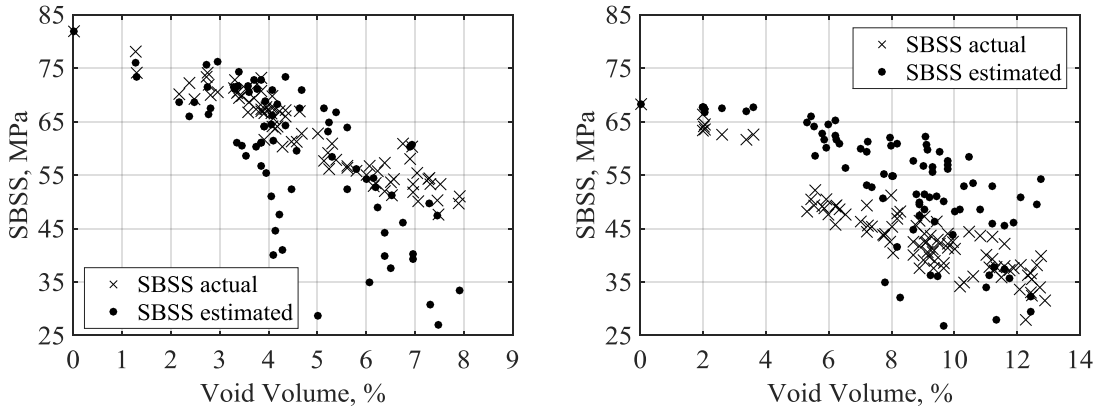

(a) IM7/8552 **(b) IMA/M21**

Figure 6-6. Prediction of the SBS strength using the projected surface area (in the length-width plane) to estimate the area of voids in the 'critical plane'.

Figure 6-6 shows that the prediction of the SBS strength using the projected surface area is better than that obtained directly calculating the actual reduced cross-sectional area from the CT-slices (shown in Figure 6-3) and when assuming a constant cross-sectional area of the voids (shown in Figure 6-4), especially for IM7/8552 samples. This is explained by the presence of one dominant largest void-network in the IM7/8552 material system, within one of the plies. Hence, taking the projected surface area of the largest void-network provides a good for prediction for IM7/8552.

It can be also seen in Figure 6-6 that there are some 'outliers' in the predicted results that do not compare well to the experimental results. This is caused by the particularly large void-networks in these samples that extend through multiple plies (*e.g.* 5 or more plies). In particular, due to their 'network' shape, these voids actually have a smaller effect on the SBS strength than what is predicted by the projected area.

To illustrate this, Figure 6-7 shows only those samples with void-networks with thicknesses that are 4 or less plies in thickness and shows that those 'outliers' are almost completely eliminated for both material systems. Thus, in subsequent investigations of the projected area, void-networks having a maximum thickness greater than 4 plies have been neglected.

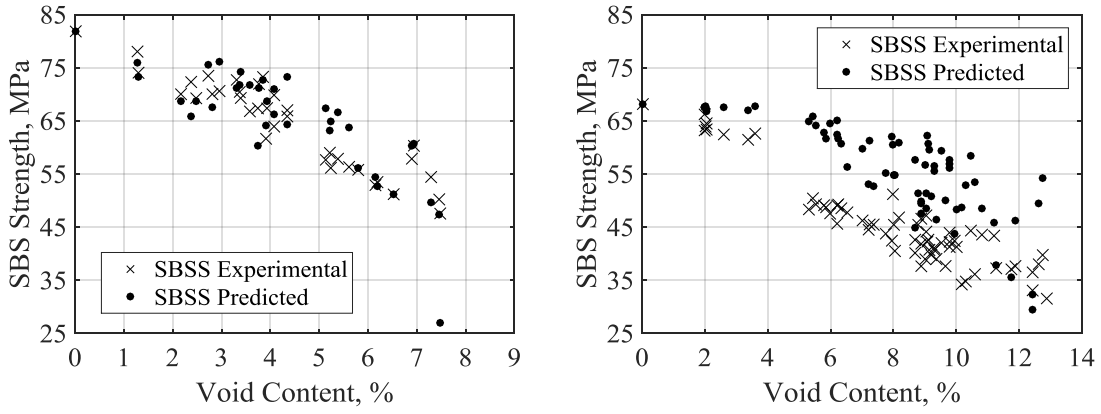

(a) IM7/8552 **(b) IMA/M21**

Figure 6-7. Prediction of the SBS strength using the projected surface area (in the length-width plane) to estimate the area of voids in the 'critical plane', neglecting samples with void-networks having a thickness greater than 4 plies.

Unfortunately, the improvement in the prediction is limited for the IMA/M21 samples. This is due to this material system not having one void that is significantly larger than the rest of the voids (as is the case for IM7/8552), but instead it has multiple large voids between the plies. In fact, CT analysis of these samples shows that the majority of the voids are located in the interface (as the resin layer of this material system is large), as shown in Figure 6-8. This could explain why the prediction underestimates the SBS strength, and suggests that a discrete 3D slice should be analysed in order to account for all the voids in each resin layer, although the actual thickness of this 3D slice needs to be investigated.

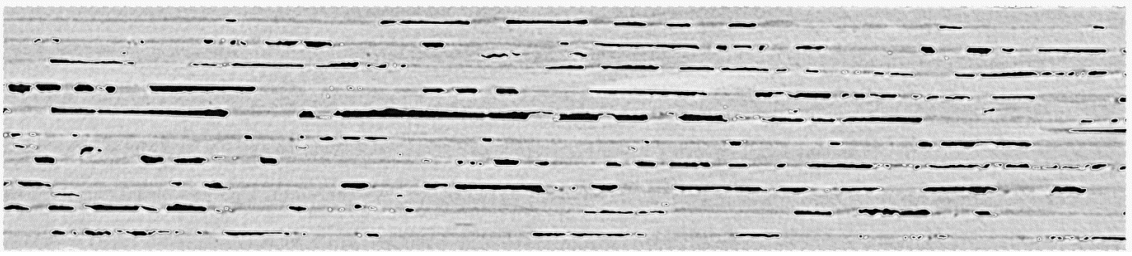

Figure 6-8. Void distribution in an IMA/M21 sample, *Vv*= 9.22%, showing that the majority of the voids are located in the ply interface.

6.2.4 Prediction using a finite slice thickness

It is expected that, even though the voids may not be centred on exactly the same length-width plane of the samples, the close proximity of the voids in the interply zones of the IMA/M21 samples means that they effectively act as a unified plane of voids. As a result, it is expected that including the projected areas of voids from a discrete 3D slice of the samples to calculate a 'critical slice' could provide a better prediction of the SBS strength.

To investigate the influence of the slice thickness, it was varied and the cumulative projected area (in the length-width plane) of all voids centred within that slice was calculated. This cumulative projected area was used to calculate a reduced cross-sectional area and thereby to predict the SBS strength using the SCF (Equation 6-3). The predictions were then compared to the experimental SBS strength in order to calculate a mean squared error.

Figure 6-9 shows these interesting results, which are very different for each material system. For the IM7/8552 samples, it can be observed that there is minimal difference between sample slices below ~0.1mm. And, in fact, taking a slice of 0 mm (*i.e.* the plane described in Section 6.2.3) is shown to provide a suitable estimate of the SBS strength for IM7/8552 samples. This is because this material system has one significantly large void-network (*i.e.* network of interconnected voids) that provides a good prediction with or without the addition of neighbouring smaller voids.

However, the results are quite different for IMA/M21 and show that taking a slice of 0 mm (as described in Section 6.2.3) provides the highest error in the SBS strength estimation, and that increasing the slice thickness decreases the obtained error. In fact, a minimum error is obtained at a slice thickness of 0.0475 mm. It is notable that the thickness of the slice is similar to the resin layer thickness of this material, which makes sense as the majority of the voids are located in the resin layer (as previously shown in Figure 6-8).

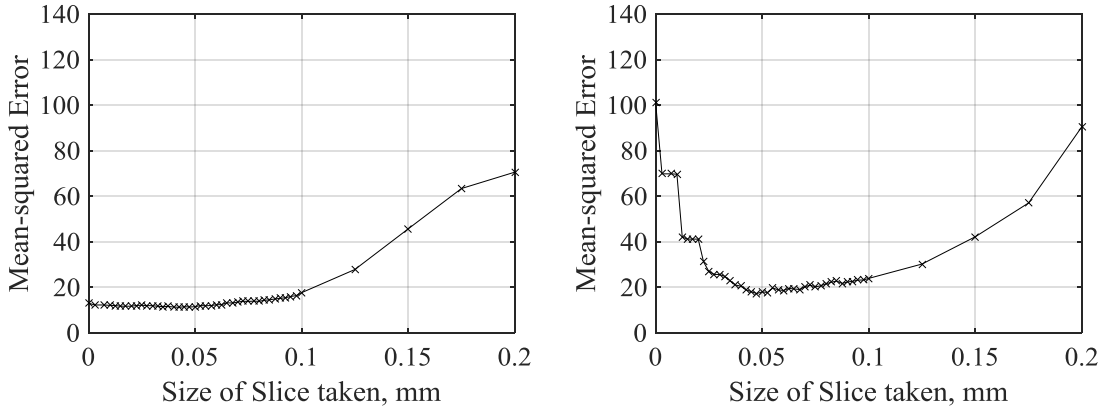

(a) IM7/8552 **(b) IMA/M21**

Figure 6-9. The mean squared error for IM7/8552 when taking different slice thicknesses (note that a 0 mm slice refers to the analysis of a 2D plane, as shown in section 6.3.2)

6.2.5 Improvement of the SBS strength prediction of the IMA/M21 samples

By using the optimal thickness of the slice for IMA/M21, a significant improvement in the prediction of SBS strength can be observed (Figure 6-10b). However, using this constant thickness value still provides scatter of the results, which can be improved further.

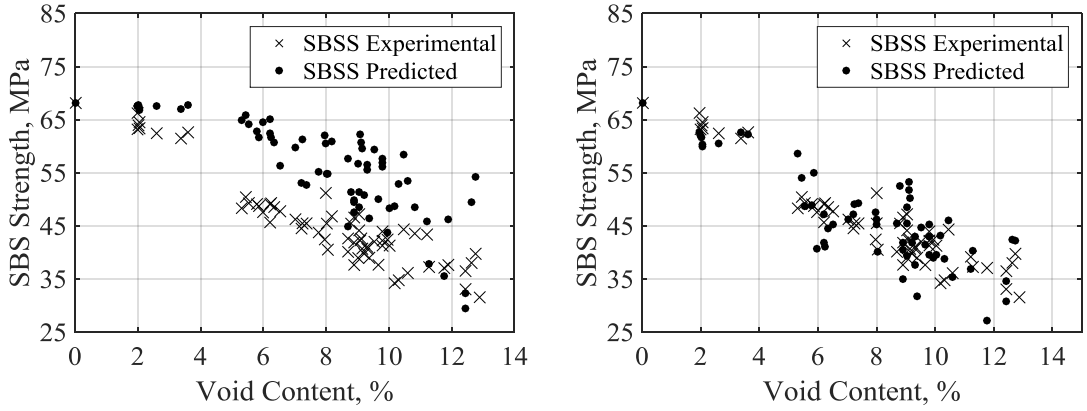

(a) Slice thickness = 0 mm **(b) Slice thickness = 0.0475 mm**

Figure 6-10. Predicted SBS strength for IMA/M21 samples when using the 'critical slice', assuming a slice thickness of 0.0475mm.

6.2.5.1 Resin layer thickness distribution in the samples

CT-images of the IMA/M21 samples reveal that the resin layer thickness actually varies between samples, and is in fact proportional to the average void content in each sample. This is illustrated in Figure 6-11 for three selected samples of increasing void content.

To provide a quantitative evaluation of the resin layer thickness, several samples of IMA/M21 were selected (in the void content range of between 2 % and 13%). A slice was taken in the middle of the sample, and the average resin layer thickness in that slice was calculated. The average resin layer thickness for the several samples is shown in Figure 6-12. As expected, the resin layer thickness increases as the average void content increases and suggests that one (constant) value of the resin layer thickness is unable to adequately represent the resin layer thickness of all samples for this material system.

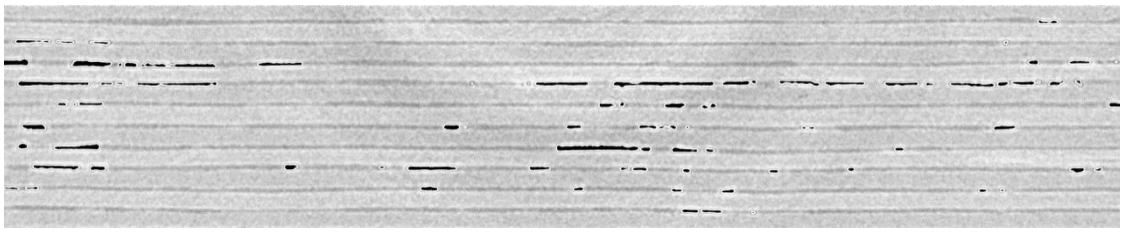

(a) *V*v = 2.04%

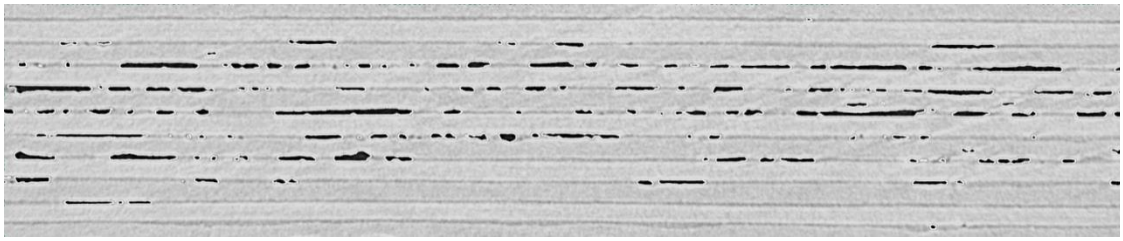

(b) *V*v = 5.34%

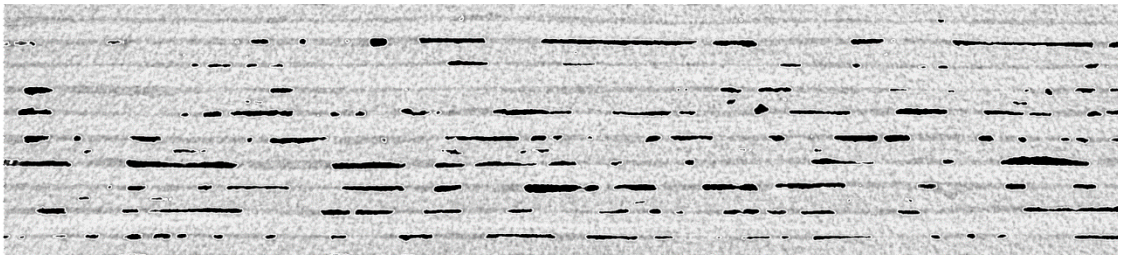

(c) *V*v = 11.59%

Figure 6-11. CT-images of IMA/M21 samples in the width-thickness direction showing an increasing of the resin layer with increase of the average void content

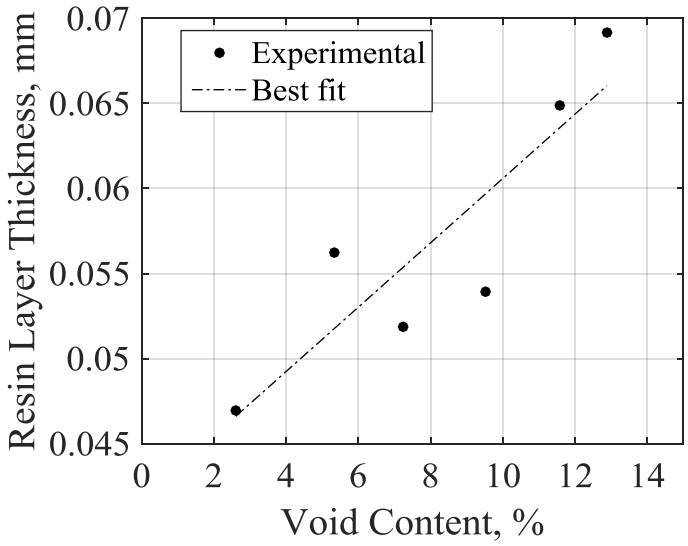

Figure 6-12. Measured average resin layer thickness of IMA/M21 samples directly from CT-images.

The difficulty is that evaluation of the average resin layer thickness using CT-images is time consuming and still only provides a snap-shot of the resin layer thickness in a particular plane, whereas in reality each resin layer thickness is variable. However, it was

previously shown that the majority of voids are located in the interface, and furthermore it is observed that the resin layer thickness is approximately the same as the average void thickness in this material system.

As a result, the resin layer thickness for each specimen can be estimated quickly (from the available CT-data provided by the VG Studio Max Defect Detection plug-in) by taking an average of the void thickness in a sample. Figure 6-13 shows the increase of the void thickness as the void content of the samples increases. This shows a similar trend as the resin layer thickness estimated directly from the CT-images (Figure 6-12), although the void thickness is slightly higher as the direct resin thickness measurement from the CT-images uses a 2D slice of the sample and so does not account for unevenness of the actual resin layer thickness. The data from Figure 6-13 can therefore be used to provide a better estimate of the in-plane average resin layer thickness.

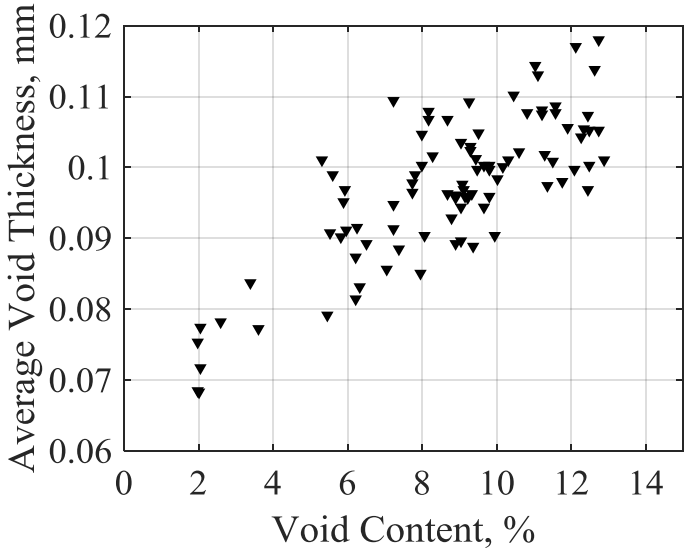

Figure 6-13. Average void thickness in IMA/M21 showing an increase with increasing of the average void content.

6.2.5.2 The effect of a variable slice thickness

This result suggests that the prediction of SBS strength can be improved by taking into account the variable resin layer thickness (*i.e.* slice thickness). To investigate this, two different parameters for the slice thickness were used – the best-fit line from the average resin layer thickness, shown in Figure 6-12, and the average thickness of the voids for each individual sample, as shown in Figure 6-13. Note that by using the average thickness of the voids of each sample (rather than a best-fit line), a prediction of the SBS strength for each sample can be obtained without knowledge of the void thicknesses of the other samples. The comparison of these two parameters is shown in Figure 6-14.

The two parameters for calculating the applied slice thicknesses provide similar predictions to the SBS strength prediction, and in both cases the mean squared error (MSE) is slightly reduced in comparison to taking a constant slice thickness for all samples, which gave a MSE of 17.24. The total error between the predicted SBS strength and experimental SBS strength is slightly smaller (MSE = 13.755) when calculating the slice thickness from the average void thickness than when calculating the slice thickness from the resin layer thickness measured directly from 2D CT-images of the samples (MSE = 14.363).

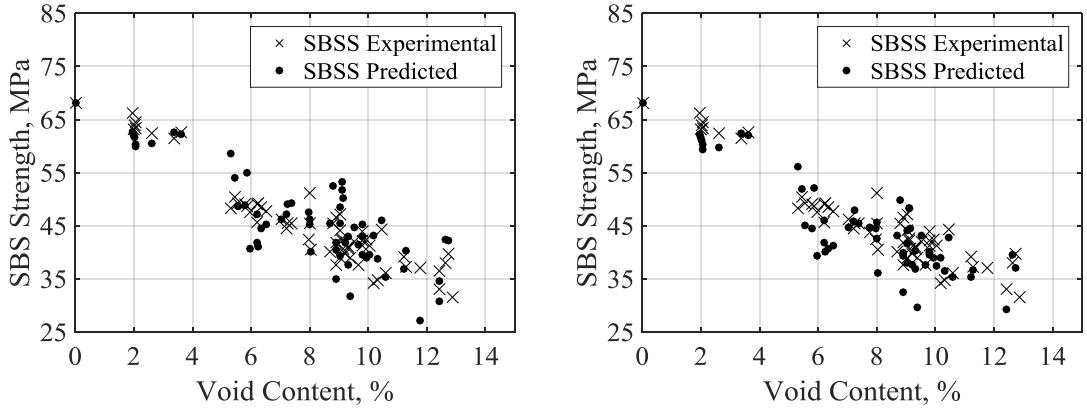

(a) Using best fit line from Fig.9

Error = 14.363

(b) Using average thickness of the voids

Error = 13.755

Figure 6-14. Prediction of the SBS strength for IMA/M21 using variable thickness of the slice based on: (a) best fit line for resin layer thickens; and, (b) average thickness of the voids.

6.2.6 Prediction of the SBS strength for angle-plies

To predict the SBS strength for the IM7/8552 angle-ply laminates, two methods previously applied to calculate the reduced cross-sectional area (see Equation 6-2) are applied here. However, in contrast to the results shown for cross-ply samples, no samples are excluded. This is because void-networks are present in almost all samples that extend through at least 4 plies. For this reason, and because there are fewer tested samples, the relative mean squared errors of the predictions between the cross-ply and angle-ply samples are not directly comparable.

Firstly, the reduced cross-sectional area is calculated in the 'critical plane' by making the assumption that each void has a constant cross-section in the thickness direction. The total cross-sectional area, $A_{porosity}$, in each plane is then calculated by adding together the cross-sectional area, A_{void}, of each void that extends through the particular plane in

question. This is the same approach adopted for the IM7/8552 cross-ply laminates in Section 6.3.2. The results are shown in Figure 6-15a and indicate that this approach significantly overestimates the SBS strength of the samples across the entire range of sample void contents.

Secondly, the reduced cross-sectional area is calculated based on the projected area of all voids whose centre crosses a particular plane. This is the same approach adopted for the IM7/8552 cross-ply laminates in Section 6.3.3. The results in Figure 6-15b show a reduced error between the actual SBS strength and the predicted SBS strength (when compared to the prediction based on assuming a constant cross-sectional area of the voids – as in Figure 6-15a), however there is still significant variation in the predicted SBSS. Whilst some of the predictions showed a close agreement to the actual SBS strength, the majority of the samples showed significant overestimation or underestimation of the SBS strength.

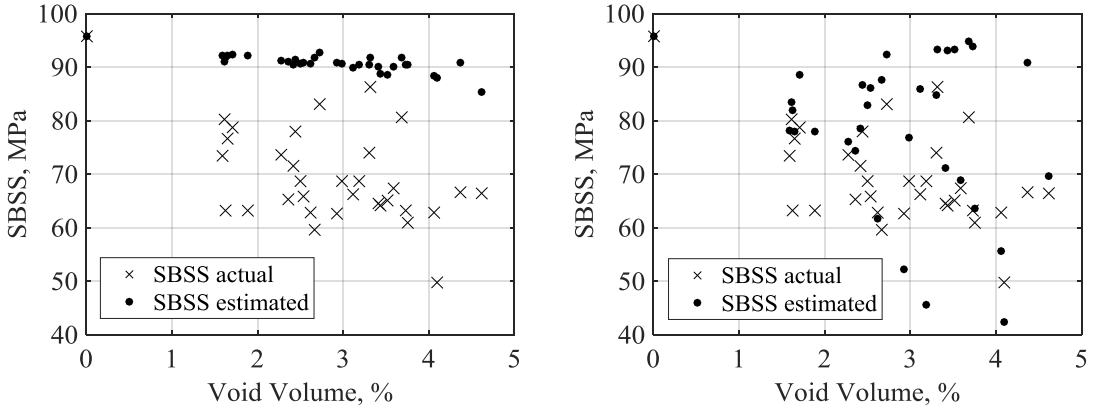

Figure 6-15. Prediction of the short beam shear strength from the reduced cross-sectional area of the 'critical plane': (a) Calculated assuming a constant cross-sectional area of the voids in the thickness direction, (b) Calculated using the projected surface area (in the length-width plane).

6.2.6.1 Prediction for angle plies using a finite slice thickness

It was shown previously (Section 6.3.5) that the best prediction for IM7/8552 cross-ply samples is found when taking the projected area of voids whose centre lie on a 'critical plane', and it is thought this is due to these samples typically containing one very large void (in comparison to the remaining voids in a sample). This seemed to be supported by the improvement in results that could be obtained for the M21/8552 samples when using the projected area of all voids within a finite 'slice' thickness, as these samples generally had a number of similarly large voids, rather than one very large void. As seen in Figure 6-16 for one representative sample, the void size distribution for the IM7/8552 angle-ply

samples is similarly more evenly spread, with no singular large void (in comparison to the remaining voids).

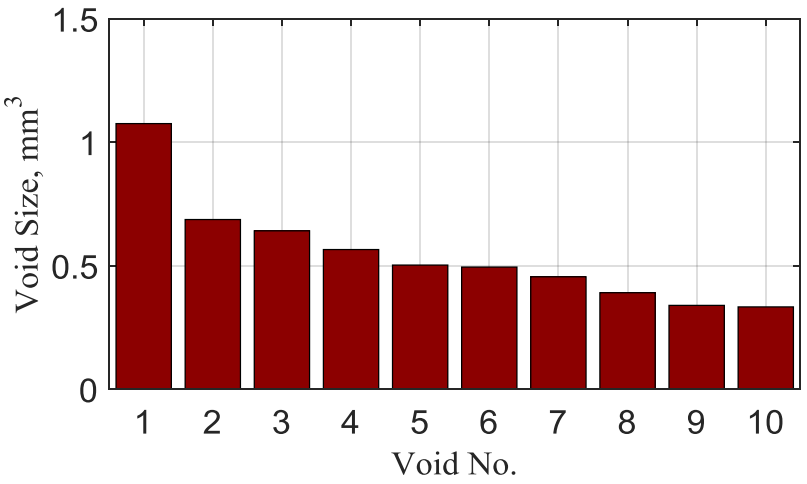

Figure 6-16. The 10 largest voids of an IM7/8552 angle-ply sample with void content, V_v = 2.53%.

This suggests that the prediction of SBS strength can be improved by taking into account a finite slice thickness, as opposed to only counting voids that are centred on a single plane. As Figure 6-17 shows, a minimum error is obtained when adding together the projected area of all voids within a slice of thickness 0.095 mm. In fact, the mean squared error (MSE = 129.42) is almost half of that obtained when using a single plane (MSE = 217.9537).

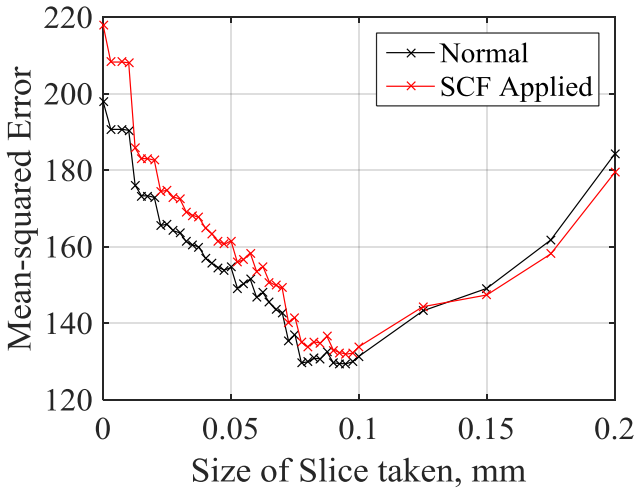

Figure 6-17. The mean squared error for an IM7/8552 angle-ply laminate when taking different slice thicknesses (note that a 0 mm slice refers to the analysis of a 2D plane, as discussed in Section 6.3.6).

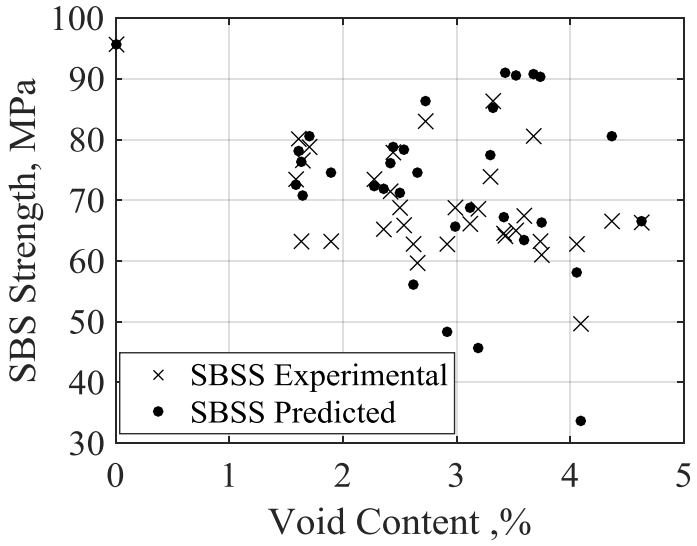

Figure 6-18. Predicted SBS strength for an IM7/8552 angle-ply samples when using the 'critical slice', assuming a slice thickness of 0.095mm.

6.2.6.2 The effect of a variable slice thickness for angle plies

In Section 6.2.5.2 it was shown that the best prediction of the SBSS for IMA/M21 cross-ply samples could be obtained by the average thickness of all voids in a given sample, which was shown to be approximately the same as the resin layer thickness.

The resin layer for IMA/M21 is relatively easy to detect due to the toughening particles that are present in the resin, however this isn't the case for IM7/8552 and so it is very challenging to calculate the thickness of the resin layer. Even so, Figure 6-19 shows that by using the average thickness of all voids for each sample, it is possible to obtain a reasonable estimate of the SBSS (MSE = 137.60). This prediction is slightly worse than the prediction obtained when taking a slice thickness of 0.095 mm (MSE = 129.42), however this technique has the advantage that it only needs information about the sample in question. Whereas obtaining the optimal slice thickness (as in section 6.4.3) requires information from many samples in order to be confident in its value.

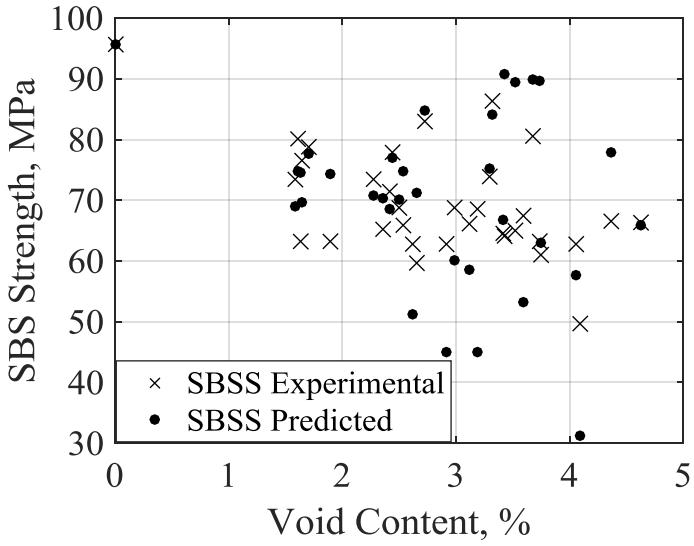

Figure 6-19. Prediction of the SBS strength for IMA/M21 using a slice thickness according to the average thickness of the voids in each sample.

6.3 Concluding Remarks

In this chapter, different methods of predicting the SBS strength in carbon/epoxy composites have been compared. The intention is that these methods will provide guidance to industry on how to predict the strength of composite materials containing voids using information obtained from the CT-images, material system data, and a reference value of the strength, without undertaking extensive testing programs.

The motivation for developing these methods of predicting the SBS strength stems from an assumption that the reduction of the SBS strength is principally influenced by a reduction of the cross-sectional area in a 'critical plane', due to the presence of voids in this plane and its combined effect with a stress concentration factor (SCF) that relates the position of the plane to the estimated stress in that particular plane. The approaches are also influenced by the information that is available concerning the voids. Although there is significant information from the CT-analysis regarding many of the characteristics of each void (*e.g.* void volume, surface area, position, projected area, and length), it doesn't automatically provide the planar void content through the thickness of the samples.

It has been shown that, even when undertaking the time-consuming process of using the CT-images to find and directly measure the void content in the 'critical plane', the results of the SBSS prediction for both material systems show significant overestimation of the strength values due to the significant 3D morphology of the voids.

As a result, less time-consuming methods are proposed that use the available void data-set obtained using the VG-Studio Defect Detection plug-in.

The first method calculated the reduced cross-sectional area by assuming that each void has a constant cross-section in the thickness direction, and totalling the cross-section of each void that crosses a particular plane. The method showed a better prediction at low void content (<4% void content) than at higher void contents for both IMA/M21 samples and IM7/8552 samples due to the regular shape of the voids at low void content. At high void content, particularly for IM7/8552, the voids form a complex void-network of interconnected voids that extend across multiple plies.

To try and take into account the effect of this 3D network on a 2D plane, the projected area of the voids (when viewed in the length-width plane) has been used to calculate the reduced cross-sectional area by finding any voids whose centre lies on a particular plane. As the centre of two voids is unlikely to exactly match, it therefore means that the calculation effectively calculates the projected area of the single largest void-network. This estimation provided good results for IM7/8552 samples, especially after neglecting samples with voids extended across more than 4 plies. This method did not work so well for the IMA/M21 material system, which had a different void morphology.

Improvements in the prediction were identified for the IMA/M21 samples when taking into account voids centred within a discrete distance of the 'critical plane', *i.e.* when totalling the projected area of voids in a thin 3D slice. This improvement is due to this material system not having one void that is significantly larger than the rest of the voids (as is the case for IM7/8552), but instead having multiple large voids in the interply region that effectively act as a 2D plane. It was also shown that the optimal slice thickness for IMA/M21 was 0.0475 mm, which is approximately the size of the resin layer where the majority of the voids are located. However, it is also known that the resin layer thickness varies between samples, and so this information was used to improve the prediction of SBS strength using a variable slice thickness for each sample. Furthermore, it was shown that the average void thickness for each sample provides a good estimate of the resin layer thickness for this material system, and thereby provides a good estimate of the optimal slice thickness.

An initial investigation into the effect of different lay-ups on the SBS strength is also undertaken using an angle-ply laminate. This showed significantly more scatter of the experimental data between void content and SBS strength than that observed for the cross-ply laminate. The prediction of the SBS strength is also further complicated by the complex shape of the voids and their influence on the failure behaviour, as the interply voids of the angle-ply have a curved shape that combines the path of both of its adjacent

plies. Even so, satisfactory predictions were obtained by taking into account voids centred within a discrete distance of the 'critical plane' (*i.e.* a slice thickness of 0.095mm). Alternatively, a similar prediction could be obtained by approximating the optimal slice thickness as the average void thickness of a particular sample.

7 MODELLING THE FAILURE BEHAVIOUR OF THE LAMINATED COMPOSITES CONTAINING VOIDS

It has been demonstrated in the preceding chapters through an extensive experimental program investigating the effect of voids in carbon/epoxy composites, that there are particular void features that have a significant effect upon the short-beam shear strength (SBSS), such as void size, void shape, void location, and the proximity between voids.

To generate a numerical understanding the effects of these individual void characteristics would require the use of detailed finite element (FE) analysis, such as micromechanical modelling, in order to provide a controlled environment in which these parameters can be altered in a well-defined manner. However, these models are complex, computationally expensive, and typically only feasible for analysing particular portions of a larger specimen. Even then, the implementation of these models requires many assumptions and simplifications to be made with respect to the experimental testing.

However, it was shown in the literature review, and has been demonstrated in the preceding chapters (see *e.g.* Section 5.3), that the reduction in mechanical properties due to porosity can be predicted satisfactorily when taking a more homogenised approach – for example, the SBSS shows a strong linear correlation to the average void content of the specimens (see Section 5.3.1). The difficulty with using these correlations to calculate a knock-down factor is that generally this requires an extensive experimental program to be implemented in order to characterise the relationship.

If a simplified FE model could be developed, which simulates and predicts the failure behaviour and/or failure stresses in composite laminates containing voids, the benefits would be appreciable. For instance, there is a need in industry for a fast and accurate FE model that can be used to pass or fail composite components based on homogenised information of porosity at a component level, or ply level. The FE model should be able

to predict the reduction in mechanical properties (*i.e.* provide a knock-down factor) using only limited knowledge of individual void features.

In this chapter, a simplified FE model is used to simulate a short beam shear (SBS) test for two laminate lay-ups: cross-ply and angle ply. A simple parametric investigation was conducted in order to identify the most critical material damage model properties and their correlation to the average void content.

7.1 Model development

A finite element model of the short beam shear (SBS) test has been generated in the explicit code LS-Dyna according to the geometry of the test samples. The elements used in the model were 8-noded hexahedral single integration point solid elements (LS-Dyna Element Formulation Type 1) in order to model the individual plies, and 8-noded cohesive elements in order to model the inter-ply failure. The mesh is generated using a Matlab script to write a keyword/input file containing the mesh information, with refinements made to allow the generation of a controlled bias in element size at the roller contact areas and near the free edges.

The developed model included 90 elements across the length of the beam, with a minimum element dimension, l_{el}, of 0.143 mm, and 30 elements across the width of the beam, with a minimum element dimension, w_{el}, of 0.238 mm. In the through-thickness direction, 1 element per ply was used.

The modelled laminates have the same lay-up as the IM7/8552 laminates that have been investigated in the previous chapters, such that the cross-ply lay-up is $[(0,90)_4,0,90,0,(90,0)_4]$ and the angle-ply lay-up is $[(0,+30,-30)_3,0,(-30,+30,0)_3]$.

The SBS test includes two rigid support rollers of 3mm in diameter beneath a composite sample, and one rigid loading roller of 6mm diameter above the sample. The composite sample has a length of 20 mm, a width of 10 mm width, and a thickness of 2.375 mm. The span between the rollers is 10 mm, in accordance with the ASTM standard (ASTM D2344) and the setup used in the experimental program. Automatic surface-to-surface contacts were created between the rollers and the composite beam, and all translational and rotational degrees of freedom of the support rollers were constrained. The sample was then loaded by assigning a prescribed motion to the loading roller. The FE model is shown in Figure 7-1 and the elastic mechanical properties of the IM7/8552 unidirectional laminate used as input are summarised in Table 7-1.

Table 7-1. Thermo-elastic properties for UD IM7/8552 laminates [2].

E_{11}, GPa	E_{22}, GPa	E_{33}, GPa	ν_{12}	ν_{13}	ν_{23}	G_{12}, GPa	G_{13}, GPa	G_{23}, GPa	α_{11}, /°C	α_{22}, /°C	α_{33}, /°C
161	11.38	11.38	0.32	0.32	0.436	5.17	5.17	3.962	0	3×10^{-5}	3×10^{-5}

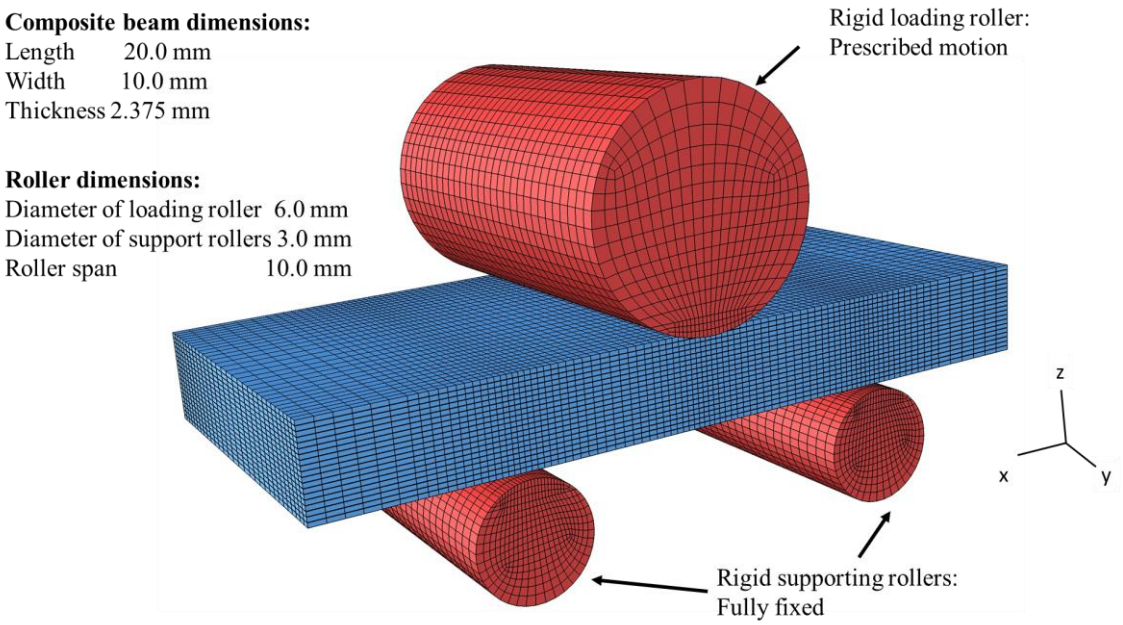

Figure 7-1. FE model set-up for the simulated short beam shear (SBS) test.

In order to accurately predict the SBS behaviour of a pristine model (*i.e.* a model without voids), it is necessary to define the mechanical constitutive behaviour of the ply and cohesive elements. This is achieved using the 'User Defined' material models developed within the Rolls-Royce UTC of the University of Bristol. The implemented models include:

Non-linear shear model - A non-linear shear stress-strain relationship was assumed in the in-plane and through-thickness direction and implemented in the following form [2]:

$$\boldsymbol{\sigma_{1i} = sgn(\gamma_{1i})\left(A\left(1 - e^{-B|\gamma_{1i}|}\right)\right), i = 2, 3} \quad \textbf{(7-1)}$$

where σ_{1i} is the shear stress and γ_{1i} is the engineering shear strain, the numeric indices denote the ply principal direction, and A and B are obtained by a least-square fit to the experimental data. For IM7/8552, A = 145 and B = 38 from [137].

Continuum damage model for transverse matrix cracking - This model is based on the work of Pinho *et al.* [105], [106] and further developed by Mukhopadhyay *et al.* [2]. This model used an initiation law, proposed in [138]:

$$f_{\mathrm{mt}} = \left(\frac{\sigma_{\mathrm{N}}}{S_{\mathrm{T}}}\right)^2 + \left(\frac{\tau_{\mathrm{L}}}{S_{\mathrm{L}}}\right)^2 + \left(\frac{\tau_{\mathrm{T}}}{S_{\mathrm{T}}}\right)^2 + \lambda\left(\frac{\sigma_{\mathrm{N}}}{S_{\mathrm{T}}}\right)\left(\frac{\tau_{\mathrm{L}}}{S_{\mathrm{L}}}\right) + \kappa\left(\frac{\tau_{\mathrm{T}}}{S_{\mathrm{T}}}\right) \quad \textbf{(7-2)}$$

where f_{mt} equals 1 at damage initiation, σ_{N} is the normal traction on the fracture plane, τ_{L} and τ_{T} are the two shear tractions (see Figure 7-2). S_{L} and S_{T} are the in-plane and transverse matrix shear strengths, respectively. S_{T} is obtained using equation 7-3 [106]:

$$S_{\mathrm{T}} = \frac{Y_{\mathrm{C}}}{2\tan(\phi_0)} \quad \textbf{(7-3)}$$

where ϕ_0 is the angle of the fracture plane in pure compression, Y_{C} is the transverse compressive strength.

Parameters κ and λ are given by:

$$\left.\begin{aligned} \kappa &= \frac{(S_{\mathrm{T}})^2 - (Y_{\mathrm{T}})^2}{S_{\mathrm{T}} Y_{\mathrm{T}}} \\ \lambda &= 2\mu_{\mathrm{L}}\frac{S_{\mathrm{T}}}{S_{\mathrm{L}}} - \kappa \end{aligned}\right\} \quad \textbf{(7-4)}$$

where Y_{T} is the transverse tensile strength and μ_{L} is the longitudinal friction coefficient.

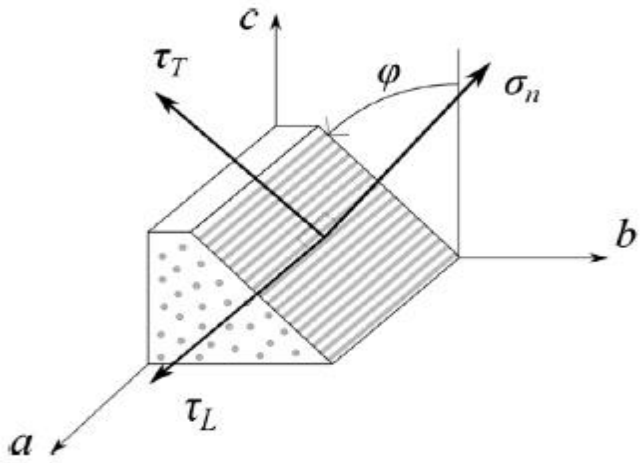

Figure 7-2. Traction components on the fracture plane, from Pinho *et al.*[105]

After failure is detected, the traction components acting on the fracture plane are degraded:

$$\left.\begin{aligned} \sigma_{\mathrm{N}} &\rightarrow (1 - D_{mc})\sigma_{\mathrm{N}} \\ \tau_{\mathrm{T}} &\rightarrow (1 - D_{mc})\tau_{\mathrm{T}} \\ \tau_{\mathrm{L}} &\rightarrow (1 - D_{mc})\tau_{\mathrm{L}} \end{aligned}\right\} \quad \textbf{(7-5)}$$

where $D_{\mathrm{mc}} \in [0,1]$ is a damage parameter, introduced as below:

$$\boldsymbol{D_{mc} = \max\left\{0, \min\left\{1, \frac{\varepsilon_f(\varepsilon_{mat} - \varepsilon_0)}{\varepsilon_{mat}(\varepsilon_f - \varepsilon_0)}\right\}\right\}} \quad \textbf{(7-6)}$$

Where $\varepsilon_{\mathrm{mat}}$ is the damage driven strain, ε_{f} is the equivalent strain at complete failure that can be obtained using the mixed mode critical fracture energy, the characteristic length and the strength at initiation of damage, and ε_0 is the strain at damage initiation. All the related equations can be found in [2].

In the model, instabilities in the numerical solution were avoided by fixing the damage parameter, D_{mc}, at 'complete failure' to be a value of 0.95.

The parameters listed in Table 7-2 have the following meaning: Y_{T}, Y_{C} and S_{L} are the tensile strength, compression strength and longitudinal shear strength, respectively. G_{IC} and G_{IIC} are the mode I and mode II fracture toughness, respectively, and α is the exponent in the power law.

Table 7-2. IM7/8552 properties for matrix crack model [2].

Y_{T}, MPa	Y_{C}, MPa	S_{L}, MPa	G_{N}, N/mm	G_{T}, N/mm	G_{L}, N/mm	α
160.0	250.0	113.0	0.26	0.26	1.002	1

Delamination model: The delamination model used in this work is a mixed mode bi-linear cohesive fracture model, based on the work of Jiang *et al.* [110]. This softening law can be illustrated in a three-dimensional map, with the pure mode I behaviour indicated in the $0 - \sigma - \delta_{\mathrm{I}}$ plane, while the mode II behaviour is indicated in the $0 - \sigma - \delta_{\mathrm{II}}$ plane (see Figure 7-3). The combined mixed-mode displacement can be calculated as follows:

$$\delta_{\mathrm{m}} = \sqrt{\delta_1^2 + \delta_2^2 + \delta_3^2} \quad \textbf{(7-7)}$$

where δ_1, δ_2 and δ_3 are the mode I, mode II, and mode III relative displacements between the surfaces of the cohesive element, respectively.

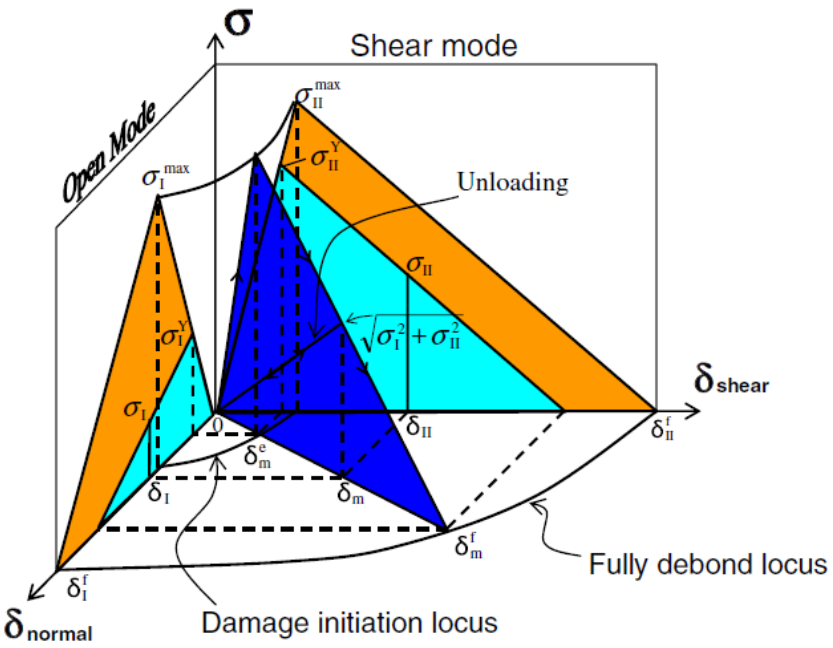

Figure 7-3. Interfacial bilinear mixed-mode softening law[110]

The numerical initiation is modelled with a stress-based criterion, while the propagation is energy driven. To initiate damage, a quadratic interaction criterion was used:

$$\boldsymbol{f_{\text{delam}} = \sqrt{\left(\frac{\langle \sigma_{33} \rangle}{\sigma_{I\,\max}}\right)^2 + \left(\frac{\sqrt{\sigma_{13}^2 + \sigma_{23}^2}}{\sigma_{II\,\max}}\right)^2}} \qquad \textbf{(7-8)}$$

where f_{delam} is equal to 1 at initiation, $\sigma_{\text{I max}}$ is the interlaminar normal strength, and $\sigma_{\text{II max}}$ is the interlaminar shear strength.

The propagation is controlled by the power law criterion:

$$\boldsymbol{\left(\frac{G_{\text{I}}}{G_{\text{IC}}}\right)^{\alpha} + \left(\frac{G_{\text{II}}}{G_{\text{IIC}}}\right)^{\alpha} = 1} \qquad \textbf{(7-9)}$$

where G_{I} and G_{II} are the mode I and mode II energy release rates associated with the current state of loading, G_{IC} and G_{IIC} are mode I and mode II fracture toughness's, and α is an empirical parameter for a given material.

The mixed-mode damage parameter $D_{\text{delam}} \epsilon$ [0,3] is defined below:

$$\boldsymbol{D_{\text{delam}} = \frac{\delta_m - \delta_m^e}{\delta_m^f - \delta_m^e}} \qquad \textbf{(7-10)}$$

where δ_m , δ_m^e, δ_m^f are the current mixed-mode displacement, displacement at damage initiation, and complete failure displacement, respectively. An assumption is made that

prior to damage initiation the top and bottom surfaces of cohesive elements are connected by high stiffness springs, defined as EI and EII in the mode I and mode II directions, respectively.

The cohesive stiffness's for this material system, shown in Table 7-3 were estimated from the isotropic mechanical properties of the resin, taking a Young's modulus, *E,* of 4.67 GPa and a Poisson's ratio, *v,* of 0.33, and assuming that the thickness of the resin rich layer is 0.01 mm.

Table 7-3. Cohesive properties for UD IM7/8552 laminates.

G_{IC}, N/mm	G_{IIC}, N/mm	σ_I^{max}, MPa	σ_{II}^{max}, MPa	E_I, N/mm^3	E_{II}, N/mm^3	α
0.26	1.002	111.0	120.0	$4.65 \cdot 10^5$	$1.75 \cdot 10^5$	1

Residual stresses were also introduced into the model to simulate the stresses developed in the laminate due to cooling from the cure temperature (180°C) down to room temperature (20°C).

The model was then implemented assuming a constant (ambient) temperature, with the loading increased until complete failure.

7.2 Failure modes

The experimental tests revealed that the cross-ply IM7/8552 laminates initially failed via multiple matrix cracks, followed by delamination. This behaviour was seen by the high-speed camera and a high resolution DSLR camera, and was further confirmed through CT-analysis of several post-failure samples.

This behaviour was also observed in the pristine SBS sample model, which showed initiation of the matrix cracks in close proximity to the rollers (loading and support rollers) and then further propagation of the matrix cracks in each of the 90° plies (see Figure 7-4). After the maximum strength of the sample was reached (*i.e.* post-failure), delamination failure was observed. Overall, this model correctly captures initiation and propagation of the failure in pristine samples when compare to the experimental results, both qualitatively (see Figure 7-4) and quantitively (see the next section, Section 7.3).

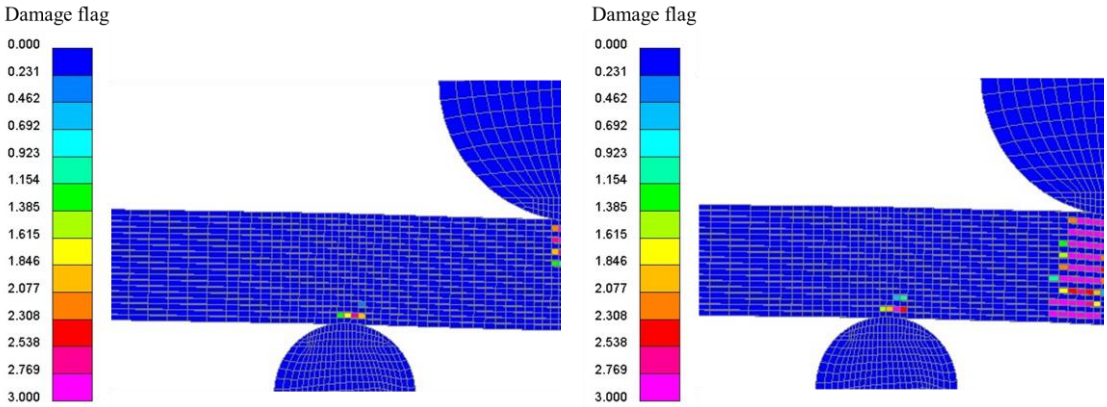

(a) Failure initiation (b) Failure propagation

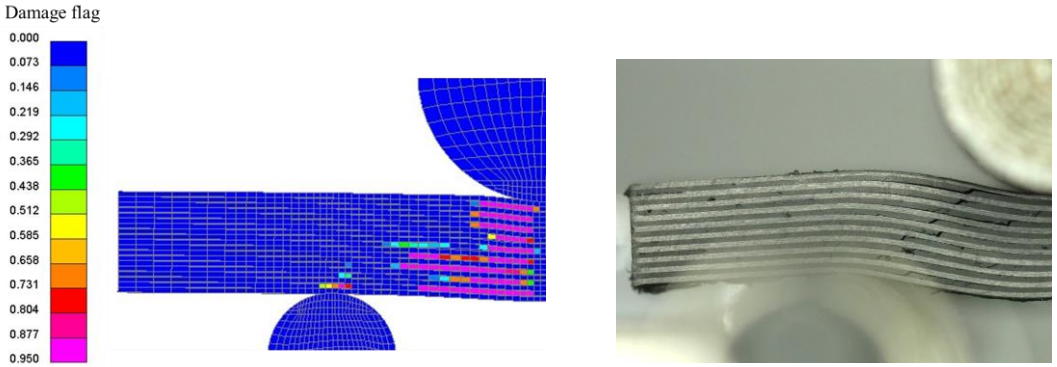

(c) Final failure – model **(d) Final failure – experiment**

Figure 7-4. Comparison of the failure mode for the pristine model and experimental results for IM7/8552 cross-ply samples. (a) the initiation of the failure and (b) the progression of the failure; (c) and (d) shows the final failure of model and experiment, respectively. The damage flag reaches 0.95 at full failure.

For the IM7/8552 angle-ply samples, the experimental failure behaviour is different in that failure initiates with delamination between adjacent plies (and close to the mid-plane in the pristine samples), with post-failure showing the development of matrix cracks in the +30° and−30° plies.

However, when implementing the matrix crack damage model in the FE analysis, the prediction was unable to replicate this behaviour, and instead failure was initiated via large areas of predicted matrix cracks (see Figure 7-5). As a result, the failure strength of the angle-ply laminates was underestimated. The possible cause for this is the smeared crack approach, that implemented into the continuum damage model for transverse matrix cracking.

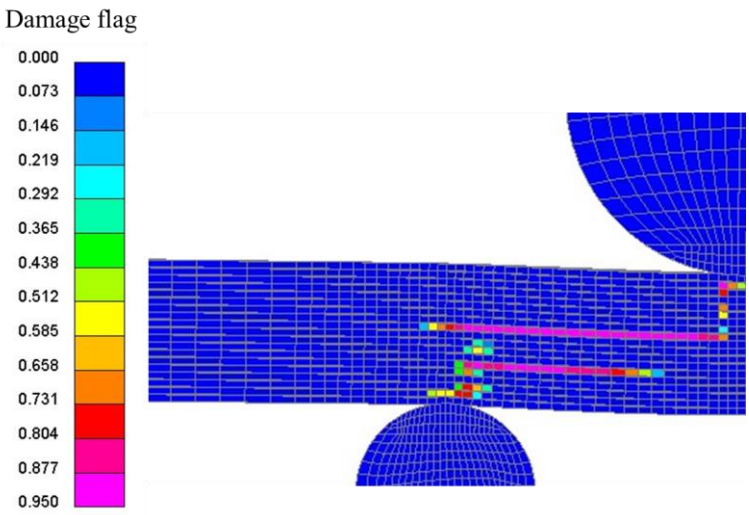

Figure 7-5. Failure of the angle-ply laminates via matrix cracking

Therefore, in order to provide a better qualitive and quantitative estimation of the failure behaviour, the matrix crack properties were suppressed. The result is that the predicted failure behaviour displays the expected delamination initiation, although consequently is unable to show matrix cracking after the delamination (Figure 7-6). However, this suppression is not expected to affect the failure load, as the matrix cracking should occur only after the maximum load occurs (*i.e.* in post-failure). This is further evidenced by the close match between the failure load of the model and the failure load of the experimental samples (see Section 7.3).

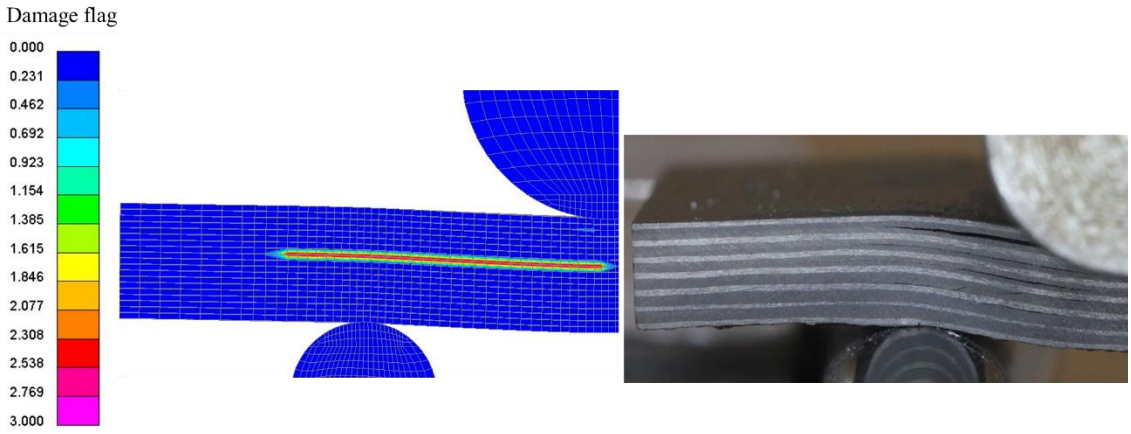

(a) pristine model **(b) experiment**

Figure 7-6. Comparison of the failure mode of the pristine model and experiment for angle ply lay-up. Note: in this case the damage parameter (shown in the legend) equal to 3 corresponds to the final failure.

7.3 Mesh sensitivity study

In order to validate the FE models, a mesh sensitivity study of the pristine models was undertaken for both the cross-ply and angle-ply laminates, using several mesh densities.

The mesh density was varied from a coarse mesh (with approximately 10,000 elements) to a fine mesh (with approximately 260,000 elements) (see Table 7-4, with the element size of all mesh formulations varying in the length-width plane of the specimen, such that the smallest elements are located at the edge of the samples and under the rollers.

Table 7-4. Mesh density variation

Model No	No of elements			Smallest element,	
	Total	Length	Width	l_{el}, mm	w_{el}, mm
1	10360	28	10	0.585	0.956
2	24864	48	14	0.310	0.650
3	51800	70	20	0.201	0.402
4	99900	90	30	0.143	0.238
5	153920	104	40	0.123	0.167
6	259000	140	50	0.076	0.106

Figure 7-7 shows that there is only a small effect of the number of elements on the failure load for both the cross-ply and angle-ply lay-ups for models with more than 50,000 elements. However, larger errors in the failure prediction develop for the cross-ply lay-ups when fewer elements are used. This is likely due in part to this coarse mesh having elements with large in-plane aspect ratios.

With regards to the failure load, it can be seen that the cross-ply lay-up slightly underpredicts the failure load, whilst the angle-ply lay-up is slightly overpredicted. The under/overprediction is perhaps due to the differing failure mechanisms of these lay-ups, although the suppressed matrix cracking parameters for the angle ply lay-up may also have caused the over-prediction of the failure load for this laminate. It is, however, worth noting that no influence of the mesh density on the overall failure behaviour was recorded.

As a result, in order to balance the requirements of accuracy and computational efficiency, a mesh having approximately 100,000 elements (90 elements in the length of the sample, 30 elements in the width dimension, and 1 element per ply in the through-thickness direction) was taken forward in this work to be analysed further. In this case, the errors between the models and the experiment tests were 7.4% for the cross-ply lay-up and 11% for the angle-ply lay-up.

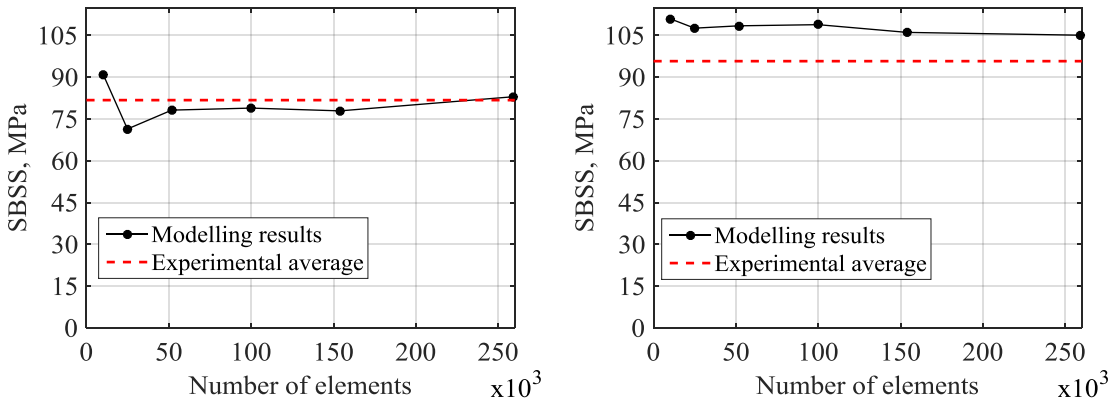

(a) Cross-ply **(b) Angle-ply**

Figure 7-7. Mesh refinement studies for (a) cross-ply laminates, (b) angle-ply laminates.

7.4 Parametric study of the material critical properties

To investigate the influence of different material properties on the SBSS of the samples, a parametric study was conducted in order to identify those material parameters that are most critical. To achieve this, selected material parameters were reduced by between 10% and 40% of the pristine values (*i.e.* those values given in Section 7.1). For each set of parameters, the SBSS of the model was calculated and compared to the SBSS value of the pristine model in order to obtain the percentage reduction of the SBSS. This reduction of the critical material parameter can then be correlated to the average void content by comparing the numerical results to the experimental data set.

In this chapter, the parametric study for each laminate system (*i.e.* the cross-ply laminate and the angle-ply laminate) are presented separately. This is due to the different failure behaviours observed for the different stacking sequences, which are expected to be influenced quite differently by each material parameter.

7.4.1 Results and discussion for cross-ply laminates

There are two material damage models that are expected to affect the failure behaviour of the cross-ply laminates – the transverse matrix cracking model and the delamination model. These two models are likely to affect the failure behaviour individually but may also show some combined influence on the short beam shear strength. In the subsequent sections, the parameters of these damage models will be investigated separately and then in combination.

7.4.1.1 Matrix crack model material parameters

The transverse matrix cracking model has several material properties that are likely to affect the SBSS (see Table 7-2). This model is based on a strength-based damage initiation criterion and fracture mechanics propagation criterion, and it is suspected that the strength and fracture toughness of the material will have some influence on the failure behaviour and the SBSS. In particular, it has been observed that the failure mode of the cross-ply samples during the experiments showed multiple cracks in the length-thickness plane at an angle of approximately 45° through-thickness (see Figure 7-4b), and so it is expected that the tensile and shear strength of the material model will have the greatest effect on the SBSS.

The dependence of the SBSS strength on the reduction of tensile strength and shear strength are shown in Figure 7-8. It can be observed that whilst the tensile strength has a negligible effect on the SBSS when reduced by less than 15%, further reduction of the tensile strength significantly affects the SBSS. In fact, a 40% reduction in the tensile strength causes a 32% reduction in the SBSS for this material system.

However, in contrast, there is a negligible effect on the SBSS when reducing the shear strength (Figure 7-8b).

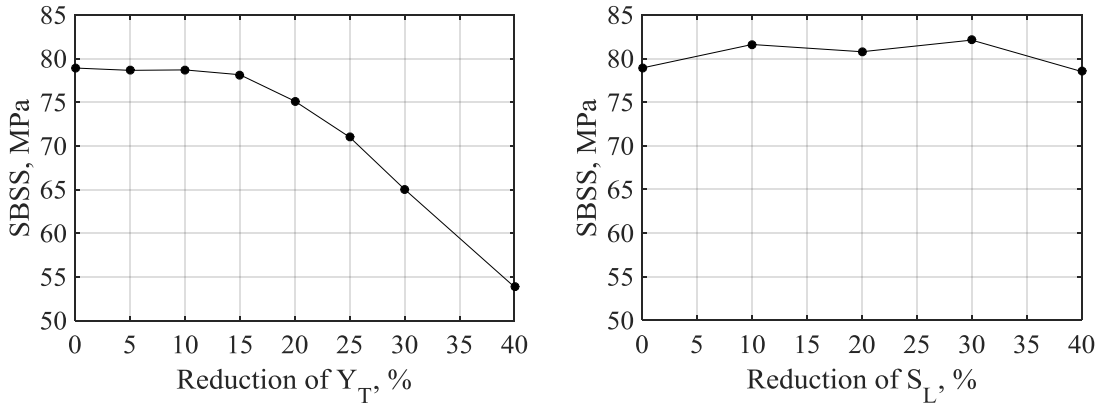

(a) **(b)**

Figure 7-8. Dependence of the SBSS reduction on the (a) percentage reduction of the tensile strength, Y_T; and (b) percentage reduction of the shear strength, S_L.

The dependence of the SBSS on the Mode I and Mode II fracture toughnesses can be seen in Figure 7-10. This shows that any reduction in the Mode I fracture toughness has a negligible effect on the SBSS (Figure 7-9a). In contrast, the reduction in SBSS when reducing the Mode II fracture toughness shows a linear dependence when the Mode II fracture toughness is reduced by more than 10%.

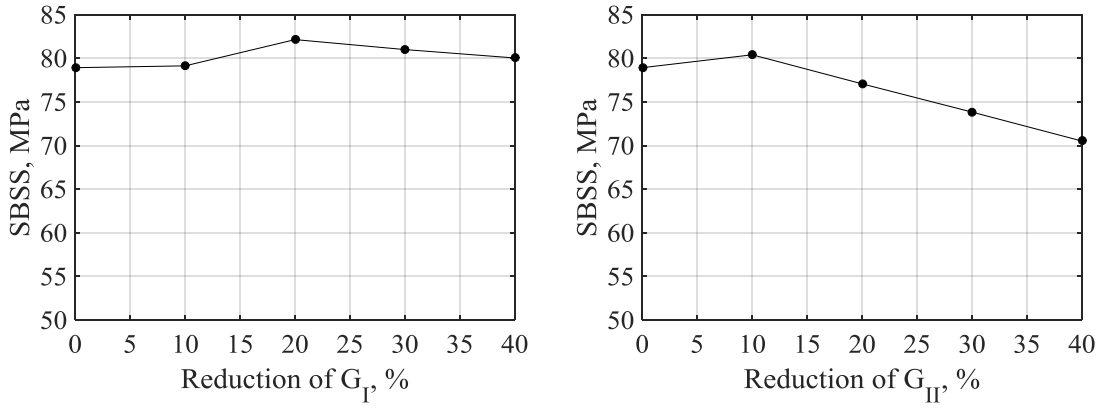

(a) **(b)**

Figure 7-9. Dependence of SBSS reduction on (a) percentage reduction of the Mode I fracture toughness, G_I; (b) percentage reduction of the Mode II fracture toughness, G_{II}.

Based on this parametric study, both the tensile strength and the fracture toughness were identified as the critical parameters in terms of their effect on the SBSS. The reduction in the SBSS of these two parameters is shown in Figure 7-10, which shows that a reduction of the tensile strength by 40% provided a 32% reduction in the SBSS. The Mode II fracture toughness influence the SBSS not as significantly as the tensile strength, however it is still possible to achieve an ~11% SBSS reduction by decreasing the Mode II fracture toughness, G_{II}, by 40%.

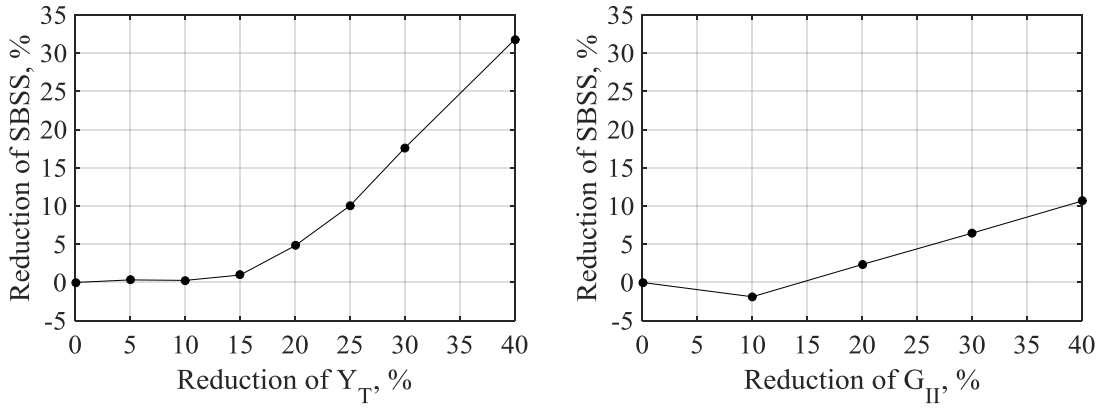

(a) **(b)**

Figure 7-10. Percentage reduction of SBSS vs (a) the percentage reduction of tensile strength, Y_T; (b) the percentage reduction of the Mode II fracture toughness, G_{II}.

However, it can be expected that when reducing both the tensile strength, Y_T and the Mode II fracture toughness, G_{II}, at the same time the reduction of the SBSS will be even greater. This is shown in Figure 7-11 and Table 7-5, which show the combined reduction of the tensile strength, Y_T, and the Mode II fracture toughness, G_{II}.

As expected, a larger reduction of the SBSS can be achieved by decreasing both parameters simultaneously. Even so, it is clear from Figure 7-11 that the tensile strength, Y_T, has a much more dominant effect on the SBSS. In fact, the dominance of this property suggests that this parameter could be used in isolation to 'replicate' the failure strength of cross-ply laminates containing voids.

Table 7-5. Percentage reduction of the SBSS due to the combined reduction of the tensile strength, Y_T, and the Mode II fracture toughness, G_{II}.

	Reduction of properties, %	Y_T 0	10	20	30	40
G_{II}	0	0.00	0.27	4.81	17.61	31.78
	10	-1.87	2.02	5.66	20.04	32.03
	20	2.35	6.59	11.56	19.07	30.69
	30	6.45	12.57	13.49	19.25	32.51
	40	10.65	12.81	14.32	21.80	33.82

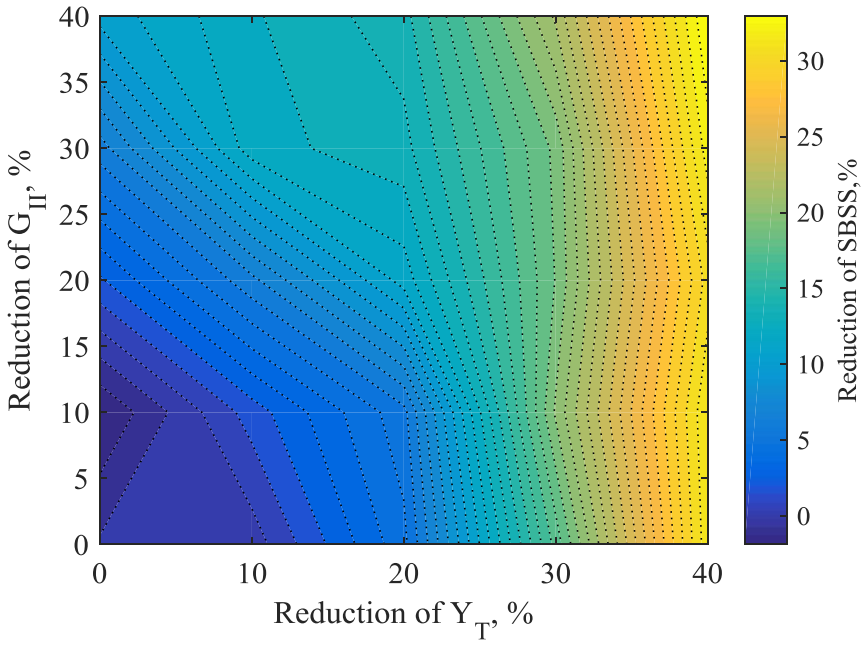

Figure 7-11. Contour plot, showing the reduction of SBSS when combining the reduction of tensile strength, Y_T, and Mode II fracture toughness, G_{II}.

7.4.1.2 Material properties of the delamination model

The failure of the cross-ply laminates also included delamination after the initial matrix cracking. Whilst delamination is primarily confined to the post-failure region (*i.e.* the failure regime after the failure strength is reached), it is possible that the reduction of the delamination model properties will also affect the failure strength. This model includes

two parameters that may have an effect upon the SBSS – the Mode II fracture toughness and the Mode II strength.

However, as shown in Figure 7-12, neither parameter has a significant effect upon the SBSS. Even when the Mode II strength is reduced by as much as 40% there is only a 3% reduction in the SBSS.

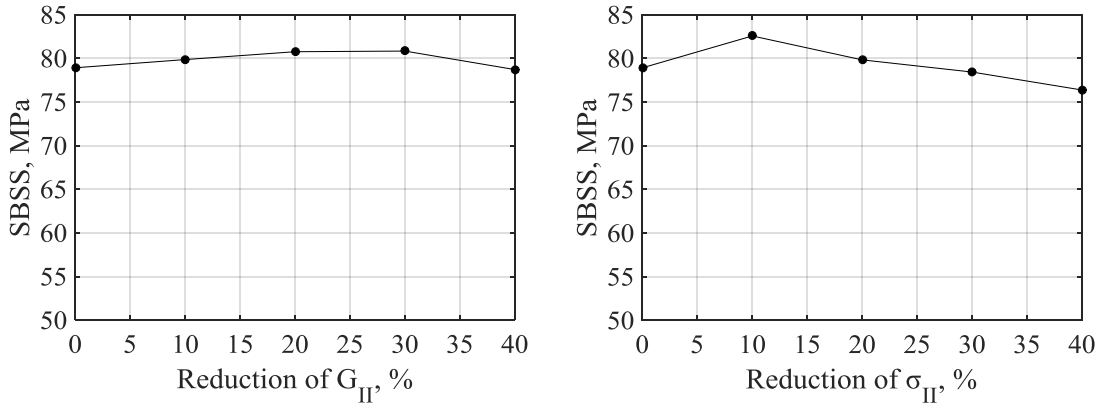

(a) **(b)**

Figure 7-12. Dependence of SBSS reduction on percentage reduction of the cohesive (a) mode II fracture toughness; (b) mode II strength.

In fact, even when analysing the combined effect of the four 'critical' parameters of the transverse matrix crack model and delamination model, the contribution of the delamination model is negligible when compared to the effect of the matrix cracking model (see Table 7-6).

It therefore appears clear that the delamination model does not have much of an effect on the SBSS, and also provides further evidence that the failure behaviour of cross-ply laminates is dominated by transverse matrix cracking.

Table 7-6.Reduction of the SBSS by reducing the critical parameters from the matrix crack and delamination models

	Matrix crack model		Delamination model		SBSS, MPa	Reduction of SBSS, %
	Reduction of					
	Y_T	G_{II}	σ_{II}	G_{II}		
Pristine	0	0	0	0	78.922	0
Reduced	30%	20%	0%	0%	63.871	19.07
	30%	20%	20%	20%	63.864	19.08

7.4.1.3 Estimating the effect of voids based on a single 'critical' parameter for cross-ply laminates

As has been shown, only the tensile strength and the fracture toughness have any significant effect upon the SBSS. However, the tensile strength is clearly the most dominant factor in determining the SBSS. This suggests that it is possible to simplify the variables in this model and vary only the tensile strength in order to replicate the effect of the average void content on the SBSS.

As is evident from Figure 7-13, there is no linear correlation between the reduction of the tensile strength and the average void content. However, there is a relationship between the tensile strength and SBSS, such that a reduction in the tensile strength can be correlated to the reduction in SBSS of an equivalent average void content. For instance, an average void content of 4% provides a 20% reduction in the SBSS (Figure 7-13a), and it is known that a 20% reduction in the SBSS can be modelled by a 32% reduction in the tensile strength of the model (Figure 7-13b).

The relationship between the reduction of tensile strength and SBSS of the model can be described well by a polynomial equation (See the red line in Figure 7-13b). Due to the complex polynomial form of this relationship, there is no unique value of the tensile reduction for a given average void content. As a result, a simplified bi-linear relationship is also shown in Figure 7-13b. This equation is given by:

$$\boldsymbol{Reduction\ of\ SBS\ strength}\ (\%), \quad \boldsymbol{f(x)} = \begin{cases} \mathbf{0} & \textbf{for } \boldsymbol{x < 17} \\ \mathbf{1.37x - 23.3} & \textbf{for } \boldsymbol{x \geq 17} \end{cases} \quad \textbf{(7-13)}$$

where x the reduction of tensile strength (%).

The relationship between the average void content of a sample and the reduction of the tensile strength of the model is therefore given by:

$$\boldsymbol{Reduction\ in\ tensile\ strength}\ (\%), \quad \boldsymbol{Y_T(V_v) = 3.58V_v + 17} \quad \textbf{(7-14)}$$

where V_v is the average void content of a sample.

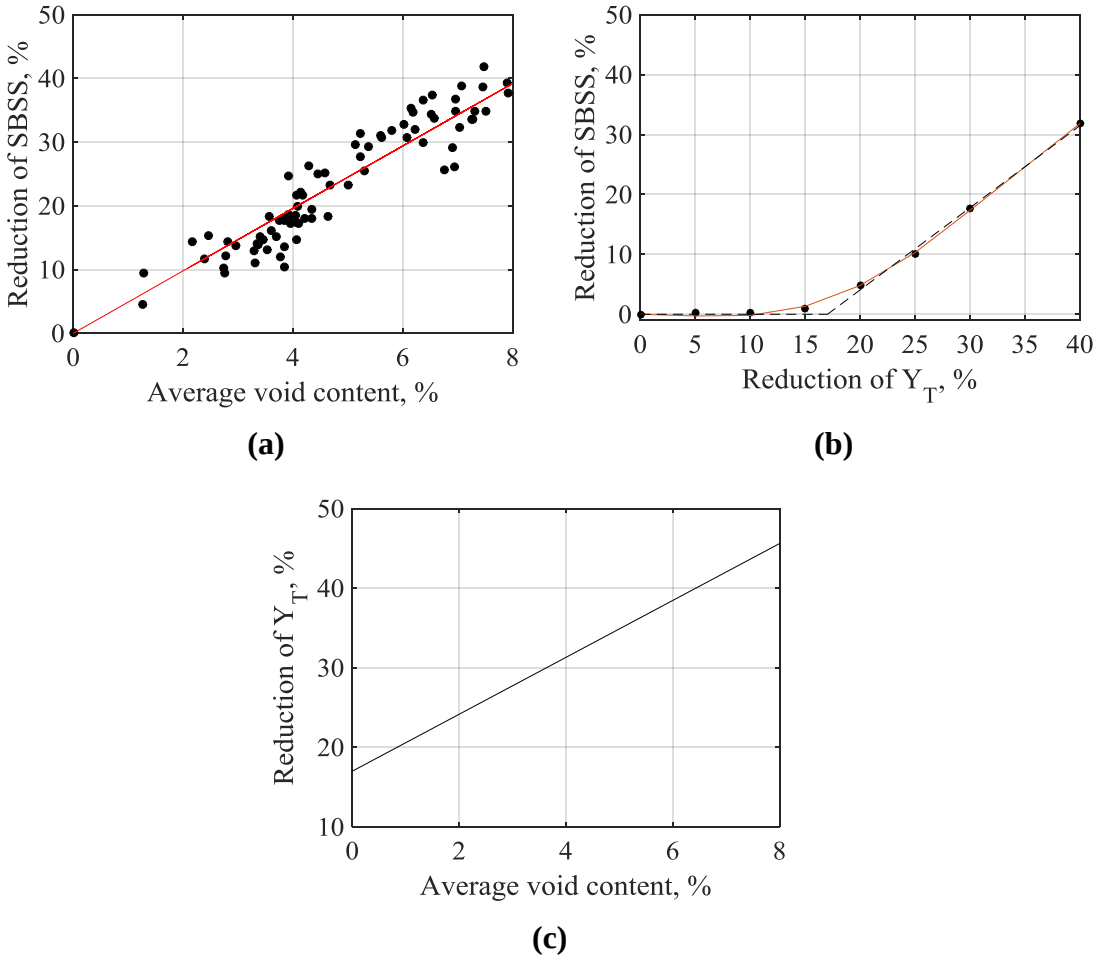

Figure 7-13. (a) The percentage reduction of SBSS with increase of the average void content based on the experimental results for cross-ply laminates; (b) the percentage reduction of SBSS *vs.* percentage reduction of Y_T ,(c) percentage reduction of Y_T reduction *vs.* average void content. Note: the red lines on the graphs correspond to a best fit line of the data. The black dotted line in (b) corresponds to a simplified bi-linear fitting.

7.4.2 Results and discussion for angle-ply laminates

The experimental SBS testing program on the IM7/8552 angle-ply laminates showed that these samples failed via delamination. Hence, it can be expected that any reduction of the material properties of the delamination model will have a significant affect upon the SBSS. Due to the test setup, *i.e.* a short beam shear (SBS) testing arrangement, the most influenced parameters will be the cohesive Mode II fracture toughness, G_{II}, and the Mode II strength, σ_{II}. However, for the sake of completeness, the effects of reducing the Mode I properties are also investigated.

As expected, a reduction of the Mode II fracture toughness, G_{II}, and Mode II strength, σ_{II}, causes a reduction in the SBS strength (See Figure 7-14). In particular, it is shown that the Mode II strength, $\sigma_{II,}$ has the most significant effect on the SBSS. In fact, by

reducing the Mode II strength, σ_{II}, by 40% it is possible to achieve a ~28% SBSS reduction, whilst reducing the fracture toughness, G_{II}, by the same amount provides only an ~11% reduction in the SBSS (see Figure 7-15).

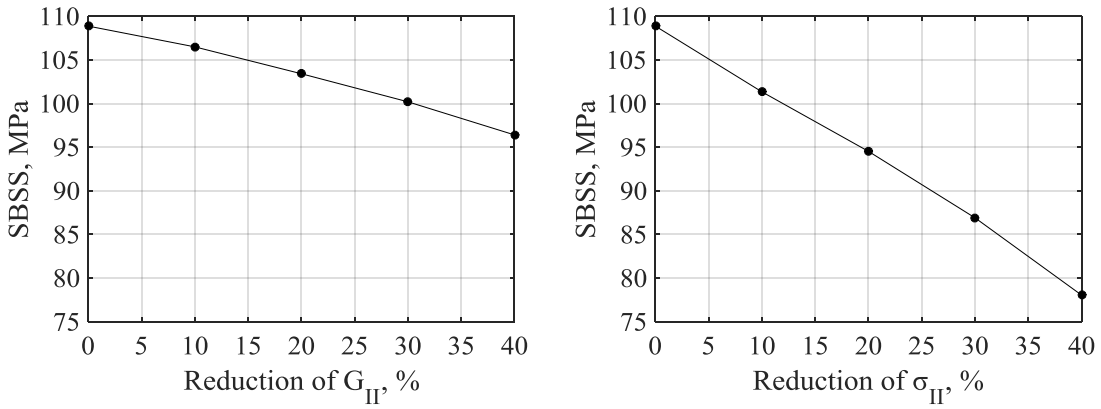

(a) **(b)**

Figure 7-14. Dependence of SBSS reduction on cohesive mode II (a) fracture toughness, G_{II}; (b) strength, σ_{II}.

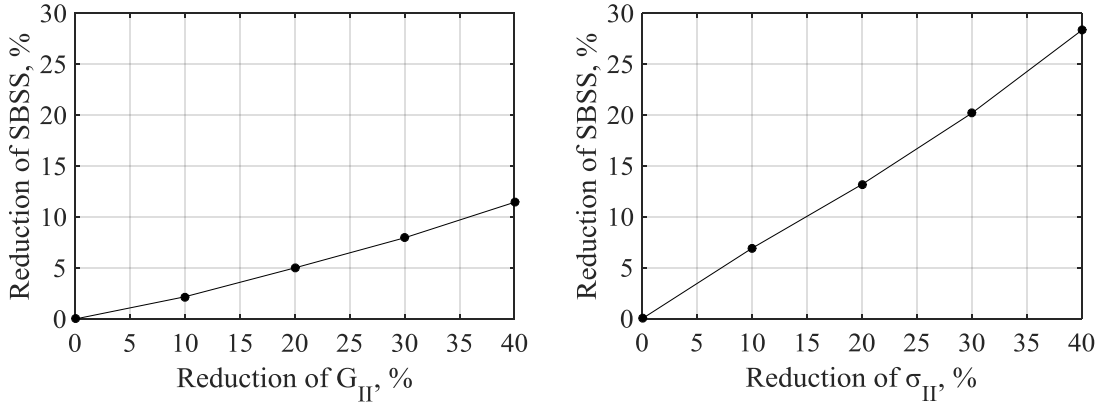

(a) **(b)**

Figure 7-15. Percentage reduction of SBSS *vs.* cohesive mode II (a) fracture toughness, G_{II}; (b) strength, σ_{II}.

Predictably, no effect is observed when varying the cohesive Mode I fracture toughness, G_I, and Mode I strength, σ_I (see Figure 7-16).

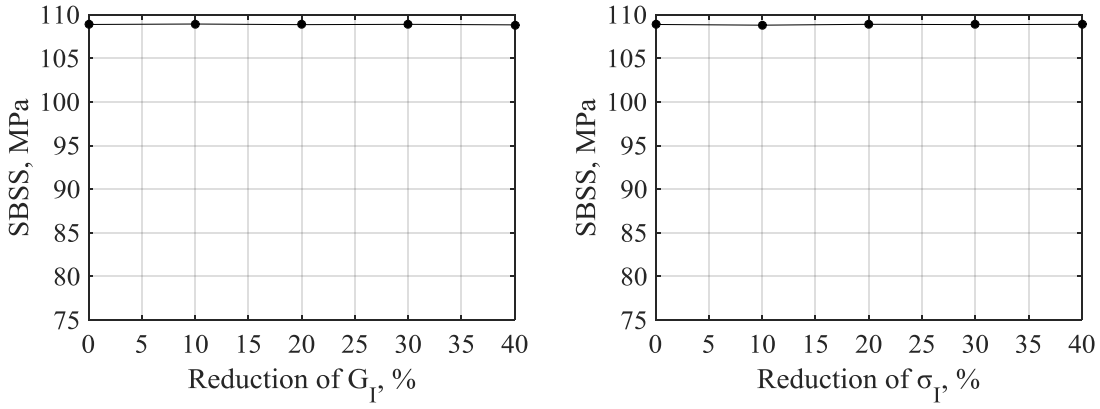

(a) **(b)**

Figure 7-16. Dependence of SBSS reduction on the percentage reduction of cohesive Mode I (a) fracture toughness G_I; and (b) strength, σ_I.

Similar to the cross-ply laminate, it was possible to identify two critical parameters that influence the failure load and SBSS. For the angle ply, these are the cohesive Mode II fracture toughness, G_{II}, and Mode II strength, σ_{II}. And, in fact, the combination of these two parameters can lead to an even greater reduction of the SBSS, as shown in Figure 7-17 and Table 7-7. In this case, the maximum reduction of the SBSS is approximately 35% when reducing both critical parameters by 40%. This contrasts with the ~11% reduction obtained when reducing only the Mode II fracture toughness and the ~28% reduction obtained when reducing just the Mode II strength.

Even so, it is clear from Figure 7-17 that the cohesive Mode II strength, σ_{II}, has a much more dominant effect on the SBSS. In fact, the dominance of this property suggests that this parameter could be used in isolation to 'replicate' the failure strength of cross-ply laminated containing voids in the same manner for the cross-ply laminates, as discussed in Section 7.4.1.3.

Table 7-7. Reduction of SBSS as function of combined reduction of σ_{II} and G_{II}

	Reduction of properties, %	σ_{II}				
		0	10	20	30	40
G_{II}	0	0	6.92	13.18	20.18	28.32
	10	2.18	8.98	15.53	21.79	29.41
	20	5.01	11.81	18.12	23.99	30.96
	30	7.97	14.70	21.00	26.58	32.73
	40	11.45	17.75	24.08	29.98	35.23

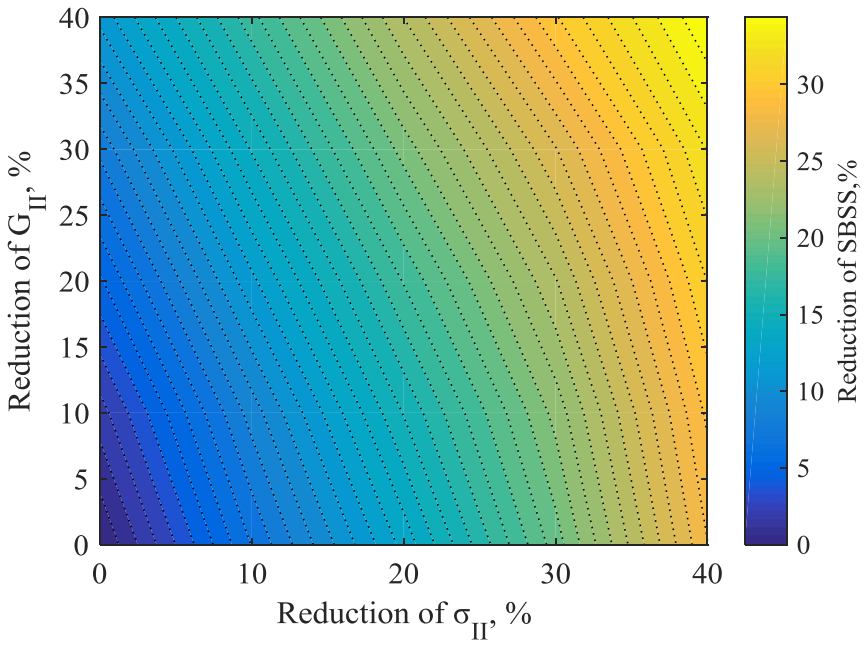

Figure 7-17. Contour plot, showing the reduction of SBSS when combining the reduction of cohesive Mode II fracture toughness, σ_{II}, and strength, G_{II}.

7.4.2.1 Estimating the effect of voids based on a single 'critical' parameter for angle-ply laminates

In the previous section it was shown that the cohesive Mode II strength and Mode II fracture toughness both have a significant effect upon the SBSS. Although, it was also shown that the cohesive Mode II strength, σ_{II}, is clearly the most dominant factor in determining the SBSS.

This suggests that it is possible to simplify the variables in this model and vary only the Mode II strength in order to replicate the effect of the average void content on the SBSS of angle-ply laminates.

From Figure 7-18, it is evident that there is a linear correlation between the reduction of the cohesive Mode II strength and the average void content of the samples. This makes it easy to calculate the reduction in the Mode II strength required to replicate the effect of an equivalent void content. For example, to model the effect of the sample with 2 % void content, the cohesive Mode II strength can be reduced by 25%.

And in fact, the relationship between the reduction of cohesive strength and SBSS of the model can be described nicely by a linear equation (See the red line in Figure 7-18b)

$$\boldsymbol{f(x) = ax} \qquad \textbf{(7-15)}$$

for this particular material system (IM7/8552), the coefficient is: $a = 0.6903$.

The relationship between the average void content of a sample and the reduction of the cohesive strength of the model can therefore be described by a polynomial equation of the same form:

$$\textbf{\textit{Reduction in cohesive strength}}\ (\%), \qquad Y_T(V_v) = 13.26V_v \qquad \textbf{(7-16)}$$

where V_v is the average void content of a sample.

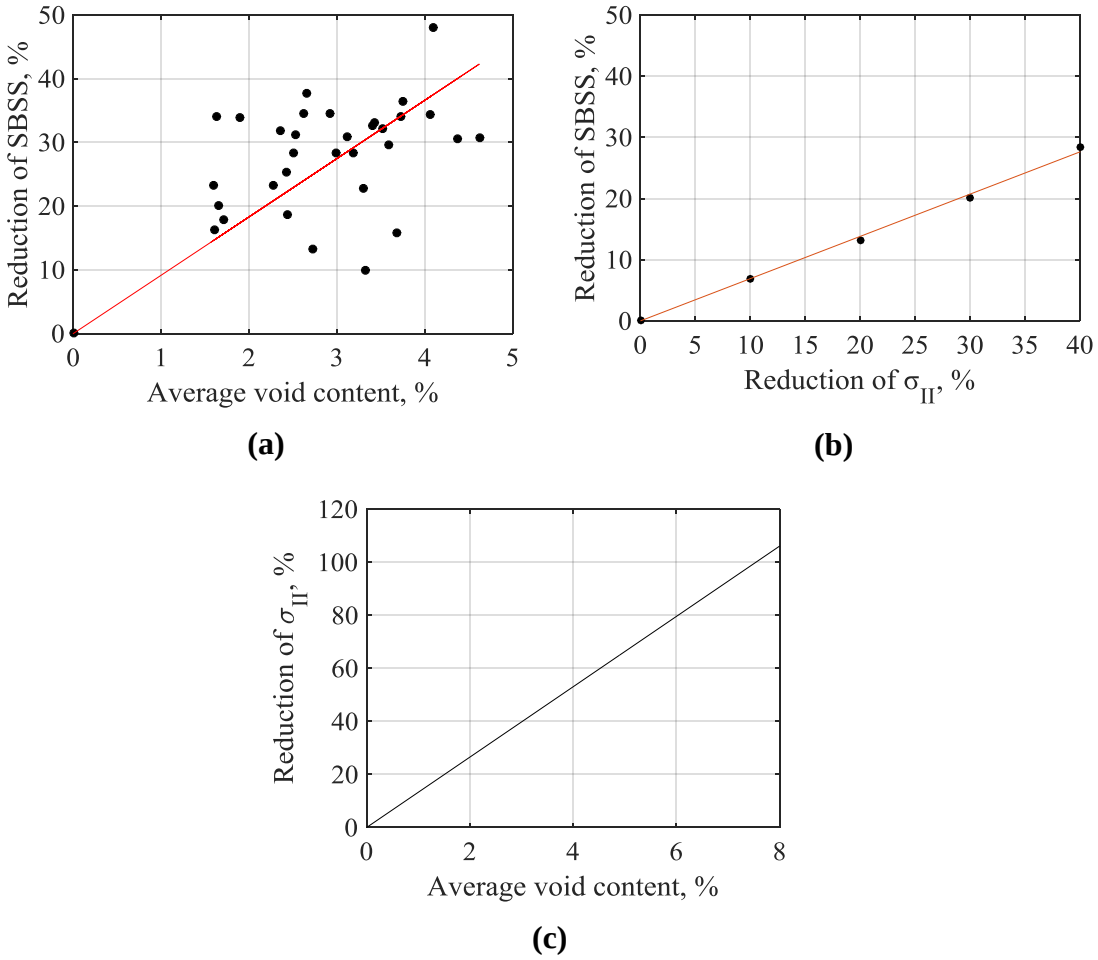

Figure 7-18. (a) The percentage reduction of SBSS with increase of the average void content based on the experimental results for angle-ply laminates; (b) the percentage reduction of SBSS *vs.* percentage reduction of cohesive Mode II strength, σ_{II},; (c) percentage reduction of cohesive Mode II strength, σ_{II}, *vs.* average void content. Note: the red lines on the graphs correspond to a best fit line of the data.

7.5 Concluding remarks

In this chapter, a simplified FE model has been developed in order to simulate the effect of voids on the SBSS. The intention behind this work was to provide industry with a simple tool that allows the reduction in mechanical properties to be predicted with simple ply-level FE model and knowledge of the average void content of the sample (*i.e.* provide a knock-down factor).

To achieve this, a parametric investigation was conducted on the SBS FE model for cross-ply and angle ply samples. To model the behaviour of these lay-ups, different material damage models were implemented, such as a transverse matrix cracking model and a delamination model. In addition, non-linear shear and thermal residual stresses were also introduced. It was also shown that to correctly model the behaviour of the angle-ply samples, the matrix crack material models needed to be supressed due to the smeared crack approach implemented in the current damage model. In future, this model could be improved by introducing a formulation for discrete matrix cracks.

For this parametric study, selected properties of the material damage models were reduced and the resultant reduction in the SBSS calculated. In this way the critical parameters, in terms of their effect on the SBSS, were identified. For the cross-ply laminates, it was shown that the most critical parameters were the tensile strength and Mode II fracture toughness of the transverse matrix crack model, whilst the delamination model didn't provide any significant effect on the failure behaviour due to delamination typically occurring after the maximum load is reached for this material system. By reducing the tensile strength and Mode II fracture toughness at the same time it was possible to achieve the highest reduction of SBSS – 34% – although this reduction is predominantly due to the reduction in the tensile strength. Using the information from the parametric study, it is possible to describe a simple polynomial relationship between the tensile strength and the reduction in the SBSS, which can then be correlated to an equivalent average void content of an experimental sample.

Similarly, the parametric study for angle-ply samples also showed that the critical parameters were the Mode II fracture toughness and tensile strength, although in this case these properties were from the delamination model rather than the matrix cracking model.

Whilst for the angle-ply laminate the two 'critical' parameters each had a pronounced effect on the SBSS, it was found that the cohesive Mode II cohesive strength has the greater effect on the SBSS. In fact, the relationship between the Mode II strength and the SBSS can be described by a linear equation. Using this equation, it is possible to estimate the reduction of the SBSS from the reduced cohesive strength, and thereby correlate this SBSS to an equivalent average void content of an experimental sample.

8 CONCLUSIONS

8.1 Original contributions

The main goal of this study has been to understand the effect of void features on the strength of composite materials, and to identify the void characteristics most influential in affecting the failure of composites. The interlaminar strength of composite materials is known to be highly affected by the presence of voids. Furthermore, the short beam shear (SBS) test was selected as it is a quick mechanical test that uses small samples, such that a large set of experimental data could be generated. The small SBS samples were also conveniently sized for CT-scanning, providing a good image resolution.

To achieve this goal, a number of technical challenges have had to be overcome, as set in Chapter 1 'Introduction'.

The author's main contributions will be summarized separately accordingly to the thesis chapters.

In order to assess existing thresholding methods used in the post-processing of X-ray CT scans of composites with voids, a parametric study of these thresholds was conducted and presented in Chapter 3.

- A simple model was developed to simulate the CT-response to porosity, which made it possible to know the 'true' value of the void volume fraction and thus the size of the voids.
- For the first time, it has been confirmed that, with knowledge of the 'true' value of the void volume fraction, the '50% thresholding method' (a common CT-segmentation thresholding method) is more accurate than other commonly used thresholding methods in all but a few situations.
- Application of the 50% threshold on unidirectional carbon/epoxy samples, containing porosity, demonstrated excellent correlation to the microscopic measurements, both qualitatively and quantitatively.
- A new adaptive threshold was introduced that is the first known thresholding method able to provide an optimal solution in the full range of commonly encountered grey level histograms. In particular, the method is able to outperform

the 50% thresholding method in the presence of a high level of scattering noise and/or a low grey value of the resin peak. In these cases, the threshold needs to be set to a lower value in order to reduce the overestimation of porosity due to resin voxels masquerading as pores because they are below the 50% threshold. This algorithm has been demonstrated using simulations to have significantly improved porosity measurement capabilities and reduced bias in the measurements.

In order to investigate the effect of voids on mechanical properties it is important to manufacture specimens in a controlled manner with a range of void contents. This is investigated in Chapter 4.

- A novel temperature- and pressure-controlled out-of-autoclave method was introduced to manufacture panels containing voids. Although it wasn't possible to achieve samples with a completely uniform void distribution, it was possible to obtain samples with a range of void contents for two different material systems, by varying process parameters.
- Different process parameters were required for different material systems (IM7/8552 and IMA/M21) and different lay-ups. It was found that the compaction pressure was the critical parameter for all the chosen materials and lay-ups.
- μCT-scanning of the samples has shown different morphology of the intra-ply voids (voids that are located within the plies) and the inter-ply voids (voids that are located in the interface between plies). Intra-ply voids are elongated in the direction of the fibres and are mostly unaffected by the particular material system and laminate lay-up. The inter-ply voids dependent strongly on the particular material system and laminate lay-up. For IMA/M21 cross-ply they appear to be circular (coin-like shape), whilst for IM7/8552 cross-ply these voids are needle-like shaped and follow the fibre direction of the one of the adjacent plies. The shape of the interply voids observed for IM7/8552 angle-ply samples differs greatly due to the orientations of the adjacent plies, as they are elongated in a curved shape that combines the path of both angled plies at the interface. To the knowledge of the author, this is the first time this phenomenon has been observed; possibly due to the previous use of 2D microscopy to analysis voids in samples.

The short beam shear test was chosen to in order to investigate the effect of the void features on laminate strength and carried out on the samples with porosity. Statistical

analysis of the experimental results is shown in Chapter 5. Different void features were analysed, and the main conclusions are as follows:

- An extensive experimental dataset has been obtained that contains 3-dimensional information of every single void in the samples. This leads to a new understanding of how the characteristics of individual voids, and the interaction of multiple voids, affect the strength of composite materials.
- The number of voids in a specimen is not a good parameter for estimating the SBS strength due to the different sizes of the voids in each sample.
- Using the maximum dimension of the largest void, the volume of the single largest void, or the 'critical ply' where most of the voids in a sample are located, has also been difficult to relate to the SBS strength. This is particularly the case for samples of IM7/8552 at larger average voids contents, at which the voids are not confined to a single ply but instead form a network of voids that bridge between the plies.
- It has been found for the first time that there is a 'critical defect size' of the voids, below which the voids do not contribute to failure and can therefore be neglected. A simple estimation of this 'critical void size' can be made using a linear elastic fracture mechanics equation, although it should be noted that this method is oversimplified as it assumes an isotropic homogeneous material subjected to pure mode II shear.
- A novel comparative analysis of samples with the same void content but different strength level was undertaken. This analysis showed that in most pairs of samples, neglecting voids smaller than the 'critical void size' explained the discrepancies between the SBSS values of the two samples in each pair. In those pairs whose respective values of SBSS could not be explained by applying the 'critical void size', the result could be explained by the presence of one large void in the critical region (where the stresses are highest) or by the close proximity of a few of the largest voids in this critical region.

It is important for industry to be able to predict the strength of composite materials containing voids without undertaking extensive testing programs. In Chapter 6, an analytical prediction of the short beam shear strength is compared with experimental results. The prediction of the SBS strength is based on an assumption that the SBS strength is caused by a reduction of the cross-sectional area in a 'critical plane'.

- For the first time, a full dataset is now available for direct calculation of the reduced cross-sectional area from the CT scans provided by VG Studio Max. The data extraction is however laborious and ultimately was unable to provide a satisfactory prediction of the SBS strength.
- Estimating the reduced cross-sectional area by assuming that each void has a constant cross-section in the thickness direction and totalling the cross-section of each void that crosses a particular plane, doesn't provide a better prediction for any of the investigated material systems and lay-ups, due to majority of the voids being complex interconnected void networks.
- Estimating the reduced cross-sectional area based on the projected area of the voids (when viewed in the length-width plane) provided a good estimation of the SBS strength for IM7/8552 cross-ply samples. However, the estimation didn't work well for IM7/8552 angle-ply samples and IMA/M21 cross-ply samples due to the different morphology of the voids.
- Improvements were made to the strength prediction for IMA/M21 cross-ply samples by totalling the projected area of all voids centred within a thin 3D slice. An optimal slice thickness of 0.0475mm was found, which is approximately the size of the inter-ply resin layer where the majority of the voids are located.
- The inter-ply resin layer in the IMA/M21 samples was shown to increase in thickness with increases in the average void content, and could be estimated using an average of the thickness of all voids in a sample. Applying a different resin layer thickness for each sample resulted in improvements in the estimated SBS strength.
- The prediction of the SBSS was more challenging for the IM7/8552 angle-ply samples due to the complex shape of the voids. However, satisfactory results were obtained by taking into account voids that are centred within a slice thickness of 0.095 mm. It is not possible to visualise the resin layer thickness in this material system, so no improvement of the prediction could be obtained by relating the slice thickness to the average thickness of the voids.

One of the objectives of this work was to provide industry with a tool that allows the reduction in mechanical properties as a function of void content to be predicted. To this end, a ply-level FE model was developed and presented in Chapter 7.

- A parametric investigation was conducted on the SBS FE model for cross-ply and angle ply samples. To model the behaviour of these lay-ups, different material

damage models were implemented. In this model, specific material properties were reduced and then correlated to the average void content of the samples.

- It was shown for cross-ply laminates that it is possible to define a simple polynomial relationship between the matrix tensile strength (which was found to have the most dominant effect on strength reduction) and the reduction in the SBSS, which can then be correlated to an equivalent average void content of an experimental sample.
- For angle ply laminates, the interlaminar Mode II strength was found to be the most critical material property. The relationship between the Mode II strength and the SBSS can be described by a linear equation. Using this equation, it is possible to estimate the reduction of the SBSS from the reduced cohesive strength, and thereby correlate this SBSS to an equivalent average void content of an experimental sample.

8.2 Further Work

This thesis has demonstrated the importance of using particular void features to correlate to the failure strength and predict the failure strength of composite materials. However, the subject is vast and a number of key challenges, described below, have been identified for the journey ahead.

Improvement of the CT simulator

In the current CT simulator, the voids were modelled as spheres. However, during this research it has been shown that the void shapes are different, based on their location, and the particular material systems and lay-ups of the samples. It would therefore be of further benefit to use the developed model to investigate irregular shaped voids and to verify the applicability of the thresholding methods.

Improvement to the manufacturing method

The developed out-of-autoclave manufacturing technique has shown its capability to produce samples with a range of void contents, as well as provide samples having voids with varying shapes and sizes that depend on the process parameters used during the manufacture. However, it would be beneficial to further develop the manufacturing techniques to allow more control of the void shapes and sizes, and size distributions, as this would allow their effects to be investigated more thoroughly.

The effects of the composite lay-up

It has been shown that the lay-up of a composite has a significant effect. Specifically, it has been shown that cross-ply and angle-ply laminates have very different void shapes, and that the failure behaviour is very different. A more thorough investigation of the effect of composite lay-up sequences would be of great benefit to the scientific community, particularly as the design freedom of composite stacking sequences is a great advantage of composites.

An investigation of other matrix-dominated properties

As the literature review revealed, there is very little investigation on the effect of voids on other properties, such as Mode I and Mode II interlaminar fracture toughness. This is perhaps due to the complexity of failure mechanisms, which has resulted in a lot of scatter in the available literature results. However, in-situ CT-scanning is becoming a more common technique and would provide an ideal tool to further investigate the exact failure mechanisms of composites containing voids. Particularly as it may reveal the precise path of the cracks as they propagate between voids.

An investigation of curved geometries

The current work has focussed on the effects of voids on flat panels. However, in practice, composite parts typically contain many corners, angles, and ply-drops. These complex geometrical features are likely to introduce different distributions of voids, as well as different void shapes. The result is that these porous parts are likely to behave somewhat differently to flat panels.

Development of the FE model to include discrete matrix cracks

In this work the matrix crack material model used was a smeared continuum damage formulation. This had to be suppressed in order to correctly model the failure behaviour of the angle-ply samples. This was due to the smeared crack approach implemented in the damage model which resulted in too wide spread damage. It is expected that the model could be improved by introducing a formulation for discrete matrix cracks.

Development of the FE model to consider non-uniform void distribution

The FE model that has been developed includes a knock-down factor that diminishes the properties across the entire sample. However, in real panels, there will be some degree of non-uniformity in the distribution of the voids. This non-uniformity can be implemented in the model, such that an improved knock-down criterion can be developed that better represents the void distribution of ‘real’ parts.

9 REFERENCES

[1] R. Talreja, "Manufacturing defects in composites and their effect on performance," in *Polymer Composites in the Aerospace Industry*, P. E. Irving and C. Soutis, Eds. Woodhead Publishing, 2015, pp. 99–116.

[2] S. Mukhopadhyay, M. I. Jones, and S. R. Hallett, "Tensile failure of laminates containing an embedded wrinkle; numerical and experimental study," *Compos. Part A Appl. Sci. Manuf.*, vol. 77, pp. 219–228, 2015.

[3] H. Zhu, B. Wu, D. Li, D. Zhang, and Y. Chen, "Influence of Voids on the Tensile Performance of Carbon/epoxy Fabric Laminates," *J. Mater. Sci. Technol.*, vol. 27, no. 1, pp. 69–73, Jan. 2011.

[4] X. Liu and F. Chen, "A review of void formation and its effects on the mechanical performance of carbon fiber reinforced plastic," *Eng. Trans.*, vol. 64, no. 1, pp. 33–51, 2016.

[5] F. C. Campbell, A. R. Mallow, and C. E. Browning, "Porosity in carbon fiber composites an overview of causes," *Journal of Advanced Materials*, vol. 26, no. 4. pp. 18–33, 1995.

[6] F. Y. C. Boey and S. . Lye, "Void reduction in autoclave processing of thermoset composites," *Composites*, vol. 23, no. 4, pp. 261–265, 1992.

[7] L. K. Grunenfelder and S. R. Nutt, "Void formation in composite prepregs – Effect of dissolved moisture," *Compos. Sci. Technol.*, vol. 70, no. 16, pp. 2304–2309, Dec. 2010.

[8] J. P. Anderson and M. C. Altan, "Formation of voids in composite laminates: Coupled effect of moisture content and processing pressure," *Polym. Compos.*, vol. 36, no. 2, pp. 376–384, Feb. 2015.

[9] J. L. Kardos, M. P. Dudukovic, and R. Dave, "Void growth and resin transport during processing of thermosetting - Matrix composites," *Adv. Polym. Sci.*, vol. 78, no. January 2016, 1986.

[10] R. Olivier, J. P. Cottu, and B. Ferret, “Effects of cure cycle pressure and voids on some mechanical properties of carbon / epoxy laminates,” *Composites*, vol. 26, no. 7, pp. 509–515, 1995.

[11] L. Liu, B.-M. Zhang, D.-F. Wang, and Z.-J. Wu, “Effects of cure cycles on void content and mechanical properties of composite laminates,” *Compos. Struct.*, vol. 73, no. 3, pp. 303–309, Jun. 2006.

[12] S. Hernández, F. Sket, J. M. Molina-Aldareguí a, C. González, and J. LLorca, “Effect of curing cycle on void distribution and interlaminar shear strength in polymer-matrix composites,” *Compos. Sci. Technol.*, vol. 71, no. 10, pp. 1331–1341, 2011.

[13] S. L. Agius, K. J. C. Magniez, and B. L. Fox, “Cure behaviour and void development within rapidly cured out-of-autoclave composites,” *Compos. Part B Eng.*, vol. 47, pp. 230–237, Apr. 2013.

[14] S. Hernández, F. Sket, C. González, and J. Llorca, “Optimization of curing cycle in carbon fiber-reinforced laminates: Void distribution and mechanical properties,” *Compos. Sci. Technol.*, vol. 85, pp. 73–82, 2013.

[15] J. F. Harper, N. A. Miller, and S. C. Yap, “Influence of temperature and pressure during the curing of prepreg carbon fiber epoxy resin,” *Polym. - Plast. Technol. Eng.*, vol. 32, no. 4, pp. 269–275, 1993.

[16] B. Thorfinnson and T. Biermann, “Production of void free composite parts without debulking,” in *Proc 31st int SAMPE symp. Las Vegas, NV: Society for the Advancement of Material and Process Engineering*, 1986, p. 10.

[17] T. Centea, L. K. Grunenfelder, and S. R. Nutt, “A review of out-of-autoclave prepregs - Material properties, process phenomena, and manufacturing considerations,” *Compos. Part A Appl. Sci. Manuf.*, vol. 70, pp. 132–154, 2015.

[18] T. S. Lundström, “Measurement of void collapse during resin transfer moulding,” *Compos. Part A Appl. Sci. Manuf.*, vol. 28, no. 3, pp. 201–214, 1997.

[19] L. Grunenfelder and S. Nutt, “Air removal in VBO prepreg laminates: effects of breathe-out distance and direction,” in *Proc 43rd int SAMPE tech conference, Fortworth, Texas, Society for the Advancement of Material and Process Engineering*, 2011.

[20] T. Centea and P. Hubert, “Out-of-autoclave prepreg consolidation under deficient pressure conditions,” *J. Compos. Mater.*, vol. 48, no. 16, pp. 2033–2045, 2014.

[21] T. Centea, M. Preau, and P. Hubert, “Effect of Layup and Ply Morphology on Void Formation in Out-of-Autoclave Prepregs,” *19th Int. Conf. Compos. Mater.*, pp. 3685–3693, 2013.

[22] Y. Ma, T. Centea, G. Nilakantan, and S. R. Nutt, “Vacuum Bag Only Processing of Complex Shapes: Effect of Corner Angle, Material Properties and Process Conditions,” *Proc. 29th Tech. Conf. Am. Soc. Compos. US-Japan Conf. Compos. Mater. D-30 Meet.*, pp. 2–17, 2014.

[23] S. M. Hughes and P. Hubert, “Out-of-Autoclave Prepreg Processing : Effect of Integrated Geometric Features on Part Quality,” *Sampe 2013*, no. June, pp. 42–56, 2013.

[24] M. R. Wisnom, T. Reynolds, and N. Gwilliam, “Reduction in Interlaminar Shear Strength by Discrete and Distributed Voids,” *Compos. Sci. Technol.*, vol. 3538, no. 96, pp. 93–101, 1996.

[25] D. E. W. Stone and B. Clarke, “Ultrasonic attenuation as a measure of void content in carbon-fibre reinforced plastics,” *Non-destructive Test.*, no. June, pp. 137–145, 1975.

[26] B. G. Martin, “Ultrasonic attenuation due to voids in fibre-reinforced plastics,” *NDT Int.*, pp. 242–246, 1976.

[27] E. A. Birt and R. A. Smith, “A review of NDE methods for porosity measurement in fibre- reinforced polymer composites,” *J. Br. Insitute NDT*, vol. 46, no. 11, pp. 681–686, 2004.

[28] N. Dominguez, “Method and device for the ultrasonic non-destructive checking of the porosity of a part made of composite material,” WO 2009/130140 A1, 2009.

[29] R. A. Smith, “Use of 3D ultrasound data sets to map the localised properties of fibre-reinforced composites,” PhD thesis, University of Nottingham, 2010.

[30] I. A. Veres, R. A. Smith, and V. J. Pinfield, “Comparison of Numerical and Effective- Medium Modeling of Porosity in Layered Media,” vol. 62, no. 6, pp. 1086–1094, 2015.

[31] R. Tayong Boumba, R. A. Smith, and V. J. Pinfield, “Acoustic Characterization of Void Distributions Across Carbon-Fiber Composite Layers,” in *Review of Quantitative NDE*, 2015.

[32] S. Gray, S. Ganchev, N. Qaddoumi, G. Beaurwgard, D. Radford, and R. Zoughi, “Porosity Level Estimation in Polymer Composites using Microwavws,” *Mater. Eval.*, vol. 53, no. 3, pp. 404–408, 1994.

[33] M. P. Connolly, “The measurement of porosity in composite materials using infrared thermography,” *J. Reinf. Plast. Compos.*, vol. 11, pp. 1367–1375, 1992.

[34] A. Ciliberto, G. Cavaccini, O. Salvetti, M. Chimenti, L. Azzarelli, P. . Bison, S. Marinetti, A. Freda, and E. Grinzato, “Porosity detection in composite aeronautical structures,” *Infrared Phys. Technol.*, vol. 43, no. 3–5, pp. 139–143, Jun. 2002.

[35] M. H. Hassan, A. R. Othman, and S. Kamaruddin, “Void Content Determination of Fiber Reinforced Polymers by Acid Digestion Method,” in *Advanced Materials Research*, 2013, vol. 795, no. September, pp. 64–68.

[36] Z.-S. Guo, L. Liu, B.-M. Zhang, and S. Du, “Critical Void Content for Thermoset Composite Laminates,” *J. Compos. Mater.*, vol. 43, no. 17, pp. 1775–1790, May 2009.

[37] S. Paciornik and J. R. M. D’almeida, “Measurement of void content and distribution in composite materials through digital microscopy,” *J. Compos. Mater.*, vol. 43, no. 2, pp. 101–112, 2009.

[38] J. E. Little, X. Yuan, and M. I. Jones, “Characterisation of voids in fibre reinforced composite materials,” *NDT E Int.*, vol. 46, pp. 122–127, Mar. 2012.

[39] J. Kastner, B. Plank, D. Salaberger, and J. Sekelja, “Defect and Porosity Determination of Fibre Reinforced Polymers by X-ray Computed Tomography,” pp. 1–12, 2010.

[40] Y. Nikishkov, G. Seon, and A. Makeev, “Structural analysis of composites with porosity defects based on X-ray computed tomography,” *J. Compos. Mater.*, vol. 48, no. 17, pp. 2131–2144, Jul. 2013.

[41] Y. Nikishkov, L. Airoldi, and A. Makeev, “Measurement of voids in composites by X-ray Computed Tomography,” *Compos. Sci. Technol.*, vol. 89, pp. 89–97, Dec. 2013.

[42] G. Seon, A. Makeev, Y. Nikishkov, and E. Lee, “Effects of defects on interlaminar tensile fatigue behavior of carbon/epoxy composites,” *Compos. Sci. Technol.*, vol. 89, pp. 194–201, Dec. 2013.

[43] A. G. Stamopoulos, K. I. Tserpes, P. Prucha, and D. Vavrik, “Evaluation of porosity effects on the mechanical properties of carbon fiber-reinforced plastic

unidirectional laminates by X-ray computed tomography and mechanical testing," *J. Compos. Mater.*, vol. 50, no. 15, pp. 2087–2098, 2015.

[44] R. Sharma, V. V. Deshpande, A. R. Bhagat, P. Mahajan, and R. K. Mittal, "X-ray tomographical observations of cracks and voids in 3D carbon/carbon composites," *Carbon N. Y.*, vol. 60, pp. 335–345, 2013.

[45] J. S. U. Schell, M. Renggli, G. H. van Lenthe, R. Muller, and P. Ermanni, "Micro-computed tomography determination of glass fibre reinforced polymer meso-structure," *Compos. Sci. Technol.*, vol. 66, no. 13, pp. 2016–2022, 2006.

[46] A. E. Scott, I. Sinclair, S. M. Spearing, M. N. Mavrogordato, and W. Hepples, "Influence of voids on damage mechanisms in carbon/epoxy composites determined via high resolution computed tomography," *Compos. Sci. Technol.*, vol. 90, pp. 147–153, Jan. 2014.

[47] Y. Watanabe, "Derivation of linear attenuation coefficients from CT numbers for low-energy photons Derivation of linear attenuation coefficients from CT numbers for low-energy photons," *Phys. Med. Biol.*, vol. 44, pp. 2201–2211, 1999.

[48] E. Weber, M. Fernandez, P. Wapner, and W. Hoffman, "Comparison of X-ray micro-tomography measurements of densities and porosity principally to values measured by mercury porosimetry for carbon–carbon composites," *Carbon N. Y.*, vol. 48, no. 8, pp. 2151–2158, Jul. 2010.

[49] H. Dinnebier and I. Ehrlich, "The effects of severe temperature changes and high humidity on porous CFRP," pp. 14–20, 2014.

[50] B. Plank, S. Senck, C. Fürst, H. Scharleitner, and J. Kastner, "Qualitative and quantitative analysis of the process chain : wood polymer composite – C-template – C / Si / SiC-ceramic by means of X-ray computed tomography," *Ict 2014*, no. March 2015, p. 8, 2014.

[51] N. Otsu, "A Threshold Selection Method from Gray-Level Histograms," *IEEE Trans. Pattern Anal. Mach. Intell.*, vol. 20, no. 1, pp. 62–66, 1979.

[52] W. Niblack, *An Introduction to Digital Image Processing*. Prentice-Hall International Inc., 1986.

[53] F. Léonard, J. Stein, A. Wilkinson, and P. Withers, "3D Characterisation of Void Distribution in Resin Film Infused Composites," *Conf. Ind. Comput. Tomogr.*, vol. 17, no. 12, pp. 69–76, 2012.

[54] M. H. Hassan, A. R. Othman, and S. Kamaruddin, “Void Content Determination of Fiber Reinforced Polymers by Acid Digestion Method,” in *Advanced Materials Research*, 2013, vol. 795, no. September, pp. 64–68.

[55] B. Plank, G. Rao, and J. Kastner, “Evaluation of CFRP-Reference Samples for Porosity made by Drilling and Comparison with Industrial Porosity Samples by Means of Quantitative X-ray Computed Tomography,” - *Proc. 7th Int. Symp. NDT Aerospace, Bremen, Deutschl.*, pp. 1–10, 2015.

[56] B. Plank, C. Gusenbauer, S. Senck, H. Hoeller, and J. Kastner, “Porosity Determination in CFRP by means of X-ray ComputedTomography Methods,” in *12th European Conference of Non-Destructive Testing*, 2018.

[57] M. N. Bureau and J. Denault, “Fatigue resistance of continuous glass fiber / polypropylene composites : consolidation dependence,” *Compos. Sci. Technol.*, vol. 64, pp. 1785–1794, 2004.

[58] A. Zhang, H. Lu, and D. Zhang, “Research on the Mechanical Properties Prediction of Carbon / Epoxy Composite Laminates With Different Void Contents,” *Polym. Compos.*, pp. 15–20, 2016.

[59] R. Protz, N. Kosmann, M. Gude, W. Hufenbach, K. Schulte, and B. Fiedler, “Voids and their effect on the strain rate dependent material properties and fatigue behaviour of non-crimp fabric composites materials,” *Compos. Part B Eng.*, vol. 83, pp. 346–351, 2015.

[60] S. Sisodia, E. K. Gamstedt, F. Edgren, and J. Varna, “Effects of voids on quasi-static and tension fatigue behaviour of carbon-fibre composite laminates,” *J. Compos. Mater.*, vol. 49, no. 17, pp. 2137–2148, 2015.

[61] Z. Gurdal, A. P. Tomasino, and S. B. Biggers, “Effect of Processing Induced Defects on Laminate Response: Interlaminar Tensile Strength,” *Sampe*, vol. 27, no. September, pp. 39–49, 1991.

[62] T. Naganuma, K. Naito, J. Kyono, and Y. Kagawa, “Influence of prepreg conditions on the void occurrence and tensile properties of woven glass fiber-reinforced polyimide composites,” *Compos. Sci. Technol.*, vol. 69, no. 14, pp. 2428–2433, 2009.

[63] A. G. Stamopoulos, K. I. Tserpes, P. Prucha, and D. Vavrik, “Evaluation of porosity effects on the mechanical properties of carbon fiber-reinforced plastic

unidirectional laminates by X-ray computed tomography and mechanical testing," *J. Compos. Mater.*, vol. 50, no. 15, pp. 2087–2098, 2015.

[64] J. Varna, R. Joffe, L. A. Berglund, and T. S. Lundström, "Effect of voids on failure mechanisms in RTM laminates," *Compos. Sci. Technol.*, vol. 53, no. 2, pp. 241–249, 1995.

[65] J. Cinquin, V. Triquenaux, and Y. Rouesne, "Porosity influence on organic composite material mechanical properties," *16Th Int. Conf. Compos. Mater.*, pp. 1–8, 2007.

[66] N. Kosmann, J. M. Karsten, M. Schuett, K. Schulte, and B. Fiedler, "Determining the effect of voids in GFRP on the damage behaviour under compression loading using acoustic emission," *Compos. Part B Eng.*, vol. 70, pp. 184–188, 2015.

[67] J. Lee and C. Soutis, "A study on the compressive strength of thick carbon fibre-epoxy laminates," *Compos. Sci. Technol.*, vol. 67, no. 10, pp. 2015–2026, 2007.

[68] J. Hapke, F. Gehrig, N. Huber, K. Schulte, and E. T. Lilleodden, "Compressive failure of UD-CFRP containing void defects: In situ SEM microanalysis," *Compos. Sci. Technol.*, vol. 71, no. 9, pp. 1242–1249, 2011.

[69] W. V. Liebig, C. Viets, K. Schulte, and B. Fiedler, "Influence of voids on the compressive failure behaviour of fibrereinforced composites," *Compos. Sci. Technol.*, vol. 117, pp. 225–233, 2015.

[70] W. V. Liebig, C. Leopold, and K. Schulte, "Photoelastic study of stresses in the vicinity of a unique void in a fibre-reinforced model composite under compression," *Compos. Sci. Technol.*, vol. 84, pp. 72–77, 2013.

[71] S. F. M. de Almeida and Z. D. S. N. Neto, "Effect of void content on the strength of composite laminates," *Compos. Struct.*, vol. 28, no. 2, pp. 139–148, Jan. 1994.

[72] Z.-S. Guo, L. Liu, M. Zhang, and S. Du, "Critical Void Content for Thermoset Composite Laminates," *J. Compos. Mater.*, vol. 43, no. 17, pp. 1775–1790, 2009.

[73] T. Hayashi and J. Takahashi, "Influence of void content on the flexural fracture behaviour of carbon fiber reinforced polypropylene," *J. Compos. Mater.*, vol. 51, no. 29, pp. 4067–4078, 2017.

[74] A. R. Chambers, J. S. Earl, C. A. Squires, and M. A. Suhot, “The effect of voids on the flexural fatigue performance of unidirectional carbon fibre composites developed for wind turbine applications,” *Int. J. Fatigue*, vol. 28, no. 10, pp. 1389–1398, Oct. 2006.

[75] P.-O. Hagstrand, F. Bonjour, and J. -a. E. Månson, “The influence of void content on the structural flexural performance of unidirectional glass fibre reinforced polypropylene composites,” *Compos. Part A Appl. Sci. Manuf.*, vol. 36, no. 5, pp. 705–714, May 2005.

[76] L. Asp and F. Brandt, “Effects of pores and voids on the interlaminar delamination toughness of a carbon/epoxy composite,” in *Proceedings of 11th International Conference on Composite Materials, Australia.*, 1997, pp. 322–331.

[77] A. P. Mouritz, “Ultrasonic and Interlaminar Properties of Highly Porous Composites,” *J. Compos. Mater.*, vol. 34, no. 3, 2000.

[78] W. D. Bascom and J. B. Romans, “MICROVOIDS IN GLASS-RESIN COMPOSITES Their Origin and Effect,” *I&EC Prod. Res. Dev.*, vol. 7, no. 3, pp. 172–178, 1968.

[79] E. J. Kohn, A. G. Sands, and R. C. Clark, “GLASS-FILAMENT-WOUND COMPOSITES AND CORRELATION OF INTERLAMINAR SHEAR STRENGTH WITH VOID CONTENT,” *I&EC Prod. Res. Dev.*, vol. 7, no. 3, pp. 179–183, 1968.

[80] Y. Nikishkov, G. Seon, and A. Makeev, “Structural analysis of composites with porosity defects based on X-ray computed tomography,” *J. Compos. Mater.*, vol. 48, no. 17, pp. 2131–2144, 2014.

[81] L. Di Landro, A. Montalto, P. Bettini, S. Guerra, F. Montagnoli, T. Aerospaziali, P. Milano, D. Meccanica, and P. Milano, “Detection of Voids in Carbon / Epoxy Laminates and Their Influence on Mechanical Properties,” *Polym. Polym. Compos.*, vol. 25, no. 5, pp. 371–380, 2017.

[82] Y. Li, Q. Li, and H. Ma, “The voids formation mechanisms and their effects on the mechanical properties of flax fiber reinforced epoxy composites,” *Compos. Part A Appl. Sci. Manuf.*, vol. 72, pp. 40–48, 2015.

[83] H. Yoshida, T. Ogasa, and R. Hayashi, “Statistical Approach to the Relationship between ILSS and Void Content of CFRP *,” *Compos. Sci. Technol.*, vol. 25, pp. 3–18, 1986.

[84] L. W. Davies, R. J. Day, D. Bond, A. Nesbitt, J. Ellis, and E. Gardon, “Effect of cure cycle heat transfer rates on the physical and mechanical properties of an epoxy matrix composite,” *Compos. Sci. Technol.*, vol. 67, pp. 1892–1899, 2007.

[85] A. A. Goodwin, C. A. Howe, and R. J. Paton, “The role of voids in reducing the interlaminar shear strength in RTM laminates,” in *ICCM-11*, 1997, vol. IV, no. July, pp. 11–19.

[86] A. Kousourakis, A. P. Mouritz, and M. K. Bannister, “Interlaminar properties of polymer laminates containing internal sensor cavities,” *Compos. Struct.*, vol. 75, pp. 610–618, 2006.

[87] J. L. Thomason, “The interface region in glass fibre-reinforced epoxy resin composites : 2. Water absorption, voids and the interface,” *Composites*, vol. 26, no. 7, pp. 477–485, 1995.

[88] M. L. Costa, M. C. Rezende, and S. F. M. de Almeida, “Strength of Hygrothermally Conditioned Polymer Composites with Voids,” *J. Compos. Mater.*, vol. 39, no. 21, pp. 1943–1961, 2004.

[89] H. Koushyar, S. Alavi-soltani, B. Minaie, and M. Violette, “Effects of variation in autoclave pressure, temperature, and vacuum-application time on porosity and mechanical properties of a carbon fiber / epoxy composite *,” *J. Compos. Mater.*, vol. 46, no. 16, pp. 1986–2004, 2011.

[90] J.-M. Tang, W. Lee, and S. George, “Effects of Cure Pressure on Resin Flow , Voids , and Mechanical Properties,” *J. Compos. Mater.*, vol. 21, no. May 1987, pp. 421–440, 1987.

[91] J. W. Mar and K. Y. Lin, “Fracture mechanics correlation for tensile failure of filamentary composites with holes,” *J. Aircr.*, vol. 14, no. 7, pp. 703–704, 1977.

[92] H. Jeong, “Effects of Voids on Mechanical Strength and Ultrasonic Attenuation of Laminated Composites,” *J. Compos. Mater.*, vol. 31, no. 3, 1997.

[93] M. L. Costa, S. F. M. d. Almeida, and M. C. Rezende, “The influence of porosity on the interlaminar shear strength of carbon/epoxy and carbon/bismaleimide fabric laminates,” *Compos. Sci. Technol.*, vol. 61, no. 14, pp. 2101–2108, Nov. 2001.

[94] H. Zhu, D. Li, D. Zhang, B. Wu, and Y. Chen, “Influence of voids on interlaminar shear strength of carbon/epoxy fabric laminates,” *Trans. Nonferrous Met. Soc. China*, vol. 19, pp. s470–s475, Sep. 2009.

[95] S. H. A. RUEDA, “Curing , Defects and Mechanical Performance of Fiber-Reinforced Composites,” UNIVERSIDAD POLITECNICA DE MADRID, 2013.

[96] K. J. Bowles and S. Frimpong, “Void Effects on the Interlaminar Shear Strength of Unidirectional Graphite-Fiber-Reinforced Composites,” *J. Compos. Mater.*, vol. 26, no. 10, pp. 1487–1509, 1992.

[97] P. L. N. Murthy and C. C. Chamis, “Intefrated Composite Analyzer (ICAN). User and Programmers Manual,” *NASA Tech. Pap. 2515*, 1986.

[98] D. Ashouri Vajari, “A micromechanical study of porous composites under longitudinal shear and transverse normal loading,” *Compos. Struct.*, vol. 125, pp. 266–276, 2014.

[99] D. Ashouri Vajari, C. González, J. Llorca, and B. N. Legarth, “A numerical study of the influence of microvoids in the transverse mechanical response of unidirectional composites,” *Compos. Sci. Technol.*, vol. 97, pp. 46–54, Jun. 2014.

[100] J. Lubliner, J. Oliver, S. Oller, and E. Oñate, “A plastic-damage model for concrete,” *Int. J. Solids Struct.*, vol. 25, no. 3, pp. 299–326, 1989.

[101] H. Huang and R. Talreja, “Effects of void geometry on elastic properties of unidirectional fiber reinforced composites,” *Compos. Sci. Technol.*, vol. 65, no. 13, pp. 1964–1981, Oct. 2005.

[102] P. a. Carraro, L. Maragoni, and M. Quaresimin, “Influence of manufacturing induced defects on damage initiation and propagation in carbon/epoxy NCF laminates,” *Adv. Manuf. Polym. Compos. Sci.*, vol. 1, no. 1, pp. 44–53, Feb. 2015.

[103] Y. Nikishkov, G. Seon, and A. Makeev, “Structural analysis of composites with porosity defects based on X-ray computed tomography,” *J. Compos. Mater.*, vol. 48, no. 17, pp. 2131–2144, 2014.

[104] P. Maimi, P. P. Camanho, J. A. Mayugo, and C. G. Davila, “A continuum damage model for composite laminates: Part I – Constitutive model,” *Mech. Mater.*, vol. 39, pp. 897–908, 2007.

[105] S. T. Pinho, L. Iannucci, and P. Robinson, “Physically based failure models and criteria for laminated fibre-reinforced composites with emphasis on fibre kinking. Part II: FE implementation,” *Compos. Part A Appl. Sci. Manuf.*, vol. 37, no. 5, pp. 766–777, 2006.

[106] S. T. Pinho, L. Iannucci, and P. Robinson, “Physically-based failure models and criteria for laminated fibre-reinforced composites with emphasis on fibre kinking: Part I: Development,” *Compos. Part A Appl. Sci. Manuf.*, vol. 37, no. 5, pp. 63–73, 2006.

[107] A. Turon, C. G. Dávila, P. P. Camanho, and J. Costa, “An engineering solution for mesh size effects in the simulation of delamination using cohesive zone models,” *Eng. Fract. Mech.*, vol. 74, no. 10, pp. 1665–1682, 2007.

[108] S. T. Pinho, L. Iannucci, and P. Robinson, “Formulation and implementation of decohesion elements in an explicit finite element code,” *Compos. Part A Appl. Sci. Manuf.*, vol. 37, no. 5, pp. 778–789, 2006.

[109] C. G. Davila, P. P. Camanho, and A. Turon, “Effective Simulation of Delamination in Aeronautical Structures Using Shells and Cohesive Elements,” *J. Aerosp. Eng.*, vol. 45, no. 2, pp. 663–672, 2008.

[110] W. G. Jiang, S. R. Hallett, B. G. Green, and M. R. Wisnom, “A concise interface constitutive law for analysis of delamination and splitting in composite materials and its application to scaled notched tensile specimens,” *Int. J. Numer. Methods Eng.*, vol. 69, no. 9, pp. 1982–1995, 2007.

[111] X. Li, S. R. Hallett, and M. R. Wisnom, “A finite element based statistical model for progressive tensile fibre failure in composite laminates,” *Composites Part B: Engineering*, vol. 45, no. 1. pp. 433–439, 2013.

[112] C. G. Davila, P. P. Camanho, and C. A. Rose, “Failure Criteria for FRP Laminates,” *J. Compos. Mater.*, vol. 39, no. 4, pp. 323–345, 2005.

[113] S. R. Hallett, B. G. Green, W. G. Jiang, K. H. Cheung, and M. R. Wisnom, “The open hole tensile test: A challenge for virtual testing of composites,” *Int. J. Fract.*, vol. 158, no. 2, pp. 169–181, 2009.

[114] B. Y. Chen, T. E. Tay, P. M. Baiz, and S. T. Pinho, “Numerical analysis of size effects on open-hole tensile composite laminates,” *Composites Part A: Applied Science and Manufacturing*, vol. 47, no. 1. pp. 52–62, 2013.

[115] E. Abisset, F. Daghia, and P. Ladevze, “On the validation of a damage mesomodel for laminated composites by means of open-hole tensile tests on quasi-isotropic laminates,” *Composites Part A: Applied Science and Manufacturing*, vol. 42, no. 10. pp. 1515–1524, 2011.

[116] F. P. van der Meer, L. J. Sluys, S. R. Hallett, and M. R. Wisnom, “Computational modeling of complex failure mechanisms in laminates,” *J. Compos. Mater.*, vol. 46, no. 5, pp. 603–623, 2011.

[117] P. P. Camanho, P. Maimi, and C. G. Davila, “Prediction of size effects in notched laminates using continuum damage mechanics,” *Compos. Sci. Technol.*, vol. 67, pp. 2715–2727, 2007.

[118] G. Allegri, M. R. Wisnom, and S. R. Hallett, “A simplified approach to the damage tolerance design of asymmetric tapered laminates. Part I: Methodology development,” *Composites Part A: Applied Science and Manufacturing*, vol. 41, no. 10. pp. 1388–1394, 2010.

[119] G. Allegri, M. R. Wisnom, and S. R. Hallett, “A simplified approach to the damage tolerance design of asymmetric tapered laminates. Part II: Methodology validation,” *Compos. Part A*, vol. 41, pp. 1395–1402, 2010.

[120] L. Kawashita, M. I. Jones, S. R. Hallett, M. R. Wisnom, and S. Giannis, “High fidelity modelling of tapered laminates with internal ply terminations,” *18th Int. Conf. Compos. Mater.*, no. ii, pp. 1–6, 2011.

[121] G. Allegri, L. F. Kawashita, R. Backhouse, M. R. Wisnom, and S. R. Hallett, “On the optimization of tapered composite laminates in preliminary structural design,” *17th Int. Conf. Compos. Mater.*, 2009.

[122] S. Mukhopadhyay, M. I. Jones, and S. R. Hallett, “Compressive failure of laminates containing an embedded wrinkle; Experimental and numerical study,” *Compos. Part A Appl. Sci. Manuf.*, vol. 73, pp. 132–142, 2015.

[123] M. L. Taylor, R. D. Franich, J. V. Trapp, and P. N. Johnston, “The effective atomic number of dosimetric gels RID B-6628-2009,” *Australas. Phys. Eng. Sci. Med.*, vol. 31, no. 2, pp. 131–138, 2008.

[124] R. A. Smith, “Ultrasonic defect sizing in carbon-fibre composites - an initial study,” *J. Br. Inst. NDT*, vol. 36, no. 8, pp. 595–605, 1994.

[125] B. Plank, C. Gusenbauer, S. Senck, H. Hoeller, and J. Kastner, “Porosity Determination in CFRP by means of X-ray Computed Tomography Methods,” in *12th European Conference of Non-Destructive Testing*, 2018, pp. 1–2.

[126] I. Gagauz, L. F. Kawashita, and S. R. Hallett, “Effect of voids on interlaminar behaviour of carbon/epoxy composites,” in *ECCM 2016 - Proceeding of the 17th European Conference on Composite Materials*, 2016, no. June, pp. 26–30.

[127] M. L. Taylor, R. D. Franich, J. V Trapp, and P. N. Johnston, “The effective atomic number of dosimetric gels,” *APESM*, vol. 31, no. 2, 2008.

[128] “ASTM 2344. Standard Test Method for Short-Beam Strength of Polymer Matrix Composite Materials.”

[129] O. J. Nixon-Pearson, J. P. H. Belnoue, D. S. Ivanov, K. D. Potter, and S. R. Hallett, “An experimental investigation of the consolidation behaviour of uncured prepregs under processing conditions,” *J. Compos. Mater.*, vol. 51, no. 13, pp. 1911–1924, 2017.

[130] Hexcel, “HexPly 8552,” 2016.

[131] Hexcel, “HexPly M21 Data Sheet,” 2015.

[132] D. H. J. A. Lukaszewicz and K. D. Potter, “The internal structure and conformation of prepreg with respect to reliable automated processing,” *Compos. Part A Appl. Sci. Manuf.*, vol. 42, no. 3, pp. 283–292, 2011.

[133] T. K. O’Brien, W. M. Johnston, and G. J. Toland, “Mode II Interlaminar Fracture Toughness and Fatigue Characterization of a Graphite Epoxy Composite Material,” *Natl. Aeronaut. Sp. Adm.*, no. NASA/TM-2010-216838, pp. 1–32, 2010.

[134] K. M. Gaddikeri, “Interface Toughness Measurements in Blade Stiffened Composite Skin Specimens,” in *18th NASAS (Eighteenth National Seminar on Aerospace Structures)*, 2014.

[135] Y. He and A. Makeev, “International Journal of Solids and Structures Nonlinear shear behavior and interlaminar shear strength of unidirectional polymer matrix composites : A numerical study,” *Int. J. Solids Struct.*, vol. 51, no. 6, pp. 1263–1273, 2014.

[136] “ASTM D2344 / D2344M-16, Standard Test Method for Short-Beam Strength of Polymer Matrix Composite Materials and Their Laminates.” ASTM International, West Conshohocken, PA, 2016.

[137] A. Makeev, G. Seon, and E. Lee, “Failure predictions for carbon/epoxy tape laminates with wavy plies,” *J. Compos. Mater.*, vol. 44, no. 1, pp. 95–112, 2010.

[138] G. Catalanotti, P. P. Camanho, and A. T. Marques, “Three-dimensional failure criteria for fiber-reinforced laminates,” *Composite Structures*, vol. 95. pp. 63–79, 2013.

10 APPENDICES

APPENDIX 1 SUPPLEMENTARY MATERIAL CHAPTER 4

Table 10-1. Average void content in different batches of cross-ply IM7/8552

Batch	No of samples	Average void content, %	SD
Batch 1	16	7.108	0.453
Batch 2	16	5.996	0.646
Batch 3	16	4.269	0.435
Batch 4	12	3.774	0.513
Batch 5	12	3.862	0.425
Batch 6	8	3.294	0.625
Batch 7	8	2.436	0.883
Batch 8	8	1.62	0.394
Batch 9 (Ref)	16	0	0

Table 10-2. Average void content in different batches of cross-ply IMA/M21

Batch	No of samples	Average void content, %	SD
Batch 1	16	10.733	1.380
Batch 2	12	9.582	1.750
Batch 3	12	10.798	1.635
Batch 4	8	9.115	0.337
Batch 5	8	6.758	1.210
Batch 6	8	8.878	2.022
Batch 7	8	8.872	0.623
Batch 8	12	5.748	0.504
Batch 9	8	2.455	0.674
Batch 10 (Ref)	16	0	0